Aus der Klinik für Diagnostische und Interventionelle Radiologie
der Universität Heidelberg
Ärztlicher Direktor: Prof. Dr. med. Hans-Ulrich Kauczor

SPATIALLY RESOLVED QUANTIFICATION OF RADIATION EXPOSURE ASSOCIATED WITH COMPUTED TOMOGRAPHY EXAMINATIONS

Towards the development of virtual dosimetry

Inauguraldissertation
zur Erlangung des Doctor scientiarum humanarum (Dr. sc. hum.)
an der
Medizinischen Fakultät Heidelberg
der
Ruprecht-Karls-Universität

vorgelegt von

ANDREA STEUWE

aus
Bünde

2019

Dekan: Prof. Dr. med. Andreas Draguhn
Doktorvater: Prof. Dr. med. Hans-Ulrich Kauczor

Im Idealfall ist die Familie Trampolin und Sprungtuch in einem.
*Stefan Wittlin (*1961)*

CONTENTS

LIST OF FIGURES

LIST OF TABLES

ACRONYMS

1D	one-dimensional
2D	two-dimensional
3D	three-dimensional
4D	four-dimensional
AAPM	American Association of Physicists in Medicine
AEC	automatic exposure control
ALARA	as low as reasonably achievable
a.p.	anterio-posterior
ATCM	angular tube-current modulation
BMI	body mass index
BREP	boundary representation
CBCT	cone beam computed tomography
CNR	contrast-to-noise ratio
CPU	central processing unit
CT	computed tomography
CTA	computed tomography angiography
CTDI	computed tomography dose index
$CTDI_{vol}$	volumetric computed tomography dose index
DAP	dose-area product
DECT	dual-energy computed tomography
DICOM	Digital Imaging and Communications in Medicine
DLP	dose-length product
DNA	deoxyribonucleic acid
DSCT	dual-source computed tomography
ED	effective dose
EVAR	endovascular aortic repair

FADS	fan-angle dependent spectra
FM	fan-angle dependent photon fluence modulation
FOV	field-of-view
GB	gigabyte
Geant4	Geometry and Tracking 4
GI	gastro-intestinal
GiB	gibibyte
GPU	graphics processing unit
HU	Hounsfield unit (unit of CT number)
ICRP	International Commission on Radiological Protection
ICRU	International Commission on Radiation Units
ID	identification
LTCM	longitudinal tube-current modulation
mAs	milliampere seconds (unit of tube-current time product)
MC	Monte Carlo
MDCT	multi-detector computed tomography
MiB	mebibytes
MIRD	Medical Internal Radiation Dose
MRI	magnetic resonance imaging
mSv	millisievert (unit of effective dose)
NIST	National Institute of Standards and Technology
NM	no photon fluence modulation
ORNL	Oak Ridge National Laboratory
PBF	physical beam-shaping filter
PDF	probability density function
PENELOPE	PENetration and Energy LOss of Positrons and Electrons
pixel	picture element
RAM	random-access memory
ROI	region-of-interest

SDD	source-to-detector distance
SID	source-to-isocenter distance
SNR	signal-to-noise ratio
SSDE	size-specific dose estimate
TCM	tube-current modulation
TCTP	tube-current time product
$TCTP_{eff}$	effective tube-current time product
$TCTP_{ref}$	reference tube-current time product
TLD	thermoluminescent detector
US	ultrasound
voxel	volume element
WED	water-equivalent diameter

1

INTRODUCTION

X-ray computed tomography (CT) describes the three-dimensional (3D) acquisition of x-ray projections of a subject or object, which are subsequently reconstructed to a 3D image data set. The main advantage of CT in diagnostic radiology is the visualization of the body structures in slices without the superimposition of tissues. Spatial resolution in the sub-millimeter range in all three dimensions can be obtained with this technique, enabling the detailed evaluation of body structures.
Of all radiological procedures utilizing ionizing radiation, 9% were CT examinations in Germany, in 2014. Despite this fairly low percentage compared to dental examinations (41%) or skeletal radiography (29%), CT contributed to the collective effective dose from radiological procedures with 65% (BfS 2016b). Because radiological examinations using ionizing radiation are frequent at present, the utilization of ionizing radiation in diagnostic procedures is controversially discussed due to the potential risk of radiation-induced cancer.
Several methods exist to estimate the dose (a measure for the energy deposition of the x-rays e.g. per unit of tissue mass) resulting from radiation exposure, by means of conversion factors, test specimen (phantoms), dose detectors (e.g. ionization chambers), or Monte Carlo (MC) simulations. These methods vary in precision, applicability, and customization options. Individualized dosimetry plays an increasing role in clinical radiology, especially for patients receiving multiple CT examinations over a short period of time, such as during a cancer treatment. The individualized dosimetry can take patient morphology and changes in morphology into account, e.g. through disease or treatment-induced weight loss. This is necessary since the body constitution, e.g. weight, height, or composition, greatly impacts dose deposition. The research presented in this thesis describes the development of a MC software tool aiming at the quantification of the radiation exposure associated with CT examinations to calculate patient-specific radiation exposure maps.

Section 1.1 introduces the clinical background of CT imaging. Afterwards, the general principle of CT, image acquisition, and the technical setup of a CT scanner are described in section 1.2. This section also provides details on the x-ray source and photon emission, photon filtration, and the utilized tube potentials of x-ray sources. The underlying physical principles of the interactions of photons in matter are explained in section 1.3. Section 1.4 covers the radiation exposure associated with CT examinations. An overview over the radiation exposure from diagnostic radiology in Germany, the related risk from ionizing radiation, and techniques for dose reduction in CT are provided in this section. Section 1.5 presents current methods for determining the radiation exposure of CT examinations. The first chapter ends with the motivation and description of the goals of this work (section 1.6).

1.1 APPLICATIONS OF COMPUTED TOMOGRAPHY (CT) IMAGING

The contrast between body tissues observed on CT images is a result of differences in attenuation properties of tissues, which are measured by the CT scanner during the acquisition. CT is advantageous for displaying bony structures and, combined with the administration of contrast agents, it allows to assess blood flow e.g. in the aorta and tissues (organ perfusion). Due to the large field-of-view (FOV) of the CT scanner (approximately 50 cm), the aorta and branching vessels, e.g. the supply of the kidneys, can be examined at the same time. CT is performed for staging of tumor diseases and follow-up examinations after chemotherapy or surgical treatment. It is a fast technique allowing image acquisition, reconstruction, and assessment within a few minutes. A typical non-enhanced (native) acquisition of the thorax and abdomen can be performed in less than 10 seconds. CT, aside from ultrasound (US) imaging, is a standard for trauma patients following accidents since fractures and free fluids (blood) can be identified quickly. Furthermore, CT is performed in vascular surgery, e.g. as immediate control and follow-up of endovascular aortic repair (EVAR), an intervention during which a stent is implanted in the aorta to remodel blood flow.
In terms of image quality, one disadvantage of CT is the low contrast between different types of soft tissues since their material composition and density properties are similar. For soft tissue imaging, magnetic resonance imaging (MRI) is superior to CT.
Due to the associated radiation exposure, pediatric CT is solely performed if alternative imaging methods, such as MRI or US, are contraindicated or not sufficient for clinical diagnosis. Due to the long acquisition times of MRI, pediatric patients might need to be anesthetized, involving separate risks and side effects. More information on the radiation exposure in CT imaging is provided in section 1.4.

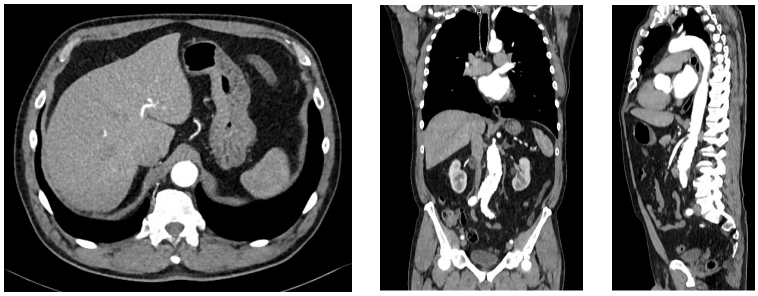

(a) Axial (b) Coronal (c) Sagittal

Figure 1.1: Axial, coronal, and sagittal reconstruction of a single contrast-enhanced computed tomography acquisition. Since this acquisition directly followed contrast-agent administration, the heart and aorta appear very bright. Due to the high density of bone, the ribs, pelvis, and spine are clearly distinguishable from soft tissue and the lungs.

1.2 OPERATING PRINCIPLE OF CT

Image acquisition in planar radiography and computed tomography is based on the attenuation (absorption and scattering) of photons (x-rays) in tissues, varying with photon energy, material composition, and density. Only unabsorbed and unscattered photons positively contribute to the image signal. Absorbed photons have lost all of their incident kinetic energy in a tissue and will not reach the image detector at all. Scattered photons have either lost parts of their incident kinetic energy, or have changed their initial direction. A scattered photon might still be detected, however, it adversely affects the image quality by increasing image noise. Bones or metals absorb and scatter photons to a higher degree than soft tissue or fat. On the reconstructed images, materials with a high density (e.g. bone) appear brighter than low-attenuating tissues. Tissues of the human body can be roughly divided into the materials soft tissue, bone, and air (lungs). The image contrast between these three material types in the reconstructed images is large. However, differences between different soft tissue types (e.g. muscle tissue, liver tissue, intestines) in terms of material composition and density are more subtle. As a consequence, the soft-tissue contrast of CT images is rather poor.

In planar radiography (x-ray imaging), a projection or superimposition of all tissues between the x-ray source and the detector is obtained as the source and the detector position are fixed for a single acquisition. Since only a two-dimensional (2D) image is obtained from planar radiography, an assessment of the third dimension (e.g. depth) is impossible. During a CT acquisition, the photon-emitting source and the detector rotate around the patient while the patient on the table (bed) is moved through the scanner gantry (either in a steady or in a step-wise motion). In CT, in contrast to planar radiography, thousands of projections from various positions are obtained, which are reconstructed to a 3D image set after acquisition. The main advantage of CT is the visualization of the body structures in slices without the superimposition of tissues. A spatial resolution in the sub-millimeter range can be obtained in all three dimensions, enabling a detailed evaluation of body structures. Images can be reconstructed in the three main planes (axial, coronal, sagittal), and additionally, in oblique planes (cf. figure 1.1).
Furthermore, the image appearance can be adapted retrospectively (window and level settings), allowing to view the reconstructed images with different contrast and brightness to enhance the visibility of specific structures (see figure 1.2).

1.2.1 TECHNICAL SETUP

A CT scanner can be divided into three main components: (1) the x-ray emitting source, (2) beam-shaping filtration, and (3) the detector for image acquisition. A schematic drawing of a CT scanner is shown in figure 1.3.
The first part, the x-ray source, produces a continuous bremsstrahlung spectrum with characteristic peaks. Section 1.2.2 provides more information on the production of the x-ray spectrum, its efficiency at different tube potentials, and the accessibility

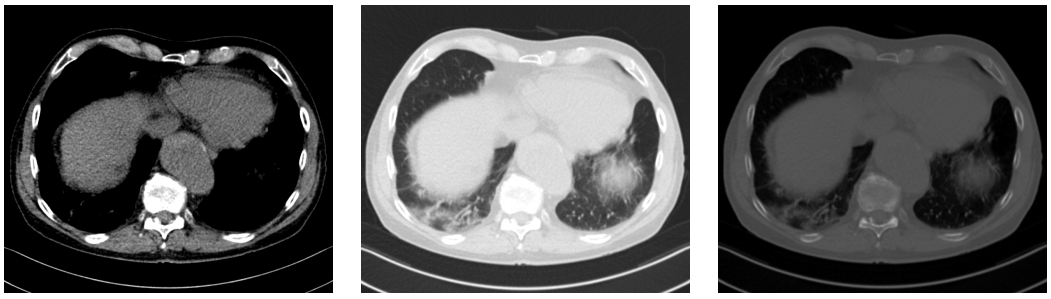

(a) Soft tissue setting (b) Lung setting (c) Bone setting

Figure 1.2: Soft tissue, lung, and bone window settings for the same slice to enhance visibility of specific structures. The abdomen window setting (window (W) = 342 HU, level (L) = 56 HU) allows to differentiate between soft tissue types. The lung window setting (W = 465 HU, L = -498 HU) provides detailed visibility of lung tissue. Here, the contrast between soft tissue types or bony structures is barely visible. The bone window setting (W = 3077 HU, L = 570 HU) enhances the visibility of differences in bone density.

of x-ray spectra of clinical CT scanners. The bremsstrahlung spectrum contains photon energies <20 keV. The chance that these photons will reach the detector without interaction is very low as they are easily absorbed already in small amounts of tissue. To reduce the amount of low-energy photons, which would only increase patient dose but not positively contribute to image quality, a filter, usually made of aluminum, is implemented as part of the x-ray source. A bremsstrahlung spectrum at 100 kV_p with characteristic tungsten peaks and the effect of additional aluminum filtration is depicted in figure 1.4. The emitted x-ray fan beam covers around 50 cm in x-direction at the isocenter of the scanner, and, depending on the specific scanner, a z-coverage of ~3-16 cm.

The second part is the beam-shaping filter, also called bowtie filter, due to its shape. The beam-shaping filter has two effects: (1) altering the photon fluence along the fan beam and (2) additional filtration of the emitted photons, especially at the edges of the fan beam. The modulation of the photon fluence and reduction of the amount of photons at the edges of the FOV is a desired effect. Due to its shape, the beam-shaping filter reduces the photon fluence towards the sides of the fan beam, resulting in a fan-angle dependent photon fluence. The reduction of photons at the fan-beam sides allows a constant exposure of the detector (ICRU 2012). An axial cut through a human's body is usually elliptical shaped (compare to the "patient" shape in figure 1.3). The reduced x-ray path length through the body towards the edges of the fan beam results in less photon attenuation, counterbalancing the reduced photon fluence in these regions. Both the dynamic range of the detector and scatter are reduced by the beam-shaping filter as the flux in paths with low attenuation is reduced (Hsieh and Pelc 2013; Steuwe et al. 2018). The side effect of the beam-shaping filter is the additional filtration of the emitted spectrum, increasing the mean spectral energy towards the side of the fan beam. This spectral distortion is called beam-hardening and especially affects photons with energies <35 keV. The mean spectral energy at the isocenter is therefore lower than the mean spectral

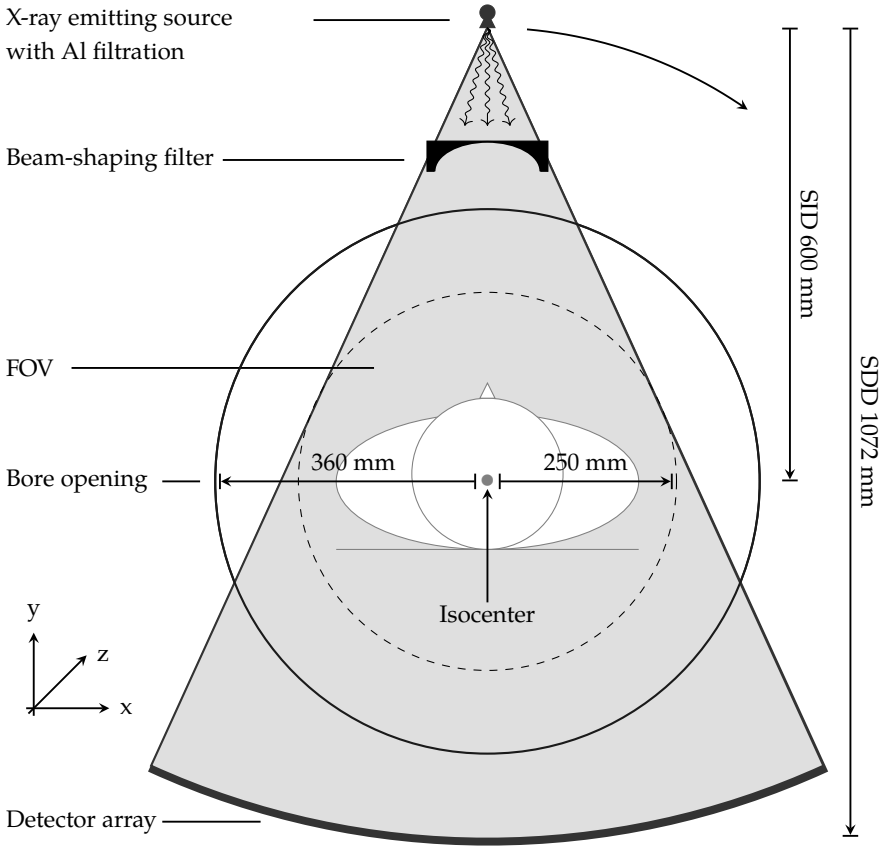

Figure 1.3: Schematic drawing of a computed tomography (CT) scanner. Dimensions in scheme correspond to an Aquilion™16 CT system, Toshiba Medical Systems Corporation, Nasu, Japan (Amber Diagnostics 2018; MHRA 2004; NHS 2009). Refer to appendix A for detailed CT scanner dimensions. Abbreviations: Aluminum (Al), source-to-detector distance (SDD), source-to-isocenter distance (SID), field-of-view (FOV).

energy at the edges of the FOV, see also figure 2.4 in the materials and methods section. Usually, a CT scanner contains two or more beam-shaping filters, differing in shape and material, which are mainly chosen based on the patient size (ICRU 2012).

Both the (aluminum) filter inside the x-ray source and the beam-shaping filter are scanner-dependent and information about their exact dimensions and materials are usually proprietary. Details on the transmission of the beam-shaping filter can be obtained by performing transmission measurements.

The third part is the image detector, combined with an anti-scatter grid to remove scattered photons prior to detection. Since the final image reconstruction is not focus of this work, the detector, reconstruction techniques, and employed kernels are not covered in detail in this thesis. Please refer to the literature for details on these contents, e.g. Bushberg et al. (2012) and Hsieh (2015).

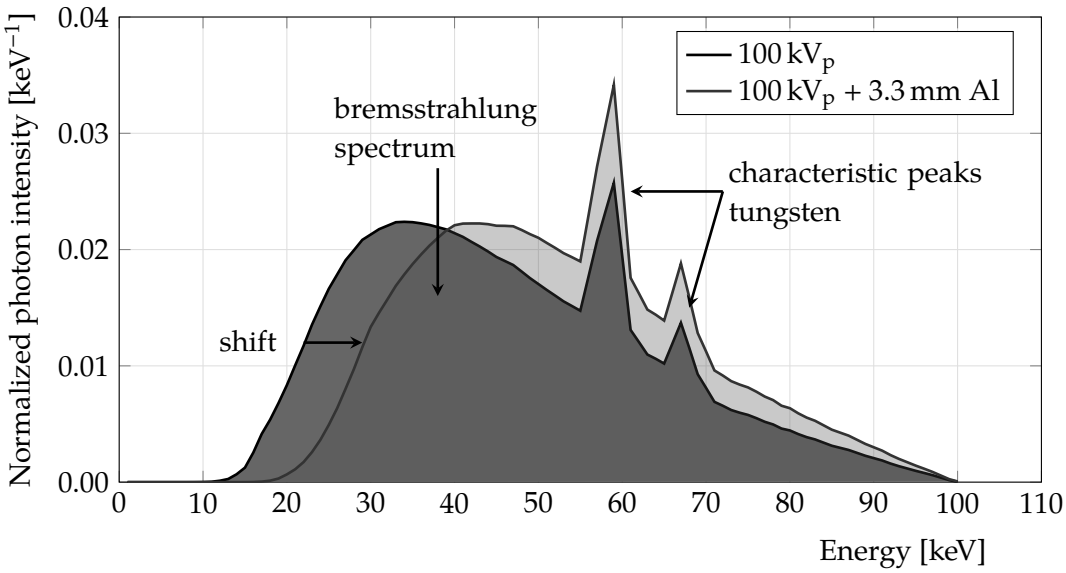

Figure 1.4: X-ray tube output: continuous bremsstrahlung spectrum and characteristic tungsten peaks (57.98, 59.32, and 67.24 keV) at a tube potential of 100 kV_p. The peaks at 57.98 and 59.32 keV are not resolved in this plot. Addition of aluminum (Al) filtration shifts the mean spectral energy from 46.7 to 52.7 keV by removing low-energy photons while maintaining the same maximum photon energy (Siemens Healthineers 2018).

1.2.2 X-RAY EMISSION

The function of the x-ray source (also referred to as x-ray tube) is the production and emission of photons. The x-ray source consists of an electron-emitting cathode and an anode as electron target. Electrons are accelerated between the cathode and the anode due to an applied potential between the two electrodes. In clinical CT, this (tube) potential is usually in the range of 70 and 150 kV. Electrons accelerated by a tube potential of 120 kV can obtain a maximum kinetic energy of 120 keV. In the anode, electrons can undergo either an interaction with the strong field of a nucleus of the target atom or with its surrounding, or they undergo an interaction with the electrons of the target atom, emitting photons of various energies. Figure 1.4 shows the emitted x-ray spectrum for a tube potential of 100 kV_p.

1.2.2.1 *Bremsstrahlung spectrum*

When electrons interact with the strong field of a nucleus or its close surrounding, bremsstrahlung is emitted. Bremsstrahlung is a polyenergetic photon distribution in a continuous spectrum. Electrons are decelerated near the nucleus due to Coulombic forces, thereby causing a change in their direction and a loss of energy. The lost energy is emitted as photons of that energy. The smaller the distance of an incoming electron to the nucleus, the larger the energy of the emitted photon. The maximum obtainable photon energy is the kinetic energy of the incoming electron (Bushberg et al. 2012, pp. 171-206).

1.2.2.2 *Characteristic peaks*

When an accelerated electron interacts with an orbital electron of one of the inner shells (e.g. K-shell), it ejects this (K-shell) electron. The vacancy in the K-shell is filled by an electron of the L-shell (electrons of other outer shells are also possible), thereby emitting a characteristic x-ray. Its energy is determined by the difference in binding energies between the K- and the L-shell. This process repeats itself until all inner shells are complete again. The emitted photons are called characteristic x-rays, as their energies are characteristic to the specific anode material. For tungsten, the characteristic x-ray energies are at 57.98, 59.32, and 67.24 keV (Bushberg et al. 2012, pp. 171-206).

1.2.2.3 *Efficiency of x-ray sources*

The efficiency of x-ray emission depends on the chosen tube potential. The higher the tube potential, the larger the number of emitted photons. In clinical CT, x-ray emission is approximately proportional to the square of the tube potential (Bushberg et al. 2012, pp. 171-206):

$$\text{x-ray emission efficiency} \propto (\text{tube potential})^2 \tag{1.1}$$

$$\text{x-ray emission efficiency at } \mathrm{kV_{p_2}} \equiv \left(\frac{\mathrm{kV_{p_2}}}{\mathrm{kV_{p_1}}}\right)^2 \tag{1.2}$$

Hence, the x-ray emission for a tube potential of $\mathrm{kV_{p_2}} = 80\,\mathrm{kV_p}$ is approximately 0.44 times the emission for a tube potential of $\mathrm{kV_{p_1}} = 120\,\mathrm{kV_p}$. Table 1.1 provides an overview of the tube-potential dependent x-ray efficiency. A reduced x-ray emission efficiency can be counterbalanced by increasing the tube current, given in milliampere (mA). An important measure in CT is the tube-current time product (TCTP), given in milliampere seconds (mAs), which is the product of the tube current and the duration of the x-ray exposure. The higher the tube current or the longer the exposure duration, the more photons are emitted from the x-ray source.

Table 1.1: Efficiency of x-ray emission at different tube potentials ($\mathrm{kV_{p_2}}$) relative to the efficiency at $\mathrm{kV_{p_1}} = 120\,\mathrm{kV_p}$, according to equation 1.2. X-ray emission efficiency increases with increasing tube potential.

Tube potential [$\mathrm{kV_{p_2}}$]	**X-ray efficiency compared to 120 $\mathrm{kV_{p_1}}$**
80	0.44
100	0.69
120	1.00
140	1.36

Patient attenuation characteristics vary at different tube potentials, which additionally needs to be taken into account for CT acquisition planning. Since low-energy photons are more easily attenuated than high-energy photons, the TCTP for a tube potential of 80 kV_p needs to be higher than the TCTP for a tube potential of 120 kV_p to obtain a similar signal-to-noise ratio (SNR)[1] on the final reconstructed image.
A practical approach for increasing the TCTP for lower tube potentials is to increase the TCTP by a factor of 1.5, for a reduction in tube potential of 20 kV_p. Hence, given a tube potential of 120 kV_p, a reduction of the tube potential to 80 kV_p requires an increase in TCTP by a factor of 2.25 (1.5 x 1.5). This factor only accounts for the reduced efficiency at a tube potential of 80 kV_p compared to 120 kV_p, but not for the higher attenuation of the low-energy photons. Bushberg et al. (2012, pp. 171-206) provide a more drastic approach, accounting for both the reduced efficiency and the higher attenuation of photon spectra with lower peak energies, increasing the necessary TCTP to a larger degree (factor of 7.6, see equation 1.3 and figure 1.5).

$$\left(\frac{kV_{p_1}}{kV_{p_2}}\right)^5 \cdot mAs_1 = mAs_2 \tag{1.3}$$

1.2.2.4 *X-ray source spectra accessibility*

To study the influence of x-ray spectra on radiation exposure, information on the source components or the emitted x-ray spectra is necessary (Ay et al. 2005). As a consequence of different x-ray tube design (e.g. anode geometry and material) and choice of additional filtration, spectra of different CT scanners and vendors differ in shape and mean spectral energy (Steuwe et al. 2018). The most comprehensive method to obtain source spectra is to model the complete source and physical effects, e.g. in MC simulations (Kim et al. 2012; Taleei and Shahriari 2009). This method requires information on x-ray source geometry, material, and filtration, which is unfortunately often proprietary (Kramer et al. 2017; Massoumzadeh et al. 2009).
The measurement of source spectra via Compton spectroscopy is one option to obtain spectral information, and also to study the effect of beam-hardening due to the beam-shaping filter (Matscheko and Ribberfors 1987). Especially the accessibility of information on spectra after beam-shaping induced spectral distortion is limited. The advantage of Compton spectroscopy is the extensive information about the spectra and corresponding mean energies gained. However, this method requires operating the CT scanner in service mode as the source rotation needs to be switched off (Bazalova and Verhaegen 2007; Steuwe et al. 2018). Other research groups determine spectra by means of transmission measurements (Duan et al. 2011; Lin et al. 2014) or half value thickness measurements (Randazzo and Tambasco 2015). Another option is the calculation of source spectra with mathematical models (Sandborg et al. 1994; Zhou and Boone 2008) or to use source spectra published in the

1 The signal-to-noise ratio (SNR) is a measure of the distinctness of an object on an image. The SNR describes the ratio of the integrated photon signal over a region-of-interest (ROI) and the measured background noise. The background noise is the standard deviation in a homogeneous background region on an image. (Bushberg et al. 2012, pp. 60-100)

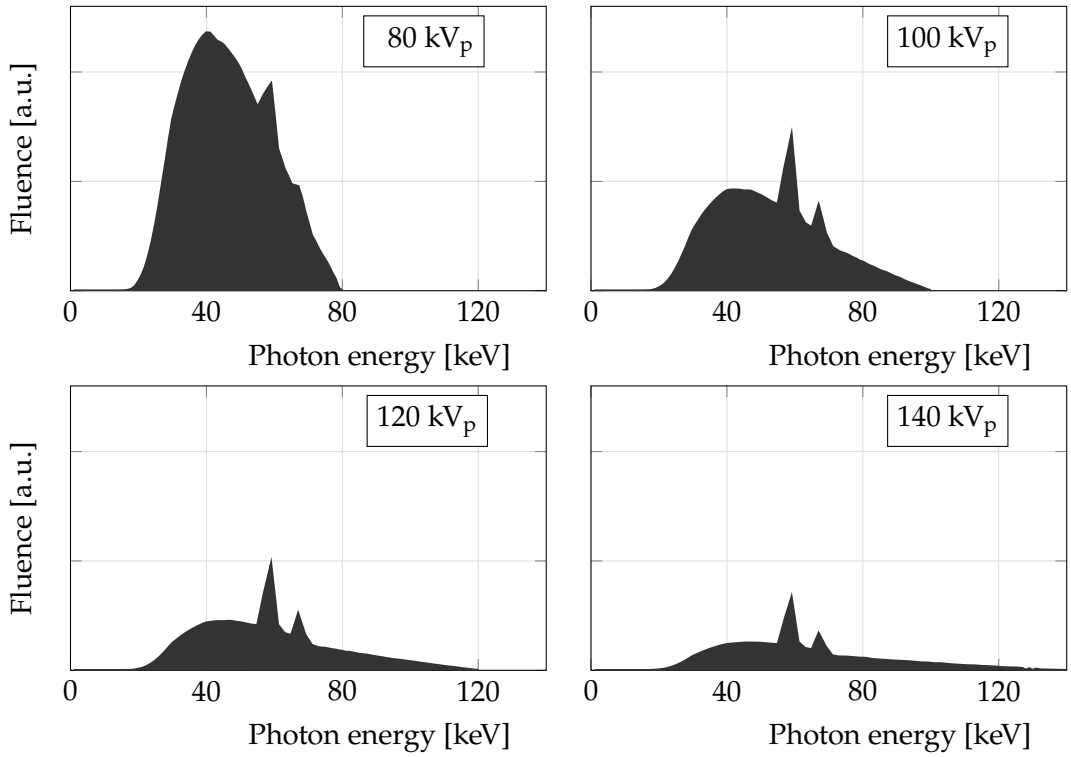

Figure 1.5: Relative tube output for taking the x-ray attenuation characteristics and tube efficiency into account (Siemens Healthineers 2018). The relative photon fluence at different tube potentials according to a reference tube-current time product (TCTP) of 120 mAs at 120 kV_p (standard value for a vascular abdomen acquisition) is presented. Corresponding TCTP values, according to equation 1.3, are 911 mAs at 80 kV_p, 299 mAs at 100 kV_p and 55 mAs at 140 kV_p. However, these values are not employed in clinical practice. Instead, considerably lower values (e.g. 210 mAs at 80 kV_p or 139 mAs at 100 kV_p) are applied to reduce radiation exposure in the patient. A tube potential of 140 kV_p is only seldom applied for abdomen acquisitions, since it is not advantageous in terms of patient dose and image quality.

literature or online (Fewell et al. 1981; Siemens Healthineers 2018). Some studies make use of energy spectra obtained from the manufacturer under non-disclosure agreements (DeMarco et al. 2005; Lin et al. 2014; Steuwe et al. 2018).

1.2.3 IMAGE ACQUISITION PARAMETERS

Prior to image acquisition, several acquisition parameters need to be configured depending on the clinical indication. These parameters influence the extent of the radiation exposure the patient receives during the acquisition.
As was described in section 1.2.2, the chosen tube potential influences both the number of emitted photons and the maximum photon energy. More photons are emitted for the same tube current at higher tube potentials. Furthermore, the higher the energy of a photon, the longer its penetration length. The TCTP is proportional to the radiation exposure. Doubling the TCTP doubles the number of emitted photons

and, hence, also doubles the energy deposition in the scanned subject. A reduction of the TCTP by a factor of 2 increases the noise by a factor of $\sqrt{2}$. A larger scan length or FOV also increases the radiation exposure.
For multi-detector computed tomography (MDCT) systems, the collimation is of importance. The collimation determines the z-axis coverage of the image detector at the isocenter of the CT scanner. It determines the thinnest available slice thickness of the final reconstructed images but also influences the SNR in each detector element. A fine collimation (e.g. 64 x 0.6 mm) allows for image reconstructions with a thin slice thickness (t = 0.6 mm) but causes a low SNR per detector element, since the integrated signal in each detector element is small. The combination of detector elements (e.g. 32 x 1.2 mm) allows a higher SNR in the combined detectors but increases the smallest slice thickness in the reconstruction to in this case t = 1.2 mm. Note that the nominal beam width $W = N \cdot t$ is equal in both examples. To counterbalance the decreased SNR for narrow collimation settings, the TCTP needs to be increased to increase the measured signal in the detector elements. This causes an increase of the patient's radiation exposure.
The pitch (unitless) is calculated as table distance, d, traveled per 360°-rotation divided by the nominal beam width, W.

$$\text{pitch} = \frac{\text{table distance per 360°-rotation}}{\text{nominal beam width}} = \frac{d}{W} \tag{1.4}$$

The pitch influences the acquisition time. For a fixed rotation time, a higher pitch decreases acquisition time and enables capturing of fast contrast-agent dynamics. For *fixed values of tube potential and TCTP*, the pitch influences the radiation exposure: if not compensated otherwise, a pitch > 1.0 decreases the radiation exposure, whereas a pitch < 1.0 increases the radiation exposure due to beam overlap. However, modern CT scanners adapt the TCTP according to the pitch (increasing the pitch causes an increase of the TCTP), keeping the radiation exposure values similar.
For each CT examination, a dose protocol is automatically created, providing information on the radiation exposure and acquisition parameters.

1.3 RADIATION PHYSICS

This section provides a brief overview of the interactions of photons with body tissues, contrast agents, and implants as well as their effect on the reconstructed images. This section is based on Bushberg et al. (2012, pp. 33-59). Interactions of electrons, such as ionization, are not provided in this section. Please refer to the literature for a more detailed explanation.

1.3.1 INTERACTIONS OF PHOTONS WITH MATTER

Interactions can be divided into two main groups: on the one hand elastic interactions (Rayleigh, Thomson scattering) and on the other hand inelastic interactions (Compton scattering, photoelectric effect).
During elastic interactions, the incident photon does not lose any energy during

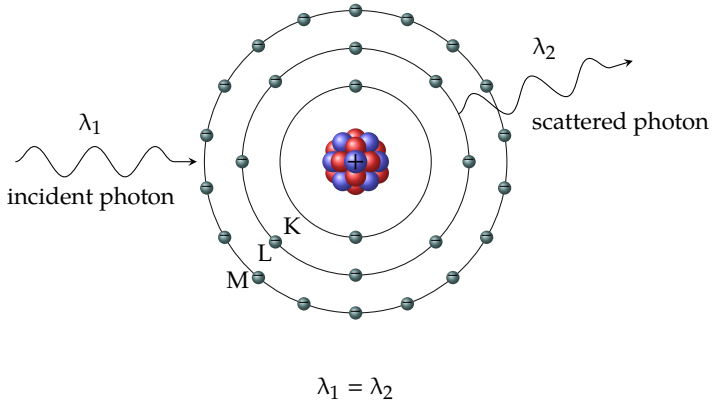

Figure 1.6: Rayleigh scattering: Interaction of the incident photon with the total atom. A photon with the same wavelength but different direction is emitted. Adapted from Bushberg et al. (2012, pp. 33-59).

the interaction, wheres for inelastic interactions, the incident photon energy is reduced. Relevant interaction types in clinical CT are Rayleigh scattering, Compton scattering and photoelectric interactions. Pair production requires photon energies >1.022 MeV, which are not used in clinical CT. Therefore, this effect is not described in the following.

1.3.1.1 *Rayleigh scattering*

Rayleigh scattering causes an oscillation of all electrons in the atom by interaction of an incident photon with the total atom (see figure 1.6). Rayleigh scattering belongs to the elastic interactions, since the incident photon does not lose energy. Instead, a photon with the same wavelength ($\lambda_1 = \lambda_2$) but with a different direction is emitted. This effect is observable only at very low x-ray energies (15-30 keV, mainly in mammography, Bushberg et al. 2012, pp. 33-59).

1.3.1.2 *Compton scattering*

During Compton scattering, an incident photon collides with an electron of the *outer* shell of an atom, which is then ejected (now called Compton electron). Both the direction and the energy of the incident photon (E_i) are changed. The angle between the direction of the incident photon and the direction of the scattered photon, θ, can be used to calculate the energy of the scattered photon, E_{sc} according to the Klein-Nishina formula (equation 1.5, see also figure 1.7):

$$E_{sc} = \frac{E_i}{1 + \frac{E_i}{511keV}(1 - \cos\theta)} \tag{1.5}$$

Compton scattering is the most frequent interaction in soft tissues at 20 keV and above for photon energies in diagnostic imaging. For very low photon energies, the incident photon undergoes elastic scattering, hence, only its direction changes but not the energy (Thomson scattering) (Bushberg et al. 2012, pp. 33-59).

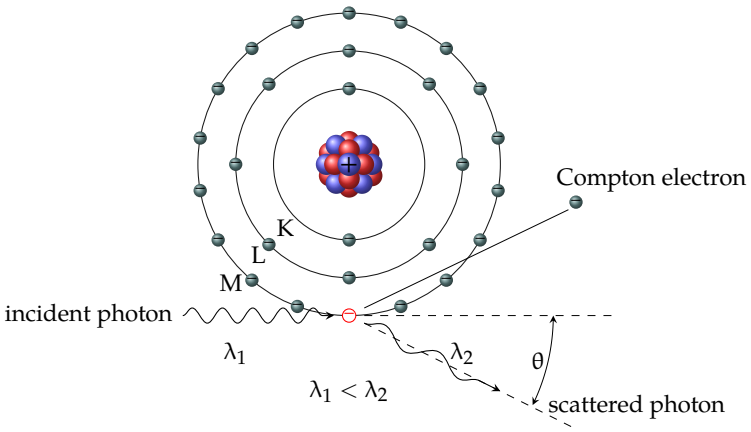

Figure 1.7: Compton scattering: The incident photon interacts with an electron of the outer shell of an atom, which is then ejected. The incident photon energy and direction change in consequence. Adapted from Bushberg et al. (2012, pp. 33-59).

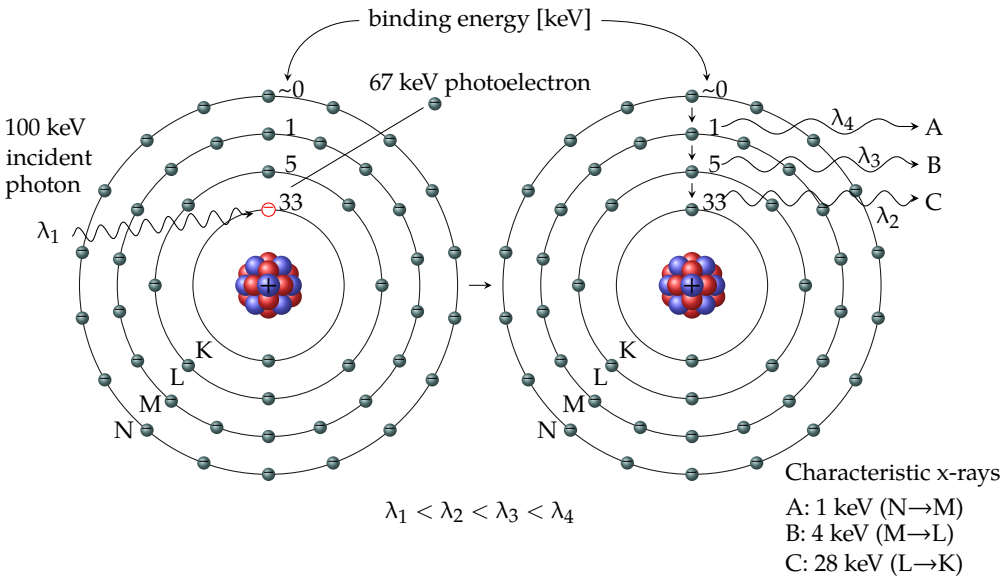

Figure 1.8: Photoelectric effect in the iodine atom (outer electrons in O-shell not shown): The incident photon (energy 100 keV) collides with an electron of the inner shell with a binding energy of 33 keV, which is ejected (photoelectron energy 67 keV). In a cascade, the electron valence of the inner shell is filled by an electron of the outer shell. Characteristic x-rays are released whose energies equal the differences in binding energies of two shells. Adapted from Bushberg et al. (2012, pp. 33-59).

1.3.1.3 *Photoelectric effect*

During a photoelectric interaction, an incident photon collides with an electron of one of the *inner* shells of an atom. The electron, now called photoelectron, is ejected from the atom. The incident photon is absorbed during this interaction. The energy of the photoelectron, E_{pe}, can be calculated by subtracting the electron binding energy, E_b, from the energy of the incident photon, E_i, see figure 1.8.

$$E_{pe} = E_i - E_b \tag{1.6}$$

The valence in the inner shell is filled by an electron of the next shell, releasing a photon (characteristic x-ray) with an energy that equals the difference in binding energies of the two shells. This process repeats itself until all inner shells are filled. The incident photon can only cause an ejection of a photoelectron if its energy is equal or higher than the binding energy of the photoelectron (Bushberg et al. 2012, pp. 33-59). For photon energies just slightly above the binding energy of an e.g. K-shell electron, there is a steep increase in the absorption coefficient. This sudden increase is called K-edge (or correspondingly L-edge for L-shell electrons), see also figure 1.9 (Lusic and Grinstaff 2013). Incident photons with energies just *above* the energies of these edges are likely to be absorbed in an atom during an interaction. The photoelectric effect forms the basis of contrast agent utilization in CT (see section 1.3.3).

1.3.2 ENERGY DEPOSITION IN DIFFERENT TISSUE TYPES

Photons that travel through a material can either be totally absorbed (photoelectric effect), scattered (Rayleigh scattering, Compton scattering), or transmitted without any directional or energy change (Rayleigh scattering). For N_0 incoming photons, the number of transmitted photons N_T is calculated as follows:

$$N_T = N_0 \cdot e^{-\mu \cdot l} \tag{1.7}$$

with the linear attenuation coefficient μ and material thickness l. The larger the linear attenuation coefficient μ or the material thickness l, the more photons are attenuated or absorbed in the material. The linear attenuation coefficient μ is dependent on the material density ρ, atomic number Z, atomic mass A, and on the x-ray energy E of the incident photon:

$$\mu = \frac{\rho Z^4}{A E^3} \tag{1.8}$$

Materials with either a high density (ρ) or high atomic number (Z) are more likely to attenuate photons, compared to materials with a lower ρ and Z-number. Especially the large influence of the atomic number (Z^4) and the energy (E^3) on the attenuation characteristics becomes apparent from equation 1.8 (Lusic and Grinstaff 2013).

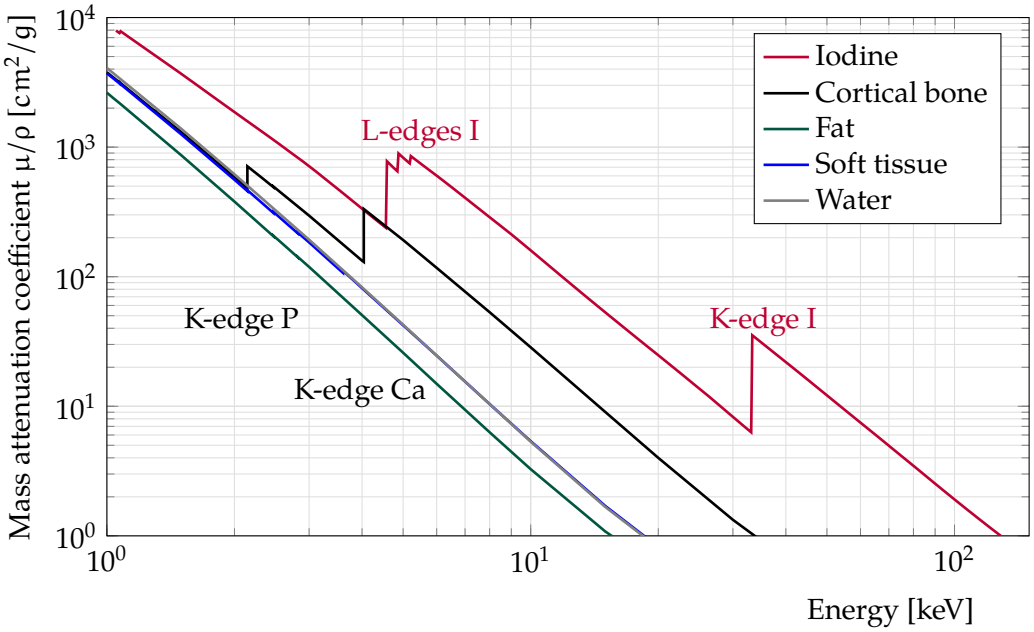

Figure 1.9: X-ray mass attenuation coeffecients of iodine (red), cortical bone (black), fat (green), soft tissue (blue), and water (gray) between 1 keV and 150 keV (Chantler et al. 2017; Hubbell and Seltzer 2018b). Note the K- and L-edges of iodine around 33.2 keV and ~5.0 keV, respectively, and the K-edges of phosphorus (~2.1 keV) and calcium (~4.0 keV) in cortical bone. Also note the logarithmic scale of the x- and y-axis.

Figure 1.9 depicts the mass attenuation coefficients for different body tissues and the contrast-agent component iodine. The highest atomic number of fat and soft tissue components is potassium (Z = 19), according to values published in report 44 of the International Commission on Radiation Units (ICRU) (Hubbell and Seltzer 2018a). For cortical bone, the highest atomic number is calcium (Z = 20) and for iodine Z = 53 (ICRU 2018). For cortical bone and iodine, the mass attenuation is higher than that of water, soft tissue, or fat. Additionally, the K-edges of phosphorus (at ~2.1 keV) and calcium (at ~4.0 keV) and the L- and K-edges of iodine (~5.0 keV and ~33.2 keV, respectively), originating from photoelectric interactions (refer to section 1.3.1.3), are visible in the plot.

1.3.2.1 *Hounsfield scale*

CT scanners measure the extent of the attenuation of photons through different materials. The final image value, measured in Hounsfield unit (HU), is quantifiable and of clinical use. The larger the difference in attenuation between tissues, the larger the contrast on the CT images. The CT number describes the linear attenuation coefficient μ of a volume element (voxel) at position (x, y, z) in relation to the linear attenuation coefficient of water (μ_{water}) for the utilized x-ray spectrum (Bushberg et al. 2012, pp. 312-374). The CT number is defined as:

$$\text{CT number}\,(x, y, z) = 1000 \cdot \frac{\mu(x, y, z) - \mu_{water}}{\mu_{water}}\ [\text{HU}] \tag{1.9}$$

For a voxel containing only water, $\mu(x, y, z) - \mu_{water} = 0$ and so is the CT number. In clinical CT, lowest CT numbers are obtained for air (-1000 HU), whereas highest CT numbers are measured in very dense materials, such as bones and metals (>+3000 HU) (Bushberg et al. 2012, pp. 312-374).

1.3.3 CONTRAST AGENTS IN CT

The visibility of interfaces between adjacent tissues on CT images is poor for materials of similar density and composition, and therefore complicates diagnosis (Lusic and Grinstaff 2013). CT can take advantage of the increased photon absorption, especially at the K-edges of high Z-materials, when administering contrast agents prior to an acquisition. Examples for applications of contrast agents are the intravenous injection of an iodinated contrast agent for highlighting blood vessels, e.g. computed tomography angiography (CTA) or the assessment of intestinal perforation by administrating contrast agents rectally. In general, contrast agents increase the contrast between similar tissues and provide functional information, e.g. information about blood flow, blood volume, or perfusion of a tissue or tumor (Lusic and Grinstaff 2013). In 2016, 57% of the CT acquisitions, performed in the clinic where this research was performed, included the administration of contrast agents (UKHD 2017). The majority of contrast agents in CT are based on iodine due to its high atomic number (Z = 53), its K-edge in the diagnostic energy range (~33.2 keV), and its sanitary tolerance. Acquisitions at 80 or 100 kV_p result in a stronger attenuation than acquisitions at 120 kV_p, and consequently in larger contrast enhancement (increase of the CT number by 40 HU at 80 kV_p, 30 HU at 100 kV_p, and 25 HU at 120 kV_p for an iodine concentration of 1 mg/ml, compared to a non-enhanced acquisition) (Bae 2010; Perisinakis et al. 2018). Less-frequently administered contrast agents are barium-based, orally administered for gastrointestinal questions (Z = 56, K-edge ~37.4 keV), gold-nanoparticles (Z = 79, K-edge ~80.7 keV), or xenon gas (Z = 54, K-edge ~34.6 keV) (Lusic and Grinstaff 2013).

Image examples of a three-phasic, contrast-enhanced CTA are presented in figure 1.10, acquired for the clinical assessment of an aortic aneurysm. A three-phasic CTA includes a non-enhanced acquisition prior to the injection of an iodinated contrast agent, an arterial acquisition (starts a few seconds after the injection), and a venous acquisition (starts ~70 seconds after the injection).
The administration of contrast agents can cause side effects which lead to contraindication for some patients. For iodine-based contrast agents, known side effects are contrast-induced nephropathy, renal toxicity, adverse cardiac events, and thyroid dysfunction (Lee et al. 2015; Lusic and Grinstaff 2013). Topic of recent research is the contrast agent-enhanced radiation damage caused by CT examinations, and to what degree contrast agents increase the risk of long-term bioeffects (Amato et al. 2013; Pathe et al. 2011; Streitmatter et al. 2017; Wang et al. 2017). It is therefore of interest, to what degree iodine causes an increase of the energy deposition (iodine-induced build-up effect), especially at tissue interfaces.

(a) Native phase (b) Arterial phase (c) Venous phase

Figure 1.10: Three-phasic computed tomography angiography acquisition of the abdomen. The liver and spleen appear fairly homogeneous on the image of the non-enhanced (native) phase (a), however, calcification of the aorta is clearly visible. The arterial phase (b) is acquired when the contrast agent bolus passes through the aorta, hence, the aorta and inferior vena cava and its branches are enhanced and appear bright. Blood perfusion through the liver and spleen is already enhanced in the arterial phase. At the time of the venous acquisition (c), the contrast agent has spread in the body, and the liver and the spleen are considerably brighter than on the image of the non-enhanced acquisition, whereas the aorta again appears darker compared to the image of the arterial phase.

1.4 RADIATION EXPOSURE IN CT

According to the annual report of the federal office for radiation protection in Germany (Bundesamt für Strahlenschutz), 135 million radiological examinations were performed in Germany in 2014, of which 55 million were dental examinations. There was only a marginal increase in overall radiological examinations between 2007 and 2014. The average annual number of radiologic examinations per capita was 1.7 for Germany in 2014, which is high in comparison to the European average of 1.1. Between 2007 and 2014, the number of conventional radiography examinations decreased, whereas the number of CT examinations considerably increased by about 40%. Similarly, the number of MRI examinations also increased between 2007 and 2014, by 55% (BfS 2016b; Nekolla et al. 2017).

1.4.1 DOSE DEFINITION

The absorbed radiation dose is the absorbed energy by ionizing radiation per unit of mass, measured in Gray [Gy], and is commonly used in radiotherapy and nuclear medicine:

$$1\ \mathrm{Gy} = \frac{1\ \mathrm{J}}{1\ \mathrm{kg}} = \frac{6.242 \cdot 10^{12}\ \mathrm{MeV}}{1\ \mathrm{kg}} \tag{1.10}$$

The equivalent dose H takes the type of radiation and its *radiation weighting factor* into account: photons and electrons have a radiation weighting factor of 1 throughout all energies, whereas neutrons and protons have radiation weighting factors between 5 and 20, as the relative biological effectiveness of neutrons and protons is higher than that of photons and electrons.

In diagnostic radiology, the effective dose, given in millisievert [mSv], is more commonly used. The effective dose additionally takes *tissue weighting factors* into account, which describe the risk of adverse effects of specific tissues. For example, lung tissue or bone marrow is more radiosensitive than the skin or the brain. Please refer to section 1.5 for more information on tissue weighting factors and (organ) dose determination methods in CT.

1.4.2 NATURAL AND CIVILIZATIONAL RADIATION EXPOSURE IN GERMANY

The average annual dose per capita from all radiological examinations was 1.7 mSv in 2015 in Germany, and in total 3.8 mSv combined with the radiation exposure from natural sources (see table 1.2, BfS 2016b). The annual dose from medical examinations increased over the last years (from 1.3 mSv in 2007) due to the increasing number of CT examinations. The annual effective dose of radiological examinations other than CT per capita (planar radiography, angiography, interventions) was fairly stable between 2007 and 2014 (BfS 2016b).
The average effective dose per CT examination underwent a moderate reduction (from ~7.5 mSv to ~6.9 mSv), whereas a stronger decrease in effective dose per angiographic and interventional procedure was noticeable (from ~6.6 mSv to ~5.5 mSv) (Nekolla et al. 2017). However, the effective dose from CT examinations per capita increased by 30% between 2007 and 2014 (BfS 2016b; Nekolla et al. 2017). This is a less strong increase than the increased number of CT examinations due to the lower effective dose per CT examination.

Table 1.2: Average effective annual dose to an individual due to ionizing radiation in 2015 in Germany (BfS 2016b).

	Average effective dose [mSv/year]
Natural radiation exposition due to	
Cosmic radiation (at sea level)	ca. 0.3
Terrestrial radiation	ca. 0.4
Inhalation of radon and its progeny	ca 1.1
Ingestion of natural radioactive substances	ca. 0.3
Total natural radiation exposure	**ca. 2.1**
Civilizational radiation exposure due to	
Fallout from nuclear weapon tests	<0.01
Accident at nuclear power plant Chernobyl	<0.01
Nuclear facilities	<0.01
Application of radioactive substances and ionizing radiation in medicine (w/o therapy)	ca. 1.7
Total civilizational radiation exposure	**ca. 1.7**

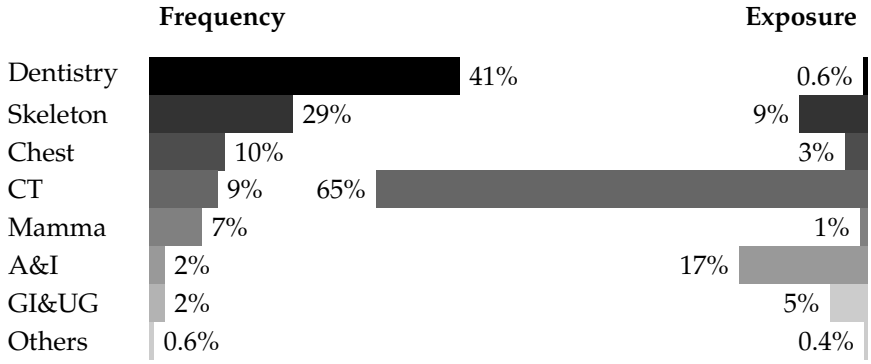

Figure 1.11: Contribution of diagnostic x-ray procedures to total frequency (left) and collective effective dose (right) in 2014 in Germany (BfS 2016b). Abbreviations: computed tomography (CT), mammography (mamma, single-sided), angiography and interventional procedures (A&I), gastro-intestinal and urogenitary track (GI&UG).

Although CT examinations only accounted for 9% of all radiological examinations, they contributed to 65% of the annual effective dose per capita (see figure 1.11, BfS 2016b). Typical effective doses for a selection of examinations for a standardized patient of 70 kg body weight are shown in table 1.3 (BfS 2016a,b). CT examinations and interventional procedures result in effective doses that are more than 100 times higher than conventional radiography acquisitions (Hall and Brenner 2008), see e.g. table 1.3 for the thorax.

1.4.3 RADIATION RISKS

Ionizing radiation is a known and proven carcinogen, especially for high doses exceeding 100 mSv (Hall and Brenner 2008; Siegel et al. 2017). From these high doses, a *deterministic* risk of induced radiation damage is originating. Deterministic effects of radiation have a threshold above which these effects increase in frequency and severity with increasing dose (Mettler 2012). In contrast, *stochastic* effects of inducing radiation damages have no threshold. Stochastic risks are originating from doses <100 mSv. The probability of a stochastic effect increases with increasing radiation exposure, however, not the severity.
The younger the patient, the higher the percentage lifetime cancer risk. One reason for this effect is the increased dose from pediatric CT examinations as less self-shielding is possible in tinier patients and organ doses are consequently higher. Self-shielding is the endogeneous filtration of low-energy photons in fat and soft tissue. Since especially fat tissue is less radiosensitive than e.g. kidney tissue, a larger fat mass (e.g. in obese patients) decreases the dose to radiosensitive organs. The second reason for the increased lifetime cancer risk at younger ages is the higher radiosensitivity of children compared to adolescents (Hall and Brenner 2008). Radiation induced double-strand breaks of the deoxyribonucleic acid (DNA) are more likely to occur in dividing cells (Foray et al. 1997; Iliakis and Okayasu 1990). Due to

the higher cell division rate at younger ages, the risk of double-strand breaks causing cell alteration is increased. Furthermore, young patients are more likely to experience any possible radiation-induced tumor (that might develop after approximately 20 years) due to their long life expectancy from the moment of the CT acquisition on, especially compared to an e.g. 80 year old multimorbid patient.
In general, a precautionary principle is applied (keep the dose as low as reasonably achievable, ALARA). Radiation doses >100 mSv are known to induce cancer, since a linear relationship between excess risk and dose exists in this range (deterministic radiation effects). The precautionary principle extends that excess risk also to the lowest doses (linear no-threshold stochastic model, Hall and Brenner 2008; Mettler 2012). Several biological and epidemiological studies have been published that demonstrate a small risk of radiation-induced cancer for organ doses associated with a few CT scans (Hall and Brenner 2008), however, the exact biological mechanisms are still unknown and there are also positive radiation effects mentioned on the opposite side (Siegel et al. 2017).
There are several task groups worldwide which regulate, supervise, and provide recommendations about the handling of radiation exposure in medicine, such as the International Commission on Radiological Protection (ICRP), the ICRU, or the American Association of Physicists in Medicine (AAPM). According to the ICRP, the nominal risk factor (lifetime risk estimate) for fatal cancer in the whole population is 5.5% per Sievert (4.1%/Sv for adult workers, ICRP 2007).

Table 1.3: Effective dose per examination in diagnostic radiology in Germany. Abbreviations: computed tomography (CT) (BfS 2016a,b).

Examination	**Typical effective doses [mSv]**
CT	
CT head	1-3
CT thorax	4-7
CT abdomen	8-20
Angiography and interventional procedures	
Arteries (angiography & intervention)	10-30
Gastrointestinal system	4-12
Planar radiography	
Pelvis	0.3-0.7
Head	0.03-0.06
Dental	<0.01
Thorax	0.02-0.04
Mammography (2-sided, in 2 planes)	0.2-0.4
Lumbar spine	0.6-1.1
Extremities	<0.01-0.1

1.4.4 TECHNIQUES FOR DOSE REDUCTION IN CT

The diagnostic indication, desired information, and patient constitution lead to the specific acquisition parameters of a CT examination. A reduction of the radiation exposure is always aimed at, while confident diagnosis should be maintained, following the ALARA principle. First of all, the number of acquisitions should be reduced if possible, e.g. a non-enhanced acquisition should be omitted if the obtained information will not contribute to the diagnosis. Furthermore, the acquisition length (coverage) should be reduced to the region of interest and carefully planned. Moreover, the desired reconstructed slice thickness should be reconsidered. A lower necessary TCTP, and therefore radiation dose, can be achieved with a larger detector collimation.
The software of modern scanners provides intrinsic dose modulation, also known as automatic exposure control (AEC). The AEC regulates both the tube potential and the tube current, based on the patient topogram (scout scan/localizer, see figure 1.12) and reference values for the tube potential and tube current.

An adjustment of the tube potential to lower values can reduce the radiation exposure. This technique has two effects: (1) the image contrast increases, especially for soft body tissues. However, due to the reduced efficiency of the x-ray tube at low tube potentials (see section 1.2.2.3), (2) the image noise also increases (Lira et al. 2015; Seyal et al. 2015). If the tube current is not increased to fully compensate for the increased noise level, low-kV imaging allows for a reduction in radiation exposure

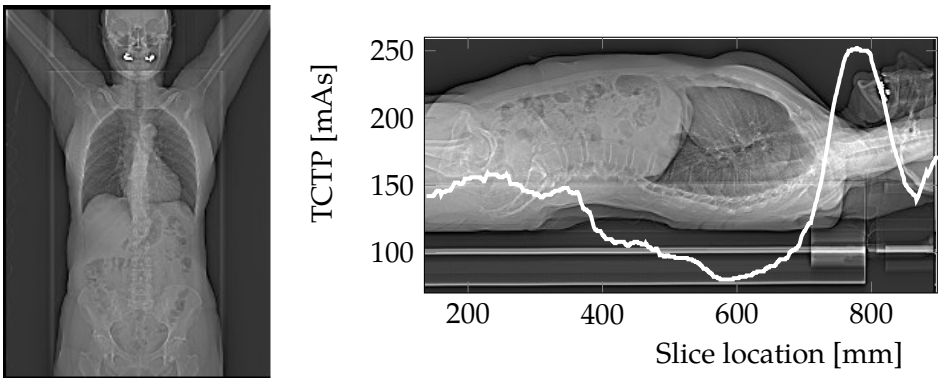

(a) Anterio-posterior topogram

(b) Lateral topogram with corresponding automatic LTCM for successive CT acquisitions, based on the topograms

Figure 1.12: Topograms, acquired prior to a computed tomography (CT) acquisition. The anterio-posterior topogram is acquired prior to any acquisition, whereas the lateral topogram may be additionally acquired. Longitudinal tube-current modulation (LTCM) and the resulting slice-specific tube-current time product (TCTP, white curve in (b)) for successive CT acquisitions is planned on the basis of the topograms. Water equivalent diameters are calculated based on the x-ray attenuation of the topogram and used to determine the appropriate tube current. For LTCM, the tube current at each z-position (slice location) is calculated relative to the maximum x-ray attenuation (in this example at the shoulders). The accuracy of LTCM increases with the additional acquisition of a lateral topogram.

(Stiller 2011). Especially for contrast-enhanced acquisitions, tube potentials lower than 120 kV_p should be used, since this does not only improve image contrast but also enables a dose reduction by up to 50% (Kalender et al. 2009; Schegerer et al. 2017).

A longitudinal tube-current modulation (LTCM) is implemented in all modern clinical CT scanner models (see figure 1.12b). LTCM is based on the patient topogram and takes the differences in attenuation along the z-axis of the patient into account. The tube current is increased in regions of large photon attenuation (shoulders, hips), whereas tube current is reduced for regions of low attenuation (thorax). Figure 1.12 shows the patient-specific modulated tube current along the longitudinal axis. Slice-specific tube current values are documented in the Digital Imaging and Communications in Medicine (DICOM)-headers of the reconstructed images.
For some vendors, the tube current is additionally based on attenuation measurements from previous 180°-rotations of the CT gantry (online/angular tube-current modulation (ATCM), Kalender et al. 1999b). The reason for this modulation are the differences in lateral and anterio-posterior (a.p.) diameter of patients (and hence, x-ray pathways), especially at the shoulder or pelvis.

Great attention should be paid to the positioning of patients in the CT gantry, since the positioning influences the efficiency of AEC and the applied radiation exposure. If the patient is positioned off-center, dose modulation will not be as effective as if the patient is positioned at the isocenter of the CT scanner. For an off-center position, the water equivalent diameters (WEDs) calculated from the topograms cannot be accurately determined since patients appear magnified on the topogram, resulting in increased tube current values (Akin-Akintayo et al. 2018). Additionally, the arms should be placed outside the desired examination region, e.g. arms elevated above the head, if the abdomen is of interest. This reduces the x-ray pathway through the patient, resulting in a reduction of the required tube current for a sufficient image signal (Liu et al. 2015).

Due to newer developments in iterative reconstruction, images with less noise can be obtained, allowing to reduce the reference tube current prior to the acquisition, enabling dose reductions of 30 to 60% (Kalender 2014; Schegerer et al. 2017; Stiller 2018). Furthermore, modern CT scanners offer the possibility of dual-energy (DE) acquisitions. From contrast-enhanced DE acquisitions, it is possible to calculate virtual non-contrast (VNC) images. These VNC images allow to omit the real non-enhanced acquisition, thereby reducing the radiation exposure to up to 25-40% (Buffa et al. 2014; Graser et al. 2009; Toepker et al. 2012). Different techniques for radiation exposure determination are described in the following section.

1.5 CT DOSIMETRY

As was mentioned in section 1.2.3, a dose protocol is automatically created by the CT scanner after an examination. The dose protocol informs about the individual acquisition parameters, e.g. the applied tube potential, the reference and effective TCTP, the x-ray tube rotation time, and the collimation width, and information on the radiation exposure, making use of the quantities computed tomography dose index (CTDI) (to be more precise, the volumetric CTDI, $CTDI_{vol}$) and the dose-length product (DLP).

COMPUTED TOMOGRAPHY DOSE INDEX (CTDI) AND DOSE-LENGTH PRODUCT (DLP)

The CTDI is a dosimetric quantity describing the radiation exposure in CT imaging. It is purely a measure for the radiation exposure, but does not describe the effective dose or dose distribution of/in a patient. The CTDI is defined as "the integral along a line parallel to the axis of rotation (z) of the dose profile (D(z)) for a single slice, divided by the nominal slice thickness T" (Bongartz et al. 1999):

$$CTDI = \frac{1}{T} \int_{-\infty}^{+\infty} D(z)\ dz \tag{1.11}$$

The measurement of dose using a CTDI phantom (see figure 1.13) and an ionization chamber is a standard for quality control in CT. CTDI phantoms are available in two sizes (body ∅ 32 cm and head ∅ 16 cm, thickness of 15 cm in both phantoms), representing a torso and a head. The phantoms are made of polymethyl methacrylate (PMMA), with a density of 1.19 g/cm^3. For the measurement of a volumetric CTDI, radiation exposure is measured at five different positions (one central position, four peripheral positions) in the phantom. For a practical CTDI measurement, the radiation exposure is integrated in each measurement position individually over a z-length L of 100 mm and results in the quantity $CTDI_{100}$ (unit mGy):

$$CTDI_{100} = \frac{1}{T} \int_{L = -50\ mm}^{L = 50\ mm} D(z)\ dz \tag{1.12}$$

From the $CTDI_{100}$, the weighted CTDI, $CTDI_w$, is calculated, taking the dose measurements in the phantom center (c) and periphery (p) into account:

$$CTDI_w = \frac{2}{3} \cdot CTDI_{100,p} + \frac{1}{3} \cdot CTDI_{100,c} \tag{1.13}$$

The volumetric computed tomography dose index ($CTDI_{vol}$), which is provided by the dose protocol, additionally takes the pitch value into account:

$$CTDI_{vol} = \frac{CTDI_w}{pitch} \tag{1.14}$$

The $CTDI_{vol}$ allows to compare the influence of different acquisition parameters (tube potential, TCTP, pitch, collimation) on the radiation exposure. Furthermore, it allows to compare the radiation exposure of different acquisitions among scanners and vendors. However, the index is independent of patient morphology and tissue

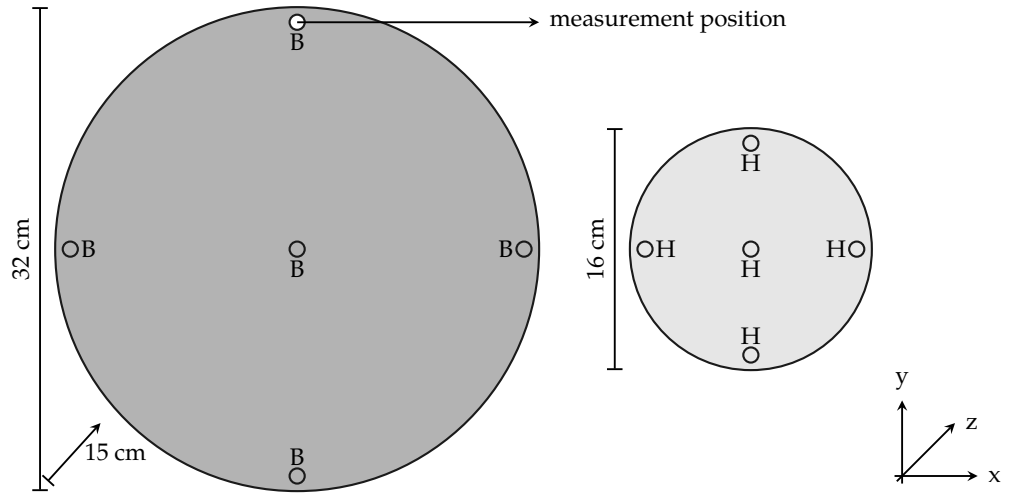

Figure 1.13: Computed tomography dose index (CTDI) phantom: CTDI body (B) (dark gray, ∅ 32 cm) and CTDI head (H) (light gray, ∅ 16 cm) phantom. CTDI phantom thickness in z-direction is 15 cm, made of polymethyl methacrylate (PMMA). Both CTDI phantoms include five measurement positions for a CT ionization chamber (one central measurement position and four positions in the periphery), fitted with PMMA plugs for homogeneous density of the CTDI phantom. One PMMA plug is replaced by an ionization chamber for measurement.

composition. Multiplying the $CTDI_{vol}$ with the scan coverage (irradiated length in cm) results in the DLP value, which again is provided by the dose protocol (unit cm·mGy):

$$DLP = CTDI_{vol} \cdot \text{scan coverage} \tag{1.15}$$

The $CTDI_{vol}$ and DLP only provide a measure of the intensity of the radiation being directed at the patient but not a measure of the effective or organ dose.

TISSUE WEIGHTING FACTORS In 1977, the ICRP published tissue weighting factors, w_T, in ICRP publication 26 for specific tissue types (e.g. bone marrow, breast, thyroid tissue) (ICRP 1977). Tissue weighting factors take the radiosensitivity of specific tissues or organs to ionizing radiation into account. The radiosensitivity of specific cell types is determined from cell experiments and re-investigated on a regular basis. Hence, the tissue weighting factors were updated and refined in ICRP publication 60 in 1991 and ICRP publication 103 in 2007, thereby altering the tissue weighting factor to the currently estimated radiation sensitivity (ICRP 1991, 2007). Especially the weighting factors for the gonads and breast have been adjusted throughout the time: for the gonads, w_T changed from 0.25 (ICRP 26) to 0.20 (ICRP 60), to 0.08 (ICRP 107), whereas for the breast, w_T changed from 0.15 (ICRP 26) to 0.05 (ICRP 60), to 0.12 (ICRP 107).
Tissue weighting factors allow for the conversion between tissue dose values (equivalent dose, unit Gy) and effective dose (in mSv). Tissue dose values can be determined by means of the anthropomorphic Rando Alderson Phantom (RSD Phantoms, CA, USA), which includes a human skeleton surrounded by tissue-equivalent materials.

It is a common dosimetry phantom in radiology and radiotherapy departments. The phantom consists of thin slabs allowing the insertion of small thermoluminescent detectors (TLDs) to measure dose values at various positions inside organs, skeleton, and surrounding tissue. Although it is a complex measurement and TLD read-out procedure, the spatially-resolved measurement of the radiation exposure in an anthropomorphic phantom, which contains human and tissue equivalent materials, allows for an increased precision and accuracy of determined dose values.

CONVERSION FACTORS The simplest and most straightforward method for the calculation of the effective dose resulting from a CT acquisition is the use of body-region specific DLP-to-effective-dose conversion factors (unit $mSv \cdot mGy^{-1} \cdot cm^{-1}$). The first conversion factors were published in the European guidelines on quality criteria for CT in 1999 based on the ICRP 60 weighting factors (Bongartz et al. 1999; ICRP 1991) and were updated in 2011 by Huda et al. (2011) based on ICRP publication 103 (ICRP 2007). The DLP-to-effective-dose conversion factors are based on the tissue weighting factors, introduced in the last paragraph.
According to Huda and Mettler (2011), dose calculation by means of the $CTDI_{vol}$ and DLP values with conversion factors are not exact and useful for all patients, since conversion factors are based on a standardized patient, although the actual patient size and the morphology has a considerable impact on the effective dose (Steuwe et al. 2016). $CTDI_{vol}$ and DLP values are only sufficient to give a rough estimate of the radiation exposure from CT dose protocols.
According to McCollough et al. (2011) and Boos et al. (2016), "estimates of individual patient risk (...) must use patient size-specific dose estimates (SSDEs)" and not just the scanner output ($CTDI_{vol}$, DLP). SSDEs are calculated by multiplication of the $CTDI_{vol}$ and a conversion factor, f, which depends on the axial diameter of a patient. The conversion factor, f, is provided by the AAPM (2011) for different lateral- and a.p.-diameters, and for effective diameters ($D_{eff} = \sqrt{a.p. \cdot lat}$), and decreases with increasing diameter. Hence, SSDE-conversion factors can be used to correct the $CTDI_{vol}$ according to the patient's habitus (Boos et al. 2016). Diameter measurements on axial CT images and calculation of D_{eff} are considered the most accurate, as they take fat shielding into account and reduce relative dose for large patients (see figure 3 in McCollough et al. 2011). In addition to SSDEs, Deak et al. (2010) have published sex- and age-specific conversion factors for CT, to increase the accuracy of effective dose values.

COMMERCIALLY AVAILABLE PROGRAMS FOR DOSE CALCULATION Apart from experimental dose measurements and the use of conversion factors, there are several commercial programs available for the determination of dose without the need of own measurements, but solely requiring a CT patient data set and the acquisition parameters. These programs are often part of dose-management systems, such as DoseTrack (Sectra Medical Systems, Cologne, Germany) and tqm | DOSE (Agfa HealthCare, Bonn, Germany), or can be purchased individually (CT-Expo or VirtualDose, Ding et al. 2015). Furthermore, open-source codes are available for research purposes, providing a high flexibility in their applications but also the need for

targeted further development. Most of these programs are based on Monte Carlo methods which are described in more detail in section 1.5.1.

1.5.1 MONTE CARLO METHODS IN RADIOLOGY

Monte Carlo methods can be defined as "statistical methods that use random numbers as a base to perform simulation of any specified situation" (Ljungberg 1998, p. 1). These statistical methods are used in a large field of applications for the simulation of stochastic processes, especially for the simulation of particle transport in scattering media (Chan and Doi 1983). They can be applied to study radiation physics aspects, physical quantities, and characteristics of detection systems such as the efficiency of gamma-ray detectors (Andreo 1991; Raeside 1976). In the medical field, MC studies can be found in nuclear medicine, radiation therapy, and diagnostic radiology. There is a broad scope of application since MC methods provide the most complete and accurate method for estimating doses in organs and tissues (Chan and Doi 1983; Christner et al. 2010; Jiang et al. 2007). In diagnostic procedures, MC methods are used for their optimization, to improve the image quality and patient-dose ratio, and for understanding radiation protection aspects, scatter, and attenuation principles (Andreo 1991; Zubal 1998).
MC methods in diagnostic radiology are advantageous because no actual x-ray unit is necessary to study the influence of x-rays in an object or patient. Furthermore, simulations do not expose patients or staff to ionizing radiation. A model of the CT scanner and various phantoms can be developed and implemented to track and determine dose deposition with full flexibility: MC methods enable the alteration or repetition of experiments at-will, allowing to easily change between different measurement setups or adjusting simulation parameters to a certain research question (Steuwe et al. 2018).
Several MC-based dose calculators are available for the calculation of dose deposition in CT (Brady et al. 2012), such as ImPACT (ImPACT 2011), or ImpactDose (IBA Dosimetry 2009; Kalender et al. 1999a). However, differences between software tools are often significant and the user has to be aware of the limitations, such as outdated mathematical phantoms and look-up tables, or outdated CT scanners (Cros et al. 2017).

1.5.1.1 *Geant4*

The open-source toolkit Geometry and Tracking 4 (Geant4) (Agostinelli et al. 2003; Allison et al. 2006) is used for the simulation of physics processes in this work. One advantage of this software compared to many commercial programs is the possibility of adjusting the simulation parameters for the specific purposes of a desired research project. Hence, geometry parameters (the choice and position of the source, phantoms, or detectors) as well as the way physics processes are tracked can be specified according to the desired simulation setup. The software and the variable input and output parameters are described in more detail in section 2.1 and 2.1.4, respectively.

1.6 MOTIVATION AND GOAL OF THIS WORK

This chapter described the increasing use of CT and the associated radiation exposure over the past decade. Especially for patients receiving follow-up examinations over a long period of time, it is of interest, to what degree these patients are exposed to radiation and where the energy of x-rays is deposited in the body. Since long-term effects of the radiation exposure from CT examinations are still not clarified, extensive long-term studies of patients without and with CT examinations need to be performed. The surveillance of individual effective and organ doses helps to evaluate the effects of ionizing radiation, especially with regard to possible induced cancerous diseases. Furthermore, deeper knowledge about the spatial distribution of the deposited x-ray energy in relation to CT acquisition parameters might help to develop technical improvements in CT in future.

The determination of the radiation exposure caused by CT is still a compromise between calculation time and accuracy. Conversion factors are advantageous because of their simple and fast use, however, they are based on standardized patients that do not represent the actual patient (Steuwe et al. 2016). The administration of potentially toxic contrast agents and the corresponding change in energy deposition is not included in the dose calculation using conversion factors, although it is well known that iodinated contrast agents increase the frequency of double strand breaks of the DNA (Streitmatter et al. 2017). In contrast to the conversion factors, determination of effective dose by MC simulations is time-intensive but yields the advantage that the actual patient morphology and tissue composition (including contrast agents) can be included. However, these simulations are only possible post hoc, after the CT acquisition has been performed.
The aim of this project was the development and validation of a software for determination of radiation exposure associated with CT that paves the way towards *virtual dosimetry* of patients. Virtual dosimetry, in contrast to experimental dosimetry, allows for prompt patient- and acquisition-specific dose calculations that can be performed for all examined patients in a diagnostic radiology department. In contrast to commercially available software, it was aimed at a program offering a high degree of flexibility to implement any source spectra, geometrical and digitized patient phantoms, and to simulate the effect of contrast agents on energy deposition. Furthermore, a flexible and comprehensive data read-out and analysis was desired, offering considerably more possibilities than commercial software.
It was the goal to understand the differences in dose distribution caused by different source spectra and primary filtration. The knowledge about possible differences in dose distribution helps to assess whether interchangeability between spectra is given or whether the measurement of own source spectra is required for an exact simulation of a CT acquisition. With the information obtained from the input source spectra, the effect of different tube potentials on the energy deposition was determined for more elaborate phantoms, without and with employing contrast agents. Since low-kV acquisitions are encouraged nowadays, their impact on the dose distribution, especially in the skin, is of interest as well as the effect on the detector signal. To allow for individual patient dosimetry, the software was further

developed to implement patient-specific phantoms. Obtaining three-dimensional maps of the energy deposition associated with CT acquisitions, allows for (a) individual dosimetry, (b) comparison between follow-up acquisitions, and (c) assessing the change in energy deposition when altering scan parameters (e.g. different tube potential) or morphological change (e.g. weight loss).

CONTRIBUTION OF OTHERS The measurement of CT x-ray spectra by Compton spectroscopy and the production of the physical beam-shaping filter model for MC simulations have been performed prior to this work by Dr. Wolfram Stiller and Dr. Stella Veloza (Veloza 2012). The methodology and results of this prior work have been reprocessed and prepared for submission during the course of the current doctoral program (Stiller et al. 2019).
The MC software programmed during this project is a further development of a MC model to simulate Compton spectroscopy measurements, which was part of the doctoral thesis of Dr. Stella Veloza (Veloza 2012).
Patient data included in this thesis has been acquired during the course of this work, as part of a clinical study (CT Angiography of the Aorta: Prospective Evaluation of an Individualized Low-Radiation Dose and Low-Volume Contrast Media Protocol with Dual-Energy CT for Detection of Endoleaks after Endovascular Aneurysm Repair). The study was organized by Dr. med. Fabian Rengier and Matthias Fink, and executed by the radiologists and technicians in the Clinic for Diagnostic and Interventional Radiology, University Hospital Heidelberg, Germany.

2

MATERIALS AND METHODS

This chapter provides necessary background information on the employed MC model of radiation transport, the workflow of the MC simulations, the MC model's individual components (x-ray source emission, phantoms), and the analyses and simulations of CT acquisitions performed during this research project.
The chapter is divided into two main parts: (1) the individual components of the MC model and (2) the performed simulations of CT acquisitions, which evaluated the effect of tube potential, phantom material choice, and contrast agent on the energy deposition and its spatial distribution in a multitude of simple and elaborate phantoms.
In section 2.1 and 2.2, a description of the used MC model and its configuration are presented as well as the implemented CT scanner geometry. In section 2.3, the employed input spectra and monoenergetic photons, beam shaping methods, as well as the implementation of different source types and acquisition modes in the simulation are described. In section 2.4, the geometrical and digitized phantoms designed in this work and used for tracking of the radiation exposure, are presented.
Finally, with the individual components of the MC model, the performed simulations are described in section 2.5. The designed phantoms increased in complexity during the course of this work. The effect of different source spectra, material choice, tube potential, and contrast enhancement were first assessed in simple phantoms (water and box phantom). Afterwards, the information gained from the simple phantoms was used to assess and understand the energy deposition in a geometrical anthropomorphic phantom and several digitized patient phantoms, as a function of the applied tube potential, contrast enhancement, and phantom morphology.
Section 2.6 describes a method used to estimate the error of the MC model.

2.1 DESCRIPTION OF THE MONTE CARLO MODEL

MC simulations were performed using Geant4, version 4.9.2.p04. Geant4 is an object-oriented simulation toolkit for simulation of radiation transport in matter, providing a set of software components implemented in the C++ programming language. The toolkit allows to implement all aspects necessary for this work, e.g. the geometry of the CT scanner and phantoms, desired primary particles, tracking of particles in materials, the required physics processes, and the storage of interaction data (Agostinelli et al. 2003; Allison et al. 2006).

The developed MC software models a CT scanner geometry and allows for simulation of CT acquisitions of patients or test specimens (phantoms). According to section 1.2.1, the CT scanner geometry consists of three main components:

1. the x-ray emitting source,
2. beam-shaping filtration, and
3. the detector for image acquisition (see figure 1.3).

The radiation exposure associated with CT acquisitions (energy deposition and its spatial distribution) is tracked and measured in

4. a phantom or patient model, positioned at the isocenter of the CT geometry.

The developed MC model emits photons and tracks their physical interactions and energy deposition between photon emission from the x-ray source and photon absorption in a phantom or detector, including all particles arising during interactions of photons in matter (i.e. electrons, called 'secondaries' or secondary electrons[2]).
In the developed MC software, the x-ray source with its individual components was not modeled since information on the geometry and materials were not available (see section 1.2.2.4). Instead, x-ray emission was modeled by the implementation of source spectra and monoenergetic photons. Details on the x-ray emission are provided in section 2.3.
Two different methods for beam-shaping filtration were implemented, which shape the x-ray fan beam and alter the photon fluence according to transmission measurements performed prior to this work. Details on the beam-shaping filtration are provided in section 2.3.5.
The third part of a CT scanner geometry is the CT detector. An experimental lead detector (see section 2.4.1.2) was implemented and employed in this work. A classical CT detector for image acquisition was additionally modeled, however, since image acquisition was not focus of this work, the latter CT detector will not be described.
The radiation exposure associated with CT examinations was simulated in a variety of phantoms (geometrical phantoms or digitized patient phantoms). Details on the implemented phantoms are provided in section 2.4.
The tracked physics processes of photons, electrons, and positrons (i.e. Compton effect, Rayleigh scattering, etc.) are defined in a 'physics list' and are described in detail in section 2.1.3.

2.1.1 USER ACTION CLASSES

The object-oriented structure of Geant4 includes a variety of classes, which the user can adapt according to the specific needs of a MC model. Three classes are mandatory for a MC simulation in Geant4, describing the photon emission, the geometry and materials of the CT model and phantoms, and the tracked interactions of particles in matter.

2 Incident/initial photons are also called primary photons or primaries. Electrons/photons arising from interactions in matter are called secondary electrons/photons or secondaries.

X-RAY EMISSION The *G4VUserPrimaryGeneratorAction* class provides information about the x-ray source, e.g. its position, number and type of particles, and the particle distribution.

CT AND PHANTOM GEOMETRY The *G4VUserDetectorConstruction* class describes information about the general scanner geometry, phantom and material selection, filtration, and the image detector. Do not get confused on the name of this class – all geometrical components belong to this class and are named 'detector', not just an image detector. All geometrical components can be made 'sensitive', meaning that energies can be scored in all geometrical components.

PHYSICS LIST The *G4VUserPhysicsList* class describes all physics processes and available particles in the simulation.

Optional user action classes, initialized in the current MC model, are *G4UserEventAction* and *G4UserRunAction*. These are classes that handle data collection and storage of data for further analysis.

2.1.2 RANDOM NUMBER GENERATOR

MC models use pseudo-random numbers as a base to perform the simulations. In this implementation, the random number generator 'MTwistEngine' is employed, which is based on the Mersenne Twister generator. It has a periodicity of $2^{199377} - 1$ events (Matsumoto and Nishimura 1998). The random number generator uses the value of a seed to generate a sequence of random numbers. Using exactly the same seed value in two repetitions of a simulation will lead to exactly the same results in both repetitions (Ljungberg 1998, p. 2). The seed value in the employed MC model is initialized using the time stamp of the system computer clock, and therefore ensures independent simulation statistics for different simulations.

2.1.3 PHYSICS LIST

The physics list determines the type of particles and processes, which are tracked during the MC simulation. The user can select from existing physics lists or develop own lists for the specific purpose of the simulation. Photon energies in diagnostic radiology range typically between 0 and 140 keV, requiring a detailed description of low-energy physics processes. For this work, physics models developed for the PENetration and Energy LOss of Positrons and Electrons (PENELOPE) code (version 2001) were employed (Baró et al. 1995; The Geant4 Collaboration 2008). These models were designed for the use in MC simulations and allow tracking of energies down to a few hundred eV. Background information on the tracked physics processes of photons can be found in section 1.3.1.
Photons, electrons, and positrons are tracked during the simulation. For photons, gamma conversion (*G4PenelopeGammaConversion*), Compton scattering (*G4PenelopeCompton*), the photoelectric effect (*G4PenelopePhotoElectric*), and Rayleigh scattering

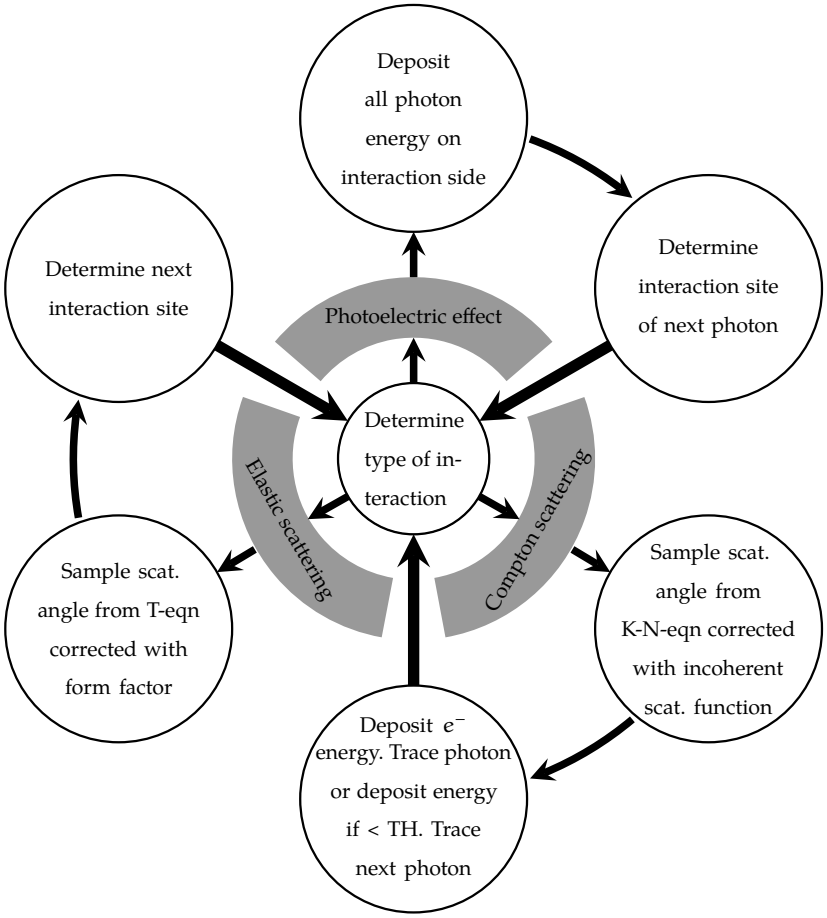

Figure 2.1: Simulation of photon processes in a scattering medium in Monte Carlo (MC) simulations, adapted from Chan and Doi (1983). Abbreviations: Klein-Nishina equation (K-N-eqn), Thomson equation (T-eqn), scattering (scat.), threshold (TH).

(*G4PenelopeRayleigh*) are tracked. For electrons and positrons, the processes multiple scattering (*G4MultipleScattering*), ionization (*G4PenelopeIonization*), and bremsstrahlung (*G4PenelopeBremsstrahlung*) are tracked. Additionally, annihilation processes (*G4PenelopeAnnihilation*) are tracked for positrons (Steuwe et al. 2018).
The range of photons, electrons, and positrons in a material depends on their energy and on the material properties. In this work, a range cut-off of 100 µm was set, corresponding to energies of 990 eV in air and 1.1 keV in water for photons and 84.7 keV in water for electrons and positrons (Steuwe et al. 2018). If the range of an photon, electron, or positron is <100 µm, its energy is deposited at its current position and the particle is not further tracked.
Chan and Doi (1983) have published a schematic overview of the photon transport as handled by MC methods, that visualizes the processes of photons and electrons after each interaction (see figure 2.1).

2.1.3.1 *Interaction cross-sections and material database*

Data of interaction cross-sections were provided by the low-energy extension of the electromagnetic processes data, version 6.2, distributed in the source file of

Geant4 (Steuwe et al. 2018). The material properties were retrieved from the National Institute of Standards and Technology (NIST), ICRU databases (Hubbell and Seltzer 2018a), and literature (Carver et al. 2017; Chang et al. 2016), see appendix B.

2.1.4 STORAGE OF INTERACTION DATA

Simulation results were stored and analyzed in Root 5.34/32 (Brun and Rademakers 1996; Steuwe et al. 2018). In Root, data can be stored in large tables (branches), which can efficiently be used for data analysis. The single branches (variables) are combined in trees and stored as a single file.
The following information was stored for every interaction (including scattering) in a tracked volume as branches in a Root tree:

- incident photon energy
- energy deposited in the phantom
- position (x,y,z) of interaction
- interaction type (photoelectric effect, ionization, Compton effect, bremsstrahlung, Rayleigh scattering, multiple scattering of charged particles in matter)
- volume in which the interaction took place
- track identification (ID) (from primary or secondary interactions)

Information stored in the different branches can be combined during analysis, e.g. the deposited energy at specific positions can be plotted or only the energy deposition resulting from a specific interaction type.
From this information, energy maps (2D- or 3D-histograms) or profiles of the spatial distribution of energy deposition inside phantoms can be calculated, as well as the total energy deposition (E_{total}) determined. An analysis of the simulation time, data storage, and required disk space for the extensive data output of the simulations can be found in appendix C.

Further analysis software tools used throughout this thesis are described in appendix D.

2.2 CT SCANNER GEOMETRY

In the developed MC model, the scanner geometry of the Aquilion™16 (formerly Toshiba Medical Systems Corporation, Nasu, Japan, now Canon Medical Systems Corporation, Ōtawara, Japan) was employed since the measurement of x-ray source spectra, beam-shaping filtration, and transmission were performed on this scanner (prior to this work). Scanner specifications can be found in appendix A. The general geometry of a CT scanner as implemented in the MC model was presented in figure 1.3. Please refer to section 2.3 for the measurement of x-ray spectra and section 2.3.5 for the employed beam-shaping methods.

2.3 X-RAY EMISSION

This section provides the x-ray spectra employed throughout in this work. Spectra were either measured at 120 kV_p (Aquilion™16) or generated using an online tool for 80, 100, and 120 kV_p (Siemens Healthineers 2018). For closer inspection, the individual spectra are plotted in appendix E.

2.3.1 MEASURED CT X-RAY TUBE SPECTRA

Prior to this work, x-ray source spectra of the Aquilion™16 CT x-ray source (CXB-750D MegaCool) were measured using Compton spectroscopy and reconstructed according to Matscheko and Ribberfors (1987) (Stiller et al. 2019). Spectra were measured for fan angles between 0° and 20°, in steps of 2°, and at 21° (see figure 2.2). From the spectral measurements, information on the photon transmission through the beam-shaping filter was obtained and further used to model a physical beam-shaping filter (PBF) for MC simulations (Veloza 2012), and to implement a probability density function (PDF) for photon fan-angle dependent photon fluence modulation (FM), see section 2.3.5.2 and figure 2.3. Dimensions and design of the beam-shaping filter developed prior to this work are given in appendix F.
Due to beam-hardening caused by the beam-shaping filter, the mean spectral energy increased from 57.7 keV at a fan angle of 0° to 76.7 keV at a fan angle of 21°. Figure 2.4 compares the shape of the 0°- and 21°-spectra for normalized photon intensities. Throughout this thesis, the measured 0°-spectrum is the reference spectrum. The mean energy of the reference spectrum, $E_{mean,ref}$, equals 57.7 keV.

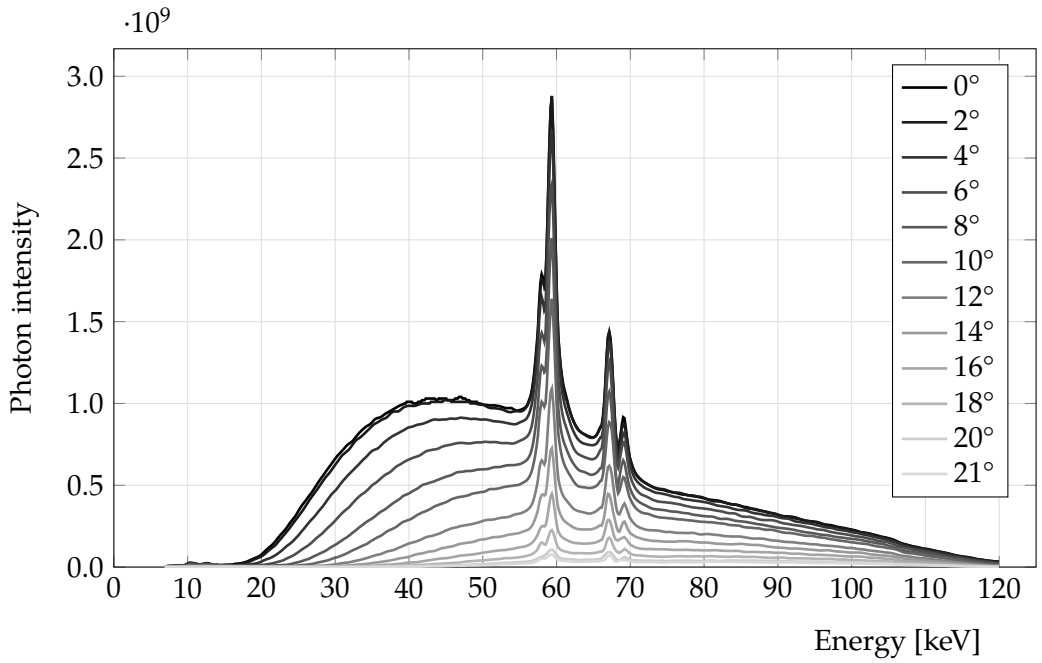

Figure 2.2: Measured fan-angle dependent Aquilion™16 spectra. Photon intensity decreased with increasing fan angle, whereas mean spectral energy increased.

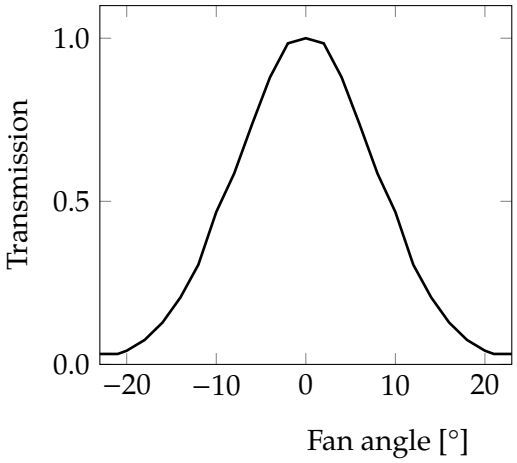

Figure 2.3: Fan-angle dependent photon transmission caused by beam-shaping filtration. The photon fluence is higher at the center of the fan beam, whereas it is reduced to the sides of the fan beam. This curve is implemented as a probability density function (PDF). Adapted from Steuwe et al. (2018).

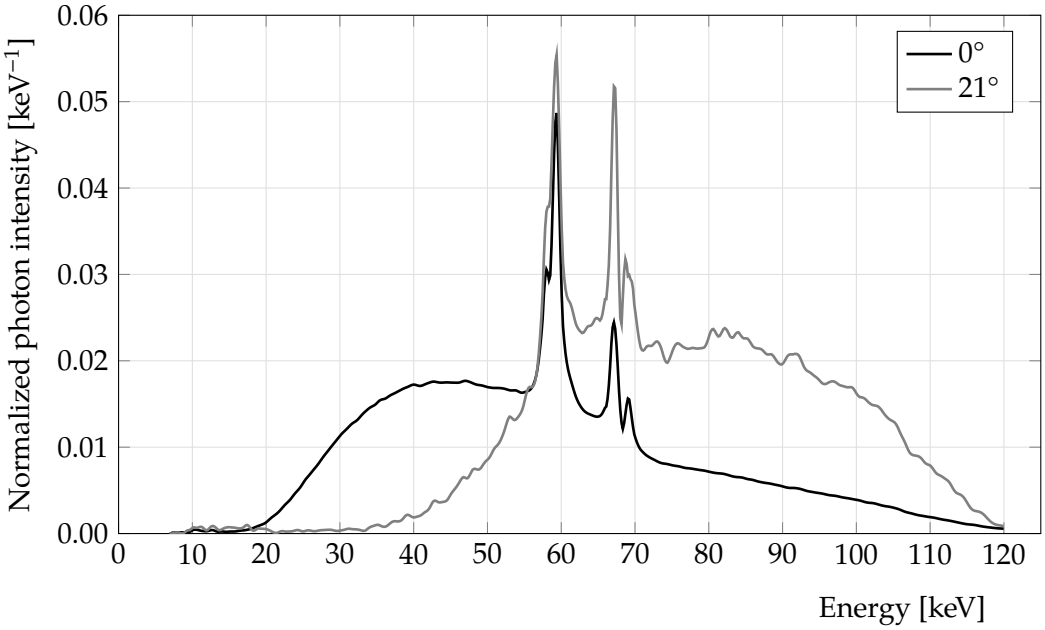

Figure 2.4: Measured normalized Aquilion™16 spectra at 120 kV_p at 0° and 21°, showing the beam-shaping filter induced spectral distortion at larger fan angles. The mean spectral energy increased from 57.7 keV at a fan angle of 0° to 76.7 keV at a fan angle of 21°.

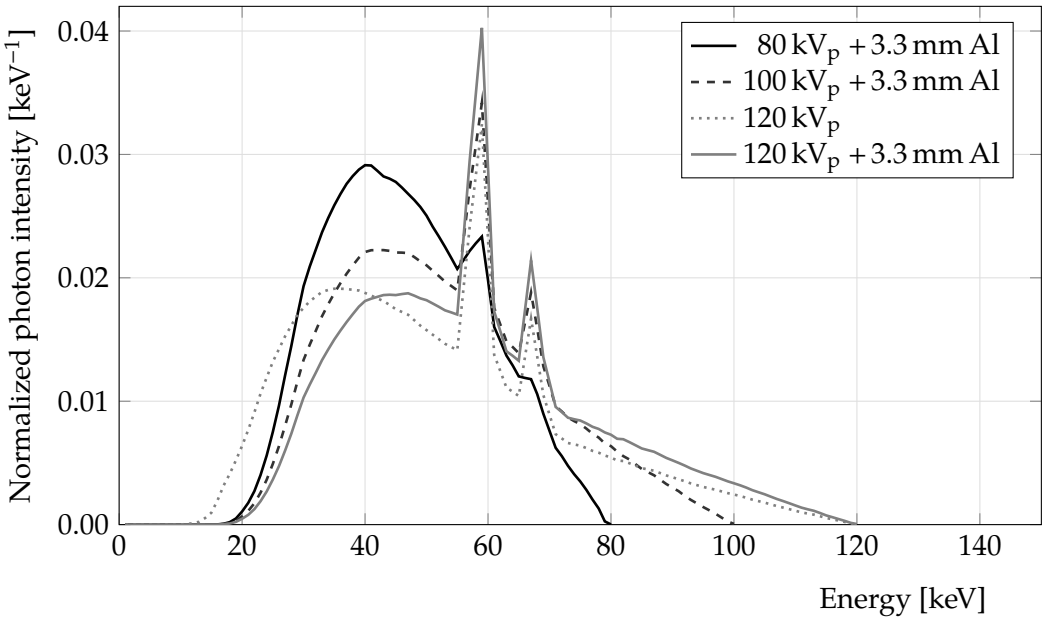

Figure 2.5: Generated spectra without (120 kV_p) and with 3.3 mm aluminum (Al) filtration (80, 100, and 120 kV_p) for matching mean energy of the generated and measured 120 kV_p spectra. Spectra available from Siemens Healthineers (2018).

2.3.2 GENERATED SPECTRA

In addition to the measured spectra, spectra were generated at tube potentials of 80, 100, and 120 kV_p using an online tool (Siemens Healthineers 2018). A filtration of 3.3 mm aluminum was added such that the mean energy for the generated 120 kV_p-spectrum matched the mean energy of the measured central spectrum, $E_{mean,ref} = 57.7$ keV. Mean energies of the generated spectra *without* 3.3 mm aluminum filtration were 40.8 keV at 80 kV_p, 46.7 keV at 100 kV_p, and 51.5 keV at 120 kV_p. Mean energies of the generated spectra *with* 3.3 mm aluminum filtration were 46.6 keV at 80 kV_p, 52.7 keV at 100 kV_p, and 57.7 keV at 120 kV_p. The filtered spectra and the unfiltered spectrum at 120 kV_p are depicted in figure 2.5.
The measured and the generated filtered spectrum at 120 kV_p are compared in figure 2.6, showing subtle differences between 20 keV and 60 keV. The peak-positions at the characteristic x-ray energies of tungsten at ~67 keV and ~59 keV are in accordance, although peak height differs slightly.

2.3.3 MONOENERGETIC PHOTONS

Since source spectra are not always available, monoenergetic photons as a simplified approximation of spectral distributions were implemented. For this purpose, the mean spectral energy of the central reference spectrum ($E_{mean,ref} = 57.7$ keV) was employed as the monoenergetic photon energy.

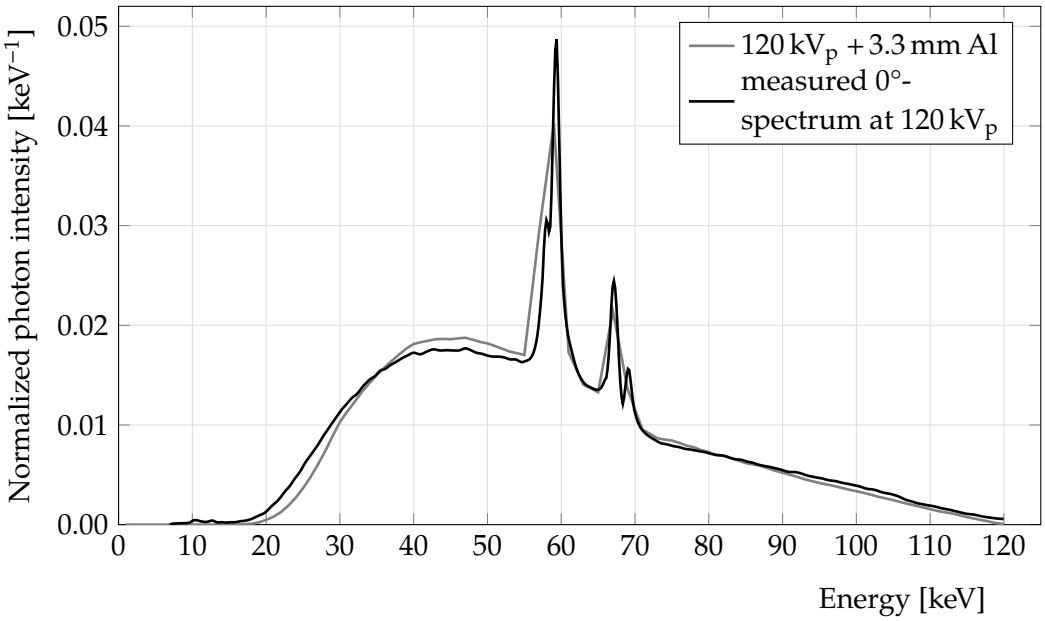

Figure 2.6: Generated spectrum with 3.3 mm aluminum (Al) filtration, for matching the mean energy of the measured 0°-spectrum at 120 kV_p. Generated spectrum available from Siemens Healthineers (2018).

2.3.4 scaling of photon statistics accounting for x-ray tube efficiency

In clinical CT, the TCTP is adapted to the tube potential since the x-ray source efficiency differs for different tube potentials (see table 1.1 and corresponding explanation in section 1.2.2.3). As mentioned in the introduction, a practical approach is to increase the exposure by a factor of 1.5 for a reduction of the tube potential of 20 kV. This factor compensates for the efficiency differences at different tube potentials (120 kV_p: efficiency 1, final exposure output 1; 100 kV_p: efficiency ~0.69, compensation factor 1.5, final exposure output 1; 80 kV_p: efficiency ~0.44, compensation factor 2.25, final exposure output 1). When comparing the influence of different tube potentials on energy deposition in this work, the compensation factors are intrinsically employed by using equal numbers of photons for the different tube potentials (same final count of emitted photons after beam-shaping filtration).

2.3.5 beam-shaping filtration

2.3.5.1 *Physical beam-shaping filter (PBF)*

A PBF in the shape of a bowtie was positioned between the x-ray source and the isocenter, at a distance of 15 cm from the source. Dimensions and material specifications are described in appendix F. The beam-shaping filter was designed prior to this work, according to Lambert Beer's law (Veloza 2012).
The PBF both models fan-angle dependent photon fluence and spectral beam-hardening, resulting in fan-angle dependent spectra (FADS). The implementation of a PBF results in fan-angle dependent photon fluence and spectral distortion since

photons are absorbed during the passage of the PBF. The number of initial photons needs to be increased by a factor of approximately 2.36 to counterbalance the loss of photons in the PBF, doubling the simulation time.

2.3.5.2 *Fan-angle dependent fluence modulation (FM)*

Fan-angle dependent photon fluences induced by the varying x-ray path lengths through the beam-shaping filter were obtained prior to this work (see section 2.3.1). The beam-shaping filter's increasing thickness towards its edges causes a reduction of the photon fluence, cf. figure 2.3, resulting in fan-angle dependent photon fluence. By implementing a PDF for the fan-angle dependent photon fluence, total photon statistics were distributed over the fan angles relative to the transmission values. Bear in mind that the implementation of the PDF only alters the fan-angle dependent fluence. Beam-hardening due to the beam-shaping filtration is not accounted for (Steuwe et al. 2018). The method for evaluation of fluence modulation (FM) using a PDF is described in section 2.5.1.3 and the results are presented in section 3.1.1.

2.3.5.3 *Fan-angle dependent spectra (FADS)*

Since FM only simulates the fan-angle dependent photon fluence, FADS need to be employed in the MC model to implement spectral hardening (see figure 2.2). Before photon emission, the angle α of the photon is determined, either from a uniform photon distribution (no photon fluence modulation (NM)) or by employing FM based on the PDF, see figure 2.3. According to this angle, the corresponding measured spectrum (refer to section 2.3.1) is determined according to table 2.1.
From the corresponding spectrum, the photon energy is sampled according to its probability in the spectrum. Hence, of all angles, angles around 0° are most probable and for this angle, photons with an energy of ~59 keV (characteristic x-ray energy of tungsten, see figure 1.4) have the highest probability of being emitted.
FADS are not commonly available without measuring them directly (refer to sections 1.2.2.4 and 2.3.1). Since FADS were only available from the Aquilion™16 CT scanner, modeling of the beam-shaping filter induced spectral distortion was not possible for the generated spectra.

2.3.6 SOURCE IMPLEMENTATIONS

Several source implementations can be selected for MC simulations of CT acquisitions, depending on the purpose of the simulation. There are two experimental sources (point source and square source) with a fixed position and a point source for the clinical axial (step-and-shoot) and helical (spiral) acquisition mode that have been used in this work. Each source can emit a photon distribution according to an energy spectrum of photons or monoenergetic photons.

2.3.6.1 *Point source*

The point source is placed at a fixed position (e.g. 9 or 12 o'clock) with a distance of 60 cm to the isocenter of the modeled CT system. The emitted photons cover

Table 2.1: Assignment of the measured spectra according to the Monte Carlo sampled photon angle α. The photon angle is either randomly chosen (uniform modulation) or based on the transmission curve (probability density function, PDF), see figure 2.3.

Condition			Spectrum
$-1 < \alpha <= 1$			0°
$1 < \alpha <= 3$	or	$-3 < \alpha <= -1$	2°
$3 < \alpha <= 5$	or	$-5 < \alpha <= -3$	4°
$5 < \alpha <= 7$	or	$-7 < \alpha <= -5$	6°
$7 < \alpha <= 9$	or	$-9 < \alpha <= -7$	8°
$9 < \alpha <= 11$	or	$-11 < \alpha <= -9$	10°
$11 < \alpha <= 13$	or	$-13 < \alpha <= -11$	12°
$13 < \alpha <= 15$	or	$-15 < \alpha <= -13$	14°
$15 < \alpha <= 17$	or	$-17 < \alpha <= -15$	16°
$17 < \alpha <= 19$	or	$-19 < \alpha <= -17$	18°
$19 < \alpha <= 20$	or	$-21 < \alpha <= -19$	20°
$20 < \alpha <= 23$	or	$-23 < \alpha <= -20$	21°

a FOV of approximately 50 cm. A specified fan angle range (e.g. ± 18°) can also be set to reduce the exposed area. In z-direction, the point source emits photons depending on the specified collimation (~±1.528° for a z-collimation of 32 mm, see figure 1.3 for the coordinate system of the CT model). This point source is employed for the acquisition of selected projections (acquisitions with one specific fixed source position).

2.3.6.2 *Square source*

The square source is placed at 12 o'clock with a distance of 60 cm to the isocenter of the modeled CT system. It is a quadratic shaped source of 10 cm x 10 cm size (parallel to x-z plane), and emits photons parallel to the scanners' y-axis. This source produces a uniform exposure of a 10 cm x 10 cm area.

2.3.6.3 *Step-and-shoot/axial acquisition mode*

For the step-and-shoot acquisition mode, the x-ray source rotates around the patient for a full rotation while the patient is in a fixed position (without table feed). After a full rotation of the source, the patient table moves (step) and the next rotation of the x-ray source starts (shoot). The z-collimation and the step length of the table are flexible. If the step length equals the z-collimation, a homogeneous coverage of the patient is achieved (contiguous coverage). For a step length longer than the z-collimation, parts of the patient are not exposed and there are gaps between the x-ray beams. If the step length of the table is shorter than the z-collimation, each part of the patient is exposed more than once (overlap of x-ray beams). The influence of the step size in the step-and-shoot mode is depicted in appendix G, figure G.1.

2.3.6.4 *Helical/spiral scquisition mode*

For the helical acquisition mode, the point source moves in a 360°-rotation around the patient during which the patient is moved. This acquisition mode is implemented in the MC simulation as follows: while the phantom is positioned stationary, the source rotates around the phantom and is translated along the z-direction depending on the user-specified detector collimation and pitch. For geometrical phantoms, the scan coverage and scan start position are user-specified, whereas these values are obtained from the DICOM-headers for voxelized patient phantoms.
If the table displacement during one source rotation equals the z-collimation, a pitch = 1.0 is achieved, with a contiguous x-ray beam coverage of the patient. For pitches > 1.0, x-ray beams are not contiguous, since the table displacement per source rotation is larger than the beam collimation. Parts of the patient are not irradiated for pitches ≥ 2.0. For pitches < 1.0, x-ray beams are overlapping along the patient and patient tissue is exposed more than once. The helical acquisition mode was implemented and compared to the implementation published by Kim et al. (2013). The influence of the pitch in the helical acquisition mode is depicted in appendix G, figure G.2.

2.3.7 TUBE-CURRENT MODULATION (TCM)

2.3.7.1 *Longitudinal TCM (LTCM)*

The tube current is modulated along the z-direction of the patient (along the body, see figure 1.12a). Information on the slice-specific exposure (in mAs) has been obtained from DICOM-headers (DICOM tag 0018,1152) of the reconstructed images. The thinner the reconstructed slices, the more detailed the information about the exposure.
Information on the exposure can either be read out in an independent program and used as input in any simulation or obtained during the simulation of a digitized patient (see section 2.4.2). For the latter case, the DICOM-header with all the necessary CT-acquisition information for the simulation is read out in the file 'DicomHandler.cc' and transferred to the file 'PhantomDicom.cc'. The effect of LTCM is depicted in appendix G, figure G.4.

2.3.7.2 *Angular TCM (ATCM)*

The ATCM modulates photon emission through a 360°-rotation, such that more photons will be emitted along the lateral path, and less photons along the a.p. path. The reason for this modulation is the difference between the lateral diameter and the a.p.-diameter of a typical patient, which becomes apparent for the shoulder or the hip region. The modulation reduces unnecessary radiation exposure for thin body regions and also homogenizes the measured detector signal along the rotation.
In the MC simulation, the ATCM was implemented using the formula

$$N_p(\beta) = N_{rot} \cdot \frac{\Delta\beta}{360^\circ} \cdot \left[1 - 0.5 \cdot \cos\left(\frac{\beta}{0.5}\right)\right] \tag{2.1}$$

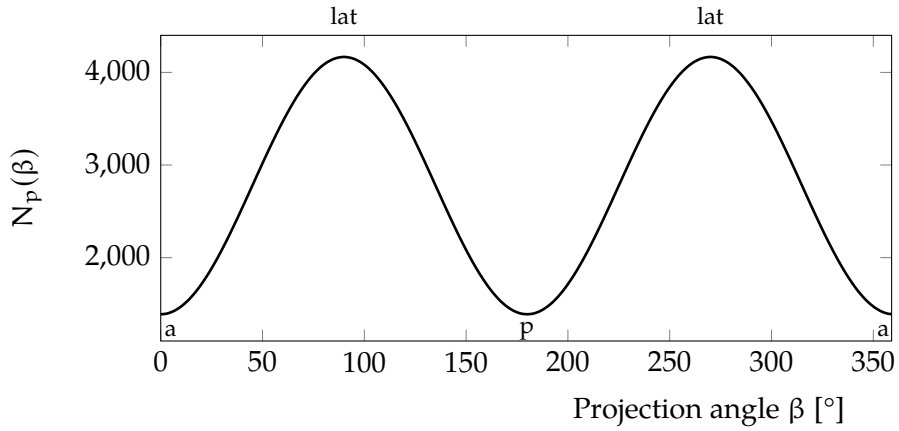

Figure 2.7: Implementation of angular tube-current modulation (ATCM), using equation 2.1 to calculate projection-angle dependent photon emission. Example with an average of $N_{rot} = 1 \cdot 10^6$ photons per rotation. Abbreviations: anterior (a), posterior (p), lateral (lat).

with β as projection angle, $\Delta\beta$ as angular displacement per projection, N_{rot} as number of photons in one rotation and N_p as number of photons per projection angle. There are 360 individual source positions during one rotation for $\Delta\beta = 1°$, whereas there are 720 individual source positions for $\Delta\beta = 0.5°$. The angular tube-current is not modulated online (during the simulation) based on patient attenuation, but beforehand. In the example in figure 2.7, N_{rot} was set to $1 \cdot 10^6$. The highest photon emission occurs at 90° and 270° (lateral path), the lowest photon emission at 0° and 180° (a.p.-path).
A similar implementation is provided by Fujii et al. (2017) with a sinusoidal function of the tube angle. The effect of ATCM on the spatial distribution of energy deposition is depicted in appendix G, figure G.5.

2.4 IMPLEMENTED PHANTOMS

2.4.1 GEOMETRICAL PHANTOMS

A series of geometrical phantoms has been designed and implemented into the MC simulation tool throughout this work. These phantoms consist of geometrical shapes (ellipsoids, cylinders, etc.), which can be combined or subtracted (Boolean operations). The advantage of geometrical phantoms is the ability to design the desired setup to answer a specific research question. The shapes (e.g. *G4Box*, *G4Tubs*, *G4Orb*) get material properties (as *G4LogicalVolume*) and information about their spatial positioning (as *G4VPhysicalVolume*).

2.4.1.1 *Water phantom*

The water phantom (see figure 2.8) is a cylindrical phantom of 32 cm diameter and 8 cm height. It is a useful phantom to observe and study effects of different x-ray source spectra on energy deposition and its spatial distribution. Geometrical

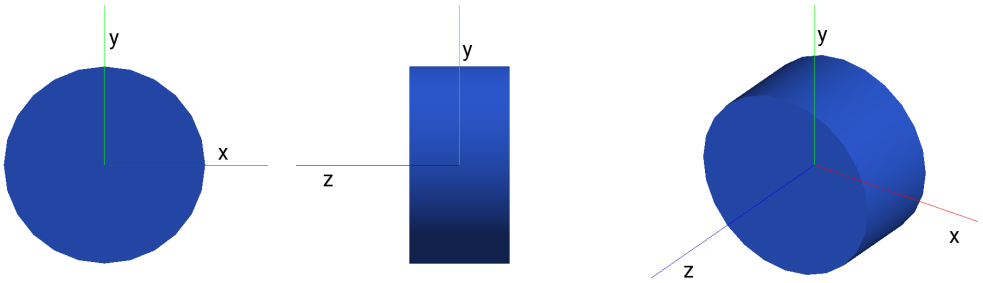

(a) Frontal view (b) Side view (c) Oblique view

Figure 2.8: Geometrical water phantom, ∅ = 32 cm, height 8 cm. Axes: red (x-axis), green (y-axis), blue (z-axis).

phantoms assigned with "water" as material property are frequently employed to study the energy deposition in MC simulations (DeMarco et al. 1998; Fogliata et al. 2007; Zhou and Boone 2008).

2.4.1.2 *Box phantom*

The box phantom (see figure 2.9) is a geometry consisting of three cuboids, each with side length of 10 cm and height 3 cm (total height of the box phantom 9 cm). Being in a distance of 3 cm underneath the phantom, a lead detector (5 cm thick) is positioned, to score as many as possible incoming photons. The materials of the three layers of the box phantom were chosen depending on the research question. The design of the phantom was taken and adapted from Verhaegen et al. (2005).

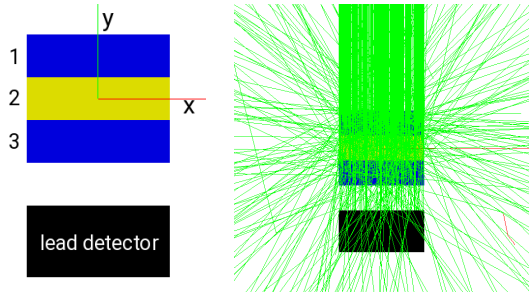

(a) Frontal view (b) Frontal view, with x-ray emission from experimental square source

Figure 2.9: Geometrical box phantom with 10 cm length in x- and z-direction and y-height per block = 3 cm. The lead detector located underneath the phantom is depicted in black. Adapted from Verhaegen et al. (2005). Axes: red (x-axis), green (y-axis).

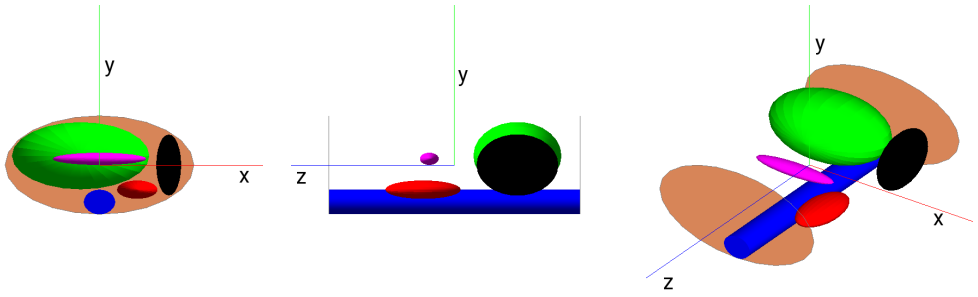

(a) Frontal view (b) Side view (c) Oblique view

Figure 2.10: Basic abdomen phantom (Amato et al. 2010), modeling the spine (blue) and the organs liver (green), spleen (black), pancreas (pink), and one kidney (red). The outlines of the soft tissue are indicated with the black lines. Axes: red (x-axis), green (y-axis), blue (z-axis).

2.4.1.3 *Abdomen phantom*

Amato et al. (2010) have published an anthropomorphic abdomen phantom with precise description of shape and positioning of the simulated organs. The phantom models the liver (green), the spine (blue), one kidney (red), the spleen (black), and the pancreas (pink), made of ellipsoids in an elliptical soft tissue tube (see figure 2.10). This abdomen phantom has a length of 40 cm in z-direction.
The basic abdomen phantom was further developed (see figure 2.11). The shape of the liver has been altered to that of the Medical Internal Radiation Dose (MIRD)-phantom (ICRP 1975). Furthermore, the aorta, a simplified GI-tract, and a second kidney have been added. The abdomen phantom now contains (from out- to inside) a 4 mm thick skin shell (gray), a 4 mm thick subcutaneous fat shell (yellow), and a 15 mm thick soft tissue shell (salmon). The phantom is now filled with fat (yellow), instead of soft tissue as the inner organs are usually surrounded by visceral fat. The

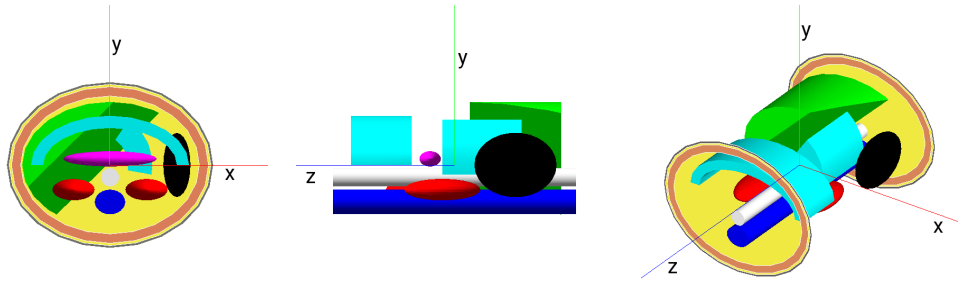

(a) Frontal view (b) Side view (c) Oblique view

Figure 2.11: Modified abdomen phantom with added aorta (gray), kidney (red), GI-track (cyan), and altered shape of liver and an increased patient diameter. Furthermore, the skin (4 mm thickness), a fat layer (4 mm thickness), and a soft tissue layer (1.5 cm) were included in the phantom. The soft tissue inside the phantom was replaced by fat. Axes: red (x-axis), green (y-axis), blue (z-axis).

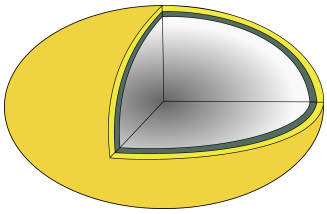

Figure 2.12: Shell structure of organs in the modified abdomen phantom. Inner core (gray), outer organ shell (green), and surrounding fat shell (beige).

diameter of the phantom was increased from 30 cm to 34 cm in x-direction, and from 16 cm to 17 cm in y-direction since the new design of the liver is slightly larger.
The organs liver, spleen, kidneys, and pancreas feature a shell structure. The organs consist of an inner organ core and an outer organ shell (thickness of 2.5 mm) where interactions can be individually tracked and energy deposition determined. The organs are surrounded by a fat shell (again thickness of 2.5 mm), which can also be individually tracked. The purpose of this design is to determine the energy deposition at interfaces of organs and the influence of iodinated contrast agents on the energy deposition at the interfaces for various tube potentials.

2.4.2 DIGITIZED PATIENT PHANTOMS

Digitized phantoms are implementations of 3D-CT image data sets as phantoms for MC simulations (see figure 2.13). 3D-CT image data sets contain density-specific CT numbers and their corresponding positions, e.g. a matrix of 512 x 512 x 200 voxels, containing 200 slices of each 512 x 512 picture elements (pixels). To obtain a digitized phantom from the image data, each image voxel is assigned to a density and a material corresponding to its CT number and morphology. From CT image

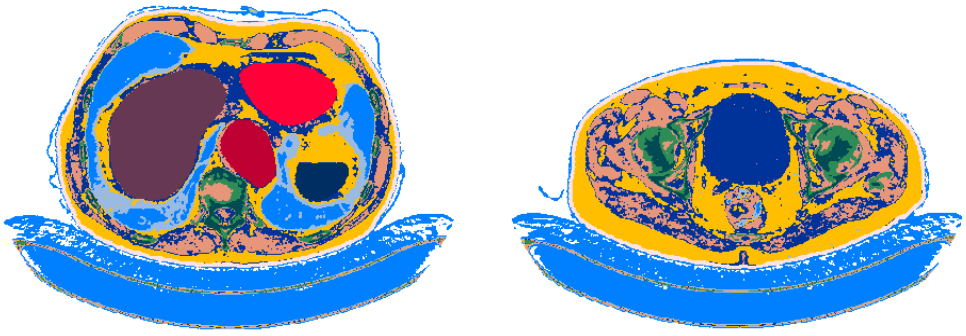

(a) Axial plane through the heart (light red), liver (purple), and lungs (light blue). An aortic aneuryism is clearly visible (red).

(b) Axial plane through the femoral neck and the bladder (water in dark blue).

Figure 2.13: Depiction of the digitized patient phantom converted from computed tomography images. Note that the table contains a material inside with a density close to that of lung tissue (probably a foam), and is automatically assigned to lung tissue.

data of patients, digitized patient phantoms can be constructed, allowing to create individualized radiation exposure maps.
Appendix H provides additional information on the development of digitized patient phantoms, including the necessary segmentation steps, (post-processing) methods of segmentation, and required input files to run the simulations.

2.4.2.1 *Segmentation of body structures*

Different automatic methods are available for the segmentation of organs from CT images, such as threshold-based methods, region growing, or shape models (Sharma and Aggarwal 2010). As CT numbers especially in the abdomen are very close to each other, automatic methods often fail in differentiating between organs of similar characteristics (and hence similar CT numbers and morphology), whereas the skeleton and the lungs can be very reliably segmented using threshold-based methods (Sharma and Aggarwal 2010).
The standard method in Geant4 is the segmentation via thresholding, making use of a 'CT-to-density' conversion table (see appendix H.1). With this method, first, the density of each voxel is calculated and afterwards, a specific material according to this density assigned. Due to the similarity in densities in the abdomen, this method is rather vague for specific organ identification.

In the geometrical abdomen phantom, the individual organs can be individually tracked and the exposure values determined, since their shape and position are mathematically defined. To allow the same measurements in the digitized patient phantoms, it is necessary to ensure proper organ identification. For this purpose, organs have been contoured using the software Oncentra® External Beam (version 4.5.2, Nucletron B.V, Veenendaal, the Netherlands, nowadays Elekta Brachytherapy), which is employed in radiotherapy for contouring of target volumes and organs-at-risk and for radiation therapy treatment planning.
The structures/organs given in table H.1 have been manually segmented and corresponding pixel values (material indices) have been associated. Shell structures (thickness 2.5 mm) for the liver, spleen, and kidneys were additionally created as has been performed for the modified abdomen phantom. Due to the small structure of the pancreas, the shell-segmentation has not been performed in this organ.
As figure 2.13 shows, the inside of the patient table is erroneously assigned to lung tissue as its material's CT number is close to that of lung tissue. Manual segmentation of the lungs allows to calculate only the energy deposition inside the lungs.
The contoured organs are saved in a structure set file format (a single RS.filename.dcm file, containing the drawn contours), and further processed in an open-source program based on ITK4 ('Importing Contours from DICOM-RT Structure Sets with ITK4', Dowling 2013). The program reads in the underlying CT images and the structure sets and converts the structures into individual binary images. Afterwards, a certain value can then be assigned to a specific structure to differentiate between organs (the software ImageJ was used during this work, see section 2.1.4).

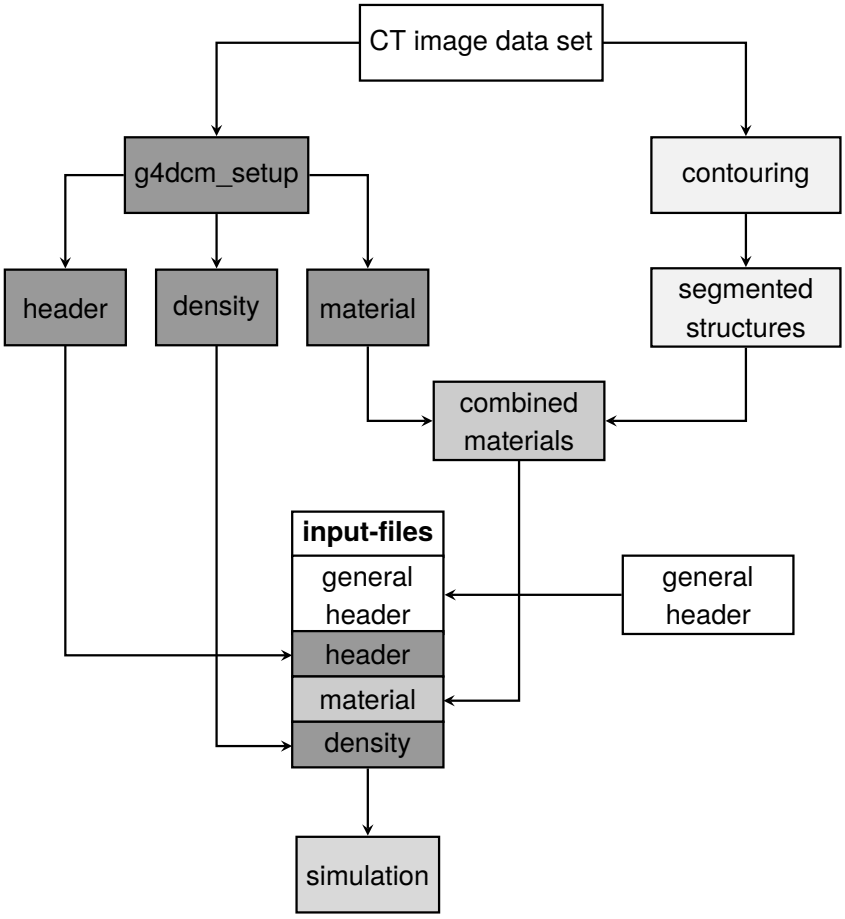

Figure 2.14: Overview of the segmentation process. CT images in DICOM format are a) segmented using an automatic thresholding method in the g4dcm-setup program, and b), specific structures are manually contoured. The automatic method assigns a material index and calculates a density according to the CT numbers of the inserted DICOM image stack. The material allocation from the automatic method and the manually segmented structures are combined in a single file together with the automatically assigned density values. This file in inserted in the simulation. Abbreviations: computed tomography (CT), Digital Imaging and Communications in Medicine (DICOM).

Figure 2.14 presents the segmentation process for tissue and material allocation of the digitized phantoms. An automatic thresholding method was employed in a first step ('g4dcm_setup') to assign a material value to each image pixel and to calculate each pixel's density from the CT numbers (figures 2.15a). Here, only air, lung tissue, water, soft tissue, and bones were automatically allocated (figure 2.15b). The densities were calculated using a 'CT2Density' lookup table (see listing H.2, figure H.1). In this table, specific densities are associated with specific CT numbers (e.g. CT number and densities for air, water, bones). The density of a specific pixel was calculated by interpolation between the fixed density/CT number pairs in the lookup table. The automatic method produced three files for each CT image: (1) a header file with information about image slice position, exposure value, and matrix size, (2) density values per pixel calculated from the CT numbers of the CT image, and (3)

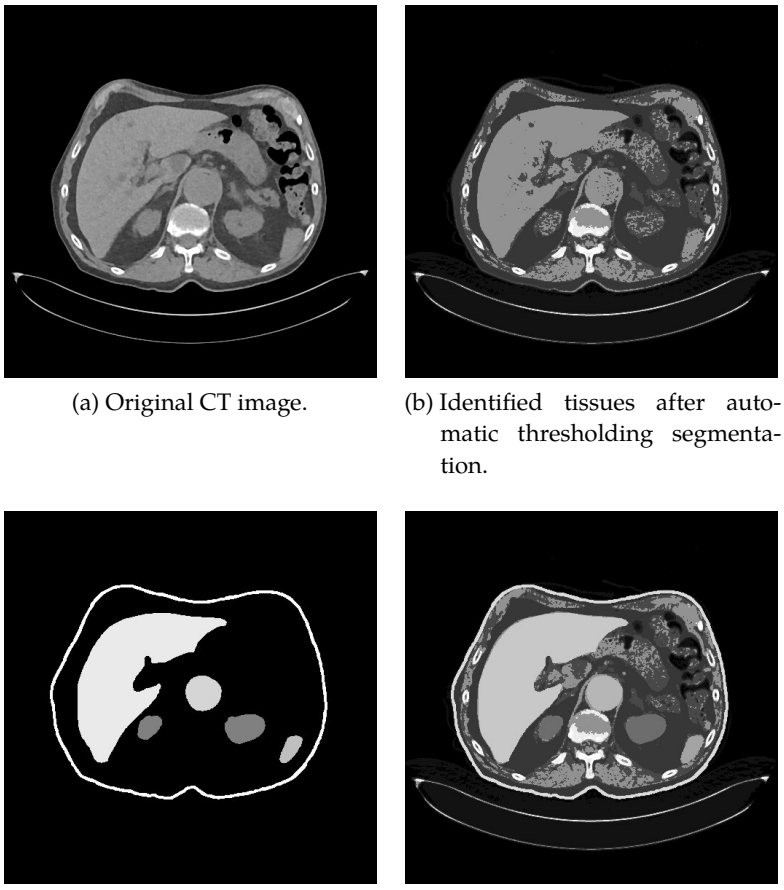

(a) Original CT image.

(b) Identified tissues after automatic thresholding segmentation.

(c) Contoured tissues as binary image mask. Different material IDs were already assigned to the structures.

(d) Material combination after automatic and manual segmentation.

Figure 2.15: Original computed tomography (CT) image (a), automatically segmented using a thresholding method (b) and manually segmented (c) using the software Oncentra® External Beam® (Nucletron, nowadays Elekta Brachytherapy). The liver, kidneys, aorta, spleen, and the skin are visible in the mask image (c). Material composition is combined after automatic and manual segmentation (d) to assure proper tissue allocation (e.g. calculation of organ exposure).

the material ID per pixel.
In a second step, the manual segmentation took place (see appendix H), and binary mask files (pixel value either 1 (inside mask) or 0 (outside mask)) were produced from the structure sets (see figure 2.15c). The binary images were multiplied with the number of the material ID (e.g. 6 for the kidneys, compare with table H.1).
To assign the precise material to the structures of interest, the manually segmented images (figure 2.15c) and the images from the threshold method (figure 2.15b) have been merged (see figure 2.15d). During the simulation, the material and density information are combined. As an example, there are several types of the material liver, consisting of the same basic composition, but differing in the assigned density (Liver_0.95, density: 0.95 g/cm^3, material: Liver_1.05, density: 1.05 g/cm^3, material:

Liver_1.15, density: 1.15 g/cm^3). The densities are always rounded to the nearest density in 0.1 g/cm^3-steps, with a minimum density of 0.05 g/cm^3 assumed for all newly created materials. The minimum difference in density needs to be 0.1 g/cm^3 to initiate a new material.
One input file for each CT image was then generated. This input file contained a general header with information about number of different materials and maximum densities. This header was the same for every inserted image file. The input files further contained an image-specific header with information about the matrix size, image position, and exposure, and finally, the slice specific material IDs and densities.

2.4.3 MATERIAL CHOICE AND CONTRAST ENHANCEMENT

The basic material compositions and densities can be found in appendix B. They are mainly based on NIST, ICRU, and ICRP databases (Hubbell and Seltzer 2018a; ICRP 2018). For geometrical phantoms, only the basic material compositions are used. For the digitized patient phantoms, the material density is additionally calculated from the image CT numbers although the material composition equals that of the basic materials.

For simulations of contrast-enhanced acquisitions, the materials of the tissues/structures aorta (blood), kidneys, liver, pancreas, and spleen were combined with the element iodine. For this purpose, a new material was designed which combined the original tissue (e.g. liver) with the element iodine by assigning a mass fraction for the tissue ($\psi_T = m_T/(m_T + m_I)$) and iodine ($\psi_I = m_I/(m_T + m_I)$), as $\psi_T = 0.995$ with $\psi_I = 0.005$, respectively. This mass fraction corresponds to a tissue iodine concentration of 5 mg/ml and is applied for the simulation of contrast-enhanced acquisitions of the geometrical abdomen and digitized patient phantoms. This mass fraction was chosen based on Amato et al. (2010). The density of the contrast-enhanced (iodinated) tissues (ρ_{TI}) was adjusted according to:

$$\rho_{TI} \cong \frac{m_T + m_I}{V_T} = \frac{m_T + m_T \frac{(1-\psi_T)}{\psi_T}}{V_T} = \frac{\rho_T}{\psi_T} \tag{2.2}$$

with m_T and m_I as tissue and iodine mass, respectively, V_T as tissue volume, $\psi_T = 1 - \psi_I$ as tissue mass fraction, and ρ_T as tissue density (Amato et al. 2010). This formula assumes that for small amounts of iodine, the volume of the iodinated tissue V_{TI} can be approximated by the volume of the original tissue $V_{TI} = V_T$. According to Amato et al. (2010), for an iodine concentration of 5 mg/ml, a maximum inaccuracy in identifying $V_{TI} \cong V_I$ of less than 0.1% is obtained. For liver tissue, the density increases from 1.060 g/cm^3 to 1.065 g/cm^3 for the iodine-enhanced acquisition (density increase of 0.47%).
Patient data from native (non-enhanced) CT acquisitions were used for both non-enhanced and iodine-enhanced acquisitions for the digitized patients. As already described, iodine administration alters the CT numbers such that material assignment would not be consistent between enhanced and non-enhanced acquisitions.

Hence, the same initial image data and density values are inserted in the simulation for both non-enhanced and enhanced acquisitions. For enhanced acquisitions, compositions of tissue and iodine are created from the basic materials and their density adapted according to equation 2.2. Due to rounding of the density to the nearest 0.1 g/cm^3-density step, the density increase by equation 2.2 had no effect on the actual density of the iodine-enhanced material. Hence, for the digitized patient phantoms, only the material composition has changed for the iodine-enhanced acquisitions, however, not the density. Still, the different densities depending on the initial image CT numbers are taken into account.

2.5 TOWARDS VIRTUAL DOSIMETRY: DESCRIPTION OF PERFORMED SIMULATIONS

Several aspects of a MC model of a CT system need to be assessed to allow for reliable and precise simulation of radiation exposure. Initially, the fundamentals of the CT scanner model were assessed, since they form the base for all further simulations. This included the evaluation of different beam-shaping methods and the influence of spectral properties on the total energy deposition, E_{total}, and its spatial distribution, $E_{spatial}$, in a water phantom. These simulations were performed for a distribution of photons corresponding to a tube potential of 120 kV_p since both measured and generated spectra were available for this tube potential. The evaluation of the beam-shaping method and the influence of different photon distributions on E_{total} and $E_{spatial}$ has already been published (Steuwe et al. 2018).
After evaluation of the fundamentals of the CT scanner model, the developed software was used to assess scientific issues in CT imaging: the choice of the tube potential and its influence on the total energy deposition in a homogeneous material and at material interfaces were assessed. Since iodinated contrast agents are employed in CT imaging, the influence of different iodine concentrations in connection with different tube potentials on the total energy deposition and its spatial distribution in different materials was evaluated. The latter two investigations were performed in a simple, box-shaped phantom, allowing for thorough understanding of the basic principles of the radiation exposure associated with CT, without having to account for potentially influencing factors caused by a complex geometry. The next step towards virtual dosimetry was the implementation and assessment of anthropomorphic phantoms. Radiation exposure was first studied in the geometrical abdomen phantom, followed by the evaluation in digitized patient phantoms.

A multitude of simulations and evaluations have been performed during this project. The following nomenclature for the simulations and evaluations was employed throughout this chapter and chapter 3: the names of the individual *simulations* consist of a capital letter (water phantom (W), box phantom (B), modified abdomen phantom (A), patients (P)), and an Arabic numeral (e.g. "W2", for simulation 2 in the water phantom). The names of the subsequent *evaluations* again consist of a capital letter according to the specific phantom, and a Roman numeral (e.g. "W-III" for the third evaluation of the water phantom).

2.5.1 ANALYSIS OF BEAM-SHAPING METHODS AND SPECTRAL PROPERTIES OF X-RAY SOURCES EMPLOYING THE WATER PHANTOM

This subsection describes the evaluation of the fundamentals of the CT scanner model. In clinical CT systems, a beam-shaping filter is installed to obtain a homogeneous signal in the image detector (see section 1.2.1) and to reduce the radiation exposure in the patient during an x-ray source rotation (reduction of unnecessary radiation exposure in shorter patient x-ray path lengths near the edges of the fan beam). The beam-shaping filter causes the desired modulated photon transmission across the FOV, however, it also results in spectral distortion due to beam-hardening. First, a 'virtual beam-shaping model' was validated against the use of a physical beam-shaping filter (PBF) in the water phantom, see sections 2.3.5 and 2.4.1.1 (evaluation W-I).
Afterwards, the influence of the obtained fan-angle dependent photon fluence on the energy deposition in the water phantom was studied (evaluation W-II).
In a next step, the influence and interchangeability of different source spectra and monoenergetic photons corresponding to a tube potential of 120 kV_p on the energy deposition was assessed since measured spectra are not always accessible, see section 1.2.2 (evaluation W-III).
The last set of simulations regarding the spectral properties of x-ray sources was the evaluation of the influence of beam-shaping filter induced spectral distortion on $E_{spatial}$ (evaluation W-IV). Evaluations W-III and W-IV are only presented for employing FM. Evaluation W-V provides an overview of the total energy deposition in the water phantom for all simulations employing either no beam-shaping filtration (NM, no PBF), or virtual beam-shaping filtration (FM).

2.5.1.1 *Performed simulations*

For all simulations described in section 2.5.1, the same general simulation setup was used. The MC model consisted of of three parts: (a) the experimental point source, (b) optional beam-shaping filtration (NM, FM, or PBF), and (c) the water phantom. The point source (section 2.3.6.1) was positioned at 12 o'clock, at a distance of 60 cm to the center of the water phantom. The center of the water phantom (section 2.4.1.1) was positioned at the isocenter of the simplified CT scanner model. Photons were emitted between -23° and +23°, resulting in a FOV of ~50 cm at the isocenter. Z-collimation was set to 32 mm, according to the Aquilion™16 CT scanner's maximum detector z-width (MHRA 2004; Steuwe et al. 2018).

Eleven simulations have been performed for the characterization of spectral properties of x-ray sources (Steuwe et al. 2018):

W1	employing the measured 0°-reference spectrum with a uniform photon fluence (NM) and the physical beam-shaping filter (PBF),

W2/W3	employing the measured fan-angle dependent spectra (FADS) with a uniform photon fluence (NM) and with fan-angle dependent fluence modulation (FM),
W4/W5	employing the measured 0°-reference spectrum with a uniform photon fluence (NM) and with fan-angle dependent fluence modulation (FM),
W6/W7	employing the generated *un*filtered spectrum with a uniform photon fluence (NM) and with fan-angle dependent fluence modulation (FM),
W8/W9	employing the generated filtered spectrum with a uniform photon fluence (NM) and with fan-angle dependent fluence modulation (FM),
W10/W11	employing 57.7 keV monoenergetic photons with a uniform photon fluence (NM) and with fan-angle dependent fluence modulation (FM).

For the first simulation W1 employing the PBF, approximately $236 \cdot 10^6$ photons were tracked to compensate for photon absorption in the beam-shaping filter, whereas $100 \cdot 10^6$ photons were tracked for all other simulations.

2.5.1.2 *Analysis and reconstruction of exposure maps*

All tracked interactions inside the phantom were stored as described in section 2.1.4. The total energy deposition, E_{total}, was calculated for all interactions inside the phantom (including scattering) for all individual simulations (see section 2.5.1.7). Furthermore, the spatial distribution of energy deposition, $E_{spatial}$, was assessed. For this purpose, 2D-histograms (bin size 1.0 x 1.0 mm^2, scored over 80 mm in z-direction) were created, which sum up the energy deposition per interaction along the z-direction in the x-y plane of the phantom.
For simulations W1, W4 and W5, the integrals of the energy maps were normalized to 1. Normalization was necessary to allow for direct comparison of $E_{spatial}$ in cases where the number of photons reaching the water phantom were not comparable (required for evaluations W-I and W-II, described hereinafter). Although the number of photons for the PBF has been increased compared to the simulation employing the fan-angle dependent fluence and spectra, the number of photons initially reaching the water phantom is not perfectly equal and requires normalization.
As the 2D-histograms only present a single 0°-projection, these maps were rotated and summed in 1°-intervals. The 360°-reconstructions allow to assess $E_{spatial}$ for a full source rotation. Relative difference maps for 360°-reconstructions were calculated, comparing the reference distribution with the distributions obtained from the generated spectra and monoenergetic photons (Steuwe et al. 2018).

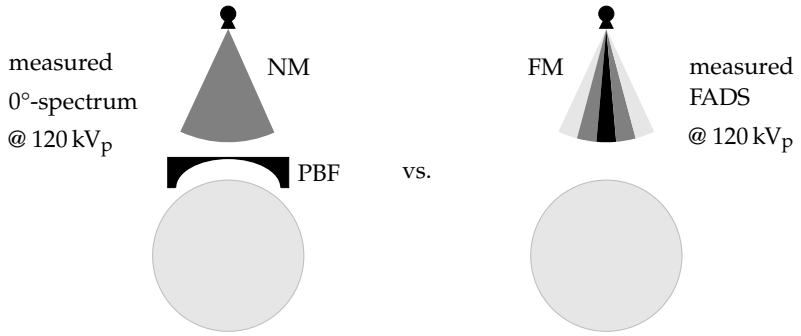

Figure 2.16: Evaluation W-I – Beam-shaping method: Schematic drawing of the simulation setup for the evaluation of the beam-shaping method. Left: The measured 0°-spectrum at 120 kV_p was employed with a uniform photon fluence (no photon fluence modulation (NM)), but with a physical beam-shaping filter (PBF) for beam-shaping and beam-hardening. Right: Measured fan-angle dependent spectra (FADS) at 120 kV_p were employed with a fan-angle dependent photon fluence (FM). The latter setup presents the *virtual beam-shaping filter* scenario.

2.5.1.3 *Evaluation W-I: Evaluation of the beam-shaping method*

The choice of the beam-shaping method was studied to evaluate the use of a virtual beam-shaping filter, i.e. the combination of fan-angle dependent photon fluence and fan-angle dependent spectra, instead of simulating a physical beam-shaping filter (evaluation W-I). The disadvantage of a PBF over a virtual filter is tracking of photons in the PBF, requiring a larger number of initially emitted photons, which decelerates computational time considerably (refer to section 2.3.5.1).
For the evaluation of the beam-shaping method, two simulation setups were compared, both including the effect of fan-angle dependent fluence and spectral distortion due to beam-hardening (see figure 2.16).
The first setup employed the measured 0°-reference spectrum at 120 kV_p with a uniform photon fluence (NM) but with a PBF, simulation W1. The second setup employed the FADS at 120 kV_p with fan-angle dependent photon fluence modulation, simulation W3. This setup resulted in fan-angle dependent spectra and photon fluence. For the direct comparison of $E_{spatial}$, the integrals of the resulting 2D-energy maps have been normalized to 1 (Steuwe et al. 2018). Results of the evaluation of the beam-shaping method are presented in section 3.1.1.

2.5.1.4 *Evaluation W-II: Influence of the photon fluence on $E_{spatial}$*

In evaluation W-II (see figure 2.17), the influence of the fan-angle dependent fluence modulation on $E_{spatial}$ has been determined, by comparing simulation W5 with simulation W4. For the direct comparison of $E_{spatial}$, the integrals of the created 2D-energy maps have been normalized to 1 (Steuwe et al. 2018). Results on the evaluation of the influence of spatial photon fluence modulation on $E_{spatial}$ are presented in section 3.1.2.

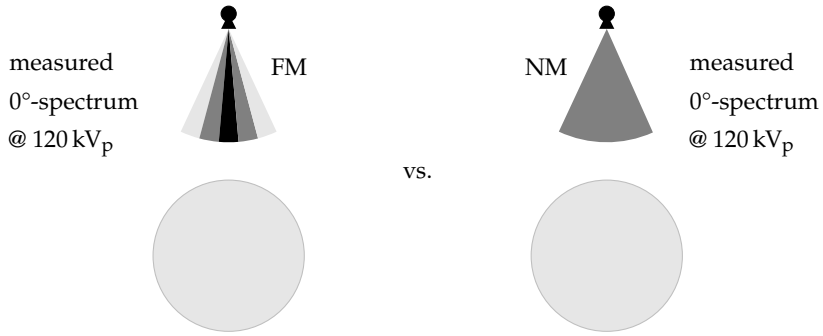

Figure 2.17: Evaluation W-II – Influence of fan-angle dependent fluence on $E_{spatial}$: Schematic drawing of the simulation setup for the evaluation of the influence of fan-angle dependent fluence on the spatial distribution of energy deposition, $E_{spatial}$. Left: Employing the measured 0°-spectrum at 120 kV_p with fan-angle dependent photon fluence modulation (FM). Right: Employing the measured 0°-spectrum at 120 kV_p with no photon fluence modulation (NM).

2.5.1.5 *Evaluation W-III: Influence of photon energy distributions on $E_{spatial}$*

A variety of source implementations and beam-shaping filtration are employed in MC simulations of CT. Several attempts are published in literature, such as modeling of the complete x-ray source, employing measured or generated spectra, or using monoenergetic photons as an approximation. A comprehensive overview over the legitimacy of using generated spectra or approximations thereof has however not been performed yet. For assessing the accuracy of dosimetric simulations of CT using MC methods, it was necessary to study the influence of different input spectra and monoenergetic photons on E_{total} and $E_{spatial}$. From the obtained information, it is

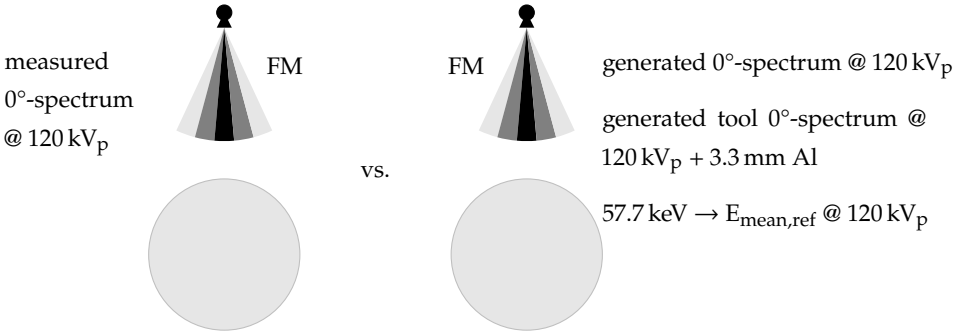

Figure 2.18: Evaluation W-III – Influence of different photon energy distributions on $E_{spatial}$: Schematic drawing of the simulation setup for the evaluation of the influence of different photon energy distributions on $E_{spatial}$. Energy maps originating from the simulations employing the generated spectrum at 120 kV_p, the generated filtered spectrum at 120 kV_p, and monoenergetic photons at 57.7 keV, the latter matching the mean energy of the measured 0°-spectrum at 120 kV_p, were compared to $E_{spatial}$ resulting from the simulation employing the measured 0°-spectrum at 120 kV_p. In all cases, fan-angle dependent photon fluence modulation (FM) was employed.

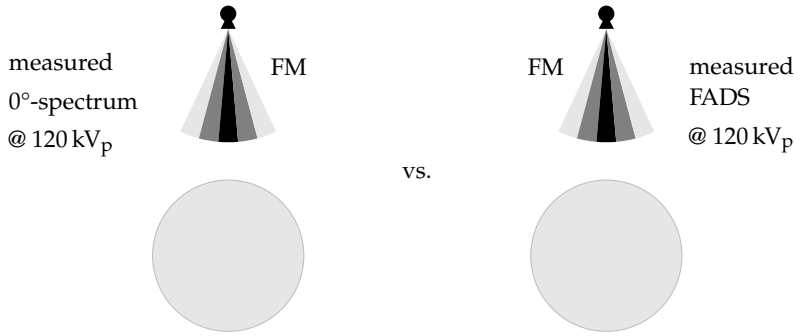

Figure 2.19: Evaluation W-IV – Influence of spectral distortion on $E_{spatial}$: Schematic drawing of the simulation setup for the evaluation of the influence of spectral distortion on the spatial distribution of energy deposition, $E_{spatial}$. Energy maps originating from the simulation employing the fan-angle dependent spectra (FADS) were compared to $E_{spatial}$ from the simulation employing the measured 0°-spectrum at 120 kV_p. In both cases, fan-angle dependent photon fluence modulation (FM) was employed.

possible to verify whether source spectra at equal tube potentials are interchangeable, and whether spectral photon distributions can be approximated by monoenergetic photons.
The effect of different photon energy distributions on $E_{spatial}$ was determined by comparing simulation W5 with simulations W7, W9 and W11 (evaluation W-III, see figure 2.18, Steuwe et al. 2018). Results on the evaluation of the influence of different photon energy distributions on $E_{spatial}$ are presented in section 3.1.3.

2.5.1.6 *Evaluation W-IV: Influence of beam-shaping filter induced spectral distortion on $E_{spatial}$*

In evaluation W-IV (see figure 2.19), the influence of beam-shaping filter induced spectral distortion on $E_{spatial}$ was assessed, by comparing simulation W5 with simulation W3. Results of the evaluation of the influence of the beam-shaping filter induced spectral distortion on $E_{spatial}$ are presented in section 3.1.4.

2.5.1.7 *Evaluation W-V: Total energy deposition E_{total}*

For simulations W2-W11, E_{total} was calculated and compared in section 3.1.5 (evaluation W-V).

2.5.2 INFLUENCE OF THE TUBE POTENTIAL AND TISSUE CONTRAST ENHANCEMENT ON THE ENERGY DEPOSITION AND DETECTOR SIGNAL IN THE BOX PHANTOM

The choice of the tube potential and the administration of contrast agents influences the energy deposition and spatial distribution inside a scanned object. However, the tube potential and the administration of contrast agents also influence the detector signal.
Prior to a CT examination of a patient, the tube potential is adjusted (either automatically or manually), depending on patient morphology, FOV, and possible administration of contrast agents. Although the effects of employing different tube potentials are visible on the reconstructed images (less contrast but also less noise on high kV_p-images, refer to sections 1.2.2.3 and 1.3.3), the effect on the energy deposition in the body, especially at the interfaced between two tissue types (e.g. muscle and blood vessels or liver and surrounding fat) is not yet thoroughly investigated. Furthermore, this section describes the assessment of the fundamental influences of simulated contrast enhancement on energy deposition and the iodine-induced energy build-up effect at the interfaces between enhanced tissues and surrounding, non-enhanced tissues.

2.5.2.1 *Performed simulations*

The box phantom (section 2.4.1.2) was employed to evaluate the influence of the tube potential and contrast enhancement on the energy deposition in different materials and on the detector signal. The material choice of the individual layers was specified according to the research question. In each simulation, $50 \cdot 10^6$ photons were emitted from the square source (section 2.3.6.2) for the generated filtered spectra at 80, 100, and 120 kV_p. Photons were tracked in the three layers and in the lead detector. The surrounding space of the phantom and detector was set to vacuum to avoid any scattering of photons prior to reaching the phantom. All tracked interactions inside the phantom were stored as described in section 2.1.4.

Simulations of the box phantom were performed, with the box layers:

B1	constructed of identical materials in each of the three layers (either liver, fat, soft tissue, or water). This setup enables to assess the influence of the tube potential on the energy deposition in the material and on the detector signal.
B2	constructed of fat tissue (layers 1 and 3) and pure liver tissue (layer 2, $\psi_I = 0.000$). This setup enabled assessing the energy deposition at tissue interfaces.

B3 constructed of fat tissue (layers 1 and 3) and iodinated liver tissue (layer 2, $\psi_I > 0.000$). In this case, different concentrations of iodine were added to the material liver in layer 2 to assess the energy build-up associated with the use of contrast agents. Iodine mass fractions ψ_I = [0.001, 0.003, 0.005, 0.010, 0.015] were used, corresponding to concentrations of 1, 3, 5, 10, and 15 mg/ml, respectively (Amato et al. 2010).

2.5.2.2 *Evaluation B-I: Influence of the tube potential on the energy deposition and detector signal in the box phantom*

Total energy deposition in the three layers of the box phantom and in the lead detector were calculated for simulation B1. The energy deposition was compared to the total input photon energy and between the applied tube potentials. The detector signal resulting from simulations B1 was compared, with regard to the material (density) and tube potential. Results of the influence of the tube potential on the energy deposition and on the detector signal are presented in section 3.2.1.

2.5.2.3 *Evaluation B-II: Influence of tissue contrast enhancement on the energy deposition in the box phantom*

$E_{spatial}$ resulting from simulations B2 and B3 were compared to assess the differences in energy deposition resulting from contrast enhancement. For this purpose, 2D-energy and difference maps (bin size 1.0 x 1.0 mm^2, scored over 100 mm in z-direction) were calculated for the simulations. Profiles along the y-axis of the box phantom were plotted, taking the inner 4 cm x 4 cm in x-and z-axis into account (see figure 2.20). Furthermore, the total energy deposition in the three layers of the box phantom for simulations B2 and B3 was calculated. Results of the influence of contrast enhancement on the energy deposition are presented in section 3.2.2.

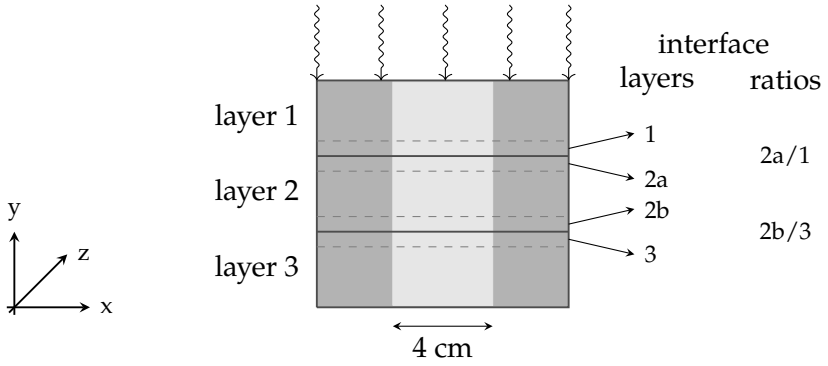

Figure 2.20: Calculation of interface ratios and profiles for the box phantom. Interfaces layers with varying thickness (1.0, 2.5, and 5.0 mm) were used to assess the energy build-up effect at material interfaces. Profiles along the y-axis were calculated from the inner 4 cm of the box phantom. The lead detector is not shown.

2.5.2.4 *Evaluation B-III: Energy build-up effect at material interfaces in the box phantom*

Energy deposition in the interface layers around the material transitions were determined and used to calculate interface ratios ('upstream' interface: 2a/1 and 'downstream' interface: 2b/3) at varying thickness of the interface layers (1.0, 2.5, and 5.0 mm) from simulations B2 and B3. Names of the interface layers and ratios are given in figure 2.20. This analysis was performed for the non-enhanced ($\psi_I = 0.000$) and enhanced ($\psi_I > 0.000$) liver layers, to differentiate between iodine-induced and material-induced energy build-up at the tissue interfaces. Results of the energy build-up effect at material interfaces are presented in section 3.2.3.
The thickness of the interface layer was of importance for later simulations of the abdomen phantom and digitized patient phantoms, to assess the energy build-up effect for different material interfaces.

2.5.3 CALCULATION OF EXPOSURE MAPS OF THE MODIFIED ABDOMEN PHANTOM

The modified abdomen phantom (section 2.4.1.3) allows to track photon interactions in a more complex geometry than the box phantom (section 2.4.1.2). The advantage of this phantom is the anthropomorphic design, the disadvantage is the larger amount of material interfaces, complicating the analysis of the reasons of specific effects.

2.5.3.1 *Performed simulations*

WHOLE MODIFIED ABDOMEN PHANTOM Simulations of the modified abdomen phantom were performed at tube potentials of 80, 100, and 120 kV_p (generated filtered spectra) in the helical acquisition mode (section 2.3.6.4) with a pitch of 1.0, z-collimation 32 mm, and enabled FM. LTCM and ATCM were not enabled. For simulations of the whole modified abdomen phantom, $129 \cdot 10^6$ photons were tracked ($3 \cdot 10^6$ photons per cm, scan coverage 43.2 cm between [-21.6 cm, 21.6 cm], with 3.2 cm z-overranging). Performed simulations were:

A1	simulation with non-enhanced tissues ($\psi_I = 0.000$) and
A2	simulation with iodinated tissues ($\psi_I = 0.005$ in liver, spleen, kidneys, pancreas, and the aorta).

AXIAL SLICE OF THE MODIFIED ABDOMEN PHANTOM Furthermore, simulations were performed with the point source (section 2.3.6.1) on a single axial slice (thickness of 6.4 cm) of the modified abdomen phantom at tube potentials of 80, 100, and 120 kV_p (generated filtered spectra). Source position along the CT scanner's z-axis was fixed. Z-coverage of the x-ray source at the isocenter was 32 mm (only the center of the slice was exposed during the acquisitions). The axial slice included liver and soft tissue, the spine, spleen, and aorta (see figure 2.21). Hence, for simulations of contrast-enhanced acquisitions, iodine-enhancement was only applied in the liver, spleen, and aorta.
First, a single projection at 270° (lateral projection, x-ray source position at 9 o'clock)

was simulated. The projection from a specific angle allows to assess the energy deposition from photons of a single point, without the effects of overlaying energy depositions from various angles around the phantom. $50 \cdot 10^6$ photons were tracked for simulations of projections (see figure 2.21a).
Afterwards, simulations were performed for a full rotation of the x-ray source in 1°-steps. $64 \cdot 10^6$ photons (simulated slice thickness of 6.4 cm, see above, and $1 \cdot 10^6$ photons per cm) were tracked for simulations of rotations (see figure 2.21b). FM was enabled for the simulated projections and rotations. Performed simulations were:

A3 simulation of an axial slice of the phantom with non-enhanced tissues ($\psi_I = 0.000$), projection at 270°,

A4 simulation of an axial slice of the phantom with enhanced tissues ($\psi_I = 0.005$ in liver, spleen, and the aorta), projection at 270°,

A5 simulation of an axial slice of the phantom with non-enhanced tissues ($\psi_I = 0.000$), full source rotation, and

A6 simulation of an axial slice of the phantom with enhanced tissues ($\psi_I = 0.005$ in liver, spleen, and the aorta), full source rotation.

All tracked interactions inside the abdomen phantom and the axial slice were stored as described in section 2.1.4.

2.5.3.2 *Evaluation A-I: Influence of the tube potential and tissue contrast enhancement on energy deposition and its spatial distribution in the modified abdomen phantom*

The total energy deposition in all tissues/organs and their spatial distribution were determined in the modified abdomen phantom for simulations of non-enhanced and enhanced CT acquisitions (simulations A1 and A2). 2D-energy and difference maps (bin size 2.0 x 2.0 mm^2, scored over 2 mm in z-direction) for simulated enhanced and non-enhanced acquisitions were calculated. Results of the total energy deposition are presented in section 3.3.1.

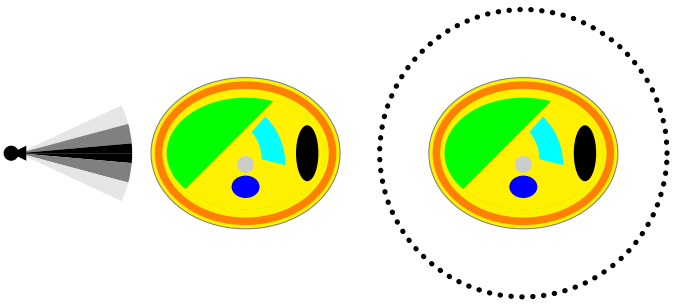

(a) Single projection at 270° (b) X-ray source rotation around 360° in 1°-steps

Figure 2.21: Modified abdomen phantom: Simulation setup for assessment of build-up effects for a single slice of the phantom. The slice contained the organs/tissues liver (green), spleen (black), GI-tract (turquoise), aorta (gray), and spine (blue).

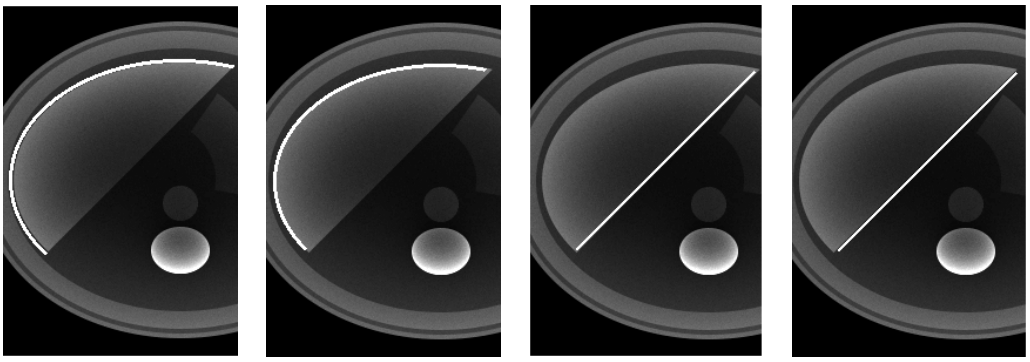

(a) ST ROI 1 (b) Liver ROI 2a (c) Liver ROI 2b (d) ST ROI 3

Figure 2.22: Position of ROIs (shown in white) in the slice of the modified abdomen phantom for calculation of energy depositions and relative differences at interfaces. Abbreviations: region-of-interest (ROI), surrounding tissue (ST, here fat).

2.5.3.3 *Evaluation A-II: Energy build-up effect at material interfaces in the modified abdomen phantom – whole phantom*

Energy deposition was calculated in the organ shells and surrounding tissue shells for simulations A1 and A2. The energy deposition was normalized to the volume per shell and interface ratios (normalized energy deposition in the organ shell divided by normalized energy deposition in the surrounding tissue shell) calculated. Results of the energy build-up effect in the whole phantom are presented in section 3.3.2.

2.5.3.4 *Evaluation A-III: Energy build-up effect at material interfaces in the modified abdomen phantom – axial slice*

For simulations A3-A6, the resulting spatial distributions of energy deposition for the simulations of the non-enhanced and the enhanced CT acquisitions and the differences in energy deposition between the two corresponding simulations were plotted as a 2D-map (energy was accumulated along the z-axis of the phantom). From these maps, energy depositions and relative differences were determined in ROIs positioned in the liver and fat tissue as depicted in figure 2.22 using ImageJ (see appendix D).
Interface ratios (ROI 2a/1 and ROI 2b/3) were calculated from the energy deposition inside the ROIs for the simulations of the full source rotations (simulations A5 and A6). For calculation of interface ratios, energy deposition in the ROI was first normalized to the number of pixels in the ROI. Results of the energy build-up effect in the axial slice are presented in section 3.3.3.

2.5.4 CALCULATION OF EXPOSURE MAPS OF DIGITIZED PATIENTS

The goal of this work was the development of a MC software for the virtual dosimetry of patients examined in a radiology department. This section describes the assessment of the influence of different tube potentials and iodinated contrast agents on energy deposition in different organs and at organ interfaces in six male patients.

PATIENT COHORT AND ACQUISITION The chosen patients took part in a clinical study, investigating a low dose and low contrast agent dose CTA acquisition for follow-up after non-invasive EVAR (Fink et al. 2018). The study was approved by the local ethics committee (S485/2017; DRKS-ID: DRKS00013082). All patients received a non-enhanced CT acquisition of the thorax and the abdomen on a Somatom® Definition Flash CT scanner system (Siemens Healthineers, Forchheim, Germany). Patients with a body mass index (BMI) <30 kgm^{-2} were acquired at a tube potential of 80 kV_p, whereas patients with BMI >30 kgm^{-2} were acquired at a tube potential of 100 kV_p. The reference TCTP ($TCTP_{eff}$) at 80 kV_p was 210 mAs ($CTDI_{vol}$ = 4.1 mGy), whereas at 100 kV_p $TCTP_{eff}$ was 87 mAs ($CTDI_{vol}$ = 3.6 mGy). Other acquisition parameters were: 0.5 sec rotation time, z-collimation 0.6 mm, and pitch 1.2. For the purpose of this work, images were reconstructed in 3 mm slice thickness with an increment of 3 mm, using an iterative algorithm (ADMIRE, kernel I30f, level 5 (smoothest reconstruction to suppress noise), Siemens Healthineers, Forchheim, Germany).
Acquisition parameters and slice-specific exposure values were extracted from the corresponding DICOM-headers of the reconstructed images and are presented in table 2.2. An overview on the morphology of the patients included in this thesis can be found in appendix I.

ABDOMINAL SCAN RANGE The abdominal scan range covered the abdomen, including the whole liver, spleen, pancreas, and kidneys, with an additional scan range of 2 x 1.8 cm in cranio-caudal direction. The length of the abdominal scan range differed per patient (range: 19.8 - 23.1 cm).
$TCTP_{eff}$ was extracted from the DICOM-headers of the reconstructed images inside

Table 2.2: Patient characteristics and dose protocol parameters for digitized patient phantoms for an *abdominal scan coverage*, including the whole liver, spleen, pancreas, and kidneys. DLP and $TCTP_{eff}$ were calculated from the slices covering the mentioned organs. All patients were originally acquired at a tube potential of 80 kV_p. Simulations covering the abdomen were run with the given number of photons. Abbreviations: identification code (ID), body mass index (BMI), volumetric computed tomography dose index ($CTDI_{vol}$), dose-length product (DLP), effective tube-current time product ($TCTP_{eff}$), number of simulated photons $N_{photons}$.

ID	**BMI [kg/ m^2]**	**Height [cm]**	**Weight [kg]**	**$CTDI_{vol}$ [mGy]**	**DLP [mGy ·cm]**	**$TCTP_{eff}$ [mAs]**	**$N_{photons}$ simulated ·10^6**
1A	21.0	172	62	3.00	59.3	152.5	59.40
1B	22.0	172	65	3.21	62.6	163.4	62.70
2A	26.4	173	79	3.05	69.6	155.3	69.66
2B	25.4	174	77	2.51	58.1	128.0	58.17
3A	28.1	178	89	2.92	66.6	148.7	66.70
3B	28.4	178	90	3.00	62.2	153.1	62.34

the abdominal scan range. According to Salvadó et al. (2005), the number of photons was set to $3 \cdot 10^6$ photons per cm scan coverage to obtain a relative standard error in one slice (1 cm thickness) of <0.5%. It was subsequently scaled to each patient's $TCTP_{eff}$. The patients were segmented according to section 2.4.2.1. For acquisitions covering the abdominal scan range, the number of photons, $N_{photons}$, given in table 2.2 was determined as follows:

$$N_{photons} = \text{scan coverage [cm]} \cdot 3 \cdot 10^6 \cdot \frac{TCTP_{eff,\,\text{patient ID}}}{TCTP_{eff,\,\text{patient 1A}}} \tag{2.3}$$

Hence, both the scan coverage and the effective TCTP determine the number of photons, thereby taking the $TCTP_{eff}$ of patient 1A as baseline. A comprehensive review of the number of tracked photons in MC simulations of CT acquisitions can be found in appendix J.
Note that the $CTDI_{vol}$ and $TCTP_{eff}$ (see Table 2.2) appear to be independent of the BMI for the six patients in this work.

2.5.4.1 *Performed simulations*

WHOLE DIGITIZED PATIENTS Energy maps of all patients were calculated at 80 kV_p (generated filtered spectra) with a pitch of 1.0 and z-collimation of 32 mm at the isocenter. FM and LTCM were enabled. To assess the influence of iodinated contrast agents, all simulations were performed with contrast-enhanced liver, spleen, pancreas, and kidney tissue, as well as blood (aorta) with a mass fraction of $\psi_I = 0.005$. The following simulations were performed:

P1	simulations at 80 kV_p for all patients (non-enhanced tissues, $\psi_I = 0.000$),
P2	simulations at 80 kV_p for all patients (enhanced liver, spleen, pancreas, kidney, aorta, $\psi_I = 0.005$),
P3	simulations at 120 kV_p for all patients (non-enhanced tissues),
P4	simulations at 100 and 120 kV_p for patient 2A (non-enhanced tissues, $\psi_I = 0.000$), and
P5	simulations at 100 and 120 kV_p for patient 2A (enhanced liver, spleen, pancreas, kidney, aorta, $\psi_I = 0.005$).

AXIAL SLICE OF A DIGITIZED PATIENT A single axial slice (slice thickness 6.4 cm, figure I.2a) of patient 1A through the liver and kidneys was used to assess the energy build-up effect in more detail. This patient resembled the modified abdomen phantom to the highest degree and was hence chosen for this analysis. CT acquisitions were simulated at 80, 100, and 120 kV_p (generated filtered spectra) with and without iodine enhancement in the organs and the aorta. The z-position of the x-ray source was stationary for these simulations. Z-coverage of the x-ray source at the isocenter was 32 mm (only the center of the slice was exposed during the acquisitions).
First, a single projection at 270° (lateral projection, x-ray source position at 9 o'clock)

was simulated, such as performed for the modified abdomen phantom. For each of the simulations, $50 \cdot 10^6$ photons were tracked.
Afterwards, simulations were performed with a full rotation of the x-ray source in 1°-steps. For each of the simulations, $64 \cdot 10^6$ photons ($1 \cdot 10^6$ photons per cm) were tracked. FM was enabled for the simulated projections and rotations. The following simulations were performed:

P6 simulation of an axial slice of patient 1A with non-enhanced tissues ($\psi_I = 0.000$), projection at 270°,

P7 simulation of an axial slice of patient 1A with enhanced tissues ($\psi_I = 0.005$ in liver, spleen, and the aorta), projection at 270°,

P8 simulation of an axial slice of patient 1A with non-enhanced tissues ($\psi_I = 0.000$), full source rotation, and

P9 simulation of an axial slice of patient 1A with enhanced tissues ($\psi_I = 0.005$ in liver, spleen, and the aorta), full source rotation.

All tracked interactions inside the digitized patients and the axial slice were stored as described in section 2.1.4.

2.5.4.2 *Evaluation P-I: Influence of the tube potential and tissue contrast enhancement on energy deposition and its spatial distribution in a digitized patient*

For this evaluation, total energy deposition in organs and tissues and their spatial distribution in patient 2A were compared, acquired from simulations of non-enhanced and enhanced acquisitions at tube potentials of 80, 100, and 120 kV_p (from simulations P1 and P2 for patient 2A, and simulations P4 and P5). Results of the total energy deposition and spatial distribution are presented in section 3.4.1. 2D-energy and difference maps were calculated with a bin size of 1.5 x 1.5 mm^2, scored over 3 mm in z-direction, corresponding to a matrix size of 256 x 256 pixels.

2.5.4.3 *Evaluation P-II: Energy build-up effect at material interfaces in a digitized patient – whole patient*

Energy deposition was calculated in the organ shells and surrounding tissue shells for patient 2A for the tube potentials 80, 100, and 120 kV_p (from simulations P1 and P2 for patient 2A, and simulations P4 and P5). The energy deposition was normalized to the number of voxels per shell and interface ratios (normalized energy deposition of organ shell divided by normalized energy deposition of surrounding tissue shell) calculated. Results of the energy build-up effect in patient 2A are presented in section 3.4.2.

2.5.4.4 *Evaluation P-III: Energy build-up effect at material interfaces in a digitized patient – axial slice*

Axial 2D-energy maps of the simulations of enhanced and non-enhanced acquisitions were calculated for patient 1A (simulations P6 - P9). Energy was summed

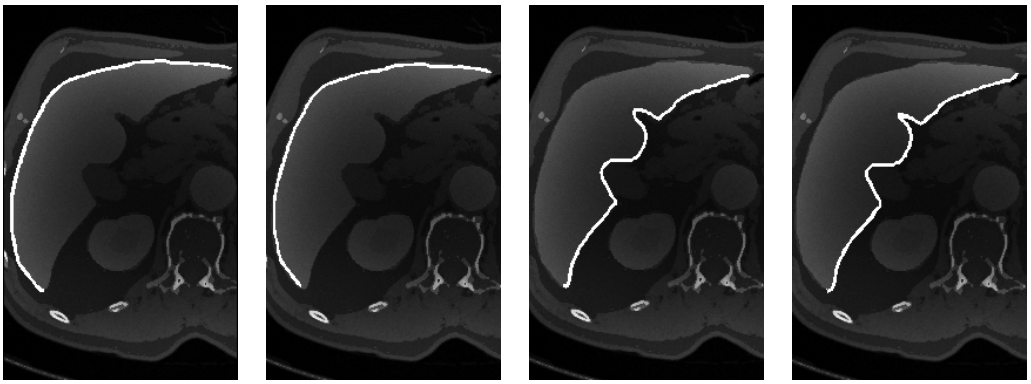

(a) ST ROI 1 (b) Liver ROI 2a (c) Liver ROI 2b (d) ST ROI 3

Figure 2.23: Position of ROIs (shown in white) in the slice of the digitized patient phantom for calculation of energy depositions and relative differences at interfaces. ROI 1 contains only fat tissue, whereas ROI 3 includes some water (gall bladder) and air (at upper tip of the liver), compare to the tissue morphology in figure I.2a. Abbreviations: region-of-interest (ROI), surrounding tissue (ST).

along the z-axis of the phantom. 2D-difference maps were calculated from the energy maps of the simulated enhanced and non-enhanced acquisitions.
The energy deposition in four ROIs was calculated for every energy and difference map (see figure 2.23). ROI 1 is positioned in the surrounding tissue at the periphery of the liver. ROIs 2a and 2b are positioned inside the liver, with ROI 2a at the periphery and ROI 2b at the medial side of the liver. ROI 3 is positioned in the surrounding tissue at the center of the phantom. ROI naming is identical for the ROIs in the modified abdomen phantom (see figure 2.22). Interface ratios (ROI 2a/1 and ROI 2b/3) were calculated from the energy deposition inside the ROIs for the simulations of the full source rotations (simulations P8 and P9). For this purpose, energy deposition was first normalized to the number of pixels inside the ROIs. Results of the energy build-up effect evaluated for the axial slice of patient 2A are presented in section 3.4.3.

2.5.4.5 *Evaluation P-IV: Influence of BMI and morphology on the energy deposition and its spatial distribution in digitized patients*

To evaluate the influence of the BMI and patient morphology on the energy deposition in digitized patients, total energy deposition and its spatial distribution were compared for all patients at 80 kV_p for simulations of non-enhanced and enhanced acquisitions (simulations P1 and P2). Results of the energy deposition depending on patient BMI and morphology are presented in section 3.4.4.

2.5.4.6 *Evaluation P-V: Influence of the tube potential on the energy deposition in the skin in digitized patients*

To evaluate the influence of the tube potential on the energy deposition in the skin, the energy deposition in each patient and in each patient's skin resulting from simulations of non-enhanced acquisitions at 80 kV_p and 120 kV_p were compared

(simulations P1 and P3). Since the scan ranges of the patients were not identical, energy deposition in the skin and in the patients was scored in a 102 mm scan region (34 image slices) covering approximately identical scan regions (the kidneys) in the abdomen. This allowed for comparison of energy deposition between patients for the same scan coverage. Relative differences in energy deposition between acquisitions at 80 and 120 kV_p were calculated for the skin and the all patient tissues in the scan region. Results are presented in section 3.4.5.

2.6 ASSESSMENT OF THE VARIATION BETWEEN IDENTICAL MC SIMULATIONS AND EVALUATION OF THE SIMULATED NUMBER OF PHOTONS IN A DIGITIZED PATIENT

To estimate the error of the results obtained with the MC model with the employed number of photon histories, re-sampling of data was used to produce sub-sets of data containing the energy deposition of every second, fifth, tenths, etc. interaction (data sets of reduced photon statistics). For this purpose, a CT acquisition of the abdominal region of patient 2A (scan covered the kidneys, total scan coverage was 15 cm, non-enhanced acquisition) was simulated twice with two different initial seeds, with a total of $45 \cdot 10^6$ photons ($3 \cdot 10^6$ photons per cm scan coverage), pitch of 0.5 and LTCM enabled. Interaction data was stored in branches for post-processing.

VARIATION BETWEEN TWO IDENTICAL SIMULATIONS WITH DIFFERENT INITIAL SEEDS

The total energy deposition in the phantom and the energy deposition in the individual organs were calculated and compared for both simulations. 2D-maps of the energy deposition were produced and relative difference maps calculated for a single axial slice (3 mm slice thickness) and for three adjacent slices (9 mm voxel thickness in z-direction).

REDUCTION OF THE PHOTON STATISTICS

3D-maps of the energy deposition were produced from all interactions, and from every second, fifth, tenth, 15th ... up till every 45th interaction. Hence, for the latter 3D-map, only 1/45th of the total number of interactions have contributed to the energy map. To allow for comparability between energy maps, the integrals of the 3D-maps were normalized to 1. Maps consisting of the reduced data were subtracted from the full data map, and the calculated differences plotted in a one-dimensional (1D)-histogram, for the full phantom volume, the kidneys, a single axial slice, and the kidneys inside a single axial slice. Only data inside the contours of the patient have been taken into account. Histograms were been fitted with a Gaussian curve. For the reduced statistics data sets, energy deposition and interaction types contributing to the energy maps were compared to ensure that all sub-sets contain equal percentages of energy depositions resulting from e.g. the Compton effect or the photoelectric effect. Results are presented in appendix J, figure J.1.

3

RESULTS

The results of this work are presented in the following chapter. The structure is as follows: first, the beam-shaping method used throughout the simulations was evaluated, followed by the evaluation of the influence of the fan-angle dependent fluence on the energy deposition (E_{total}) and its spatial distribution ($E_{spatial}$) in a variety of geometrical and digitized phantoms. Afterwards, the influence of the spectral properties of x-ray sources and the tube potential on energy deposition is described. This is followed by a more detailed analysis of the energy deposition for varying tube potentials and material types. Then, the influence of contrast-agents on the energy deposition, especially at material interfaces, is demonstrated. Moving from simple theoretical phantoms to more elaborate phantoms, the energy deposition in an anthropomorphic abdomen phantom is assessed. This chapter is completed by presenting energy maps of a set of digitized patient phantoms. The evaluation of the beam-shaping method and the influence of spectral properties of x-ray sources on energy deposition have already been published (Steuwe et al. 2018).

3.1 ANALYSIS OF BEAM-SHAPING METHODS AND SPECTRAL PROPERTIES OF X-RAY SOURCES EMPLOYING THE WATER PHANTOM

3.1.1 EVALUATION W-I: EVALUATION OF THE BEAM-SHAPING METHOD

Two beam-shaping methods were compared (cf. figure 2.16 in section 2.5.1.3): on the one hand, a *physical* beam-shaping filter (PBF) was modeled which altered photon fluence as its thickness increased towards the edges of the filter and which resulted in fan-angle dependent spectra (FADS) with increasing mean energies towards the sides of the FOV. In this scenario, a photon distribution matching the measured 0°-spectrum was uniformly (NM) emitted across the FOV. On the other hand, a *virtual* beam-shaping method was modeled, implementing fluence modulation (FM) by means of a probability density function (PDF), combined with the measured FADS. The virtual filter models both photon fluence according to the measured transmission curve and the spectral distortion caused by a physical beam-shaping filter.

Figure 3.1 presents the relative difference in $E_{spatial}$ between the *physical* and the *virtual* beam-shaping filter scenario. Both scenarios modeled fan-angle dependent fluence and spectral distortion. A maximum relative difference in $E_{spatial}$ of 3% was observed at the center of the water phantom, showing that employing the virtual beam-shaping method with a PDF for FM and FADS was reasonable in this work (Steuwe et al. 2018).
Simulation time was 25.5 hours for the physical beam-shaping scenario (PBF and NM) and 12.4 hours for the *virtual* beam-shaping scenario (FADS and FM). In both

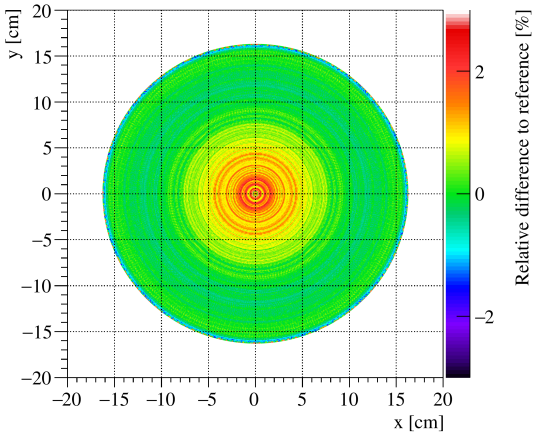

Figure 3.1: Evaluation W-I: Influence of beam-shaping methods with regard to the spatial distribution of simulated deposited energy, $E_{spatial}$. Comparison of $E_{spatial}$ resulting from the simulation using *physical* beam-shaping scenario (physical beam-shaping filter with measured 0°-reference spectrum and uniform photon fluence) vs. the *virtual* beam-shaping scenario (fan-angle dependent spectra and fluence modulation). Both scenarios modeled fan-angle dependent fluence and spectral distortion. For better visibility of the phantom periphery, background color outside the water phantom was set to white. Adapted from Steuwe et al. (2018).

cases, approximately equal numbers of photons reached the surface of the water phantom ($9.24 \cdot 10^7$ (PBF) vs. $9.27 \cdot 10^7$ (FM)).

3.1.2 EVALUATION W-II: INFLUENCE OF THE PHOTON FLUENCE ON $E_{SPATIAL}$

The influence of the photon fluence on $E_{spatial}$ was compared, see section 2.5.1.4. Figure 3.2 depicts the effect of fan-angle dependent photon fluence on $E_{spatial}$. In figure 3.2a, photon fluence was modulated as a function of the fan angle (FM), whereas in figure 3.2b, a uniform fluence (NM) was employed across the x-ray fan. For a single projection and employed fluence modulation, $E_{spatial}$ was concentrated at the center of the x-ray beam entrance side. The uniform fluence resulted in a more homogeneously distributed $E_{spatial}$ across the x-ray fan.
Comparing $E_{spatial}$ for a uniform photon fluence with that for fan-angle dependent fluence (after normalization), $E_{spatial}$ was overestimated at the phantom periphery by up to 250% (at the sides of the fan beam), whereas $E_{spatial}$ was underestimated by up to -50% at the center of the fan beam (see figure 3.2c). Relative energy differences were within ± 50% for a full 360°-rotation (see figure 3.2d). A decreased energy deposition was noticeable at the center of the phantom and an increased energy deposition noticeable in the periphery (Steuwe et al. 2018).

3.1.3 EVALUATION W-III: INFLUENCE OF PHOTON ENERGY DISTRIBUTIONS ON $E_{SPATIAL}$

After evaluation of the beam-shaping method implemented for this work and the assessment of its beam-shaping effect, the effect of employing different source spec-

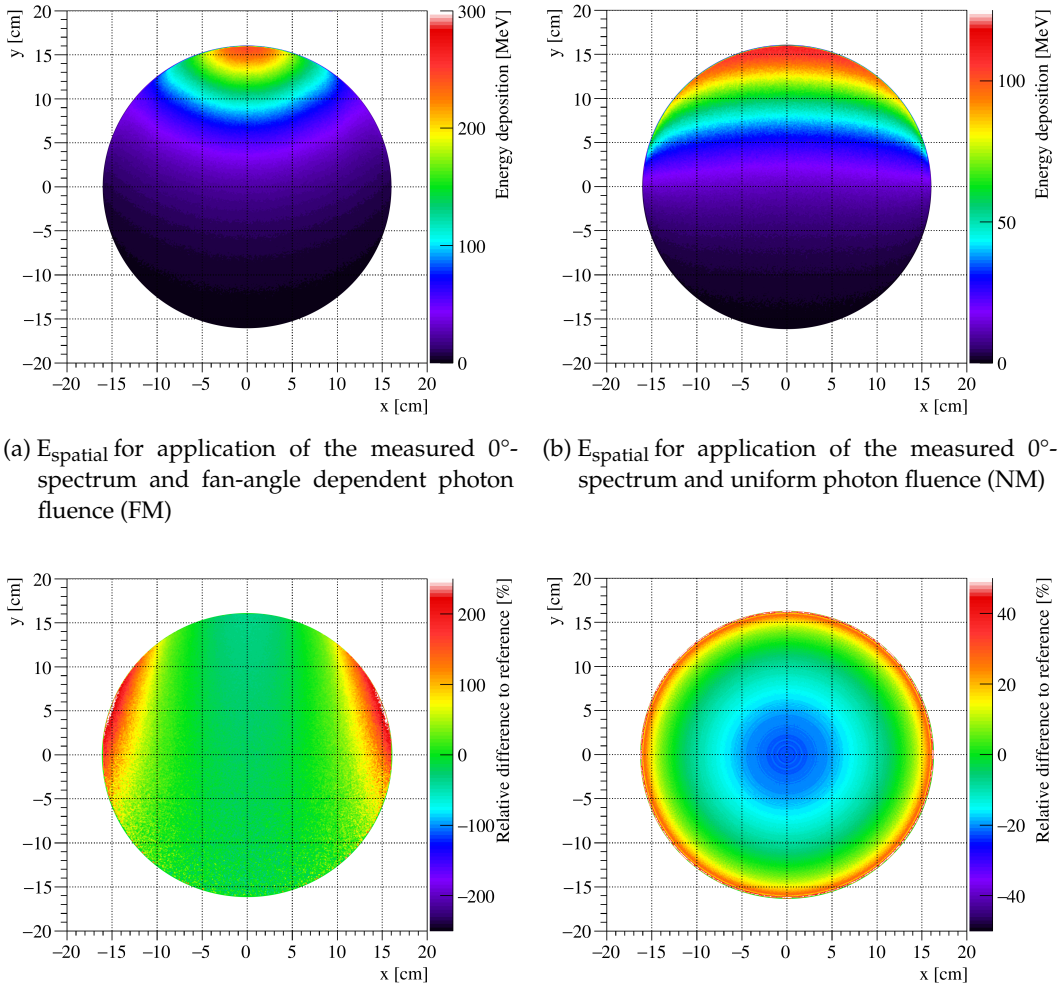

(a) $E_{spatial}$ for application of the measured 0°-spectrum and fan-angle dependent photon fluence (FM)

(b) $E_{spatial}$ for application of the measured 0°-spectrum and uniform photon fluence (NM)

(c) Relative difference in $E_{spatial}$ between simulations without and with fluence modulation, 0°-projection

(d) Relative difference in $E_{spatial}$ between simulations without and with fluence modulation, 360°-reconstruction

Figure 3.2: Evaluation W-II: Influence of fan-angle dependent fluence on spatial distribution of simulated deposited energy, $E_{spatial}$. For both the 0°-projection and the 360°-reconstruction, energy maps were normalized prior to calculation of difference maps. Please note the different scalings of the color bars. For better visibility of the phantom periphery, background color outside the water phantom was set to white. Adapted from Steuwe et al. (2018).

tra and monoenergetic photons on E_{total} and $E_{spatial}$ was assessed (see section 2.5.1.5). This comparison aims at evaluating whether x-ray spectra and monoenergetic photons can be interchanged for dosimetric purposes, in cases where the original source spectrum is not available.

Figure 3.3 presents $E_{spatial}$ for employing the measured 0°-reference spectrum (a), monoenergetic 57.7 keV photons (b), the generated unfiltered (c), and filtered (d) 120 kV_p-spectra. The single projections showed only subtle differences at the entrance side of the phantom in terms of shape and penetration length for the spectra. The maximum local energy deposition for monoenergetic photons (~200 MeV) was

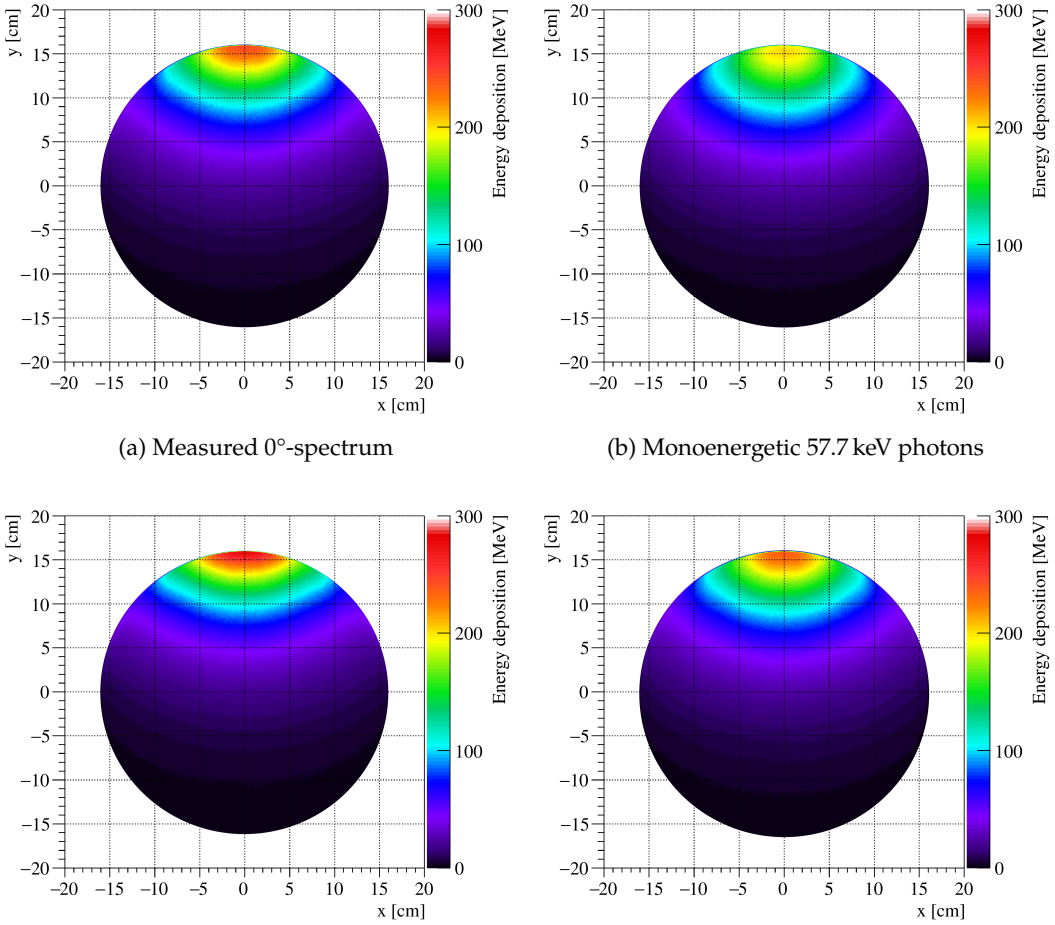

(a) Measured 0°-spectrum

(b) Monoenergetic 57.7 keV photons

(c) Generated unfiltered 120 kV_p-spectrum

(d) Generated filtered 120 kV_p-spectrum

Figure 3.3: Evaluation W-III: Spatial distribution of simulated deposited energy, $E_{spatial}$, for different input spectra and monoenergetic photons. Projection from 12 o'clock source position. Fan-angle dependent fluence (FM) was applied in all simulations. For better visibility of the phantom periphery, background color outside the water phantom was set to white. Adapted from Steuwe et al. (2018).

lower than for the employed photon spectra (~250-270 MeV).
The relative differences in $E_{spatial}$ compared to $E_{spatial}$ of the reference spectrum are presented in figure 3.4 for the reconstructed 360°-projections. The differences are more conspicuous than they were in figure 3.3. $E_{spatial}$ for the 57.7 keV photons was underestimated at the periphery of the phantom (-20%), whereas at the center, $E_{spatial}$ was overestimated by +10% (see figure 3.4a). The unfiltered generated spectrum led to an overestimation of $E_{spatial}$ at the phantom periphery (+20%) and an underestimation (-20%) at the phantom center (figure 3.4b). Due to the lack of additional filtration, this spectrum is softer than the reference spectrum. Hence, more photons were absorbed at the entrance side of the phantom, whereas less energy was deposited at the center. The effect of the additional filtration on energy deposition is depicted in figures 3.4c-3.4d. Beam-hardening due to the aluminum filter reduced

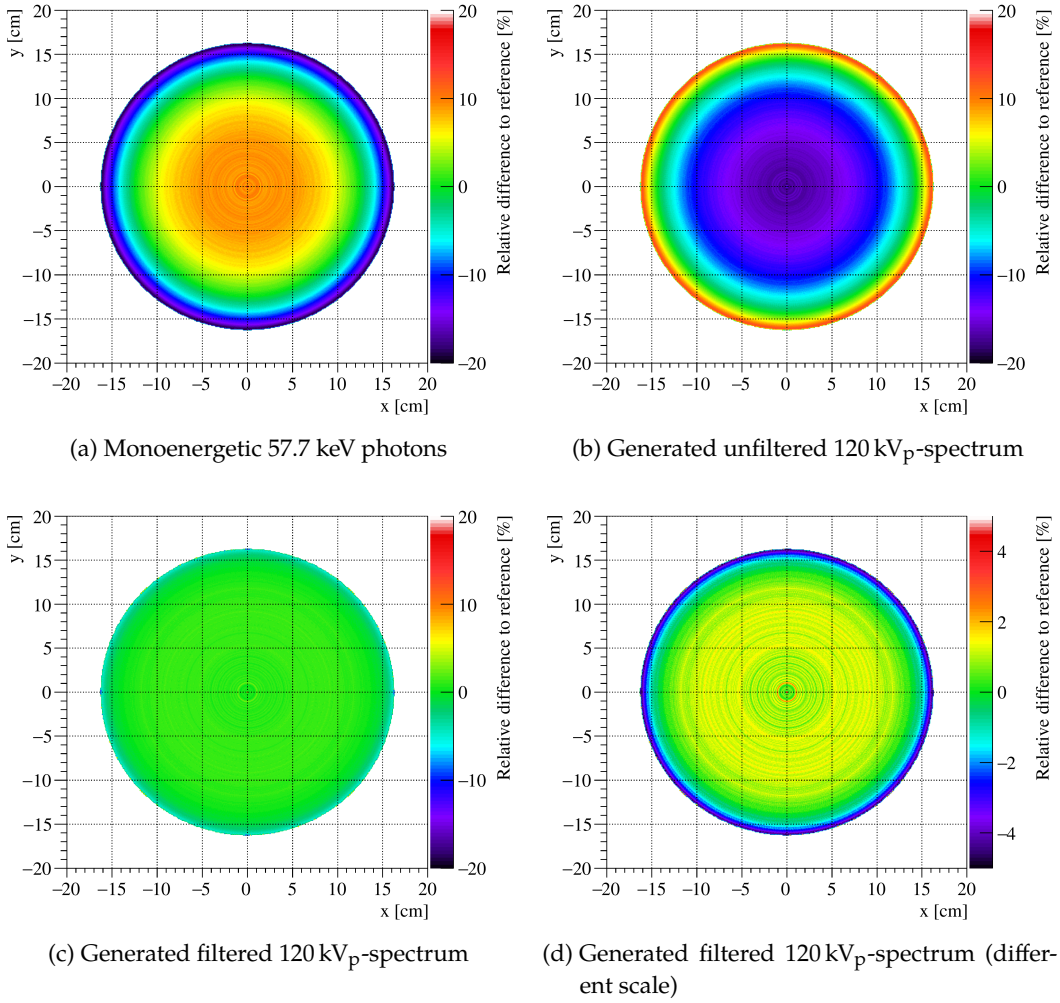

(a) Monoenergetic 57.7 keV photons

(b) Generated unfiltered 120 kV_p-spectrum

(c) Generated filtered 120 kV_p-spectrum

(d) Generated filtered 120 kV_p-spectrum (different scale)

Figure 3.4: Evaluation W-III: Relative difference of spatial distribution of simulated deposited energy, $E_{spatial}$, for simulations employing different emitted photon energy distributions (360°-reconstruction). Reference for the difference maps was $E_{spatial}$ generated using the measured 0°-spectrum. Photon fluence modulation was applied in all simulations. Note that $E_{spatial}$ presented in (d) displays the same data as in (c) but uses a smaller range of relative difference values in order to resolve subtle differences. For better visibility of the phantom periphery, background color outside the water phantom was set to white. Adapted from Steuwe et al. (2018).

relative differences in $E_{spatial}$ compared to the reference spectrum to ~3% (Steuwe et al. 2018).

3.1.4 EVALUATION W-IV: INFLUENCE OF BEAM-SHAPING FILTER INDUCED SPECTRAL DISTORTION ON $E_{SPATIAL}$

The last sections presented the influence of the photon fluence and the choice of central source spectra and monoenergetic photons on $E_{spatial}$. Although fan-angle

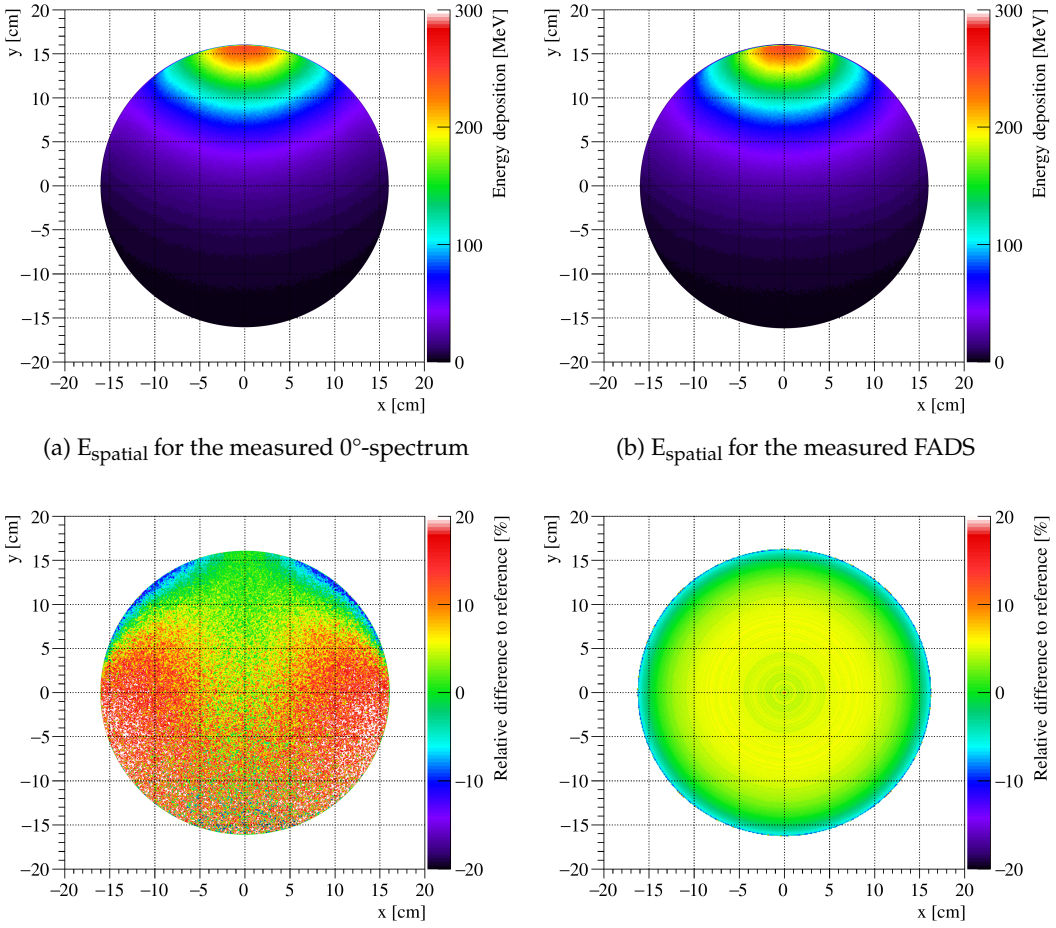

(a) $E_{spatial}$ for the measured 0°-spectrum

(b) $E_{spatial}$ for the measured FADS

(c) Relative difference in $E_{spatial}$ between simulations employing the FADS and the measured 0°-spectrum, 0°-projection

(d) Relative difference in $E_{spatial}$ between simulations employing the FADS and the measured 0°-spectrum, 360°-rotation

Figure 3.5: Evaluation W-IV: Influence of bowtie-filter induced spectral distortion on spatial distribution of simulated deposited energy, $E_{spatial}$. Fan-angle dependent photon fluence (FM) was employed. FADS: fan-angle dependent spectra. For better visibility of the phantom periphery, background color outside the water phantom was set to white. Adapted from Steuwe et al. (2018).

dependent photon fluence caused by the beam-shaping filter was implemented in the simulations by the filter's PDF of the transmission curve, the spectral distortion due to beam-shaping filtration was not represented as only the central source spectrum across the whole fan beam was employed. As FADS are not commonly available without measuring them directly (refer to section 2.3.5.3), the influence of omitting spatial distortion was evaluated, see section 2.5.1.6.

There were only subtle differences visible between $E_{spatial}$ for the measured 0°-spectrum and FADS (see figure 3.5a and 3.5b). For a single projection and employing FADS, $E_{spatial}$ was reduced at the outer sides of the x-ray fan beam (see figure 3.5c, ~-10%), compared to employing only the central spectrum. The central spectrum is softer than the spectra at the outer sides of the fan beam, as the low-energy

photons are filtered out by the beam-shaping filter, thereby increasing the mean spectral energy from 57.7 keV (0°-spectrum) to 76.7 keV for the 21°-spectrum. The beam-hardened spectra led to an increased energy deposition at the phantom center (cf. figure 3.5d), whereas the reduced amount of low-energy photons caused a reduction of $E_{spatial}$ at the phantom periphery, for the 360°-reconstruction (Steuwe et al. 2018).

3.1.5 EVALUATION W-V: TOTAL ENERGY DEPOSITION E_{TOTAL}

E_{total} was highest for the virtual beam-shaping scenario (printed in bold) which, however, only resulted in a relative difference of +2.22% (FM/NM) compared to E_{total} of the reference spectrum. The generated filtered spectrum showed the lowest deviation (NM +0.12%, FM +0.14%). The relative differences increased if no additional filtration was employed (NM -4.93%, FM -5.35%). Simulations with monoenergetic 57.7 keV photons resulted in a slightly lower energy deposition (NM -1.48%, FM -1.06%, Steuwe et al. 2018).

Table 3.1: Evaluation W-V: Simulated total energy deposition (E_{total}) in the water phantom for simulations without (NM) and with (FM) photon fluence modulation. The values printed in bold shows E_{total} for the simulation modeling a 'full beam-shaping filter' (*virtual beam-shaping scenario*), with modeled fan-angle dependent photon fluence and spectra (Steuwe et al. 2018).

Emitted x-ray photons	**Uniform fluence (NM)**		**Fan-angle dependent fluence (FM)**	
	E_{total} [GeV]	Rel. diff. to reference [%]	E_{total} [GeV]	Rel. diff. to reference [%]
Measured 0°-spectrum @ 120 kV_p (reference)	2074.1		3063.1	
Generated 0°-spectrum @ 120 kV_p, unfiltered	1971.8	-4.93	2899.3	-5.35
Generated 0°-spectrum @ 120 kV_p, 3.3 mm Al	2076.6	+0.12	3067.3	+0.14
57.7 keV → $E_{mean, ref}$ @ 120 kV_p	2043.5	-1.48	3030.7	-1.06
Measured fan-angle dependent spectra @ 120 kV_p	2120.3	+2.22	**3131.2**	**+2.22**

3.2 INFLUENCE OF THE TUBE POTENTIAL AND TISSUE CONTRAST ENHANCEMENT ON THE ENERGY DEPOSITION AND DETECTOR SIGNAL IN THE BOX PHANTOM

Until now, only 120 kV_p-spectra and corresponding moneoenergetic photons were assessed in this work regarding the energy deposition and its spatial distribution. In the following, the results for the analysis of different tube potentials on energy deposition and detector signal in the box phantom are presented. For all simulations presented from here onward, only the generated filtered spectra at 80, 100, and 120 kV_p were applied.

3.2.1 EVALUATION B-I: INFLUENCE OF THE TUBE POTENTIAL ON THE ENERGY DEPOSITION AND THE DETECTOR SIGNAL IN THE BOX PHANTOM

First, all three layers of the box phantom were constructed of identical materials (either fat, water, soft tissue, or liver), see section 2.5.2.2. Between the tube potentials 80, 100, and 120 kV_p, E_{total} was approximately equal for each respective material in the phantom (see table 3.2). For water, soft tissue, and liver tissue, E_{total} was slightly higher at 80 kV_p than at 120 kV_p (difference of a maximum of 1.8%). The relative energy deposition compared to the total input photon energy was highest at 80 kV_p for all materials and lowest at 120 kV_p.

Table 3.2: Evaluation B-I: Simulated total energy deposition, E_{total}, in the box phantom for the materials fat, water, soft tissue, and liver for the tube potentials 80, 100, and 120 kV_p. Individual layers inside the box phantom contained the identical material.

	Tube potential	**E_{total} [GeV]**		**Relative difference to 120 kV_p-acquisition [%]**	
Material	**[kV_p]**	**Phantom**	**Detector**	**Phantom**	**Detector**
Fat	80	660.7	500.5	-1.80	-28.31
	100	658.8	614.7	-2.10	-11.95
	120	672.9	698.1		
Water	80	878.6	386.5	1.76	-33.98
	100	860.9	501.0	-0.28	-14.41
	120	863.4	585.4		
Soft tissue	80	936.2	370.1	1.63	-33.71
	100	918.5	478.4	-0.29	-14.31
	120	921.2	558.3		
Liver	80	938.0	369.7	1.64	-33.72
	100	920.3	477.9	-0.27	-14.32
	120	922.8	557.8		

For liver tissue at 80 kV_p, 41% of the total input energy was absorbed in the phantom, whereas at 120 kV_p, only 32% of the total input energy was absorbed in the phantom. The maximum difference in E_{total} compared to the simulation at 120 kV_p was -2.1% for the material fat at 100 kV_p. Although E_{total} in the box phantom was nearly equal for all three tube potentials, $E_{spatial}$ varied: with increasing tube potential, energy deposition occurred at increasing depths due to the longer range of high-energy photons (deeper penetration). Hence, the highest entrance deposition was visible for the 80 kV_p-setting, whereas energy deposition was distributed to larger depths for the 120 kV_p-setting.
Relative differences between tube potentials were considerably higher for the energy deposition in the detector. Compared to E_{total} in the detector at 120 kV_p, E_{total} was 11-14% lower at 100 kV_p and 28-34% lower at 80 kV_p. The total deposited energy in the detector increased with increasing tube potential. The relative energy deposition in the detector compared to the total input photon energy was highest at 100 kV_p (~23%) and lowest at 80 kV_p (~16%) for all materials.
Table 3.3 shows the ratio between detector signal for the different materials (i.e. for two box phantoms in adjacent position, neglecting cross-scattering between boxes). Largest differences between detector signal were visible at 80 kV_p and decreased slightly with increasing tube potential. Furthermore, larger differences in density caused larger differences in detector signal (compare detector ratios of liver and fat tissue vs. liver and soft tissue).

Table 3.3: Evaluation B-I: Difference in detector signal between two adjacent materials. Ratios were calculated from the detector signals presented in table 3.2. Ratios did not include cross-scattering between the materials. The larger the deviation from a ratio of 1.0, the larger the difference in detector signal between two materials.

Material	**Tube potential [kV_p]**	**Fat**	**Water**	**Soft tissue**	**Liver**
Fat	80	1.000	0.772	0.739	0.739
	100	1.000	0.815	0.778	0.777
	120	1.000	0.838	0.800	0.799
Water	80		1.000	0.958	0.957
	100		1.000	0.955	0.954
	120		1.000	0.954	0.953
Soft tissue	80			1.000	0.999
	100			1.000	0.999
	120			1.000	0.999
Liver	80				1.000
	100				1.000
	120				1.000

3.2.2 EVALUATION B-II: INFLUENCE OF TISSUE CONTRAST ENHANCEMENT ON THE ENERGY DEPOSITION IN THE BOX PHANTOM

In this section, the individual layers of the phantom were constructed of different materials, to investigate the energy deposition in non-enhanced and enhanced tissues, see section 2.5.2.3. In this case, the box phantom was constructed of fat (layer 1), liver (layer 2), and fat (layer 3). This setup represented the material interfaces present in an axial slice through the abdomen at liver height. For simulations of contrast-enhanced acquisitions, iodine was added to the material liver with mass fractions of ψ_I=[0.001, 0.003, 0.005, 0.010, 0.015], corresponding to iodine concentrations of 1, 3, 5, 10, and 15 mg/ml, respectively.
The total energy deposition in the box phantom was almost equal for the three tube potentials (772.9, 764.3, and 773.6 GeV at 80, 100, and 120 kV_p, respectively, for ψ_I = 0.000). However, relative to the incident photon energy, the highest percentage was deposited at 80 kV_p (~33.2%) and the lowest percentage at 120 kV_p (~26.8%).
Figure 3.6 depicts 2D-energy maps of the whole phantom at 80, 100, and 120 kV_p for the simulation of a non-enhanced (ψ_I = 0.000) and an enhanced (ψ_I = 0.010) acquisition. The incident photons reached layer 1 at y = +45 mm, underwent the first material transition from fat to liver at y = +15 mm, the second material transition from liver to fat at y = -15 mm, and left layer 3 at y = -45 mm. Subtle color differences in figure 3.6 show differences at the interfaces between the layers.
Even without contrast enhancement, $E_{spatial}$ increased considerably at the interface between the fat and the liver layer, due to the higher density of liver tissue (1.06 g/cm^3) compared to fat tissue (0.95 g/cm^3).

The energy deposition along the y-axis of the box phantom for a simulation of a non-enhanced (ψ_I = 0.000) and an enhanced acquisition with an iodine mass fraction of ψ_I = 0.010 are presented in figures 3.7-3.8. Energy deposition was highest at the interface between layer 1 and layer 2 for the 80 kV_p-setting and reduced for higher tube potentials. Energy deposition in layer 1 was comparable for both the simulation of the non-enhanced and the enhanced acquisition, though energy deposition increased considerably in layer 2 for the simulation of the enhanced acquisition. The 80 kV_p-profiles showed the steepest gradient in layer 2. The profiles for 100 and 120 kV_p were fairly identical in the first and second layer, but differed in the third layer. Here, energy deposition was highest for the 120 kV_p-spectrum and decreased with decreasing tube potential.
The iodine concentration corresponding to the mass fraction ψ_I = 0.010 (10 mg/ml) is usually only achieved in the aorta directly after injection of the contrast agent and not in the liver. However, this mass fraction was chosen for data presentation since the differences between tube potentials are more easily apparent for larger mass fractions.

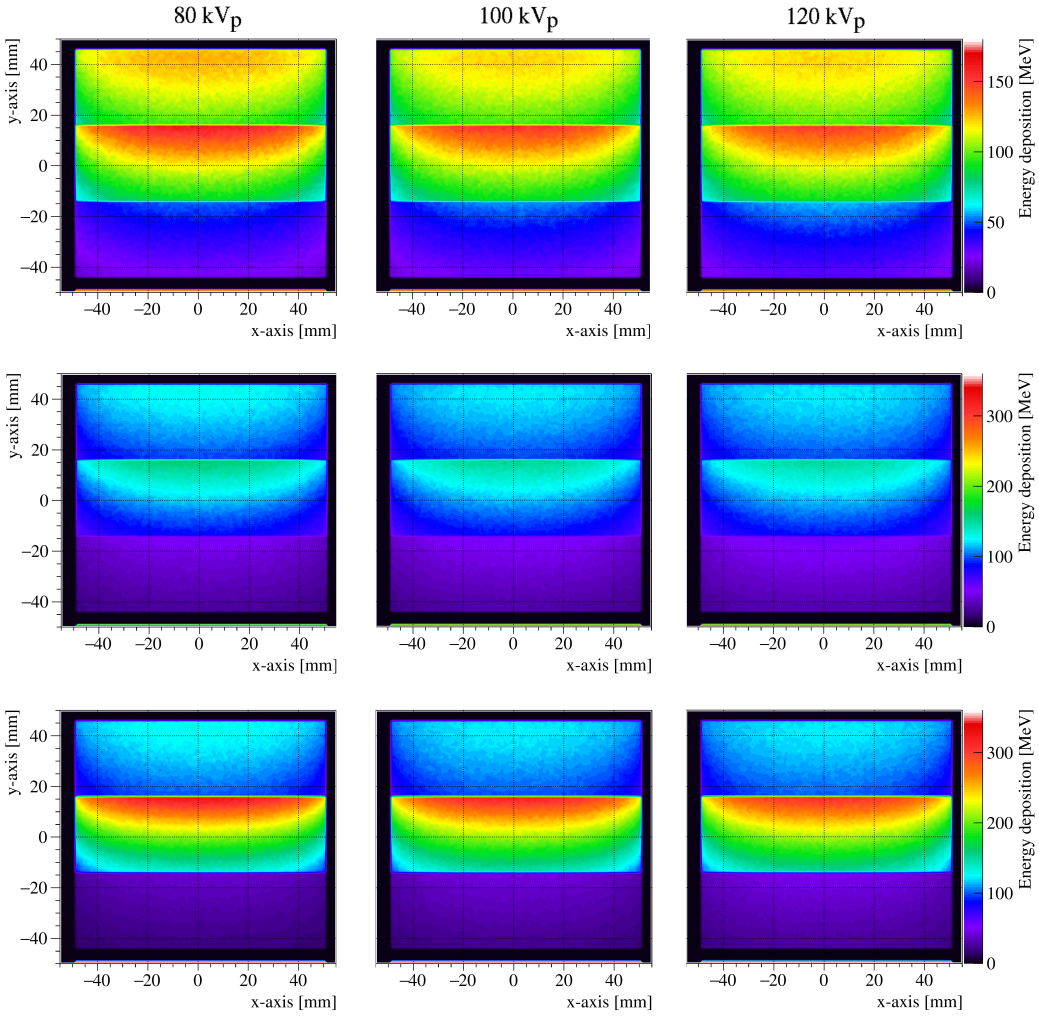

Figure 3.6: Evaluation B-II: Summed energy deposition along the z-axis in the box phantom for the material combination in the three layers fat-liver-fat at 80 kV_p (left), 100 kV_p (middle), and 120 kV_p (right). Top row: non-enhanced liver, middle row: non-enhanced liver with different color scale, bottom row: enhanced liver (ψ_I = 0.010). Incident photons reach layer 1 at y = +45 mm, undergo the first material transition from fat to liver at y = +15 mm, the second material transition from liver to fat at y = -15 mm, and leave layer 3 at y = -45 mm. Please note the different color bars for energy maps of simulations of non-enhanced and enhanced acquisitions.

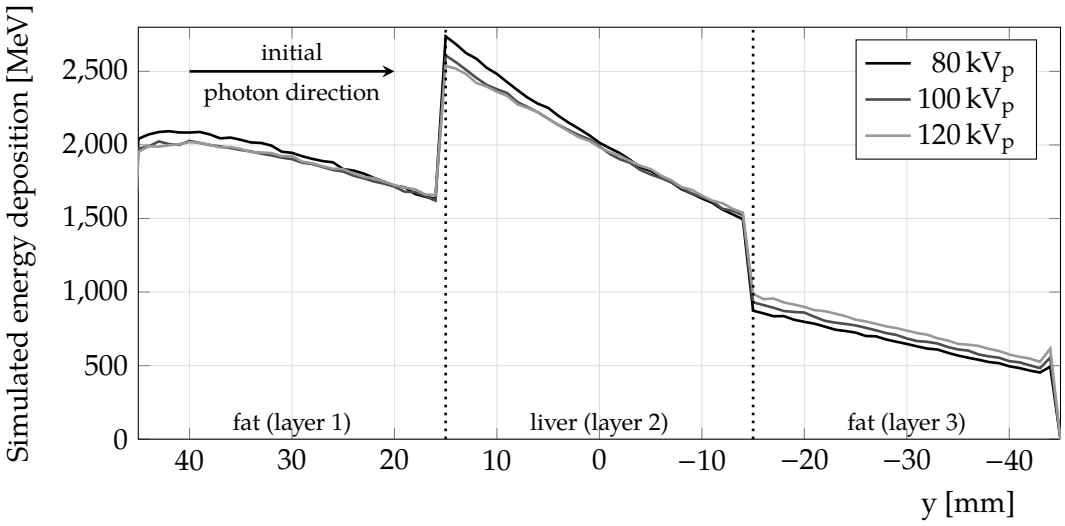

Figure 3.7: Evaluation B-II: Profile through the box phantom, constructed of fat (layer 1), liver (layer 2), and fat (layer 3) at 80, 100, and 120 kV_p. For calculation of the profiles, only the inner 4 cm in x- and z-direction (between -20 mm and +20 mm) were used to take only the homogenous distribution inside the phantom into account (the energy deposition is less homogenous at the edges of the phantom as scattered photons in these regions are only produced but their energy is not deposited). Please note the different vertical axis scaling in the profiles in figures 3.7-3.8.

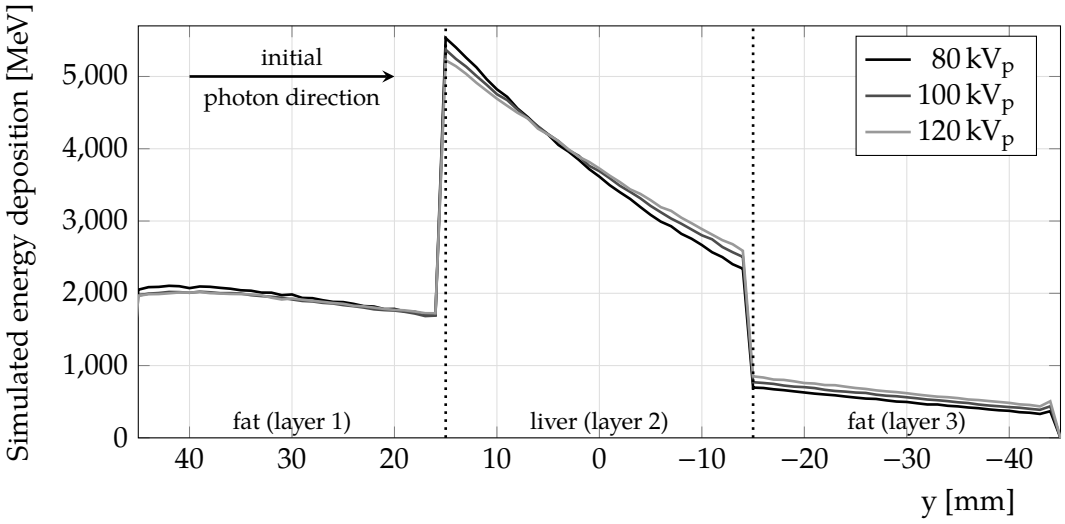

Figure 3.8: Evaluation B-II: Profile through the box phantom, constructed of fat (layer 1), enhanced liver (layer 2, $\psi_I = 0.010$), and fat (layer 3) at 80, 100, and 120 kV_p. Simulated energy deposition is highest for the 80 kV_p-simulation up to y = +5 mm. From y = +5 mm onwards until y = -45 mm, energy deposition is highest for the 120 kV_p-simulation. For calculation of the profiles, again only the inner 4 cm (between -20 mm and +20 mm) in x- and z-direction were used, to take only the homogenous distribution inside the phantom into account. Please note the different vertical axis scaling in the profiles in figures 3.7-3.8.

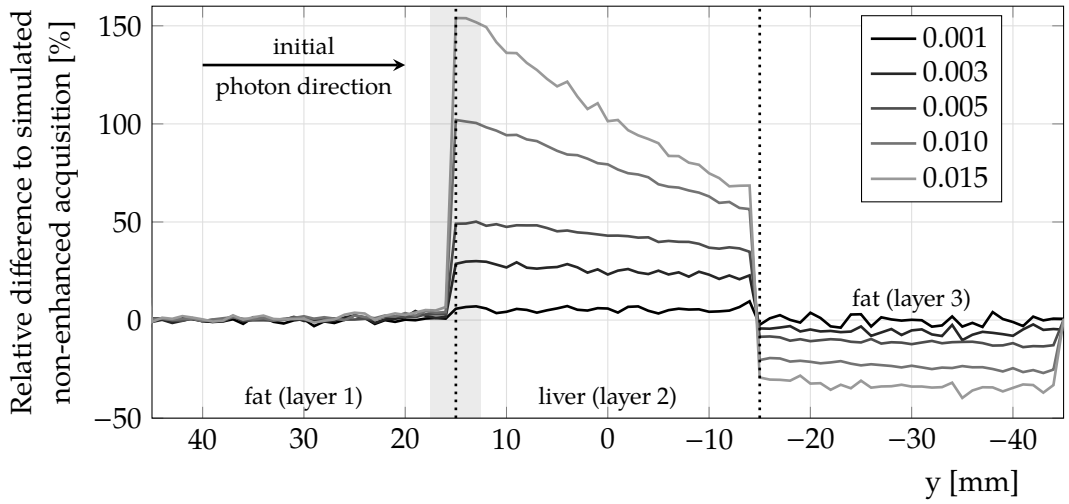

Figure 3.9: Evaluation B-II: Relative difference to simulated non-enhanced acquisition for iodine mass fractions of ψ_I = 0.001, 0.003, 0.005, 0.010, 0.015 at 80 kV_p. Only the inner 4 cm in x- and z-direction were used for calculation of the profiles to take only the homogenous distribution inside the phantom into account. The shaded area in the plot highlights the interface layers covered by the interface 2a/1 and an interface layer thickness of 2.5 mm. Please note the different vertical axis scaling in the profiles in figures 3.9-3.10.

Figure 3.9 presents the increased energy deposition in the box phantom compared to a simulated non-enhanced acquisition (pure liver in layer 2) for all simulated mass fractions ψ_I = [0.001, 0.003, 0.005, 0.010, 0.015] (enhanced liver in layer 2) at 80 kV_p. For the profiles of the energy deposition along the y-axis, only the inner 4 cm of the phantom (in x- and z-direction, between -20 mm and +20 mm) were taken into account, as $E_{spatial}$ in this range was fairly homogeneous. The higher the iodine concentration, the higher the relative difference in energy deposition between simulated enhanced and non-enhanced acquisitions. For very small iodine concentrations (1-3 mg/ml), the energy increase was relatively stable along the y-axis of the phantom (along layer 2, between y = -15 mm and y= +15 mm), whereas for high iodine concentrations (5 - 15 mg/ml), the difference in energy deposition decreased along the y-axes of the phantom. The larger the distance from the fat/liver-tissue interface (layer 1/2) towards the detector, the lower the relative increase in energy deposition. In layer 3, the energy deposition for simulated enhanced acquisitions was lower compared to the energy deposition for simulated non-enhanced acquisitions (negative relative differences) since a high percentage of photons was already absorbed in layer 2.

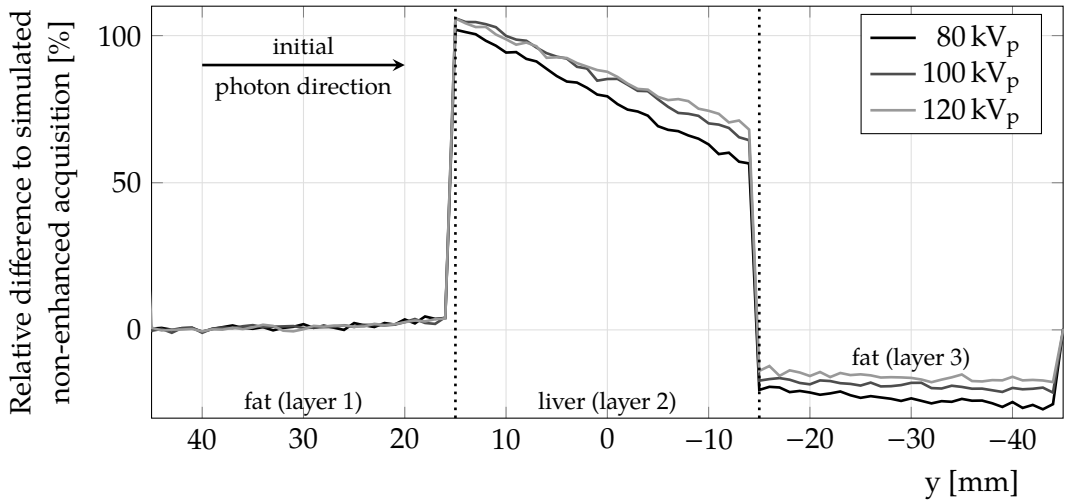

Figure 3.10: Evaluation B-II: Relative difference in energy deposition between simulated enhanced and non-enhanced acquisitions, at 80, 100, and 120 kV_p. Profile through the box phantom, constructed of fat (layer 1), liver (layer 2, $\psi_I = 0.010$), and fat (layer 3). Only the inner 4 cm in x- and z-direction were used for calculation of the profiles to take only the homogenous distribution inside the phantom into account. Please note the different vertical axis scaling in the profiles in figures 3.9-3.10.

To check whether the energy build-up effect varied between tube potentials, the relative difference between simulated enhanced and non-enhanced acquisitions was plotted as a profile through the inner 4 cm of the box phantom, see figure 3.10, for an iodine mass fraction of $\psi_I = 0.010$. At the interface between layer 1 and 2 (interface fat to liver), no clear differences were visible between the tube potentials 100 and 120 kV_p, whereas for 80 kV_p, a slightly lower relative increase was noticed. At larger depths, the relative difference in energy deposition of the simulated 80 kV_p-acquisition dropped with a steeper gradient compared to the simulated 100 and 120 kV_p-acquisitions.

3.2.3 EVALUATION B-III: ENERGY BUILD-UP EFFECT AT MATERIAL INTERFACES IN THE BOX PHANTOM

Section 3.2.2 demonstrated that the total energy deposition for different tube potentials was comparable although $E_{spatial}$ varied along the y-axis (see figures 3.6, 3.7 and 3.8). A closer look at the interfaces between layers 1 and 2 and between layers 2 and 3 was therefore necessary, see section 2.5.2.4. Refer to figure 2.20 for the names of interface layers. For this purpose, the deposited energy around the material transition from fat to liver (interface 2a/1) and around the material transition from liver to fat (interface 2b/3) were determined in the 4 cm x 4 cm central block of the box phantom. This was performed for interface layer thicknesses of 1.0, 2.5, and 5.0 mm in y-direction. Interface ratios (2a/1 and 2b/3) were calculated from the results of the simulations of non-enhanced and enhanced acquisitions and presented in table 3.4. More interactions were taken into account with increasing layer thickness (larger cumulative energy deposition, more signal). However, with increasing distance from the interface, the energy build-up effect at the entrance side of the photon beam decreased (decreasing energy deposition with increasing distance from interface). This becomes apparent at the material interfaces in the profiles, see figures 3.7 and 3.8). The ratio at the 'upstream' interface 2a/1, hence, the transition from fat (layer 1) to liver (layer 2) increased with decreasing interface layer thickness due to the larger difference in energy deposition between interface layer 2a and 1 for thinner interface layers. The reverse effect was visible for the 'downstream' interface 2b/3, the transition between liver (layer 2) and fat (layer 3). The thickness of the interface layer was a compromise between signal and ratio for the energy build-up effect.
For the assessed tube potentials, the energy build-up effect at the interfaces was highest at 80 kV_p and lowest at 120 kV_p. The energy build-up effect increased with increasing iodine mass fraction for the assessed tube potentials.

The thickness of the interface layer was of importance for later simulations of the abdomen phantom and digitized patient phantoms, to assess the energy build-up effect for different interfaces. The profile of the difference in energy deposition between the simulated enhanced and non-enhanced acquisitions was fairly stable for 2.5 mm after entrance in layer 2 for iodine mass fractions ψ_I up to 0.005 (see shaded area in figure 3.9). Hence, for the simulations of the abdomen phantom and digitized patient phantoms, a thickness of 2.5 mm was used for the organ shells.

Table 3.4: Evaluation B-III: Ratios for liver/fat-interfaces for different interface widths (1.0 mm, 2.5 mm, and 5.0 mm) at 80, 100, and 120 kV_p (generated filtered spectra). Interface 2a/1 is the transition between layers 1 and 2, interface 2b/3 is the transition between layers 2 and 3. For these ratios, the energy deposited in the liver layer was divided by the energy deposited in the fat layer. See figure 2.20 for a schematic drawing of the interfaces in the box-phantom. Interface ratios 2a/1 and 2b/3 for simulated non-enhanced (ψ_I = 0.000) and enhanced (ψ_I = 0.005) acquisitions are marked grey for easier comparison to ratios calculated for the abdomen and digitized patient phantoms, refer to tables 3.7-3.8 and tables 3.11-3.12.

Interface width		**5.0 mm**		**2.5 mm**		**1.0 mm**	
	ψ_I	**Interface 2a/1**	**Interface 2b/3**	**Interface 2a/1**	**Interface 2b/3**	**Interface 2a/1**	**Interface 2b/3**
80 kV_p	0.000	1.57	1.86	1.63	1.76	1.67	1.71
	0.001	1.66	1.98	1.73	1.88	1.77	1.83
	0.003	1.99	2.40	2.07	2.29	2.12	2.21
	0.005	2.29	2.80	2.38	2.63	2.43	2.53
	0.010	3.02	3.71	3.17	3.48	3.25	3.36
	0.015	3.71	4.61	3.90	4.28	4.01	4.06
100 kV_p	0.000	1.50	1.77	1.56	1.68	1.61	1.64
	0.001	1.60	1.87	1.67	1.78	1.69	1.73
	0.003	1.94	2.27	2.00	2.17	2.05	2.09
	0.005	2.24	2.65	2.33	2.50	2.36	2.43
	0.010	2.98	3.57	3.11	3.35	3.17	3.24
	0.015	3.66	4.40	3.82	4.09	3.90	3.90
120 kV_p	0.000	1.46	1.68	1.51	1.61	1.53	1.55
	0.001	1.54	1.79	1.59	1.72	1.63	1.66
	0.003	1.92	2.27	1.99	2.16	2.03	2.08
	0.005	2.17	2.52	2.25	2.38	2.29	2.31
	0.010	2.88	3.37	2.99	3.17	3.04	3.05
	0.015	3.56	4.13	3.70	3.88	4.01	4.06

3.3 CALCULATION OF EXPOSURE MAPS OF THE MODIFIED ABDOMEN PHANTOM

The next section describes the energy deposition in the modified abdomen phantom (see section 2.4.1.3). This phantom consists of several organs and material interfaces. Particular focus was the energy increase in an organ and at the interfaces between visceral fat and organ tissue for simulations of iodine-enhanced acquisitions. Figure 3.11 shows the axial, coronal, and sagittal energy map of the simulated modified abdomen phantom. Simulation parameters for this simulated non-enhanced acquisition were a tube potential of 80 kV_p, spiral acquisition mode (pitch = 1.0), and a scan coverage of 43.2 cm (40 cm phantom length + 2 x 1.6 cm overscanning). The exposure along the z-axis of the phantom was homogeneous (no LTCM applied), however, fan-angle dependent fluence modulation (FM) was enabled. The influence of the spiral acquisition mode with the pitch 1.0 was visible in the coronal and sagittal planes. At the phantom center, energy deposition was uniform, whereas gaps in energy deposition are visible at the phantom periphery.

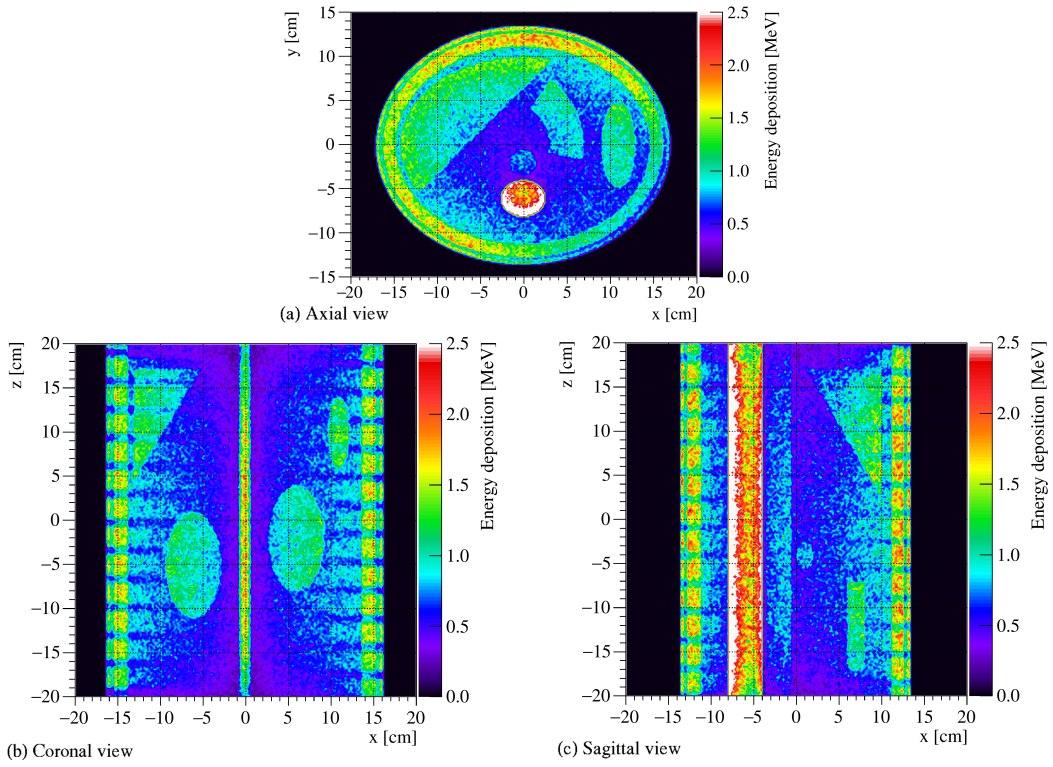

Figure 3.11: Axial (a), coronal (b), and sagittal (c) energy deposition map of the modified abdomen phantom. Simulated non-enhanced (ψ_I = 0.000) acquisition at 80 kV_p with the spiral acquisition mode (pitch = 1.0). Voxel size: 2 x 2 x 2 mm^3.

3.3.1 EVALUATION A-I: INFLUENCE OF TUBE POTENTIAL AND TISSUE CONTRAST ENHANCEMENT ON ENERGY DEPOSITION AND ITS SPATIAL DISTRIBUTION IN THE MODIFIED ABDOMEN PHANTOM

Table 3.5 presents an overview of the total energy deposition in the modified abdomen phantom, for simulated non-enhanced and enhanced acquisitions at 80, 100, and 120 kV_p (refer to section 2.5.3.2). Furthermore, the calculated relative differences in energy deposition between the simulated enhanced and the non-enhanced acquisition are shown. In general, energy deposition in all structures of the phantom increased with increasing tube potential, except for the skin (difference in energy deposition of -4.6% between the 120 kV_p- and 80 kV_p-setting). The increase amounted to approximately (~) + 12% for the the whole phantom. For individual tissues, the increase ranged between 2% (soft tissue) and 35% (aorta). Energy deposition in tissues close to the phantom center was increasing to a stronger degree with increasing tube potential compared to energy deposition in tissues at the periphery.
For simulated contrast-enhanced acquisitions, energy deposition increased considerably for the enhanced tissues (between ~30% and 50%) compared to the energy deposition in simulated non-enhanced acquisitions. For all enhanced tissues, the relative increase in energy deposition was highest at 120 kV_p, although differences between 80 and 100 kV_p were larger than between 100 and 120 kV_p. For all tube potentials, the energy deposition in the pancreas yielded the highest increase (50.7% at 120 kV_p). Energy deposition in the largest organ, the liver, increased by 31-35%.
For the surrounding non-enhanced tissues, energy deposition was lower for simulated enhanced acquisitions than for simulated non-enhanced acquisitions (-1 to -4%). The largest difference was obtained in the spine (reduction of ~-3.7%). The relative difference in energy deposition for non-enhanced tissues between simulated enhanced and non-enhanced acquisitions were approximately equal for all tube potentials.
Figure 3.12 shows an overview of an axial slice through the liver, GI-tract, spleen, aorta, and the spine for simulated non-enhanced (top row) and enhanced (second row) acquisitions at 80, 100, and 120 kV_p. Since simulations of CT acquisitions were performed in helical mode with a pitch of 1.0, $E_{spatial}$ at the posterior and anterior side of the phantom was not homogeneous for an axial slice. Energy deposition in the subcutaneous fat and visceral fat between the organs and the aorta was considerably lower than in the organs as the physical density of fat is lower than the density of organ tissue (e.g. $\rho_{fat} < \rho_{liver}$). With increasing tube potential, energy deposition at the phantom center increased due to the longer range of high-energy photons, similar to the energy deposition in the box phantom, presented in section 3.2.1. Energy deposition decreased with increasing surface-to-center distance of the phantom, which was especially visible for the liver. The third row in figure 3.12 depicts the relative difference in $E_{spatial}$ between the simulated enhanced and non-enhanced acquisitions. At 120 kV_p, relative differences in energy deposition at the phantom center were more homogeneously distributed than at 80 kV_p, which was especially visible in the area between the liver and the aorta.

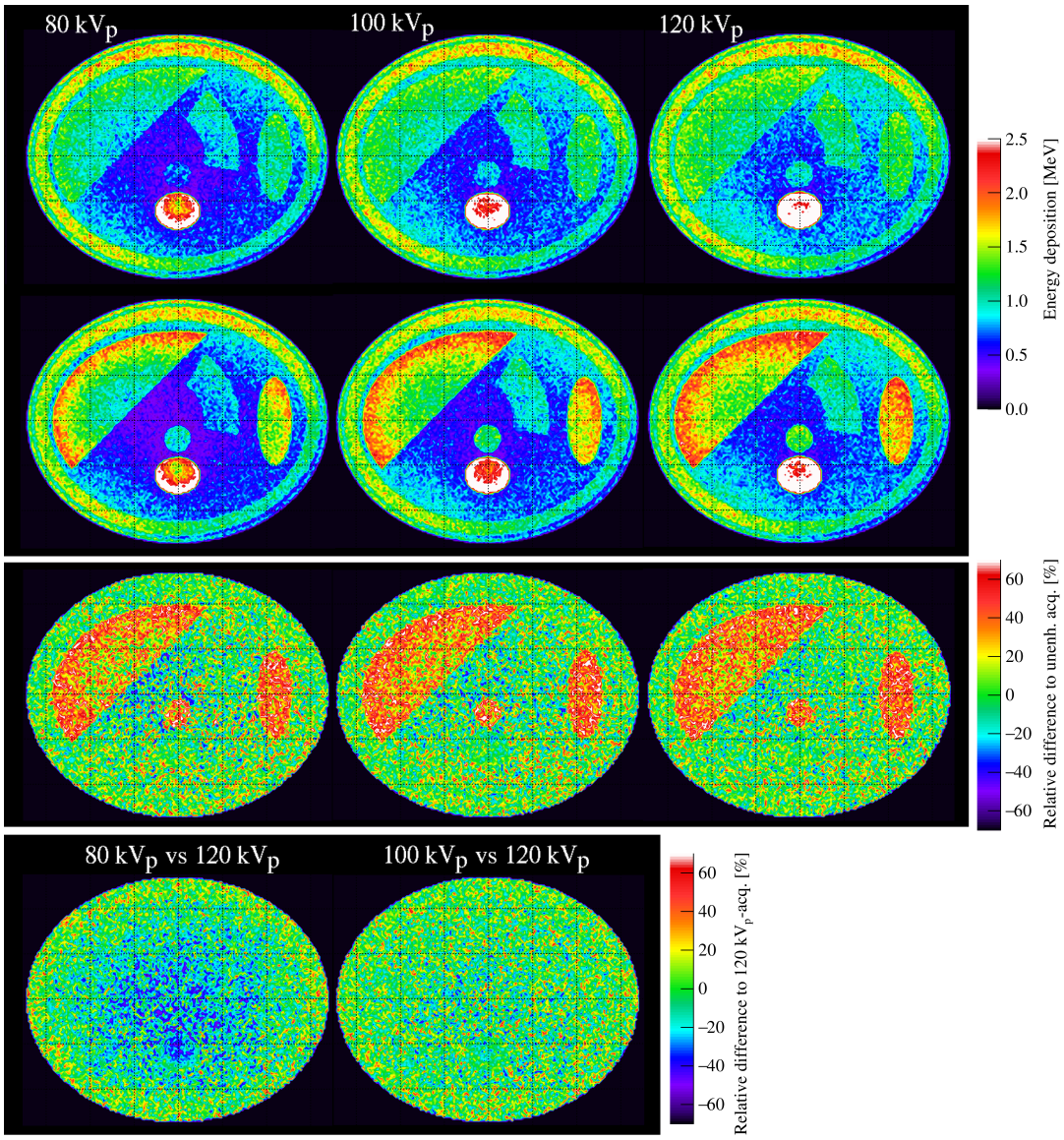

Figure 3.12: Evaluation A-I: Simulated energy deposition in the modified abdomen phantom at 80, 100, and 120 kV_p. Energy deposition for simulated non-enhanced acquisitions (top row), for simulated enhanced acquisitions (second row), relative difference in energy deposition between simulated enhanced and non-enhanced acquisitions (third row). Left: 80 kV_p-, middle: 100 kV_p-, right: 120 kV_p-simulation. Fourth row: relative difference in $E_{spatial}$ between the simulations at 80 and 120 kV_p (left) and between the simulations at 100 and 120 kV_p (right), relative difference shown for simulated non-enhanced acquisitions. Contrast-enhanced tissues: aorta, liver, spleen, kidneys, and pancreas ($\psi_I = 0.005$).

Whereas the spatial distribution of the deposited energy was fairly equal for 100 and 120 kV_p, large differences appeared at the phantom center at 80 kV_p due to the shorter photon range at this tube potential (visible in third and fourth row of figure 3.12).

Table 3.5: Evaluation A-I: Comparison of the energy deposition in the modified abdomen phantom for simulated non-enhanced and enhanced computed tomography acquisitions at 80, 100, and 120 kV_p. Relative differences in energy deposition between simulated enhanced and non-enhanced acquisitions were calculated for corresponding tube potentials. Soft tissue includes the gastro-intestinal tract and the soft tissue layer at the phantom periphery. Contrast-enhanced tissues: aorta, liver, spleen, kidneys, and pancreas ($\psi_I = 0.005$). Left (L), right (R).

Simulated energy deposition [GeV]											
							Whole organ				
	Phantom	**Soft tissue**	**Spine**	**Skin**	**Fat**	**Aorta**	**Liver**	**Spleen**	**Kidney R**	**Kidney L**	**Pancreas**
Simulated non-enhanced acquisition											
80 kV_p	3251.11	1010.69	216.03	251.65	1413.77	23.44	230.13	36.66	15.01	14.96	5.03
100 kV_p	3450.44	1014.23	249.69	241.96	1549.51	27.75	251.32	39.25	16.68	16.66	5.81
120 kV_p	3630.65	1029.07	270.81	240.18	1667.59	30.98	267.49	41.28	17.95	17.98	6.39
Simulated enhanced acquisition											
80 kV_p	3305.19	998.26	208.05	250.06	1378.71	32.99	301.75	52.51	21.88	21.92	7.41
100 kV_p	3521.22	1000.14	240.47	240.14	1510.91	39.94	338.21	57.40	24.91	24.91	8.74
120 kV_p	3711.12	1014.08	261.09	238.21	1627.26	44.79	363.02	60.66	26.83	26.91	9.63
Relative difference to non-enhanced acquisition [%]											
80 kV_p	1.66	-1.23	-3.69	-0.63	-2.48	40.70	31.12	43.25	45.73	46.52	47.36
100 kV_p	2.05	-1.39	-3.69	-0.75	-2.49	43.93	34.58	46.24	49.34	49.55	50.48
120 kV_p	2.22	-1.46	-3.59	-0.82	-2.42	44.56	35.71	46.93	49.48	49.67	50.65

3.3.2 EVALUATION A-II: ENERGY BUILD-UP EFFECT AT MATERIAL INTERFACES IN THE MODIFIED ABDOMEN PHANTOM – WHOLE PHANTOM

The energy deposition in the organ and tissue shells of the modified abdomen phantom was assessed in the following (refer to section 2.5.3.3). Particular focus was the energy deposition at material interfaces. In the modified abdomen phantom, organs are surrounded by visceral fat. Table 3.6 provides the energy deposition per organ and surrounding tissue shell for the six performed simulations. Furthermore, the corresponding relative differences in energy deposition between simulations of enhanced and non-enhanced acquisitions are given.
The largest change from the whole organ to the organ and surrounding fat tissue shells was visible in the liver. Whereas the relative difference in energy deposition between the simulation of enhanced and non-enhanced acquisition was only ~+31-35% in the complete liver (see table 3.5), this value increased for the liver shell to ~+43%. This increase was due to the large size of the liver and its heterogeneous energy deposition. Along the outer rim of the liver, energy deposition was approximately twice as high as at the inner rim, positioned close to the aorta. For the other organs, the relative differences in energy deposition between the simulation of the enhanced and the non-enhanced acquisition increased only slightly.
Energy deposition decreased in the surrounding visceral fat shell for a simulation of an enhanced acquisition for all organs. The relative difference was strongest for the liver (~-7%) and least observable for the left kidney (~-4 %).
Energy deposition was highest for simulations at 120 kV_p and lowest at 80 kV_p as were the relative differences in energy deposition for the *organ shells*. Relative differences between simulations of enhanced and non-enhanced acquisitions behaved contrary for the *surrounding fat shells*: largest differences were visible at 80 kV_p.

Table 3.6: Evaluation A-II: Comparison of the energy deposition in the modified abdomen phantom for simulated non-enhanced and enhanced acquisitions at 80, 100, and 120 kV_p. Relative differences in energy deposition between simulations of enhanced and non-enhanced computed tomography acquisitions were calculated for the corresponding tube potentials. Contrast-enhanced tissues: aorta, liver, spleen, kidneys, and pancreas ($\psi_I = 0.005$). Left (L), right (R).

Simulated energy deposition [GeV]										
	Organ shell					**Surrounding fat shell**				
	Liver	**Spleen**	**Kidney R**	**Kidney L**	**Pancreas**	**Liver**	**Spleen**	**Kidney R**	**Kidney L**	**Pancreas**
Simulated non-enhanced acquisition										
80 kV_p	32.22	7.60	4.01	3.99	2.02	21.32	5.11	2.83	2.83	1.64
100 kV_p	34.43	8.07	4.42	4.41	2.31	23.51	5.61	3.25	3.25	1.96
120 kV_p	36.09	8.45	4.74	4.77	2.55	25.49	6.06	3.59	3.59	2.20
Simulated enhanced acquisition										
80 kV_p	45.57	11.13	5.93	5.94	2.98	19.86	4.84	2.70	2.72	1.54
100 kV_p	49.36	12.03	6.67	6.67	3.50	21.98	5.36	3.11	3.14	1.86
120 kV_p	51.82	12.61	7.21	7.20	3.84	23.81	5.79	3.47	3.48	2.10
Relative difference to non-enhanced acquisition [%]										
80 kV_p	41.44	46.51	47.85	48.85	47.78	-6.84	-5.32	-4.82	-3.83	-6.05
100 kV_p	43.38	49.05	50.80	51.47	51.32	-6.50	-4.46	-4.37	-3.56	-5.32
120 kV_p	43.58	49.32	52.04	50.92	50.58	-6.59	-4.37	-3.44	-3.05	-4.56

Table 3.7: Evaluation A-II: Calculated interface ratios between organ shell and surrounding fat shell at 80, 100, and 120 kV_p. Energy deposition was normalized to the volume of the shells prior to calculation of the interface ratios. Contrast-enhanced tissues: aorta, liver, spleen, kidneys, and pancreas ($\psi_I = 0.005$). Left (L), right (R).

Interface ratio (organ shell / surrounding fat shell)					
	Liver	**Spleen**	**Kidney R**	**Kidney L**	**Pancreas**
Simulated non-enhanced acquisition					
80 kV_p	1.649	1.679	1.649	1.654	1.578
100 kV_p	1.598	1.625	1.583	1.587	1.516
120 kV_p	1.545	1.576	1.538	1.558	1.493
Simulated enhanced acquisition					
80 kV_p	2.504	2.598	2.561	2.560	2.483
100 kV_p	2.450	2.536	2.497	2.492	2.423
120 kV_p	2.375	2.460	2.422	2.425	2.356

Table 3.7 presents the calculated ratios at the organ-surrounding tissue interface. For this purpose, the energy deposition in each shell was first normalized to the volume of the shell followed by the calculation of the organ/tissue shell ratios. The same pattern as was seen in the box phantom (c.f. table 3.4) was observed for the abdomen phantom, although here, interfaces 2a/1 and 2b/3 could not be separated into 'upstream' and 'downstream' interfaces due to the full rotation of the x-ray source around the modified abdomen phantom (stationary x-ray source in the box phantom). For increasing tube potential, the interface ratio decreased. Ratios for the simulated non-enhanced acquisitions ranged between 1.5 and 1.7, whereas ratios for the simulated enhanced acquisitions ranged between 2.3 and 2.6.

3.3.3 EVALUATION A-III: ENERGY BUILD-UP EFFECT AT MATERIAL INTERFACES IN THE MODIFIED ABDOMEN PHANTOM – AXIAL SLICE

The energy build-up effect was further assessed in one specific axial slice of the abdomen, containing parts of the organs liver and spleen, simulated with an increased number of photons for higher statistical occupation of the energy map (see figure 3.13 and section 2.5.3.4).
Both the simulation of the non-enhanced and enhanced acquisition were performed for the tube potentials of 80, 100, and 120 kV_p for a single 270°-projection (x-ray source position at 9 o'clock) and for a full source rotation. Figure 3.13 depicts $E_{spatial}$ for the projection and the rotation, simulated with a tube potential of 80 kV_p (simulated enhanced ($\psi_I = 0.005$) acquisition).

Table 3.8 presents the energy deposition and interface ratios for the ROIs depicted in figures 2.22a-2.22d for the simulation of a full source rotation around the phantom. Comparing the energy deposition between the enhanced and the non-enhanced setting, energy deposition increased considerably in the liver ROI (~+46% for ROI 2a, 34-40% for ROI 2b). A slight increase was noted in ROI 1 (~+1%) and a decrease noted in ROI 3 (~-10-14%). For the simulated non-enhanced acquisitions, both interface ratios ranged between 1.45 and 1.68. For the enhanced acquisitions, interface ratios were higher: for the interface 2a/1, ratios ranged between 2.15 and 2.28, whereas for interface 2b/3, ratios ranged between 2.39 and 2.61.

Figures 3.14-3.17 present the x-axis profiles of the energy maps marked in figure 3.13 for the evaluated tube potentials for simulations of the non-enhanced and enhanced acquisitions. The material transitions from air to skin, subcutaneous fat, soft tissue, visceral fat, and liver are clearly visible in all profiles.
Near the entrance side of the photon beam (at $x = \pm 17$ cm), energy deposition was

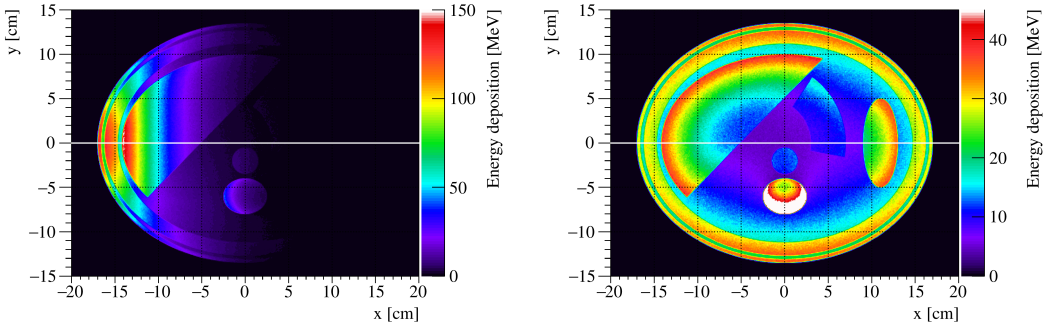

(a) Projection at 270° (b) 360°-rotation

Figure 3.13: Evaluation A-III: Energy deposition for a simulated enhanced acquisition of a single slice of the modified abdomen phantom at 80 kV_p. Profiles along the x-axis (white lines) are presented in figures 3.14-3.17. Energy deposition was not scored in the air for this setup, hence energy deposition equals zero outside the phantom. Contrast-enhanced tissues: aorta, liver, and spleen ($\psi_I = 0.005$). Please note the different scaling of the color bars.

Table 3.8: Evaluation A-III: Energy deposition and relative difference in energy deposition between simulations of enhanced and non-enhanced computed tomography acquisitions for the regions of interest (ROIs) depicted in figures 2.22a-2.22d at 80, 100, and 120 kV_p for the simulation of the full source rotation. Energy deposition and relative differences were determined from placing ROIs on calculated 2D energy/difference maps. For calculation of interface ratios, energy deposition in the ROIs was normalized to the number of pixels in the ROI. ROI 1 and ROI 3 are positioned in the surrounding tissue (fat), ROI 2a and ROI 2b in the liver.

Simulated energy deposition [MeV]					**Interface ratio**	
	ROI 1	**ROI 2a**	**ROI 2b**	**ROI 3**	**2a/1**	**2b/3**
Simulated non-enhanced acquisition						
80 kV_p	15.19	22.30	14.42	8.59	1.556	1.677
100 kV_p	15.74	22.37	15.40	9.68	1.505	1.591
120 kV_p	16.47	22.64	16.19	10.53	1.456	1.536
Simulated enhanced acquisition						
80 kV_p	15.40	33.19	19.77	7.58	2.282	2.608
100 kV_p	15.95	33.44	21.69	8.67	2.221	2.502
120 kV_p	16.60	33.74	22.98	9.60	2.153	2.394
Relative difference to non-enhanced acquisition [%]						
80 kV_p	1.35	46.13	34.13	-13.60		
100 kV_p	1.28	46.91	38.79	-11.62		
120 kV_p	0.70	46.57	40.30	-9.75		

highest for the 80 kV_p-spectrum for both the projection and the rotation. In the liver tissue between x = -14 and -5 cm, the slope of the 80 kV_p-profile was steepest. As a result, energy deposition was higher at 120 kV_p towards the center of the phantom compared to the energy deposition resulting from the 80 kV_p-setting. For the projection, energy deposition at the entrance side of the liver (x = -14 cm) was highest for the 80 kV_p-setting, albeit only marginally. For the full rotation, energy deposition at the entrance side of the liver was approximately equal for all tube potentials for simulated non-enhanced acquisitions. For simulated enhanced acquisitions, energy deposition at the entrance side of the liver was highest at 120 kV_p. However, profile data was noisy for the full rotation and might not describe small differences between tube potentials.

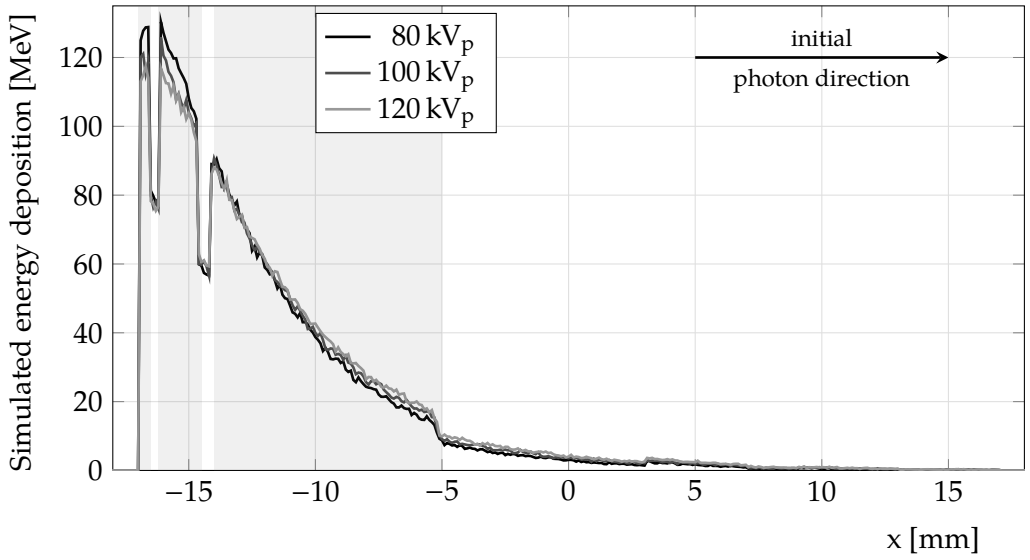

Figure 3.14: Evaluation A-III: Central x-axis profile through the 2D-energy map of a lateral projection at 80, 100, and 120 kV_p for the simulated *non-enhanced* acquisition. The following materials are traversed from left (x = -17 cm) to right (x = +17 cm) and visible on the profile: skin (shaded area, left), subcutaneous fat, soft tissue (shaded area, middle), visceral fat, liver (shaded area, right), visceral fat, gastrointestinal tract, and again visceral fat. Please note the different vertical axis scaling in the profiles in figures 3.14-3.15.

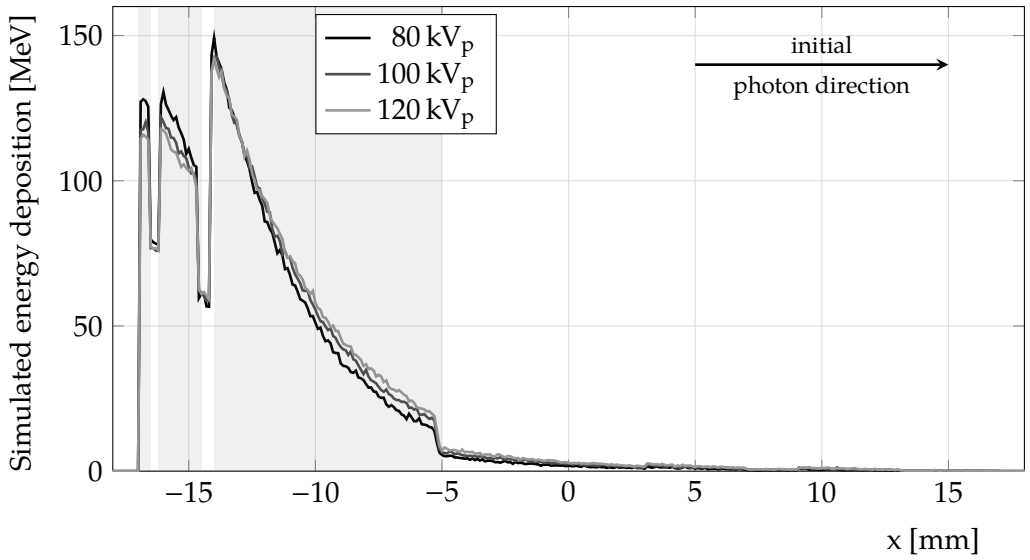

Figure 3.15: Evaluation A-III: Central x-axis profile through the 2D-energy map of a lateral projection at 80, 100, and 120 kV_p for the simulated *enhanced* acquisition. The following materials are traversed from left (x = -17 cm) to right (x = +17 cm) and visible on the profile: skin (shaded area, left), subcutaneous fat, soft tissue (shaded area, middle), visceral fat, liver (shaded area, right), visceral fat, gastrointestinal tract, and again visceral fat. Contrast-enhanced tissues: aorta, liver, and spleen (ψ_I = 0.005). Please note the different vertical axis scaling in the profiles in figures 3.14-3.15.

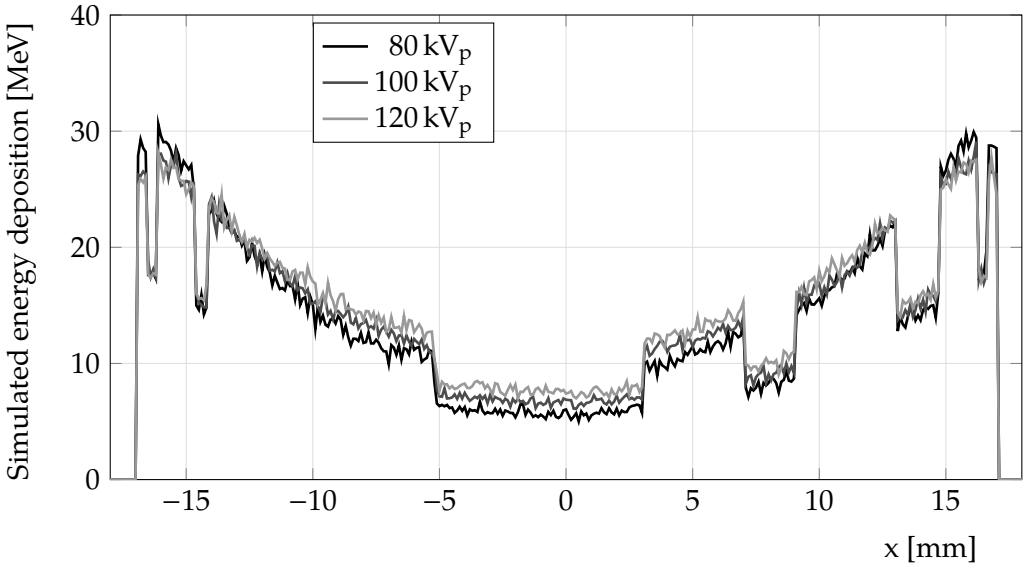

Figure 3.16: Evaluation A-III: Central x-axis profile through the 2D-energy map for a full source rotation at 80, 100, and 120 kV_p for the simulated *non-enhanced* acquisition. The following materials are traversed from left (x = -17 cm) to right (x = +17 cm) and visible on the profile: skin, subcutaneous fat, soft tissue, visceral fat, liver, visceral fat, gastro-intestinal tract, visceral fat, spleen, visceral fat, soft tissue, subcutaneous fat, and the skin.

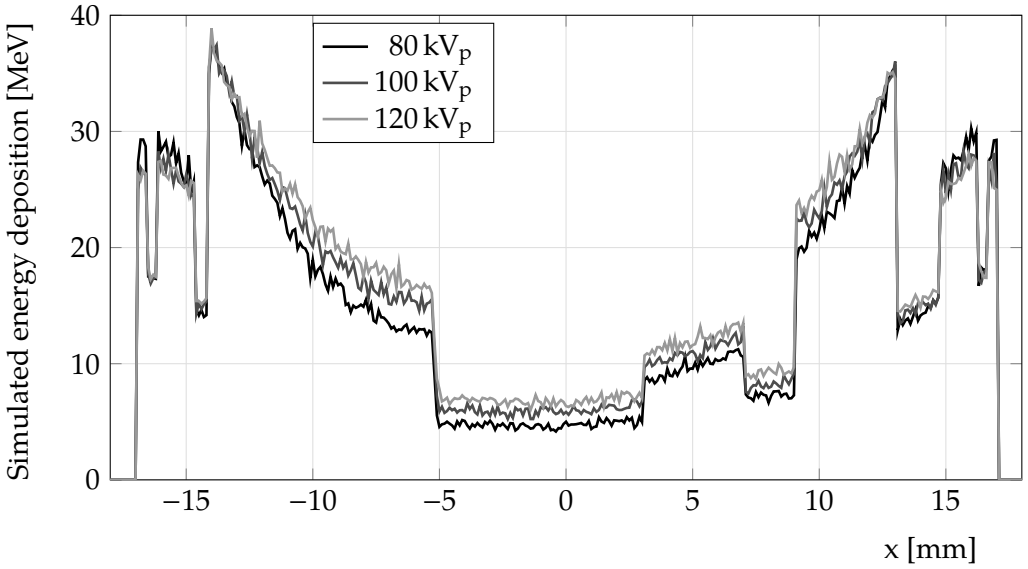

Figure 3.17: Evaluation A-III: Central x-axis profile through the 2D-energy map for a full source rotation at 80, 100, and 120 kV_p for the simulated *enhanced* acquisition. The following materials are traversed from left (x = -17 cm) to right (x = +17 cm) and visible on the profile: skin, subcutaneous fat, soft tissue, visceral fat, liver, visceral fat, gastro-intestinal tract, visceral fat, spleen, visceral fat, soft tissue, subcutaneous fat, and the skin. Contrast-enhanced tissues: aorta, liver, and spleen (ψ_I = 0.005).

3.4 CALCULATION OF EXPOSURE MAPS OF DIGITIZED PATIENTS

The MC software was further developed to allow for modeling and simulation of CT acquisitions of patients to calculate the radiation exposure depending on the acquisition parameters (e.g. tube potential), contrast enhancement, patient morphology, or BMI. Figure 3.18 presents the energy deposition of a simulated non-enhanced acquisition in the axial, coronal, and sagittal plane (patient 3A). Energy deposition was highest in the bones (ribs, spinal processes, ilium) due to the high material density and lowest in the lungs. Due to the density differences in the lungs, subtle differences in energy deposition were visible in the lungs.

3.4.1 EVALUATION P-I: INFLUENCE OF THE TUBE POTENTIAL AND TISSUE CONTRAST ENHANCEMENT ON ENERGY DEPOSITION AND ITS SPATIAL DISTRIBUTION IN A DIGITIZED PATIENT

For this evaluation, energy deposition in the abdominal scan range of patient 2A was simulated for the tube potentials 80, 100, and 120 kV_p for a simulation of a non-enhanced and an enhanced acquisition (see section 2.5.4.2 and figure I.2b). Results of $E_{spatial}$ for an axial slice through the liver, spleen, and lungs are presented in figure 3.19 for the simulated non-enhanced acquisitions in the top row and for the simulated enhanced acquisitions in the second row.
At 120 kV_p, energy deposition in the liver and the spleen was more homogeneously distributed compared to the energy deposition resulting from the simulated non-

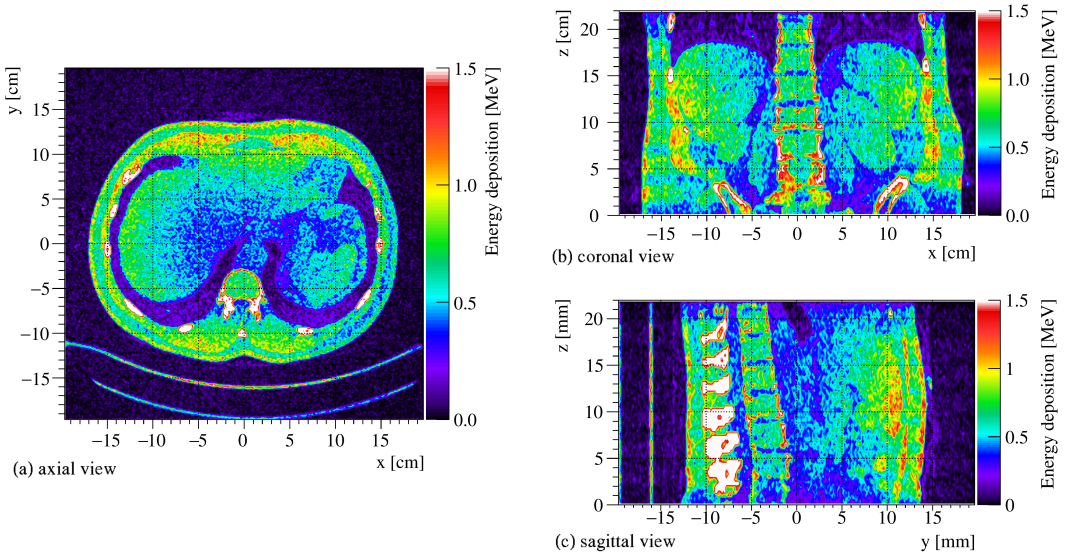

Figure 3.18: Axial (a), coronal (b), and sagittal (c) energy deposition map for patient 3A. Simulated non-enhanced acquisition (ψ_I = 0.000) at 80 kV_p, with the spiral acquisition mode (pitch = 1.0), tube current modulation enabled. Voxel size: 1.54 x 1.54 x 3 mm^3. Original computed tomography images for the presented maps are shown in figure I.1.

enhanced 80 kV_p-acquisition, especially at the center of the abdomen.
The difference maps in figure 3.19, third row, show that the differences in energy deposition between simulations of enhanced and non-enhanced acquisitions (for the enhanced tissues) increased slightly with increasing tube potential. The difference between the results of the 80 kV_p- and the 120 kV_p-setting was considerably higher than the differences between the results of the 100 kV_p- and the 120 kV_p-setting.
For the simulated 80 kV_p-acquisition, mean photon ranges were shorter, which lowered the energy deposition at the center of the patient compared to the 120 kV_p-setting (difference between tube potentials visible in the bottom row), similar to the energy deposition in the modified abdomen phantom, see section 3.3.1. The difference in energy deposition at the center of the patient was smaller between 100 and 120 kV_p.

Total energy deposition in patient 2A for the different tube potentials is presented in table 3.9 for the organs and tissues. Energy deposition in the enhanced tissues increased by ~+38% for the liver and up to ~+50% for the pancreas (refer to table 3.9). Energy deposition decreased in non-enhanced soft tissue, bones, skin, and fat by approximately -3%.
The higher the tube potential, the higher the energy deposition in all tissues, except for the skin. Here, energy deposition was highest at 80 kV_p due to the higher number of low-energy photons in the 80 kV_p-spectrum (difference of +4.5% compared to the skin deposition at 120 kV_p). The mean spectral energy of the initial photons directed towards the patient was ~20% lower for the 80 kV_p- compared to the 120 kV_p-spectrum.
The largest differences between the simulated 120 kV_p- and 80 kV_p-acquisition were found in the pancreas and the aorta (~+30%), which are both organs/tissues positioned centrally in the patient. Differences between these tube potentials were lower in the organ periphery (spleen ~+14%, soft tissue ~+6%). In the total patient, energy deposition at 120 kV_p was ~10% higher than at 80 kV_p.

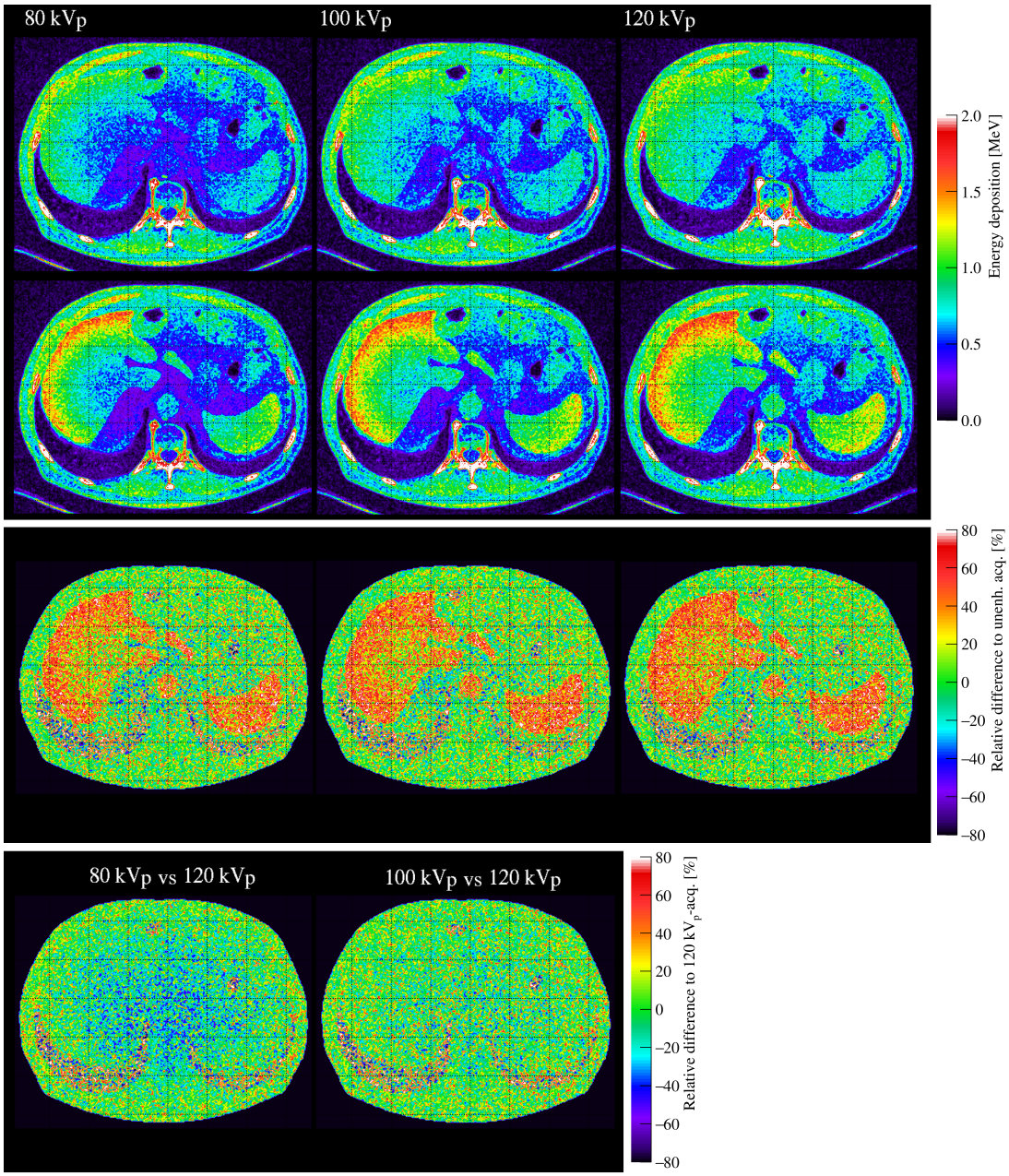

Figure 3.19: Evaluation P-I: Simulated energy deposition in patient 2A at 80, 100, and 120 kV_p. Energy deposition for simulated non-enhanced acquisitions (top row), for simulated enhanced acquisitions (second row), relative difference in energy deposition between simulated enhanced and non-enhanced acquisitions (third row). Left: 80 kV_p-, middle: 100 kV_p-, right: 120 kV_p-simulation. Fourth row: relative difference in $E_{spatial}$ between the simulated acquisition at 80 and 120 kV_p (left) and between the simulated acquisition at 100 and 120 kV_p (right), relative difference shown for simulated non-enhanced acquisitions. Contrast-enhanced tissues: aorta, liver, spleen, kidneys, and pancreas (ψ_I = 0.005). Original axial computed tomography image shown in figure I.2b.

Table 3.9: Evaluation P-I: Simulated energy deposition in patient 2A for non-enhanced and enhanced computed tomography acquisitions at 80, 100, and 120 kV_p. The simulation covered the liver, spleen, pancreas, and kidneys with an additional scan range of 36 mm in cranio-caudal direction. Contrast-enhanced tissues: aorta, liver, spleen, kidneys, and pancreas ($\psi_I = 0.005$).

Simulated energy deposition [GeV]								**Whole organ**			
	Total patient	**Soft tissue**	**Bone**	**Skin**	**Fat**	**Heart**	**Aorta**	**Liver**	**Spleen**	**Kidneys**	**Pancreas**
Simulated non-enhanced acquisition											
80 kV_p	1768.48	304.22	178.68	110.27	522.19	9.12	8.87	145.62	18.38	28.31	3.75
100 kV_p	1855.30	313.90	187.73	106.13	564.61	10.04	10.38	157.68	19.67	31.88	4.30
120 kV_p	1937.98	324.01	193.00	105.56	604.18	10.73	11.48	167.08	20.76	34.62	4.75
Simulated enhanced acquisition											
80 kV_p	1810.26	298.49	173.79	109.61	509.96	8.61	12.79	195.48	26.66	39.77	5.45
100 kV_p	1908.75	307.18	182.24	105.56	551.24	9.53	15.20	217.11	29.24	45.94	6.45
120 kV_p	1997.38	316.95	187.60	104.81	589.94	10.24	16.80	231.22	30.92	50.08	7.12
Relative difference to non-enhanced acquisition [%]											
80 kV_p	2.36	-1.88	-2.74	-0.60	-2.34	-5.58	44.20	34.24	45.03	40.44	45.45
100 kV_p	2.88	-2.14	-2.92	-0.54	-2.37	-5.05	46.41	37.69	48.68	44.10	49.92
120 kV_p	3.07	-2.18	-2.80	-0.71	-2.36	-4.62	46.33	38.39	48.94	44.65	49.83

3.4.2 EVALUATION P-II: ENERGY BUILD-UP EFFECT AT MATERIAL INTERFACES IN A DIGITIZED PATIENT – WHOLE PATIENT

In the following subsection, the the energy build-up effect at material interfaces in the digitized patient is evaluated (see section 2.5.4.3), as was performed for the modified abdomen phantom. Total energy deposition in patient 2A for the different tube potentials is presented in table 3.10 for the surrounding organ and tissue shells. Taking only the organ and surrounding tissue shells in to account, energy deposition increased considerably for the liver (~+44%, see table 3.10).

The build-up effect was assessed in the liver, spleen, and kidneys. Due to the size and structure of the pancreas, the shell structure could not be implemented. Interface ratios between the organ shells and the surrounding tissue shells are presented in table 3.11 for patient 2A and tube potentials of 80, 100, and 120 kV_p. The clear trend of an increasing ratio with decreasing tube potential, which was noted in the box phantom and the modified abdomen phantom, was also noticeable for the digitized patient. For simulations of non-enhanced acquisitions, ratios ranged between 1.13 and 1.33, whereas for simulations of enhanced acquisitions, ratios ranged between 1.70 and 2.03.

Table 3.10: Evaluation P-II: Simulated energy deposition in organ and surrounding soft tissue shells for patient 2A at 80, 100, and 120 kV_p. The simulation covered the liver, spleen, pancreas, and kidneys with an additional scan range of 36 mm in cranio-caudal direction. Contrast-enhanced tissues: aorta, liver, spleen, kidneys, and pancreas (ψ_I = 0.005).

Simulated energy deposition [GeV]						
	Organ shell			**Surrounding tissue shell**		
	Liver	**Spleen**	**Kidneys**	**Liver**	**Spleen**	**Kidneys**
Simulated non-enhanced acquisition						
80 kV_p	17.26	3.35	6.43	15.91	2.66	5.36
100 kV_p	18.29	3.58	7.21	16.83	2.88	6.12
120 kV_p	19.06	3.74	7.81	17.69	3.09	6.75
Simulated enhanced acquisition						
80 kV_p	24.69	4.95	9.10	15.26	2.58	5.04
100 kV_p	26.37	5.36	10.44	16.19	2.83	5.85
120 kV_p	27.55	5.62	11.34	17.07	3.03	6.53
Relative difference to non-enhanced acquisition [%]						
80 kV_p	43.01	47.83	41.50	-4.07	-2.98	-6.05
100 kV_p	44.21	49.87	44.68	-3.82	-1.69	-4.28
120 kV_p	44.58	50.26	45.10	-3.50	-1.86	-3.18

Table 3.11: Evaluation P-II: Interface ratios calculated from normalized energy depositions (per voxel) in the shells for patient 2A at 80, 100, and 120 kV_p. The simulation covered the liver, spleen, pancreas, and kidneys with an additional scan range of 36 mm in cranio-caudal direction. Contrast-enhanced tissues: aorta, liver, spleen, kidneys, and pancreas ($\psi_I = 0.005$).

	Interface ratio (organ shell / surrounding tissue shell)		
	Liver	**Spleen**	**Kidneys**
Simulated non-enhanced acquisition			
80 kV_p	1.141	1.330	1.320
100 kV_p	1.142	1.312	1.297
120 kV_p	1.133	1.281	1.273
Simulated enhanced acquisition			
80 kV_p	1.701	2.026	1.987
100 kV_p	1.713	2.000	1.961
120 kV_p	1.697	1.961	1.908

3.4.3 EVALUATION P-III: ENERGY BUILD-UP EFFECT AT MATERIAL INTERFACES IN A DIGITIZED PATIENT – AXIAL SLICE

The build-up effect at material interfaces was furthermore assessed for an axial slice through the liver and kidneys in patient 1A (see figures 3.20 and I.2a, and section 2.5.4.4). This slice, especially the liver, resembled the chosen slice of the modified abdomen phantom.

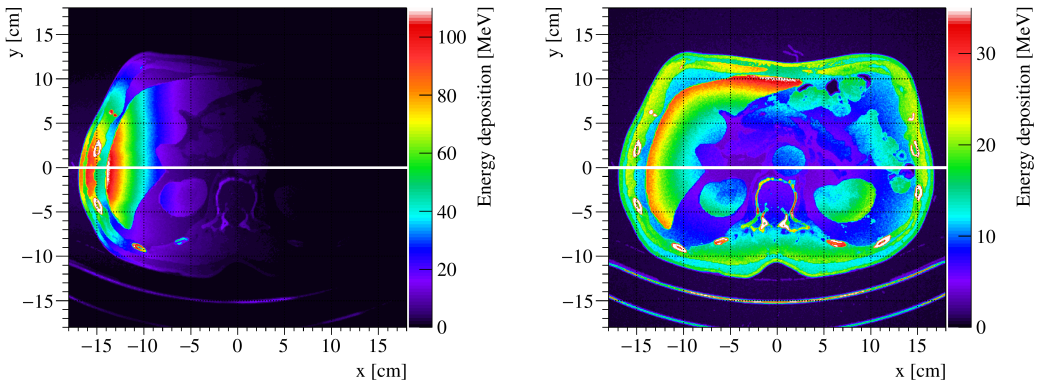

(a) Projection at 270° (b) 360°-rotation

Figure 3.20: Evaluation P-III: Simulation of an enhanced acquisition of a single slice of patient 1A at 80 kV_p. Profiles along the x-axis are presented in figures 3.21-3.24. Energy deposition was scored in the air for this setup, hence energy deposition outside the patient is non-zero. Contrast-enhanced tissues: aorta, liver, spleen, kidneys, and pancreas ($\psi_I = 0.005$). The original computed tomography image of the presented axial slice is shown in figure I.2a. Please note the different scaling of the color bars.

Energy deposition and relative difference in energy deposition between simulations of enhanced and non-enhanced acquisitions in the ROIs depicted in figures 2.23a-2.23d are presented in table 3.12 for the simulation of the full source rotation around the digitized patient. Comparing the energy deposition between the simulated enhanced and non-enhanced acquisition, energy deposition increased considerably in the liver ROI (~+57% for ROI 2a, 34-41% for ROI 2b). A slight increase was noted in ROI 1 (~+1%) and a decrease noted in ROI 3 (~-10-14%). For all interfaces, ratios decreased with increasing tube potential. The interface ratio 2a/1 ranged between 1.47 and 1.52 for the non-enhanced setting, and between 2.27 and 2.35 for the enhanced setting. Whereas the ratios of the modified abdomen phantom and the digitized patient were similar for the simulated non-enhanced acquisitions, ratios for the simulated enhanced acquisitions were slightly higher for the digitized patient. The interface ratio 2b/3 ranged between 1.36 and 1.42 for the simulated non-enhanced acquisition, and between 2.11 and 2.23 for the simulated enhanced acquisition. In both the non-enhanced and the enhanced setting, ratios were slightly lower compared to the interface ratios 2b/3 for the modified abdomen phantom.

Table 3.12: Evaluation P-III: Energy deposition and relative difference in energy deposition between simulated enhanced and non-enhanced acquisitions for the regions of interest (ROIs) depicted in figures 2.23a-2.23d at 80, 100, and 120 kV_p, for the simulation of the full source rotation in patient 1A. Energy deposition and relative differences were determined from placing ROIs on calculated 2D-energy/difference maps. For calculation of interface ratios, energy deposition in the ROIs was normalized to the number of pixels in the ROI. ROI 1 and ROI 3 are positioned in the surrounding tissue, ROI 2a and ROI 2b in the liver.

Simulated energy deposition [MeV]					**Interface ratio**	
	ROI 1	**ROI 2a**	**ROI 2b**	**ROI 3**	**2a/1**	**2b/3**
Simulated non-enhanced acquisition						
80 kV_p	14.11	18.31	11.81	8.68	1.517	1.421
100 kV_p	14.27	18.23	12.44	9.42	1.492	1.379
120 kV_p	14.69	18.42	13.06	10.07	1.465	1.355
Simulated enhanced acquisition						
80 kV_p	14.28	28.71	16.11	7.53	2.350	2.234
100 kV_p	14.47	28.77	17.60	8.45	2.323	2.176
120 kV_p	14.83	28.84	18.53	9.16	2.274	2.111
Relative difference to non-enhanced acquisition [%]						
80 kV_p	1.14	57.03	34.17	-13.95		
100 kV_p	1.48	58.12	39.90	-10.79		
120 kV_p	0.87	56.89	40.70	-9.31		

Again, profiles were plotted along the central x-axis of the axial energy map, for the single 270°-projection (source position at 9 o'clock, cf. figure 3.20a and figures 3.21-3.22) and for the full source rotation (see figure 3.20b and figures 3.23-3.24). For both simulations of non-enhanced and enhanced acquisitions of the projection, energy deposition at the entrance side of the digitized patient was highest at 80 kV_p, whereas only small differences were visible between 100 and 120 kV_p. The higher energy deposition of the simulated 80 kV_p-acquisition was clearly visible in the skin and soft tissue layer between x = -17 and x = -15 cm. When entering the visceral fat layer (at x = -15 cm) between the outer soft tissue layer and the liver tissue layer, energy deposition was highest for the simulated 120 kV_p-acquisition. The profile of the 80 kV_p-setting had the steepest gradient in the liver tissue. At the entrance of the liver, energy deposition was highest at 80 kV_p, whereas it was lowest towards the center of the digitized patient. This pattern was also visible in the modified abdomen phantom.

For the full source rotation, energy deposition in the skin was highest at 80 kV_p for both the simulated non-enhanced and the enhanced acquisition. For the subcutaneous fat and the soft tissue following the subcutaneous fat, energy deposition for all spectra was too noisy to determine the tube potential reaching maximum energy deposition. For the patient center (visceral fat, liver tissue, aorta, and GI-tract) from approximately x = -15 to x = +15 cm), energy deposition was highest for the simulated 120 kV_p-acquisition. Although all profiles follow the same pattern, there was an offset of the 80 kV_p-profile relative to the 100 kV_p- and 120 kV_p-profile, especially at the patient center.

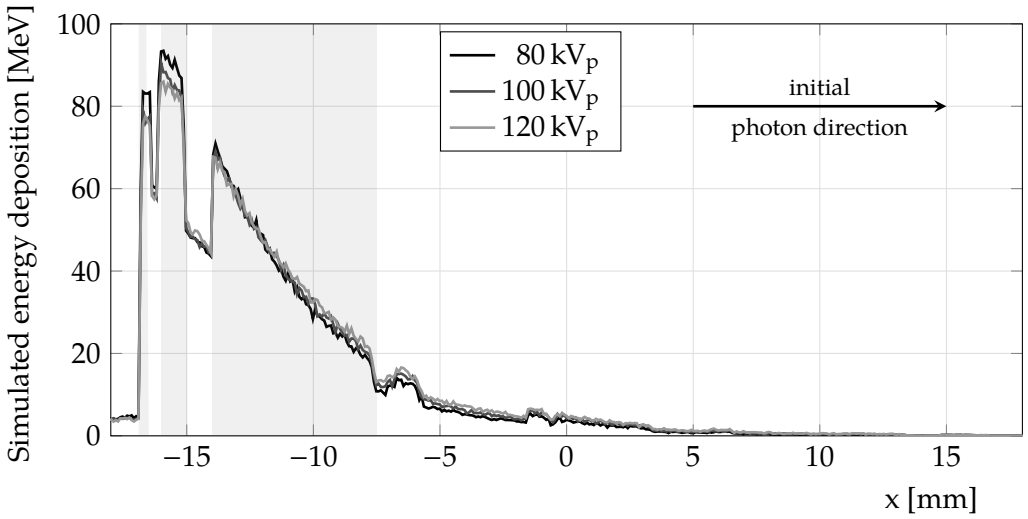

Figure 3.21: Evaluation P-III: Central x-axis profile through the 2D-energy map of a lateral projection at 80, 100, and 120 kV_p for the simulated *non-enhanced* acquisition. The following materials are traversed from left (x = -17 cm) to right (x = +17 cm) and visible on the profile: air, skin (shaded area, left), subcutaneous fat, soft tissue (shaded area, middle), visceral fat, liver (shaded area, right), visceral fat, gall bladder, visceral fat, aorta, visceral fat, GI-tract, visceral fat, soft tissue, subcutaneous fat, and the skin. Please note the different vertical axis scaling in the profiles in figures 3.21-3.22.

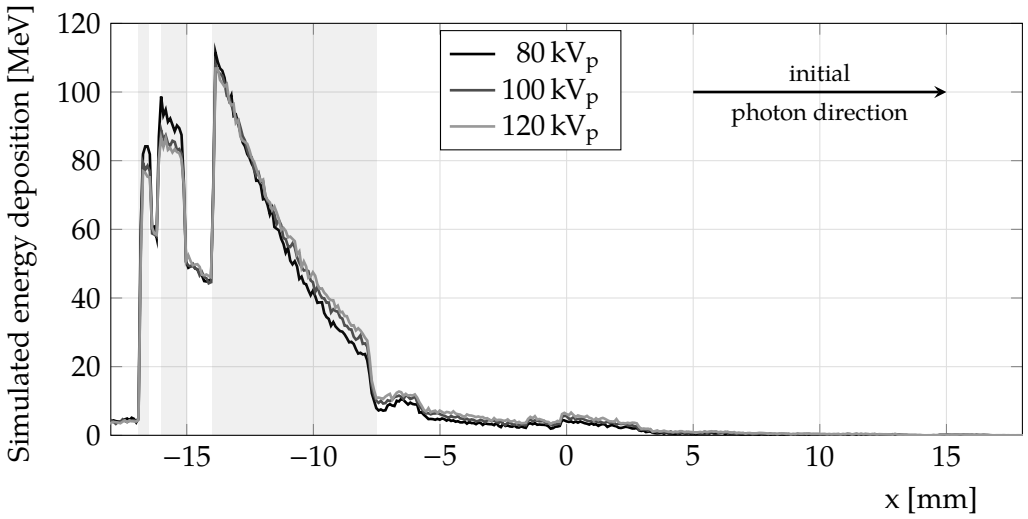

Figure 3.22: Evaluation P-III: Central x-axis profile through the 2D-energy map of a lateral projection at 80, 100, and 120 kV_p for the *enhanced* acquisition. The following materials are traversed from left (x = -17 cm) to right (x = +17 cm) and visible on the profile: air, skin (shaded area, left), subcutaneous fat, soft tissue (shaded area, middle), visceral fat, liver (shaded area, right), visceral fat, gall bladder, visceral fat, aorta, and visceral fat. Contrast-enhanced tissues: aorta, liver, spleen, kidneys, and pancreas ($\psi_I = 0.005$). Please note the different vertical axis scaling in the profiles in figures 3.21-3.22.

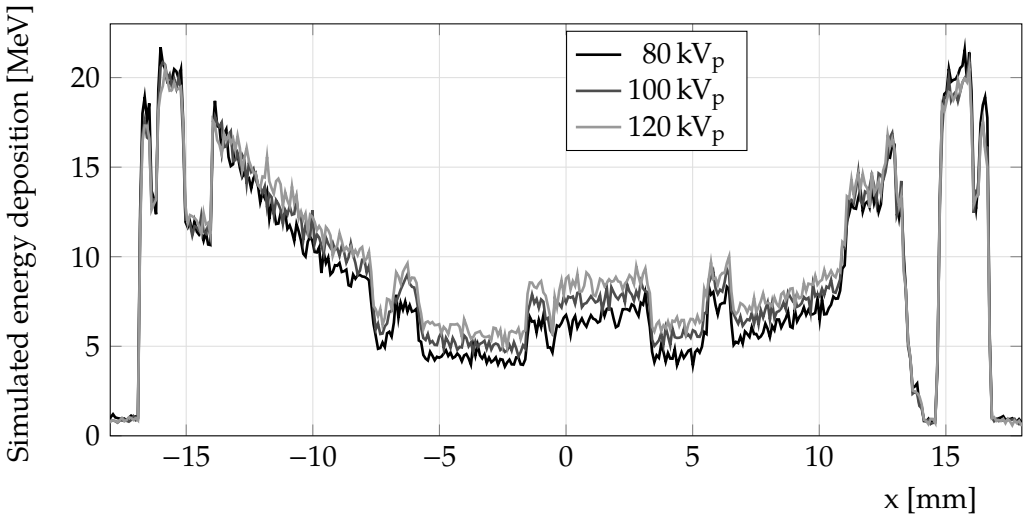

Figure 3.23: Evaluation P-III: Central x-axis profile through the 2D-energy map for a full source rotation at 80, 100, and 120 kV_p for the simulated *non-enhanced* acquisition. The following materials are traversed from left (x = -17 cm) to right (x = +17 cm) and visible on the profile: air, skin, subcutaneous fat, soft tissue, visceral fat, liver, visceral fat, gall bladder, visceral fat, aorta, and visceral fat. Please note the different vertical axis scaling in the profiles in figures 3.23-3.24.

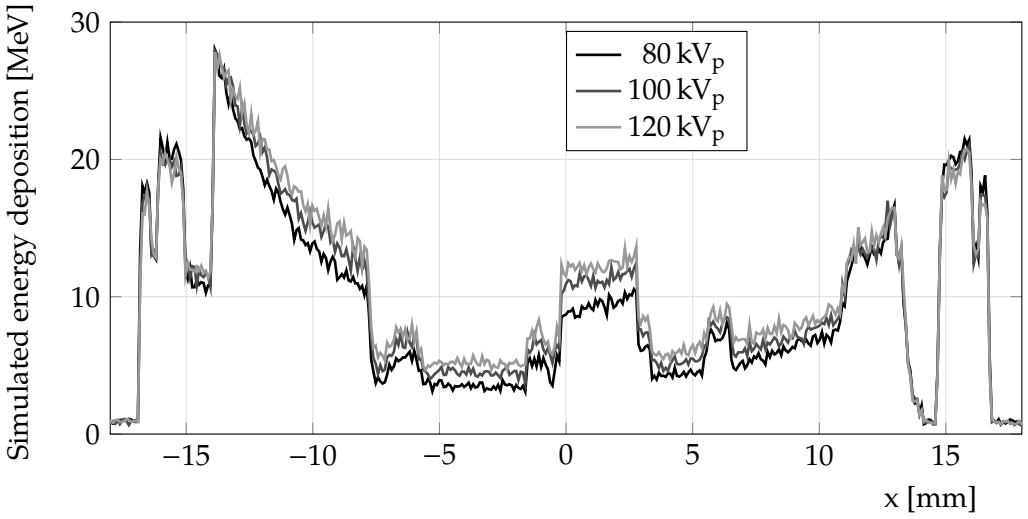

Figure 3.24: Evaluation P-III: Central x-axis profile through the 2D-energy map for a full source rotation at 80, 100, and 120 kV_p, for the simulated *enhanced* acquisition. The following materials are traversed from left (x = -17 cm) to right (x = +17 cm) and visible on the profile: air, skin, subcutaneous fat, soft tissue, visceral fat, liver, visceral fat, gall bladder, visceral fat, aorta, visceral fat, GI-tract, visceral fat, soft tissue, subcutaneous fat, and the skin. Contrast-enhanced tissues: aorta, liver, spleen, kidneys, and pancreas (ψ_I = 0.005). Please note the different vertical axis scaling in the profiles in figures 3.23-3.24.

3.4.4 EVALUATION P-IV: INFLUENCE OF BMI AND MORPHOLOGY ON THE ENERGY DEPOSITION AND ITS SPATIAL DISTRIBUTION IN DIGITIZED PATIENTS

The influence of the patient morphology and BMI on energy deposition and its spatial distribution was assessed (see section 2.5.4.5 and figure I.3). Figure 3.25 presents the energy deposition maps of all patients for the simulated contrast-enhanced acquisitions at 80 kV_p, for the same abdominal slices as are presented in figure I.3. An abdominal slice where both kidneys and the liver were visible was chosen, although the shape of the organs differed considerably among the patients. Note that the spleen was still visible for patient 1B on this slice, and that the shape and position of the aorta deviated from the other patients.
The total energy deposition in the tracked tissues is presented in tables 3.13-3.14. The incoming number of photons was dependent on the scan range and $TCTP_{eff}$. There was no clear trend for the relative difference between simulations of enhanced and non-enhanced acquisitions with respect to BMI, shape, or diameter of the patients.
Normalizing the tissue energy deposition to the initially emitted photon energies revealed a trend in the fat tissue and the aorta. For patients 2A and 3B (effective diameter, D_{eff} >32.5 cm), the relative energy deposition in fat tissue amounted to approximately 15%, whereas this value amounted only to 10% for patients 1A, 1B, and 2B (D_{eff} <28.8 cm, 13% for patient 3A, D_{eff} = 30.5 cm). For the centrally positioned aorta, relative energy deposition ranged between 0.6% and 1.0% for patients 1A, 1B, and 2B, whereas this value only amounted to 0.3-0.5% for patients 2A, 3A, and 3B.

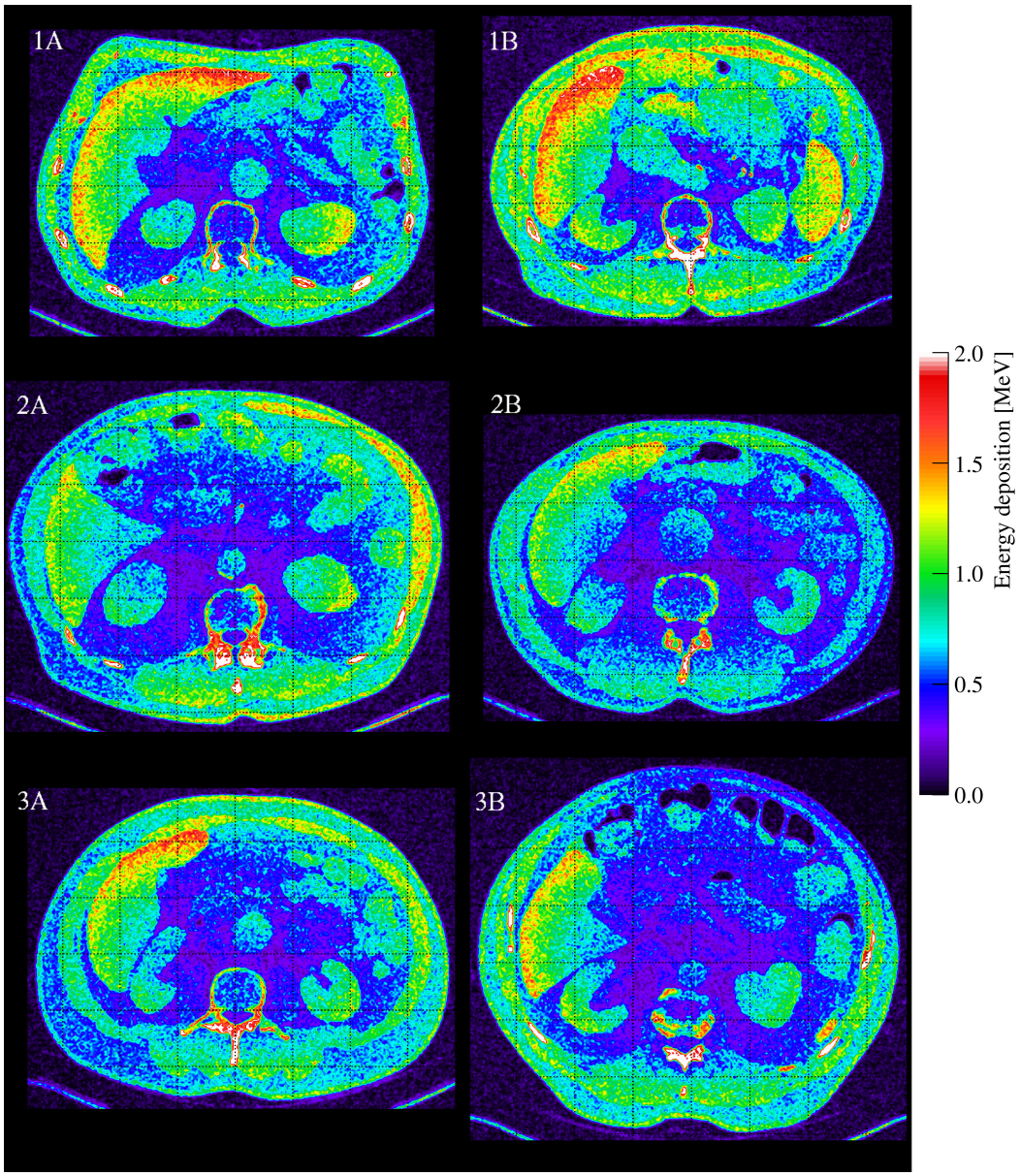

Figure 3.25: Evaluation P-IV: Simulated energy deposition for all patients within an axial slice through the abdomen at 80 kV_p. The energy map of the simulated contrast-enhanced acquisition was printed. Contrast-enhanced tissues: aorta, liver, spleen, kidneys, and pancreas ($\psi_I = 0.005$). The original computed tomography images of the presented axial slice are shown in figure I.3.

Table 3.13: Evaluation P-IV: Comparison of the simulated energy deposition in patients 1A, 2A, and 3A at 80 kV_p. The simulations covered the liver, spleen, pancreas, and kidneys with an additional scan range of 36 mm in cranio-caudal direction. $3 \cdot 10^6$ photons per cm scan coverage were initialized. Resulting photon statistics: patient 1A: $59.40 \cdot 10^6$, patient 2A: $69.66 \cdot 10^6$, and patient 3A: $66.70 \cdot 10^6$. Longitudinal tube-current modulation was applied. Contrast-enhanced tissues: aorta, liver, spleen, kidneys, and pancreas ($\psi_I = 0.005$).

Simulated energy deposition [GeV]											
								Whole organ			
	Total patient	**Soft tissue**	**Bone**	**Skin**	**Fat**	**Heart**	**Aorta**	**Liver**	**Spleen**	**Kidneys**	**Pancreas**
Patient 1A											
Non-enhanced	1406.57	235.45	132.59	80.18	290.70	25.74	17.63	141.43	13.99	20.95	4.11
Enhanced	1447.82	228.39	128.35	79.51	282.48	24.59	23.70	190.20	20.59	30.14	6.08
Rel. diff. [%]	2.93	-3.00	-3.20	-0.83	-2.83	-4.46	34.45	34.48	47.21	43.85	47.94
Patient 2A											
Non-enhanced	1768.48	304.22	178.68	110.27	522.19	9.12	8.87	145.62	18.38	28.31	3.75
Enhanced	1810.26	298.49	173.79	109.61	509.96	8.61	12.79	195.48	26.66	39.77	5.45
Rel. diff. [%]	2.36	-1.88	-2.74	-0.60	-2.34	-5.58	44.20	34.24	45.03	40.44	45.45
Patient 3A											
Non-enhanced	1671.69	348.59	164.26	109.50	403.94	15.76	11.73	197.86	30.59	26.67	5.84
Enhanced	1720.85	337.62	157.08	108.37	392.82	14.85	16.06	259.24	43.58	36.78	7.84
Rel. diff. [%]	2.94	-3.15	-4.38	-1.03	-2.75	-5.76	36.91	31.02	42.44	37.90	34.14

Table 3.14: Evaluation P-IV: Comparison of the simulated energy deposition in patients 1B, 2B and, 3B at 80 kV_p. The simulations covered the liver, spleen, pancreas, and kidneys with an additional scan range of 36 mm in cranio-caudal direction. $3 \cdot 10^6$ photons per cm scan coverage were initialized. Resulting photon statistics: patient 1B: $62.70 \cdot 10^6$, patient 2B: $58.17 \cdot 10^6$, and patient 3B: $62.34 \cdot 10^6$. Longitudinal tube-current modulation was applied. Contrast-enhanced tissues: aorta, liver, spleen, kidneys, and pancreas ($\psi_I = 0.005$).

Simulated energy deposition [GeV]											
								Whole organ			
	Total patient	**Soft tissue**	**Bone**	**Skin**	**Fat**	**Heart**	**Aorta**	**Liver**	**Spleen**	**Kidneys**	**Pancreas**
Patient 1B											
Non-enhanced	1461.5	250.1	143.2	97.6	293.0	12.3	21.2	149.8	25.3	23.5	2.5
Enhanced	1510.6	241.6	138.6	96.8	285.9	11.7	29.0	201.3	37.1	33.0	3.8
Rel. diff. [%]	3.36	-3.39	-3.26	-0.85	-2.43	-4.90	36.98	34.35	46.97	40.72	48.33
Patient 2B											
Non-enhanced	1435.7	357.0	121.5	92.0	245.0	15.5	21.3	175.5	20.0	33.8	6.4
Enhanced	1485.5	344.6	116.5	91.2	236.7	14.6	28.6	232.9	28.7	46.8	8.6
Rel. diff. [%]	3.46	-3.49	-4.13	-0.91	-3.38	-5.95	34.52	32.65	43.31	38.62	33.76
Patient 3B											
Non-enhanced	1587.4	224.8	131.7	101.2	458.2	17.9	9.3	119.5	18.1	26.0	3.0
Enhanced	1623.9	220.4	128.1	100.6	448.1	16.9	13.4	160.3	26.5	36.8	4.3
Rel. diff. [%]	2.30	-1.98	-2.73	-0.59	-2.21	-5.66	44.85	34.13	46.26	41.62	44.99

Table 3.15: Evaluation P-V: Simulated energy deposition in the skin and in the patients (all organs/tissues) in a 102 mm scan region of the abdomen, and relative differences between simulated acquisitions at 80 and 120 kV_p.

	Simulated energy deposition in skin [GeV]		**Rel. diff. to 120 kV_p**	**Simulated energy deposition in patient [GeV]**		**Rel. diff. to 120 kV_p**
ID	**80 kV_p**	**120 kV_p**	**[%]**	**80 kV_p**	**120 kV_p**	**[%]**
1A	46.2	44.8	3.16	818.6	891.1	-8.13
1B	57.4	55.3	3.95	878.8	956.3	-8.10
2A	54.8	52.4	4.74	893.8	988.0	-9.54
2B	44.3	42.8	3.63	698.3	767.7	-9.04
3A	55.6	53.4	4.08	850.1	938.6	-9.43
3B	55.7	53.1	4.83	891.6	981.3	-9.13

3.4.5 EVALUATION P-V: INFLUENCE OF TUBE POTENTIAL ON ENERGY DEPOSITION IN THE SKIN IN DIGITIZED PATIENTS

The influence of the tube potential on the energy deposition in the skin was compared for a 102 mm abdominal scan region (see section 2.5.4.6). The skin exposure for simulated acquisitions at 80 kV_p was maximum 4.8% higher than the skin exposure for simulations at 120 kV_p for the modified abdomen phantom and digitized patients for employing identical numbers of emitted photons for the 80 kV_p- and the 120 kV_p-setting per patient (see table 3.15). In contrast to the increase of ~4% total skin exposure, the total energy deposition in the patients (all tissues/organs) is reduced by ~9% for the 80 kV_p-setting compared to the 120 kV_p-setting, again employing identical numbers of emitted photons for the 80 kV_p- and the 120 kV_p-setting per patient. Relative to the total energy deposition in the scored scan region, skin energy deposition was ~7% at 80 kV_p and ~6% at 120 kV_p. Maximum differences in skin exposure between the six simulated patients were ~30% for both the simulated acquisition at 80 kV_p and at 120 kV_p.

3.5 ASSESSMENT OF THE VARIATION BETWEEN IDENTICAL MC SIMULATIONS AND EVALUATION OF THE SIMULATED NUMBER OF PHOTONS IN A DIGITIZED PATIENT

VARIATION BETWEEN TWO IDENTICAL SIMULATIONS WITH DIFFERENT INITIAL SEEDS

The variation between two identical simulated acquisitions with different initial seeds was less than 1% for complete organs (including the smallest tracked organ, the pancreas, see table 3.16) but considerably higher (up to 60%) for single voxels (1.5 x 1.5 x 3 mm^3, see figure 3.26). Differences ranged between ± 30% if the energy deposition was summed over multiple slices (1.5 x 1.5 x 9 mm^3 voxel size).

Table 3.16: Comparison of the energy deposition resulting from two identical simulations of a non-enhanced computed tomography acquisition with different initial seeds for patient 2A. Results presented for the total patient and the three organs/tissues with the highest relative differences in energy deposition between the two samples. Simulation parameters were: scan coverage of 15 cm (abdomen), $45{\cdot}10^6$ emitted photons, pitch 0.5, longitudinal tube-current modulation enabled.

Simulated energy deposition [GeV]	**Total patient**	**Pancreas**	**Spleen**	**Aorta**
Sample 1	1161.12	2.28	5.36	4.06
Sample 2	1161.06	2.26	5.37	4.05
Rel. diff. [%]	0.01	0.69	-0.10	0.08

REDUCTION OF THE PHOTON STATISTICS Figures 3.27-3.30 present the differences in normalized energy deposition between data sets with full photon statistics and data sets with reduced photon statistics, to assess the influence of a lower number of initially emitted photons on the obtained energy deposition (see section 2.6). Four different sets of histograms were produced: (1) for the whole volume of the abdomen (figure 3.27), (2) for the kidneys in the abdomen (figure 3.28), (3) for a single axial slice (figure 3.29), and (4) for the kidney tissue of that axial slice (figure 3.30).
The larger the number of entries, the lower the mean difference between data sets with full photon statistics and data sets with reduced photon statistics. The mean difference between the full statistics data sets and the reduced statistics data sets was zero in all four sets of histograms until only every 15th interaction was included in the reduced data sets. Reducing the included number of interactions further caused a shift of the mean, which was easily visible by the position of the peak of the Gaussian curve. The differences between full and reduced photon data increased while reducing the number of included interactions (larger tail towards positive differences) causing a poorer fit between the Gaussian curve and the histograms.
Depending on the volume of interest, the number of incident photons can be reduced without shifting the simulation results towards lower or higher energy depositions. All reduced data stacks contained identical distributions of interaction types (see figure J.1) and mean energies per interaction.

(a) DICOM image of corresponding axial slice 17

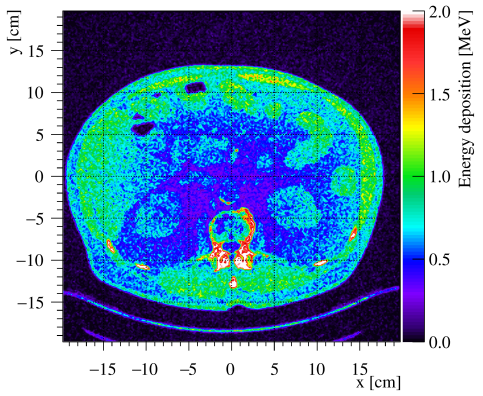

(b) 2D-energy map of sample 1 (1.5 x 1.5 x 3 mm^3, slice 17)

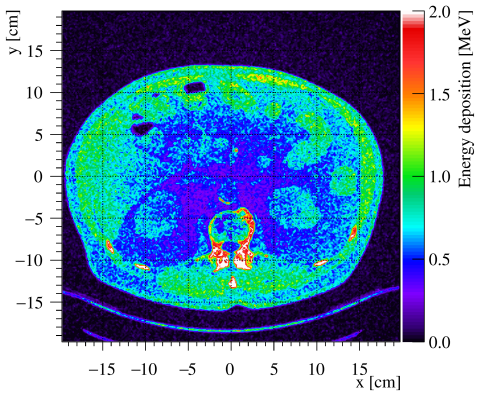

(c) 2D-energy map of sample 2 (1.5 x 1.5 x 3 mm^3, slice 17)

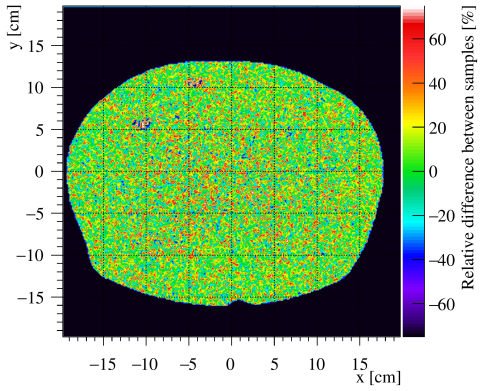

(d) Difference map for a single slice (1.5 x 1.5 x 3 mm^3, slice 17)

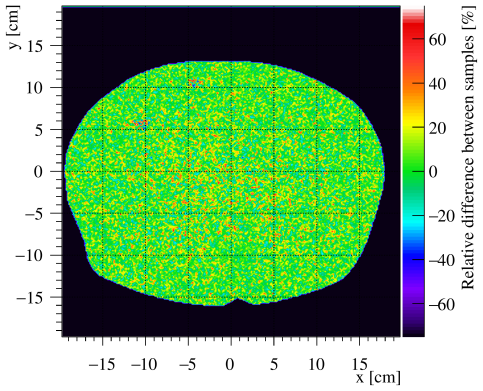

(e) Difference map for three adjacent slices (1.5 x 1.5 x 9 mm^3, slices 16-18)

Figure 3.26: Evaluation of the differences in energy deposition in a digitized patient between two identical simulations of computed tomography acquisitions with different initial seeds. (a) Anatomy of the evaluated axial slice number 17, (b) 2D-energy map of sample 1, (c) 2D-energy map of sample 2, (d) relative difference in energy deposition between sample 1 and sample 2 for a single axial slice (slice 17), and (e) for three adjacent slices (slices 16-18).

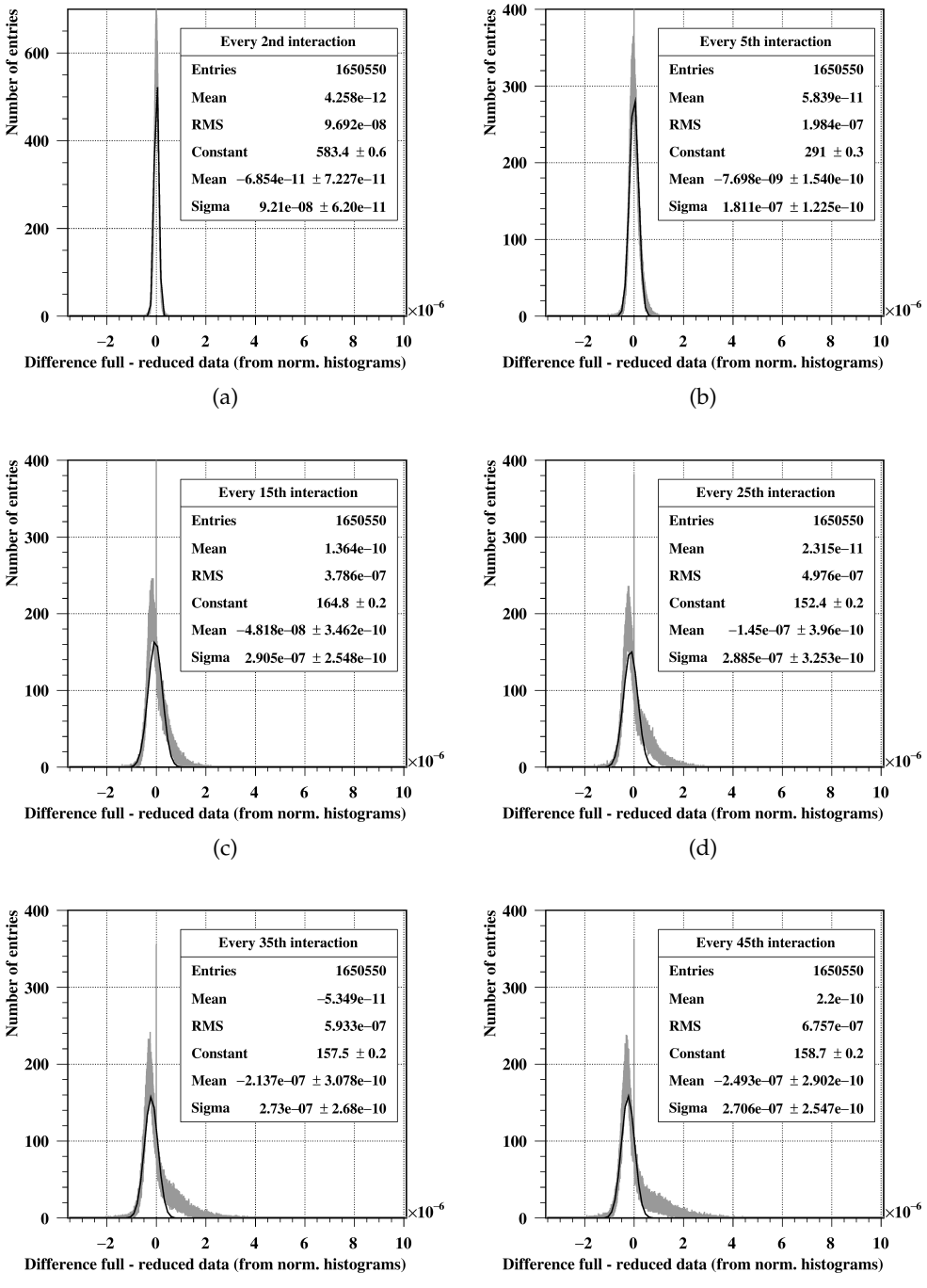

Figure 3.27: Abdomen: 3D-energy maps were created from all interactions and every second, fifth, tenth, and so on. Energy maps were normalized to the integral value 1. Normalized energy maps of the reduced photon statistics data set were subtracted from the normalized energy maps of the original data set with full photon statistics (containing the complete data) and differences were plotted in 1D-histograms. Furthermore, histograms have been fitted with a Gaussian curve.

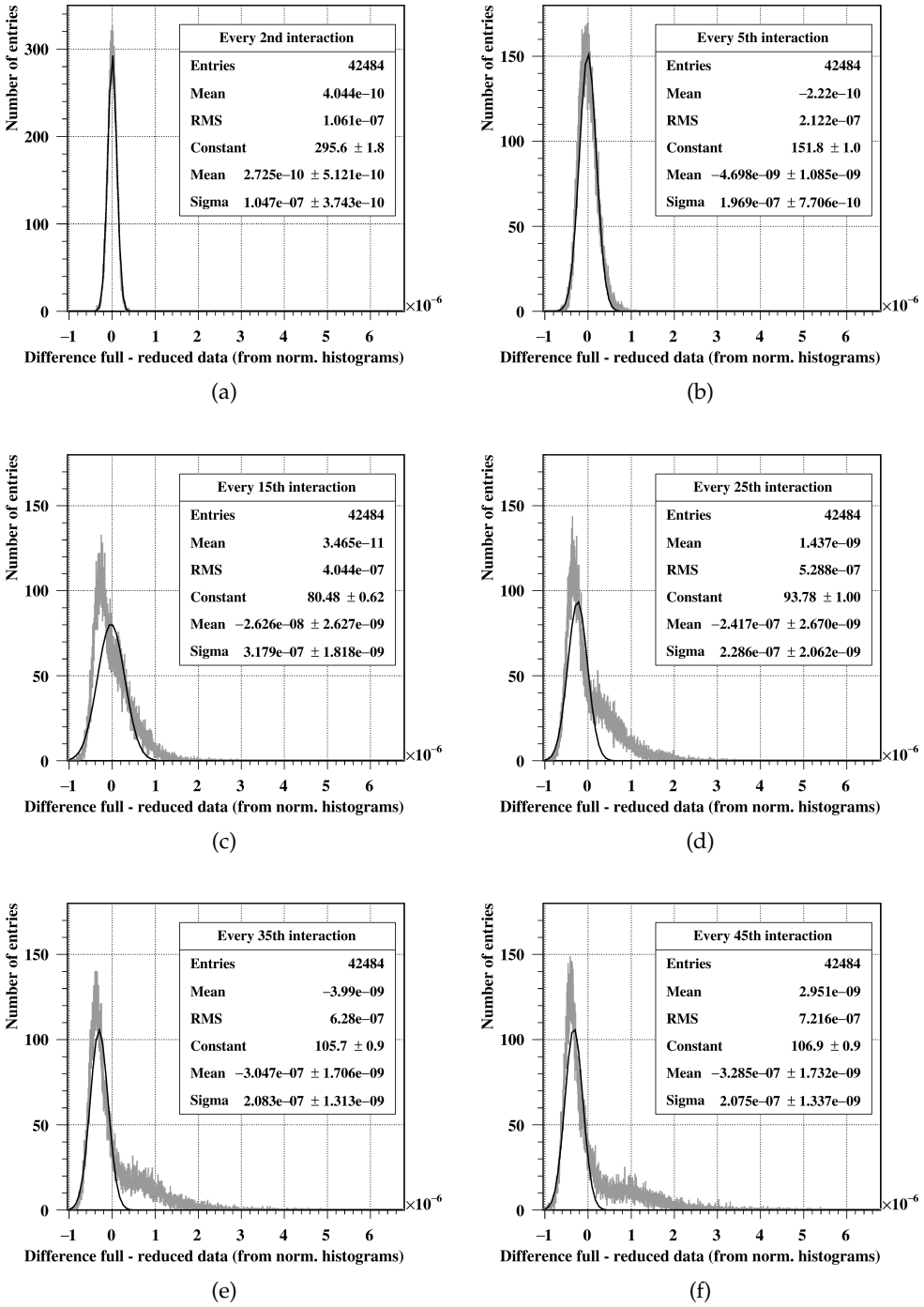

Figure 3.28: Kidneys: 3D-energy maps were created from all interactions and every second, fifth, tenth, and so on. Energy maps were normalized to the integral value 1. Normalized energy maps of the reduced photon statistics data set were subtracted from the normalized energy maps of the original data set with full photon statistics (containing the complete data) and differences were plotted in 1D-histograms. Furthermore, histograms have been fitted with a Gaussian curve.

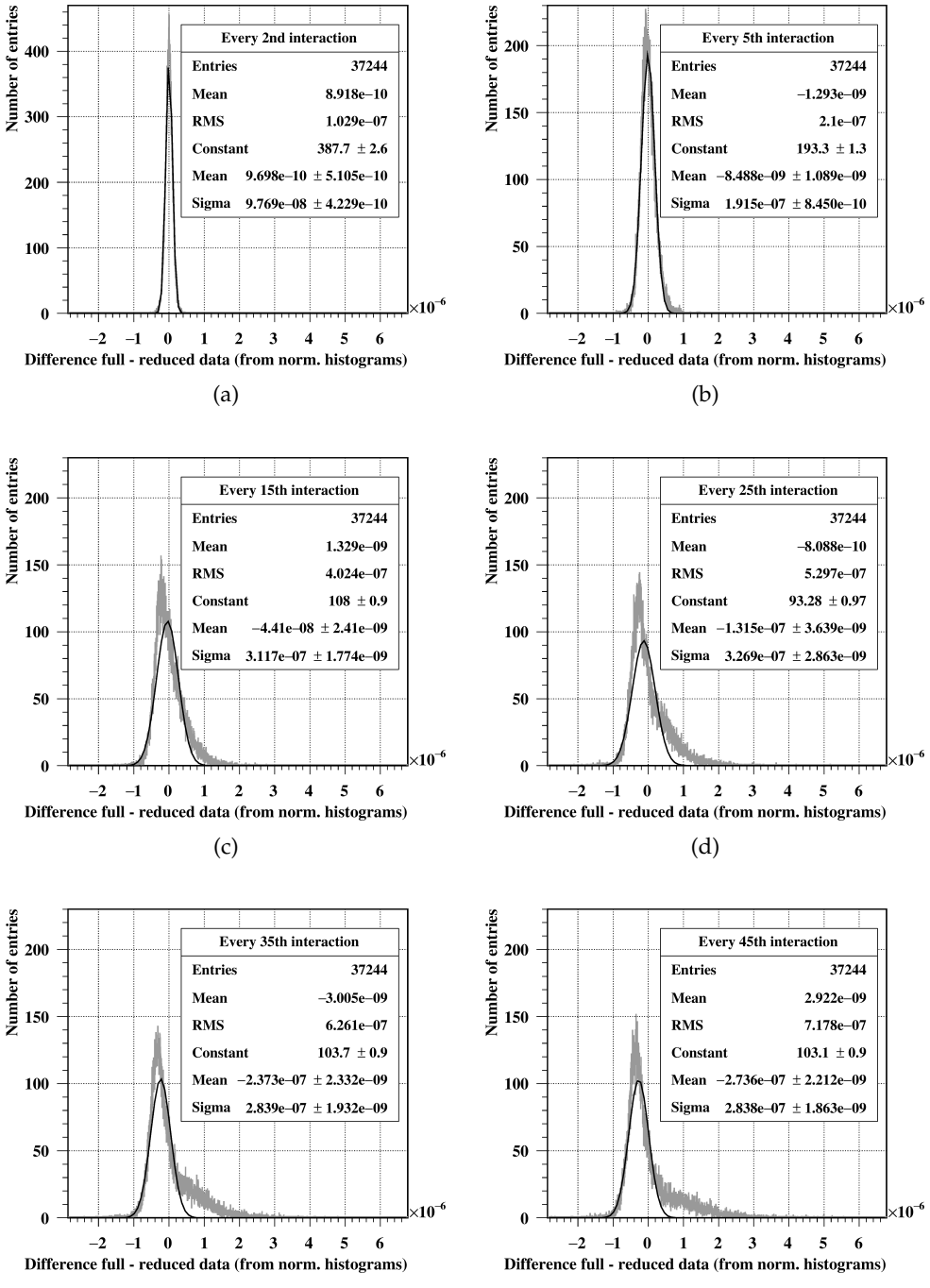

Figure 3.29: Axial slice: 3D-energy maps were created from all interactions and every second, fifth, tenth, and so on. Energy maps were normalized to the integral value 1. Normalized energy maps of the reduced photon statistics data set were subtracted from the normalized energy maps of the original data set with full photon statistics (containing the complete data) and differences were plotted in 1D-histograms. Furthermore, histograms have been fitted with a Gaussian curve.

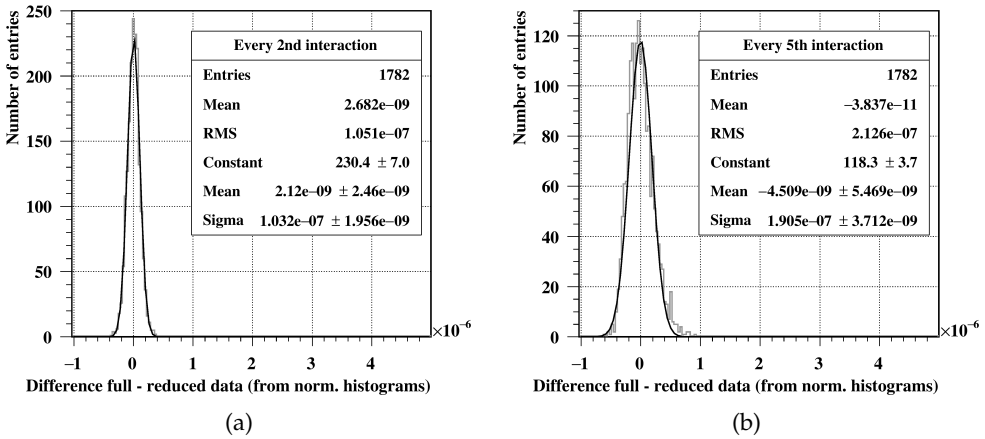

(a)

(b)

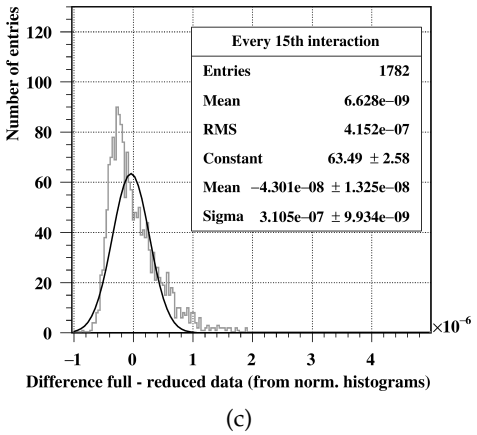

(c)

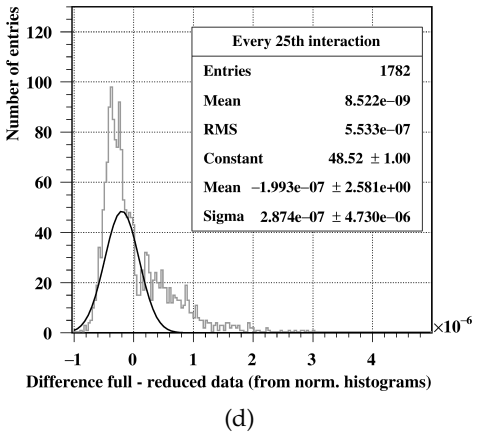

(d)

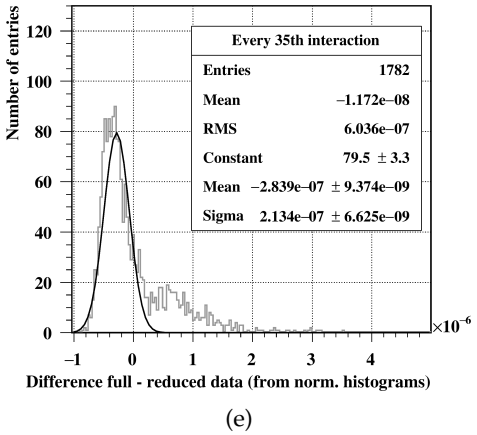

(e)

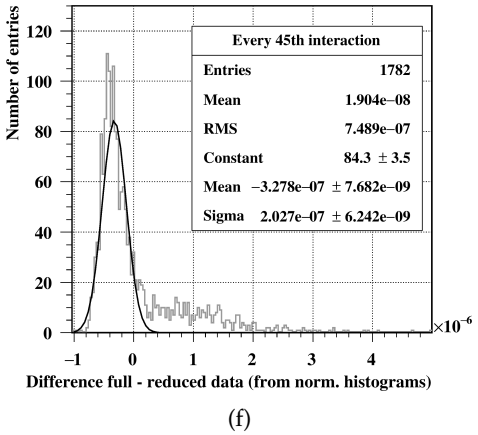

(f)

Figure 3.30: Kidney tissue in an axial slice: 3D-energy maps were created from all interactions and every second, fifth, tenth, and so on. Energy maps were normalized to the integral value 1. Normalized energy maps of the reduced photon statistics data set were subtracted from the normalized energy maps of the original data set with full photon statistics (containing the complete data) and differences were plotted in 1D-histograms. Furthermore, histograms have been fitted with a Gaussian curve.

4

DISCUSSION

Although only 9% of all diagnostic x-ray procedures in Germany in 2014 were computed tomography (CT) examinations, they contributed to the annual effective dose with 65%. The number and the resulting annual effective dose per capita of CT examinations have increased between 2007 and 2014 by 40% and 30%, respectively (BfS 2016b). High doses of ionizing radiation (>100 mSv) are known to be carcinogenic, however, the effects of lower doses (e.g. those occurring in diagnostic CT examinations) on the induction of tumors in different tissue types are still unclear (Hall and Brenner 2008). Hence, the increase in effective dose requires thorough understanding of the spatial dose distribution inside the human body and how this distribution is influenced by CT acquisition parameters, patient morphology, age, or the administration of contrast agents. Individualized dosimetry plays an increasing role in clinical radiology, especially for patients receiving multiple CT examinations over a short period of time, such as during a cancer treatment. Individualized dosimetry offers a precise evaluation of the radiation exposure, even for non-average sized or pediatric patients, where conversion factors fail. Furthermore, the increased sensitivity of pediatric patients to ionizing radiation requires surveillance, to allow for the execution of overdue long-term studies regarding the radiation dose of diagnostic procedures and their potential adverse effects.

Several MC-based dose calculators are available for the calculation of dose deposition in CT (Brady et al. 2012), such as ImPACT (ImPACT 2011) or ImpactDose (IBA Dosimetry 2009; Kalender et al. 1999a). Unfortunately, they are usually limited by restricted input options, such as the CT scanner system or predefined patient models, and by inflexible output and analysis options. Therefore, the goal of this work was the development and validation of a Monte Carlo (MC) software for the simulation of CT acquisitions, which offers the desired flexibility in both input and analysis options to approach virtual dosimetry.

The results of this work are discussed in the following. In section 4.1, the x-ray emission and beam-shaping methods employed in the developed MC model are discussed for 120 kV_p-equivalent photon distributions. Section 4.2 and section 4.3 discuss and contextualize the influence of the tube potential and iodinated contrast agents on energy deposition in organs and at tissue interfaces, respectively. The implemented geometrical abdomen and digitized patient phantoms and their design are reviewed in section 4.4. The number of tracked photons and the data output of the software are evaluated in section 4.5. Section 4.6 discusses the methodology of the developed software and the limitations of the results, and offers an outlook on future developments.

4.1 EVALUATION OF X-RAY EMISSION AND BEAM-SHAPING METHODS

The individual components of the developed MC software for the simulation of CT acquisitions and the determination of the associated radiation exposure in phantoms and digitized patients were first assessed to ensure proper functionality and efficiency of the MC model. This initial analysis also aimed at understanding the underlying physics processes of CT, the effects of beam-shaping filtration (photon fluence and beam-hardening), and the effects of different input photon distributions (monoenergetic photons, measured, or generated spectra) on the absorption of photons in matter (i.e. phantoms or patients). Photon absorption was described by means of the total energy deposition, E_{total}, and its spatial distribution, $E_{spatial}$.

BEAM-SHAPING METHOD Clinical CT scanners include one or more beam-shaping filters to equalize the measured signal in the detector and to reduce unnecessary radiation exposure in shorter patient x-ray path lengths near the edges of the fan beam. Two beam-shaping methods were implemented in the MC model.
At first, the *virtual* beam-shaping method was evaluated, which implemented both fan-angle dependent photon fluence and fan-angle dependent spectra (FADS). This method resulted in only 3% difference in $E_{spatial}$ compared to the results obtained by implementation of a *physical* beam-shaping filter (PBF, see figure 3.1). The advantage of the virtual method is the increased efficiency in computation time compared to the implementation of a PBF as the latter causes a photon loss prior to any interaction in a phantom due to the absorption inside the filter: more than twice the number of photons were necessary to obtain approximately equal numbers of photons impinging on the phantom (after filtration), thereby doubling the simulation time.
Omission of the beam-shaping effect of the filter caused relative differences in $E_{spatial}$ of up to 50% for the simulation of a full x-ray source rotation in the water phantom (see figure 3.2). Hence, a method for modulating photon fluence is required in a MC model of a CT scanner, independent of the emitted photon distribution. Due to the small differences in energy deposition in the phantom between the physical and the virtual filter (3%), and the considerably higher efficiency of the latter, the virtual beam-shaping method was employed during this work (Steuwe et al. 2018).

SPECTRAL PROPERTIES X-ray spectra are unique for a specific CT scanner's x-ray tube design in conjunction with specific beam filtration. Since experimentally measured x-ray spectra are not always available, this work evaluated the usage of different generated spectra and monoenergetic photons, corresponding to a tube potential of $120\,kV_p$ as alternatives and simplified approximations for measured spectra. The selected monoenergetic photon energy matched the mean energy of the experimentally measured 0°-spectrum, $E_{mean,ref}$.
Regarding E_{total} in the water phantom (see table 3.1), only subtle differences were visible between the usage of the measured 0°-spectrum and the generated (unfiltered and filtered) $120\,kV_p$-spectra and monoenergetic photons (max. 5%). Hence, considering only E_{total} in a phantom, even monoenergetic photons seem feasible as

approximation of the actual x-ray source's emitted spectrum (Steuwe et al. 2018).
Although differences in E_{total} were small when comparing results obtained with monoenergetic photons and the measured 0°-spectrum, differences in $E_{spatial}$ were considerably higher (± 20%). For monoenergetic photons, absorption at the center of the phantom was overestimated, whereas absorption was underestimated at the periphery of the phantom. The mean energy of a photon spectrum cannot approximate the absorption pattern of a polyenergetic photon distribution, since photons of lower and higher energy are not represented by monoenergetic photons.
For the generated unfiltered spectrum at 120 kV_p, $E_{spatial}$ was overestimated in the periphery, whereas it was underestimated at the center compared to the measured 0°-spectrum. The generated unfiltered spectrum is softer than the measured spectrum and thus contains more low-energy photons and less high-energy photons. Additional aluminum filtration reduced low-energy photons and shifted the total spectrum to a higher mean spectral energy. Hence, a matching peak tube potential and mean spectral energy results in $E_{spatial}$ close to the one of the measured 0°-spectrum (difference of only 3%).
The influence of different x-ray spectra, e.g. with varying tube potential and aluminum filtration, on the dose deposition within phantoms in- and outside the scan field was previously studied by Caon et al. (1998) and Boone et al. (2000). In line with the results of this work, they noticed an increasing dose deposition and deeper penetration of tissue layers with increasing filtration (Caon et al. 1998). However, in contrast to the current work, the detailed spatially resolved dose deposition was not investigated in their work.
The results obtained from the assessment of the influence of different photon distributions on E_{total} and $E_{spatial}$ emphasize the interchangeability of spectra for matching tube potential and mean spectral energy. The mean spectral energy of a CT x-ray source is easier measured than central or fan-angle dependent spectra. Both the peak tube potential and mean spectral energy can be measured with an accuracy of up to 2%, according to manufacturers (Cobia Flex, RTI, Mölndal Sweden, or with the Diavolt Universal All-in-one QC Meter, PTW, Freiburg, Germany). This accuracy is sufficient, when taking the differences in x-ray spectra between x-ray sources of different vendors into account (cf. figure 2.6), especially in the low energy range (Steuwe et al. 2018).

SPECTRAL DISTORTION DUE TO BEAM-SHAPING FILTRATION A beam-shaping filter results in spectral distortion of the primary emitted x-ray spectrum. Section 3.1.4 showed that spectral distortion should be included in a CT model for correct reproduction of x-ray emission and the precise and accurate calculation of E_{total} and $E_{spatial}$. Differences between the implementation of FADS and the implementation of solely the 0°-spectrum were 5% in $E_{spatial}$ for a full source rotation. Spectral distortion can be modeled by implementing fan-angle dependent spectra directly (as was performed during this work), by calculation of energy-dependent transmission and attenuation of photons (Jarry et al. 2003), or by employing a physical beam-shaping filter model (Steuwe et al. 2018).
Lopez-Rendon et al. (2014) assessed differences in deposited dose for simulations modeling the full beam-shaping effect (FM + FADS) and simulations employing

only the fan-angle dependent fluence (FM) without taking the spectral hardening into account. The largest differences between the full beam-shaping effect and only FM were noticed at the thickest parts of the beam-shaping filter, hence, towards the edges of the fan beam. The number of low-energy photons increased if only FM without spectral hardening was applied, whereas the number of high-energy photons decreased. Although Lopez-Rendon et al. (2014) only used computationally generated spectra, their results are in agreement with the results of the work presented here (Steuwe et al. 2018).

The initial analysis of the x-ray source emission has demonstrated that generated spectra can be employed as an alternative for measured spectra if peak tube potential and mean spectral energy match. Furthermore, the beam-shaping filter induced modulated photon fluence should be taken into account for modeling of clinical CT scanners (Steuwe et al. 2018).

4.2 INFLUENCE OF TUBE POTENTIAL ON THE ENERGY DEPOSITION AND THE DETECTOR SIGNAL

Since CT acquisitions are often performed at other tube potentials than 120 kV_p, depending on the indication, region of interest, and patient morphology, this work additionally evaluated the energy deposition and detector response for other diagnostic tube potentials.
To understand the principles of energy deposition for the different tube potentials, first, the shapes of the x-ray spectra at 80, 100, and 120 kV_p were compared, see figure 2.5. Although the spectra are very similar in the range between 20 and 80 keV, the range between 20 and 55 keV has a higher statistical occupation for the 80 kV_p-spectrum, whereas the range between 55 and 80 keV is statistically higher occupied for the 120 kV_p-spectrum.

TOTAL ENERGY DEPOSITION AND ITS SPATIAL DISTRIBUTION Energy deposition was first simulated in a box phantom with identical materials in all three layers (either liver, fat, water, or soft tissue) and afterwards, with a fat and liver tissue combination. In the latter case, photons first passed fat tissue, then liver tissue, and finally again fat tissue. This tissue sequence can be found in the human abdomen, although the box phantom is obviously a very simplified representation. Still, the basic principles of energy deposition at material interfaces can be derived by means of the box phantom. Since the 120 kV_p-spectrum nearly completely encompasses the 80 kV_p-spectrum, the energy deposition in the box phantom for both tube potentials was almost equal (difference in $E_{total} \leq 2.1\%$ for all simulated materials, table 3.2).
For more complex phantoms, such as the modified abdomen phantom and the digitized patient phantom, differences in E_{total} were more notable. Energy deposition increased with increasing tube potential, except for the skin (this will be discussed later in this section, page 118). Due to the shorter mean range of photons in the 80 kV_p-spectrum, less photon interactions occur at the center of the phantom compared to simulations with a 120 kV_p-spectrum. This results in a lower energy deposition at

the phantom center at 80 kV_p. While there is barely a difference in energy deposition at the phantom periphery between simulations at 80 and 120 kV_p (e.g. skin, subcutaneous fat, soft tissue ring, all <5%), differences are larger in centrally positioned organs (aorta, pancreas, ~30%).

For the box phantom, the modified abdomen phantom, and the patient phantom, profiles of the energy deposition in the phantoms were presented (see figures 3.7, 3.14 and 3.21). For all phantoms, the highest energy deposition was found at the beam entrance for a tube potential of 80 kV_p. For larger depths, energy deposition was highest for a tube potential of 120 kV_p. In all phantoms, the profile of the simulated 80 kV_p-acquisition shows the steepest gradient in the liver tissue. At the center of the modified abdomen phantom and digitized patient phantom, energy deposition was highest at 120 kV_p. This was visible both on the profiles (cf. figures 3.16 and 3.23), and on the energy maps (figures 3.12 and 3.19).
To date, the biological effect of low radiation doses and low-kV acquisitions is insufficiently understood. Although $CTDI_{vol}$ values for low-kV acquisitions are lower, the percentage of the total input energy absorbed in tissues is largest at 80 kV_p compared to acquisitions at 100 or 120 kV_p (see section 3.2.2 and Wang et al. 2012). More research is required on this topic, especially with regard to changes in patient morphology: worldwide, the prevalence of overweight and obesity has increased from approximately 29% to 38% in adults between 1980 and 2013 (Smith and Smith 2016). Physical phantoms (i.e. Alderson phantoms) are based on fairly lean, averaged sized persons. The increased amount of fat tissue in overweight and obese patients leads to deviations in energy deposition from CT acquisitions of standard patients. A larger patient diameter with a larger amount of fat tissue results in fat shielding of the radiosensitive internal organs (Wang et al. 2012). The detailed distribution of the radiation exposure from CT acquisitions needs to be thoroughly investigated, i.e. by MC simulations.

In current literature, MC simulations of CT acquisitions are usually performed at a tube potential of 120 kV_p, independent of the scan region (Amato et al. 2010; Fujii et al. 2017; Li et al. 2011b; Perisinakis et al. 2018, this listing can be extended). There were only three publications employing lower tube potentials for abdominal or thoracic examinations (Chen et al. 2012; Deak et al. 2008; Nowik et al. 2017). None of the publications directly compared the influence of different tube potentials on energy deposition and its spatial distribution.
Although 120 kV_p-acquisitions in CT imaging are widespread, low-kV acquisitions (i.e. at 80 kV_p) at increased tube-current time product (TCTP) for abdominal scan regions are encouraged nowadays, due to the increased contrast of the reconstructed CT images and the decreased expected radiation dose (Lira et al. 2015; Seyal et al. 2015). Increased TCTPs are possible in current CT scanners due to new x-ray tube technology and higher generator power. However, the influence of lower tube potentials than 120 kV_p on the patient's radiation exposure is still insufficiently studied (Wang et al. 2012). This work, in contrast to the previously published studies, provides a comprehensive comparison of the influence of varying tube potentials on total energy deposition and its spatial distribution in CT.

DETECTOR SIGNAL The detector signal was assessed for the box phantom for a homogeneous material distribution (see section 3.2.1). Whereas the differences in E_{total} between tube potentials were small in the box phantom, differences were larger in the detector. The high energy photons (>80 keV) of the 120 kV_p-spectrum are, to a large extent, transmitted through the phantom and absorbed in the detector. Hence, energy deposition in the detector was considerably higher at 120 kV_p than at 80 kV_p (see table 3.2).
The detector signal height influences the SNR but does not directly affect the image contrast, which is dependent on the ratio of detector signals of adjacent materials. Table 3.3 presents the ratio of the detector signal when comparing two materials at 80, 100, and 120 kV_p. For adjacent materials, the detector ratio between e.g. liver and fat would be lowest at 80 kV_p (0.739) and highest at 120 kV_p (0.799), ignoring cross-scattering of photons between tissues. Hence, detector signals are more similar for the simulated 120 kV_p-acquisition than for the simulated 80 kV_p-acquisition. The largest differences in detector signal were found to be at 80 kV_p and decrease with increasing tube potential, except for the tissue combination liver and soft tissue. Due to their identical density and similar composition, differences in detector signal were not expected.
The contrast of CT images increases with decreasing tube potential for typical tube potentials utilized in clinical CT, see section 1.4.4 and Stiller (2011). If there are only slight differences in attenuation between two tissues, these slight differences will have a greater impact on low-energy photons than on high-energy photons. Hence, reconstructed CT images acquired at high tube potentials often appear 'gray on gray' (with a high SNR though) compared to the large visible contrast of CT images acquired at 70 or 80 kV_p. Unfortunately, the use of low-kV acquisitions is limited in obese patients, due to a potentially insufficient number of photons reaching the detector, leading to excessive image noise. Obese patients therefore often have approximately 50% higher radiation doses than non-obese patients due to the required increase of the tube potential (Wang et al. 2012). However, newer techniques in CT, such as the iterative reconstruction, improve the feasibility of low-kV acquisitions in larger patients, by decreasing the image noise (Shaqdan et al. 2018; Stiller 2018).

SKIN EXPOSURE The skin exposure is often mentioned when performing CT acquisitions with tube potentials of 70 or 80 kV_p. Although CTDI values are lower for 70 or 80 kV_p-acquisitions compared to 120 kV_p-acquisitions, the presumed strong increase in skin exposure often causes discussions about the true advantages of acquisitions employing low tube potentials. Energy deposition in the skin increased by ~4%, whereas total energy deposition decreased by ~9% when lowering the tube potential from 120 to 80 kV_p (see table 3.15). This slight increase in skin exposure was caused by the larger number of low-energy photons in the 80 kV_p- compared to the 120 kV_p-spectrum. Differences in the skin energy deposition for the same tube potential and scan coverage (for this analysis 34 slices, 102 mm) resulted in considerably larger differences between patients than the increase in skin exposure due to the usage of the lower tube potential.
The increase in skin exposure might only affect very thin, emaciated patients, which need to undergo frequent follow-up CT examinations, e.g. during the course of a

cancer treatment. According to ICRP publication 103, the tissue weighting factor for skin ($w_T = 0.01$) is considerably lower than the tissue weighting factors for abdominal organs (liver, colon, stomach: $w_T = 0.12$, ICRP 2007, see section 1.5 for more information on tissue weighting factors). This is due to the fact that the skin is less radiosensitive than abdominal organs. Furthermore, the skin exposure from regular diagnostic CT-examinations is nowhere near the 2 Gy threshold for deterministic skin effects, such as skin burns and epilation (Huda 2007). Even for CT guided interventions, resulting in repeated CT scans of the same anatomical region, skin doses were lower than 2 Gy (for conventional CT scanners and for scanners with spiral CT fluoroscopy) in a study of Teeuwisse et al. (2001). Hence, the advantage of the lower cumulative dose from 80 kV_p-acquisitions (and lower exposure of radiosensitive tissues) exceeds the disadvantage of the slightly increase skin exposure for these patients.

4.3 INFLUENCE OF CONTAST ENHANCEMENT ON ENERGY DEPOSITION

The usage of iodinated contrast agents is common in clinical CT imaging for the examination of blood vessels or tissue perfusion (see section 1.3.3). Almost 60% of all CT acquisitions made use of contrast agents in 2016 in the clinic, where this work was performed (UKHD 2017). The increased contrast on the reconstructed images is a result of increased scattering and absorption of photons due to interactions with iodine. It is therefore of interest, how iodine changes the energy deposition in tissues and at material interfaces.

4.3.1 TOTAL ENERGY DEPOSITION AND ITS SPATIAL DISTRIBUTION

The influence of contrast enhancement on energy deposition was again first assessed in the box phantom (section 3.2.2), and afterwards, in the modified abdomen (section 3.3.1) and in the digitized patient phantoms (section 3.4.1). For the box phantom, the addition of iodine in the liver tissue increased the energy deposition considerably in the enhanced layer 2 (see figure 3.9), whereas a decrease in energy deposition was noted in the 'downstream' fat tissue (layer 3).
In comparison, Verhaegen et al. (2005) used the box phantom to study contrast-enhanced radiotherapy with kilovolt x-rays. They employed higher iodine concentrations (50 and 300 mg/ml) and monoenergetic photons with energies of 35, 55, 75, and 95 keV. Furthermore, all layers were filled with water (layer 2 was a water-iodine mixture) instead of liver and fat tissue. In line with the results of this work, a steeper dose gradient in the second layer was noticed at higher iodine concentrations, caused by the increased photon absorption in the contrast-enhanced layer (Verhaegen et al. 2005). Hence, the higher the iodine concentration in a tissue, the more heterogeneous is the resulting energy deposition from CT acquisitions. This topic is of importance for the contrast-enhanced radiotherapy, where a homogeneous dose distribution in a tumor or metastasis is desired (Pérez-López and Garnica-Garza 2011; Verhaegen et al. 2005).

For the modified abdomen and the digitized patient phantoms, energy deposition in the enhanced tissues (liver, spleen, pancreas, kidneys, aorta) increased considerably, whereas energy deposition in the surrounding non-enhanced tissues decreased slightly, when comparing contrast-enhanced acquisitions to non-enhanced acquisitions. The highest increase in energy deposition for contrast-enhanced acquisitions was noticed for simulated 120 kV_p-acquisitions. The increase was slightly lower at 100 and 80 kV_p (see tables 3.5 and 3.9). For the modified abdomen phantom, the increase in energy deposition resulting from contrast enhancement amounted to ~+33% in the liver and to ~+50% in the pancreas (cf. table 3.5). For the digitized patient phantoms, the increase in energy deposition varied between the patients. However, similar relative increases were noticed: ~+34% in the liver and +34-48% in the pancreas. The difference maps (see figures 3.12 and 3.19) were more homogeneous at 120 kV_p compared to lower tube potentials, especially at the center of the liver.
The increase in energy deposition for contrast-enhanced acquisitions strongly depends on the patient/phantom morphology. Although patients were divided into BMI-dependent groups in this work, with matching body heights and weights in each group, the shape of the patients differed considerably, see figure I.3, especially between patients 3A and 3B. This resulted in large differences in the increase of energy deposition between simulations of enhanced and non-enhanced acquisitions, e.g. in the pancreas (range +34-48%) or in the kidneys (range +38-44%) at 80 kV_p (see tables 3.13-3.14). A proper comparison in energy deposition between BMIs should consider larger patient groups, or groups that are based on patient diameters for a specific slice (e.g. D_{eff} or water-equivalent diameter (WED)).

Amato et al. (2010, 2013), Perisinakis et al. (2018), and Sahbaee et al. (2017a) also studied the increase in radiation exposure as a result of iodine enhancement for simulations performed at a tube potential of 120 kV_p. Amato et al. (2010, 2013) employed an anthropomorphic abdomen phantom of which the further developed modified abdomen phantom in this work was based on. Their simulations performed on the abdomen phantom utilized a uniform photon fluence along the fan beam. Additionally, they calculated the increase in energy deposition for simulated contrast-enhanced acquisitions for several patients, based on the increase in CT numbers.
Perisinakis et al. (2018) also calculated the increased energy deposition as result of contrast enhancement in anthropomorphic phantoms at 120 kV_p. Moreover, they determined the iodine uptake of each tissue from the increase in CT number of non-enhanced and enhanced acquisitions and successively simulated CT-acquisitions.
Sahbaee et al. (2017a) simulated the radiation exposure in 58 patient models, which included a pharmacokinetic model of the blood flow.
Table 4.1 summarizes the increase in energy deposition of simulated contrast-enhanced acquisitions for published studies and the present work. For all studies, the increase in energy deposition due to contrast enhancement is found to be lowest in the liver although the increase varied between +20% (Perisinakis et al. 2018) and +47% (Amato et al. 2010). Direct comparison between these values is difficult, as the iodine concentration in the enhanced tissues and the morphology of the phantoms

differed. Perisinakis et al. (2018) determined a mean iodine uptake range between 0.02-0.46% w/w (weight of iodine per weight of tissue) for their investigated tissues, while an iodine mass fraction of $\psi_I = 0.005$ ($\psi_I = 0.5\%$) was employed in this work. The unit iodine w/w (m_I/m_T) is very similar to the weight fraction of iodine ($\psi_I = m_I/(m_I + m_T)$) used in this work for small amounts of iodine: for a liver mass of 1561 g and an iodine mass of 8 g, $\psi_I = 8\,g/(1561\,g + 8\,g) = 0.0051$ corresponding to $8\,g/1561\,g = 0.0051\,w/w$. The smaller mass fraction employed by Perisinakis et al. (2018) might explain the differences in relative energy increase in the liver and the spleen compared to this work.

4.3.2 ENERGY BUILD-UP EFFECT AT MATERIAL INTERFACES

Since contrast agents increase the contrast between material types on reconstructed images, a change in energy deposition at the interface between two materials is expected. The energy build-up was first assessed in the box phantom, and afterwards, in the modified abdomen and digitized patient phantom.
In the box phantom, the energy deposition was calculated at the fat-to-liver and the liver-to-fat interface. For this purpose, ratios of varying interface thicknesses (1.0, 2.5, and 5.0 mm) were compared for varying iodine concentrations (see section 3.2.3 and table 3.4). The summed energy deposition increased with increasing interface thickness (more 'signal'), however, the ratio between liver and fat tissue decreased with increasing interface thickness since the build-up effect is most notable in the near vicinity of the interface and blurs with increasing distance to the interface.
For further calculation of interface ratios in the modified abdomen and the digitized patient phantom, an interface thickness of 2.5 mm was chosen, which is a compromise between the signal and the interface ratio. In a first analysis, the whole organ shells were taken into account for an x-ray source which rotated around the phan-

Table 4.1: Relative increase in energy deposition in digitized patient phantoms and geometrical phantoms for contrast-enhanced acquisitions compared to the energy deposition in non-enhanced acquisitions. Results given for a tube potential of $120\,kV_p$. Amato et al. (2010) (abdomen phantom) and this work employed an iodine mass fraction of $\psi_I = 0.005$. Other iodine mass fractions were dependent on the difference in CT number between enhanced and non-enhanced acquisitions. For Perisinakis et al. (2018): weight per weight (m_I/m_T) 0.23% (liver), 0.29% (spleen) and 0.45% (kidneys). References: [1] Amato et al. (2010), [2] Amato et al. (2013), [3] Perisinakis et al. (2018), [4] Sahbaee et al. (2017a). Abbreviations: GAP: geometrical anthropomorphic phantom, Pat.: patients.

	[1]		**[2]**	**[3]**	**[4]**	**This work**	
Organ	**GAP**	**Pat.**	**Pat.**	**GAP**	**GAP**	**GAP**	**Pat.**
Liver	47%	22%	22%	20%	35%	36%	38%
Spleen	65%	34%	33%	31%	30%	47%	49%
Kidneys	78%	74%	71%	50%	54%	50%	45%
Pancreas	95%	28%	33%	-	24%	51%	50%

toms (helical acquisition, see sections 3.3.2 and 3.4.2). Hence, there was only a single interface ratio calculated for each organ for each simulation, but interface ratios could not be separated into 'upstream' (interface ratio 2a/1) and 'downstream' (interface ratio 2b/3) interfaces.

The interface ratios in the box phantom increased with decreasing tube potential and ranged between 1.51 and 1.76 for simulated non-enhanced acquisitions ($\psi_I = 0.000$) and between 2.25 and 2.63 for simulated enhanced acquisitions ($\psi_I = 0.005$), see shaded cells in table 3.4. The interface ratios of the modified abdomen phantom ranged between 1.54 and 1.64 for simulated non-enhanced acquisitions and between 2.41 and 2.54 for simulated enhanced acquisitions (averaged over all organs, compare to table 3.7). Hence, the interface rations were comparable to those of the box phantom for $\psi_I = 0.000$ and $\psi_I = 0.005$, when averaging the ratios 2a/1 and 2b/3 of the box phantom to compensate for the 360°-rotation in the simulations of the modified abdomen phantom. Between the different organs in the abdomen phantom, interface ratios were approximately equal. Thus, independent of the different material densities, an *iodine*-induced build-up effect in the enhanced tissues is noticeable. The interface ratios in the digitized patient phantom were considerably lower (between 1.23 and 1.26 for the simulated non-enhanced acquisition and between 1.86 and 1.90 for the simulated enhanced acquisition) than the ratios for the box and the abdomen phantom (compare tables 3.7 and 3.11). In contrast to the surrounding tissue shells of the abdomen phantom, which were constructed of fat tissue, the surrounding tissue shells of the digitized patient also contained other materials than fat (i.e. bones, air) since material assignment in the surrounding tissue shells was not defined manually. The heterogeneous material composition of the surrounding shells in the digitized patient phantom influenced the energy deposition and probably caused the differences in interface ratios.
Interface ratios were further determined in more detail on single axial slices in the abdomen (table 3.8) and a digitized patient phantom (table 3.12). In this evaluation, ROIs were drawn in the 'upstream' visceral fat, liver periphery, medial liver, and 'downstream' visceral fat. The axial slice of patient 1A was chosen since the shape of the liver resembled the shape of the liver in the abdomen phantom. The surrounding tissue shell of patient 1A in that specific slice mainly contained fat tissue (though water and air were present to a small degree, see figures 2.23 and I.2a). Interface ratios were very similar for the abdomen and the digitized patient phantom due to the nearly identical tissue composition of the surrounding tissues ROIs (mainly fat tissue). Interface ratios were only calculated for the 360°-rotation as energy deposition in the liver and surrounding tissue ROIs was too heterogeneous for the projections, see figures 3.13a and 3.20a.

This work demonstrated that contrast agents increase the energy deposition in enhanced tissues and cause an iodine-induced energy build-up effect at material interfaces. The energy build-up effect at material interfaces was highest at 80 kV_p, although the highest increases in energy deposition for simulated contrast-enhanced acquisitions were noticed at 120 kV_p. The lower tube potential has a large impact at material transitions due to the larger amount of low-energy photons being absorbed

at material interfaces. The opposite behavior of radiation absorption at material interfaces and for full organs demonstrates the need for the detailed, spatially resolved dosimetry, since the total energy deposition or organ/effective doses are not meaningful for heterogeneous phantoms or when only small regions around material interfaces are of interest.

INFLUENCE OF VESSEL SIZE ON ENERGY DEPOSITION IN TISSUE The build-up effect is of special interest for well-vascularized organs, such as the kidneys. In the presence of iodine, photoelectric interactions and the production of secondary electrons occur more frequently, causing an increase in energy deposition. The smaller the distance between the contrast agent in a blood vessel and the surrounding tissue, the more likely the deposition of energy by secondary electrons in the surrounding tissue cells. Although Sahbaee et al. (2017a) determined a dose increase for simulated contrast-enhanced acquisitions of +35% and +54% in the liver and kidneys, respectively, they predicted a *biologically relevant* dose increase of <18% for the liver and <27% for the kidneys. The biologically relevant dose increase was defined as absorbed dose to tissue since they differentiated between tissue and blood vessels. Furthermore, this measure took the proximity of iodine to the organs into account as it distributes through the blood vessels. Capillaries experience a closer proximity to surrounding cells than arteries or veins, causing a high dose increase in the surrounding cells of capillaries. In comparison to capillaries, energy deposition in tissues surrounding arteries and veins is lower. The differentiation between organ tissue and blood vessels was not implemented in the current work, impeding the possibility of differentiating between general and *biologically relevant* dose increase (Sahbaee et al. 2017a). However, since contrast agents are known to extravasate from blood vessels into tissues (Behzadi et al. 2018), it is a fair approximation to apply a homogeneous iodine concentration in the contrast-enhanced tissues in this work.

The flexibility of dosimetry using self-developed software enables the calculation of the radiation exposure in various ROIs in a multitude of implemented phantoms and digitized patients. Individualized dosimetry in digitized patients offers a precise evaluation of the radiation exposure, even for non-average sized or pediatric patients, where conversion factors fail. Virtual dosimetry allows for prompt patient- and acquisition-specific dose calculations for all examined patients in radiology departments over the course of their lifetime. This enables scientific studies, investigating the long-term effects of ionizing radiation from CT acquisitions, in a large patient cohort.

4.4 VALUE OF ANTHROPOMORPHIC PHANTOMS IN MC SIMULATIONS

Digitized patient phantoms represent patients' morphologies and internal anatomies and therefore serve as basis for the best organ dose calculation (Stepusin et al. 2017). This thesis showed that the processes to create a digitized patient phantom requires manual adjustment for organ dosimetry and is not feasible for clinical routine yet.

An easier but less accurate option are computational reference phantoms (Stepusin et al. 2017).
A large number of anthropomorphic reference phantoms are employed in MC simulations. Computational phantoms have changed over the last decades, from very basic designs to detailed representations, including pharmacokinetic models (Ding et al. 2015; Sahbaee et al. 2017b). Stylized phantoms were developed prior to the 1980s, voxel phantoms were developed since the late 1980s, and boundary representation (BREP) phantoms were developed since the mid of the 2000s (Ding et al. 2015). A comprehensive review of computational phantoms was published by Xu (2014). The modified abdomen phantom implemented in this work belongs to the stylized phantoms, whereas the digitized patient phantoms belong to the voxel phantoms.

INACCURACY OF REFERENCE PHANTOMS Commercially available software often makes use of reference phantoms and precalculated organ doses, stored in large databases, to predict the radiation exposure of patients undergoing CT examinations. Ding et al. (2015) used 25 whole-body BREP phantoms (reference adults (male and female), pediatric patients at different ages and pregnant females at three gestational stages, overweight and obese patients) for the VirtualDose software to produce a large dose database, based on MC simulations. Carver et al. (2017) provide organ and effective doses for 80 pediatric reference patients for chest, abdomen, and pelvic CT acquisitions. They suggest that pediatric patients should be matched to a reference phantom based on the age, stature, and diameter to predict the dose prior to a CT scan. Stepusin et al. (2017) studied six matching metrics for phantoms: (a) age and gender, (b) height and weight, (c) effective diameter D_{eff}, and (d) WED. The latter two were either calculated based on the average over all image slices or based on the central slice of an image stack. The effective diameter is a common metric applied in dosimetry, such as in the calculation of SSDEs (Boos et al. 2016), although it depends strongly on the patient's body posture. Often, effective diameters of phantoms are calculated from a standing posture, whereas patient diameters are measured from their CT images in lying position. Effective doses for patients and computational phantoms are not comparable if effective diameters are measured in different postures. The WED, which accounts for attenuation of internal anatomy within the patient, was shown to be superior in terms of percent difference of organ dose estimates (Stepusin et al. 2017). As was seen from figure I.3, patient anatomy varied internally, whereas computational phantoms are designed based on ideal geometry and anatomy location. The morphometrics and lean body masses vary, which needs to be taken into account when patients are matched to reference phantoms (Stepusin et al. 2017). Especially patients 3A and 3B, despite nearly identical height and weight, have considerably different diameters, distribution of muscle and fat tissue, and probably lean body masses.

4.4.1 THE DIGITIZED PATIENT PHANTOM

This work employed both geometrical (stylized) phantoms and voxelized patient phantoms, derived from CT-acquisitions. The correct realization of the phantom in

terms of material and density assignment, and hence, the accuracy of dose calculation, depends on the implementation of either automatic or manual segmentation methods.

For the automatic segmentation process, a conversion table from CT number to electron density is necessary. Three methods to convert CT number to a material are described by Jiang et al. (2007). The first method is based on a stoichiometric calibration of CT number with mass density and elemental weights (Jiang et al. 2007; Schneider et al. 1996; Vanderstraeten et al. 2007). For this method, a set of materials with known elemental composition and physical density is scanned to measure the corresponding CT number at different tube potentials. The results are then fitted to a theoretical parameter equation interrelating the CT number, density, and atomic number (Z) of each material. The fitted parameters are used to calculate the CT numbers of patient tissues (Vanderstraeten et al. 2007).

For the second method, the materials air (HU≤-950), lung (-950<HU≤-700), soft tissue (-700<HU≤+125), and bone (HU>+125) are defined with ICRP tissue compositions. The density is defined via interpolation of predefined density values of the CT number (Jiang et al. 2007). This method was employed in this work, although more than four basic materials were defined (here, one additional type of lung and bone tissue was defined, as well as fat and water, see listing H.2). Furthermore, the CT number-density pairs at maximum density varied (see. table 4.2).

In the third method, no tissue compositions are differentiated. All materials are specified as water of various densities with varying stopping power, dependent on the CT number. The higher the CT number, the higher the stopping power relative to water (Jiang et al. 2007).

The described methods result in different material assignments and ultimately in

Table 4.2: Comparison of computed tomography (CT) number-to-density conversion tables. *ctcreate* values obtained from Jiang et al. (2007). Densities (given in g/mm^3), other than those provided in the table, are calculated by interpolation between the CT number/density pairs.

ctcreate		**This work**	
Maximum density [g/cm^3]	**CT number [HU]**	**Maximum density [g/cm^3]**	**CT number [HU]**
0.001	-1000	0.0	-5000
0.044	-950	0.0	-1000
0.302	-700	0.602	-400
1.101	+125	0.95	-130
2.088	+2000	1.0	0
		1.075	100
		1.145	300
		1.856	2000
		3.379	4927

different E_{total} and $E_{spatial}$. Automatic segmentation works well for a limited number of tissues, e.g. air, lung tissue, soft tissue, bones. However, automatic methods often fail when differentiating between soft tissue types since there are only slight differences in CT numbers between different soft tissue types (Sharma and Aggarwal 2010). Furthermore, assignment of specific tissue types fails if CT numbers of e.g. the liver deviate from expected values. Patients with fatty livers have lower CT numbers than the expected values of ~60 HU in the liver which might result in wrong tissue assignment. The density of the liver in this case is lower and probably correctly determined, however, liver voxels might be assigned as fat tissue and not be included in the calculation of the liver dose. Also, CT numbers are known to differ between CT scanners of different vendors for the same material (Lamba et al. 2014), which requires fitting the CT number-to-density conversion file ('CT-2-density') to the CT scanner output. To circumvent the addressed problems, abdominal organs were manually segmented in this work, allowing for exact organ and tissue allocation. However, the surrounding tissue shells were not manually segmented and the material allocation was done automatically using the 'CT-2-density' table. The difference in design between the geometrical and the digitized phantoms resulted in different interface ratios for the whole organs (refer to results of the energy build-up effect in section 4.3.2).

4.4.1.1 *Comparison of geometrical and digitized phantoms*

Although the modified abdomen phantom was designed to resemble a real patient, there are large differences in organ positioning, see figure 4.1. The liver, pancreas, spleen, and the kidneys are often to be found at the same height in humans. The length of the abdomen from start of the liver until below the kidneys is ~19-23 cm. However, the length covering the organs of the abdomen phantom is ~30 cm, hence,

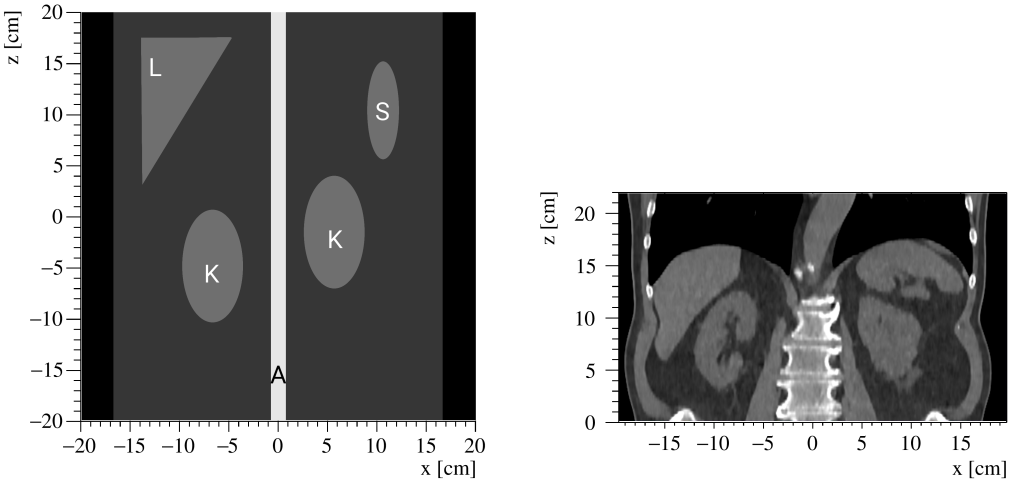

(a) Modified abdomen phantom (b) Patient 2A

Figure 4.1: Coronal view of modified abdomen phantom and patient 2A through the liver (L), kidneys (K) and spleen (S), parts of the aorta (A), and the spine (digitized patient).

approximately 1.5 times the length in the human body. The organs are more distributed along the length, such that only the liver and the spleen are at the same height, however, the pancreas and the kidneys are placed in a different position. Employing the tube current modulation derived from real patient examinations is not applicable for the abdomen phantom, since its morphology differs from the patients to a too large degree. The modified abdomen phantom does not contain lung tissue, although large parts of the lung reach into the abdomen. Lung, due to its low density, alters the energy deposition in the liver considerably since less photons are being absorbed prior to reaching the liver.
The structure and shape of the single axial slice used to determine the energy build-up effect from the abdomen and the digitized patient phantoms are fairly similar (section 2.5.3.4 and 2.5.4.4), especially regarding the sequence of materials at the x-ray beam entrance side for the simulation of the 270°-projection (compare figure 3.13 and figure 3.20). However, in contrast to the modified abdomen phantom, the digitized patient phantom includes the patient table, influencing the 360°-dose distribution (this is discussed later in the limitations section).

In terms of computational time, simulations of geometrical phantoms are considerably faster than simulations of digitized phantoms. As an example, the simulation of the 270°-projection of the single axial slice took 10 hours for the modified abdomen phantom and 24 hours for the digitized phantom. Geometrical phantoms consist of predefined geometries of a fixed material composition and density, whereas for digitized patient phantoms, several material types for a single material exist due to the CT number-based densities. Whereas the organ boundaries in geometrical phantoms are predefined, voxel-to-voxel transitions need to be tracked for digitized patient phantoms, increasing the computational time by more than a factor of 2.

4.4.2 IMPLEMENTATION OF IODINATED CONTRAST AGENTS IN MC MODELS

The implementation of iodine as contrast agent in this work was performed by combining the element iodine with the defined basic materials (e.g. liver tissue). The composition of the two parts was defined by mass fractions ψ_I and ψ_T, respectively. The composition of contrast-enhanced tissues contained the element iodine, which alters the photon attenuation properties of the tissue (see section 1.3.3 and section 2.4.3). Additionally, the density of the contrast-enhanced tissue was altered according to the iodine mass fraction.
Pérez-López and Garnica-Garza (2011) added iodine into the tissue by adjusting the mass fraction of each of the elements present in the original tissue, which corresponds to the implementation of this work. However, they do not mention an altered material density. Verhaegen et al. (2005) implemented different iodinated contrast agents such as Omnipaque (GE Healthcare, Chicago, USA) or Optiray (Guerbet, Sulzbach, Germany) based on their specific composition. Hence, they do not solely implement the element iodine but use the mass density and atomic constituents of the full contrast agent. According to their presented atomic constituents of contrast agents, the iodine mass fraction does not increase linearly with increasing contrast-

agent concentration. According to table 1 in their publication, an iodine weight fraction of $\psi_I = 0.047$ corresponds to an iodine concentration of 50 mg/ml, whereas $\psi_I = 0.09$ and $\psi_I = 0.224$ correspond to iodine concentrations of 100 and 300 mg/ml, respectively (Verhaegen et al. 2005).
For the abdominal simulations (both geometrical abdomen and digitized phantoms) in this work, an iodine mass fraction of $\psi_I = 0.005$ was used, which, according to Amato et al. (2010), corresponds to an iodine concentration of 5 mg/ml. They also used other mass fractions of 10^{-3}, $5 \cdot 10^{-3}$, $7 \cdot 10^{-3}$, 10^{-2}, which should correspond to iodine concentrations of 1, 5, 7 and, 10 mg/ml, respectively.

For the geometrical phantoms, the material composition and density was altered depending on the chosen iodine mass fraction (see section 2.4.3). For the digitized patient phantoms, the material composition and density of the *basic* tissue material was altered (increased) according to the chosen mass fraction. However, due to the subsequent rounding of the material density during the setup of the digitized phantoms according to the CT numbers of the inserted CT images (density steps of 0.1 g/cm), the density was effectively not altered. The difference in density between enhanced and non-enhanced materials is 0.5% for the liver, according to equation 2.2, for $\psi_T = 0.995$. However, a density step of 0.05 g/cm^3, e.g. from 1.00 to 1.05 g/cm^3, results in a difference in density of 5.0%. The difference in the density due to rounding (5.0%) is ten times the difference in density between enhanced and non-enhanced materials (0.5%) and, hence, has a considerably higher effect on energy deposition. Rounding during the phantom construction ensures that only a limited number of materials are produced, which again limits computational time. However, the accurate density originally calculated from CT data for simulated non-enhanced acquisitions and the density difference for simulated enhanced acquisitions suffer from this implementation.
During this work, image data of non-enhanced CT acquisitions have been used for organ assignment and density calculation. If image data of arterial acquisitions would have been used, the 'CT-2-density' conversion table would need to be adjusted, as CT numbers of enhanced tissues do not correspond to CT numbers of non-enhanced acquisitions. CT numbers of the aorta in arterial acquisitions can reach 200-500 HU, which corresponds to a density of ~1.145 g/cm^3 (for 300 HU). The density of non-enhanced blood is considerably lower, with 1.060 g/cm^3. From the increased density, an iodine concentration of 74 mg/ml can be calculated, according to equation 2.2: $\psi_I = 1\text{-}(1.06/1.145) = 0.074$. However, realistic maximum iodine concentrations reached in the aorta are considerably lower, with approximately 15 mg/ml. The high CT number for contrast-enhanced tissues demonstrates a high photon attenuation, however not a high tissue density. According to Perisinakis et al. (2018), the considerable increase in the absorption efficiency of iodinated tissue may not be attributed to the increase of density, but to the increase of effective atomic number Z in consequence of iodine uptake. Hence, utilizing CT images of non-enhanced acquisitions and including the contrast agent in a successive step is a reasonable method to obtain appropriate densities and contrast enhancement.

4.5 OTHER SIMULATION PARAMETERS

NUMBER OF INITIAL PHOTONS The number of tracked photons influences the accuracy of dose calculations but also the simulation run times. Appendix J reviews the effect of the number of tracked photons in MC simulations of CT acquisitions. Since results of MC simulations using larger numbers of photons are unknown (i.e. the result for an infinite number of photons), different approaches were taken to determine the required number of photons to reach a specific maximum error.
Figures 3.27-3.30 demonstrated that a reduced number of photons caused deviations from the original simulation results. The larger the tracked volume, the larger the possibility to reduce the number of photons without altering the results. Small volumes were more vulnerable to a smaller statistical occupation than large volumes. The initial number of photons employed for anthropomorphic phantom simulations in this work was based on the study design of Salvadó et al. (2005) who obtained relative standard errors of <0.5% in 1 cm thick axial slices, employing $3 \cdot 10^6$ tracked photons per 1 cm-image slice. For two identical simulations with two different initial seeds in this work, differences in organ energy deposition were <1% even for the smallest organ (see section 3.5), caused by the statistical variation in MC simulations. However, differences between the two simulations were up to 60% on a voxel scale (1.5 x 1.5 x 3 mm^3) and ~30% when averaging over three voxels.

DATA STORAGE AND ANALYSIS Most publications related to CT dosimetry only store 3D-distributions but not the complete tracking information, such as interaction type or track lengths (Angel et al. 2010; Belley et al. 2014; Deak et al. 2008). Compared to commercially available tools for dose calculation, the presented software allows more options for data in- and output: although not presented in the results of this work, it is possible to combine radiation exposure maps with specific requirements, e.g. an exposure map only from photoelectric interactions or scatter maps. Unfortunately, the flexibility of the comprehensive output options comes at the cost of large output data files (21.5 GiB (23.1 GB) for full output vs. 144.7 MiB (151.7 MB) for solely the 3D energy distribution, see appendix C), although simulation times did not differ considerably. If solely the 3D-energy distribution is of interest, the reduced output is considerably less memory expensive.

4.6 LIMITATIONS AND FUTURE DEVELOPMENT

EVALUATION OF X-RAY EMISSION AND THE CT GEOMETRY The characterization of the geometry and the material of beam-shaping filters is difficult, since detailed information on their design is often proprietary. However, according to Boone (2010) and Zhou and Boone (2008), most beam-shaping filters are sufficiently similar in terms of performance across vendors. This would allow for applying beam-shaping filters or transmission curves from one CT system to be adopted onto another system, if information about these parts is unavailable (for the same FOV or imaged body region).
Although CT acquisitions of the digitized patients were originally acquired on a

Somatom® Definition Flash (Siemens Healthineers, Forchheim, Germany), the simulations employed the geometry of the Aquilion™16 CT scanner (Toshiba Medical Systems Corporation, Nasu, Japan). This was done, as the transmission measurements leading to the implementation of the fan-angle dependent fluence modulation (FM) were performed on the Aquilion™16. Although the combination of the Siemens scanner geometry and the beam-shaping characteristics of the Toshiba scanner would probably be adequate according to Boone (2010) and Zhou and Boone (2008), this mixture of geometries was avoided. Furthermore, the generated spectra might not correspond to the Somatom® Definition Flash. In the worst case, this would result in the combination of transmission characteristics of the Aquilion™16 with the CT scanner geometry of a Somatom® Definition Flash and spectra of yet again a different CT scanner model.
Fan-angle dependent x-ray spectra and transmission measurements of other CT scanners (i.e. Somatom® Definition Flash) need to be performed to allow for matching CT scanner geometries and x-ray spectra. Furthermore, obtaining information on the geometry of CT scanners of other vendors would allow to increase the limited number of implemented CT scanners in the developed MC model.

ENERGY BUILD-UP EFFECT AT INTERFACES For the calculation of the energy build-up effect, energy deposition was calculated with an interface layer width of 2.5 mm, as a compromise between signal (accumulated energy deposition in an interface layer) and noise (a decreasing energy deposition with larger distance from the interface). The choice of the 2.5 mm seam around the organs corresponds to a width of only 3-4 pixels in the ROIs for the abdomen and digitized patient phantom (see figures 2.22 and 2.23). This width is vulnerable to volume artifacts (partial volume effect) of nearby voxels. For a closer analysis of the energy build-up effect in arteries and capillaries on cell level, a higher resolution of the original CT data or more detailed geometrical phantoms are necessary.

EMPLOYED IODINE CONCENTRATION The employed iodine concentration in this work neglects the physiology of the blood flow. Although the iodine concentration is both time-dependent and tissue-dependent after contrast-agent administration, an identical concentration in all organs and the aorta was assumed in this work. Sahbaee et al. (2017a,b) extensively implement contrast-agent dynamics in their anthropomorphic phantoms. The iodine concentration in this work (5 mg/ml) is slightly overestimated for the liver and underestimated in the aorta in comparison to their implementation (maximum peak at ~3 mg/ml for the liver and at ~10 mg/ml for the aorta, as per Sahbaee et al. (2017a,b)). However, this iodine concentration was employed here since it is a fairly realistic assumption and simplification of the time- and organ-dependent iodine concentration.
One option to overcome the necessity of modeling blood flow, or of using approximations of iodine concentrations is the calculation of difference images from non-enhanced and arterial/venous phase acquisitions. This, however, requires the registration of the employed image data sets. With current CT technology, iodine maps, representing tissue iodine concentrations, can be calculated, i.e. from dual energy CT (DECT) acquisitions, and could serve as input for MC simulations.

AUTOMATIC AND MANUAL MATERIAL ASSIGNMENT Automatic material assignment by thresholding lacks precision for soft tissue types since the CT numbers of these tissues are similar. The 'CT-2-density' conversion table only provides a rough classification of tissues, which causes misclassification of voxels. As an example, the liver in figure 2.13b is surrounded by a 'clutter' of pixels assigned as water, fat, and soft tissue. In reality, these pixels should probably be assigned as homogeneous fat tissue. This tissue assignment is due to the transition from fat (CT number ~-115 HU) to soft tissue (CT number ~+60 HU). As a consequence of the partial volume effect, pixels between fat and soft tissue are frequently assigned as water (CT number ~0 HU)

Personalized 'CT-2-density' conversion tables will reduce misclassifications, however, they will not eliminate them completely due to the similarity of CT numbers in the abdomen and partial volume effects. Manual segmentation reduces this issue, however, this introduces further limitations. Manual segmentation is time intensive and its execution and consistency between patients is strongly dependent on the person that is contouring the patient. Patients in this thesis often had calcification of their aorta and smaller blood vessels. The material blood was assigned to the segmented aorta, which often included calcified areas. The density values of these areas are correctly calculated since they are based on the CT numbers, however, material allocation and composition in this case corresponds to blood and not to calcium. The erroneous material composition of calcification will influence photon attenuation and energy deposition in these areas. The patients included here are not strongly affected by aortic calcification. Patients with higher degree of calcification, implanted stent grafts, or implants (pacemaker/joints) will need to be contoured in greater detail for correct material assignment.

CT PATIENT TABLE During this work, the CT system's patient table was not manually segmented, as was performed by Nowik et al. (2017). They studied the influence of the patient table on effective dose, noticing an overestimation of the effective dose by 5% if the patient table was not included in the simulation. The doses in individual organs were overestimated by 8% for spiral acquisitions. Since their employed software ImpactMC (AB-CT Advanced Breast-CT GmbH, Erlangen, Germany) did not include a carbon fiber mixture, they assigned muscular tissue as table material (Nowik et al. 2017). In this thesis, the table was automatically converted into soft tissue and trabecular bone, with lung tissue inside the table for the digitized patient phantoms. This does not correspond to the realistic material composition, however, the table and its attenuating characteristics are included. For the modified abdomen phantom, the table has not been included, which needs to be taken into account when directly comparing the results of the modified abdomen and the digitized patient phantom.

In future simulations, a model of the table with realistic dimensions and material composition should be designed and included for both digitized and geometrical phantoms to account for the correct photon attenuation in the table.

NUMBER OF PATIENTS AND EVALUATIONS Only a limited number of patients were included in this work. Therefore, only a limited number of evaluations was per-

formed, which limits the explanatory power. However, the goal of this work was the development of a MC software, which enabled the simulation of CT acquisitions, calculation of the radiation exposure of digitized patients, and the flexibility of software input and output/analysis options. The feasibility of virtual dosimetry with the developed software was presented by means of a selected number of patients and research topics of current interest. Simulations of more patients with larger scan coverage, higher spatial resolution (especially for a thinner slice thickness), and larger number of initial photons requires more computational power (i.e. a computer cluster).

VALIDATION AGAINST GROUND TRUTH Results of the MC simulations were not validated against experimental measurements, but only compared with results of other MC simulations. The basic principles of radiation exposure and the functionality of the software can be sufficiently assessed. However, for proper validation, results of simulations and experimental measurements need to be compared, i.e. for a validation against CTDI measurements for different CT acquisition settings or against TLD measurements in an Alderson phantom.

4.7 CONCLUSIONS

Since the annual effective dose to individuals from CT acquisitions is increasing, thorough understanding of the radiation exposure distribution inside the patient's body is necessary. The MC software developed in this work offers flexibility in both data input, output, and analysis options of the energy deposition caused by the x-rays in CT imaging. The main conclusions and consequences of this work are as follows:

1. X-ray source spectra are interchangeable when matching mean spectral energy and peak tube potential. The two effects of beam-shaping filtration, modulated photon fluence and spectral distortion, need to be included for an accurate and precise CT model.

2. Administration of contrast agents needs to be implemented in patient dosimetry, since contrast agents alter total energy deposition and its spatial distribution in patients.

3. Geometrical phantoms are useful to assess general principles of energy deposition. Geometrical anthropomorphic phantoms serve as an approximation for digitized patient phantoms, decreasing simulation time and complexity of the materials

4. Digitized patient phantoms offer the best realization for individualized patient dosimetry. The conversion of CT numbers to density offers the direct implementation of density values. However, correct tissue allocation requires manual segmentation. Furthermore, simulation time and complexity is increased compared to geometrical phantoms.

5. Applying lower tube potentials than 120 kV_p for non-enhanced and enhanced CT acquisitions for increased tissue contrast and dose reduction is recommended where possible. Radiation exposure can be decreased considerably for an abdominal scan coverage by choosing 80 kV_p, compared to higher tube potentials, without increasing the skin exposure considerably.

The results of this work demonstrate that knowledge about spatially resolved radiation exposure is necessary to fully understand the effects of changing CT acquisition parameters or administration of contrast agents. Full body or organ doses are not sufficient to describe the interactions of photons at material interfaces. Individualized dosimetry offers a precise evaluation of the radiation exposure, even for non-average sized or pediatric patients, where conversion factors fail. Furthermore, MC simulations allow to implement contrast agents, in contrast to the usage of conversion factors or common physical phantoms (e.g. the Alderson phantom). Once implemented in a larger computer cluster for faster run-times, the developed virtual dosimetry software allows for prompt patient- and acquisition-specific dose calculations for all examined patients in radiology departments over the course of their lifetime. This enables scientific studies, investigating the long-term effects of ionizing radiation from CT acquisitions. Furthermore, knowledge about the influence of CT acquisition parameters on dose deposition may provide positive impulses for both acquisition execution and technical improvements in CT.

5

SUMMARY

Since the range of indications of and the accessibility to computed tomography examinations in diagnostic radiology are constantly expanding, their number and the associated effective dose to patients have increased over the last decades. Thorough understanding of the radiation effects induced by the utilized ionizing x-rays is necessary to evaluate the risks and benefits of computed tomography examinations. Ionizing radiation is a proven carcinogen, especially for high radiation doses (>100 mSv), however, the long-term health risks of lower doses are still unknown. To correlate computed tomography examinations with potential side effects from ionizing radiation, studies need to be performed, which determine the spatially resolved dose deposition associated with computed tomography examinations for large patient cohorts over the course of decades. Monte Carlo methods offer the most precise way to investigate the effective dose from computed tomography examinations inside a variety of test specimen (phantoms), providing a spatially resolved measure of the radiation exposure without exposing patients or staff to ionizing radiation. Several commercial Monte Carlo software tools for dose calculation in computed tomography are available, which are, however, often restricted in terms of predefined scanner or phantom geometries, x-ray source spectra, and data output.

The goal of this work was the development of a Monte Carlo software tool for the simulation of computed tomography acquisitions and the determination of the associated radiation exposure in individual patients. The software aimed at enabling flexible integration of source spectra and scanner geometries, implementation of self-designed geometrical and digitized patient phantoms, and the possibility of extensive data analysis, paving the way towards virtual dosimetry – the prompt and accurate calculation of spatially resolved radiation exposure in individual patients. For this purpose, the open-source toolkit Geant4 has been employed during this work, for the simulation of radiation transport in matter during computed tomography examinations. The toolkit was further developed and adapted to provide detailed information (e.g. interaction type and position) about the energy deposition in phantoms for the retrospective creation of energy maps. The developed Monte Carlo software modeled a computed tomography scanner, including x-ray emission and optional beam-shaping methods, experimental and anthropomorphic phantoms of varying complexity, and a photon detector. Several acquisition modes and tube-current modulation were implemented. Digital patient phantoms were constructed via automatic threshold-based and manual segmentation from computed tomography image data sets and translated into voxelized phantoms.

In a first step, the basic functionality of the Monte Carlo model was reviewed with regard to the implemented beam-shaping methods and the spectral characteristics of x-ray emission for a set of 120 kV_p-equivalent photon distributions. This

analysis was important since x-ray tube-specific spectra are not easily accessible, often resulting in the necessity to either simulate source spectra, or employ spectra from mathematical models or online tools. Computed tomography examinations often apply other tube potentials than 120 kV_p and are frequently supported by the administration of contrast agents. However, a contrast agent-enhanced radiation damage caused by computed tomography examinations strengthens the need for profound research on the effect of contrast agents on the energy deposition, especially at material interfaces. Therefore, in a second step, the influence of the applied tube potential (80, 100, 120 kV_p) and the administration of iodinated contrast agents on total energy deposition (E_{total}) and its spatial distribution ($E_{spatial}$) was assessed in a simple box phantom for a variety of iodine concentrations (1-15 mg/ml). The evaluation employing the box phantom served as basis for further simulations of computed tomography acquisitions in a geometrical abdomen phantom, and finally, in six digitized patients of varying body mass index and morphology. For the anthropomorphic phantoms (abdomen phantom and digitized patient phantoms), the influence of the tube potential and the administration of iodinated contrast agents on E_{total} and $E_{spatial}$ was evaluated, employing contrast-enhanced tissues (aorta, kidneys, liver, spleen, and pancreas) with an iodine concentration of 5 mg/ml. Energy deposition was further assessed in more detail at tissue interfaces.

The results of this work demonstrated that Monte Carlo models of clinical computed tomography scanners need to include the effect of beam-shaping filtration. The performed evaluation on the spectral characteristics has demonstrated that spectra are interchangeable between vendors and scanner models for matching mean spectral energy and peak tube potential. Whereas E_{total} was approximately equal for the applied tube potentials in the simple box phantom, $E_{spatial}$ differed considerably, indicating the necessity of spatially resolved dosimetry. Simulations of the implemented anthropomorphic phantoms for an abdominal scan coverage demonstrated that energy deposition decreased with decreasing tube potential for the exposed tissues/organs, except for the skin. In the skin, energy deposition increased by ~4% when decreasing the tube potential from 120 to 80 kV_p. The increase in skin exposure is negligible compared to the overall reduction of the energy deposition by ~9%, especially when taking the low radiosensitivity of skin into account. The addition of iodine caused an increase in energy deposition for contrast-enhanced tissues (up to +50% for an iodine concentration of 5 mg/ml). The relative difference increased with increasing iodine concentration and tube potential. In contrast to the enhanced tissues, energy deposition decreased slightly in the surrounding non-enhanced tissues for the anthropomorphic phantoms. An energy build-up effect was visible at material interfaces even without the addition of iodine, due to differences in physical density. However, an additional iodine-induced energy build-up effect, which increased with increasing iodine concentration, was visible for contrast-enhanced acquisitions. In contrast to the total energy deposition in enhanced tissues, the energy build-up effect increased with decreasing tube potential. Hence, for low tube potentials (e.g. 80 kV_p), larger differences between energy deposition in organ and surrounding tissues were measured than for higher tube potentials.

In conclusion, the developed software for the simulation of computed tomography acquisitions paves the way towards individualized virtual dosimetry of patients. The results of this work demonstrated that spatially resolved dosimetry is needed, due to the differences in the spatial distribution of energy deposition depending on tube potential, contrast agents, and material interfaces. Individual patient dosimetry is necessary to understand differences in radiation exposure for varying patient morphology and to estimate the radiation burden for patients undergoing frequent examinations. Furthermore, widening the knowledge about the dose distribution helps to improve computed tomography for dose-saving techniques in future.

6

ZUSAMMENFASSUNG

In den letzten Jahrzehnten sind die Anzahl von Computertomographieaufnahmen und die damit einhergehende Strahlenbelastung für Patienten durch die größere Anzahl von Indikationen und die leichte Verfügbarkeit dieser Aufnahmen deutlich gestiegen. Ein gründliches Verständnis der Strahleneffekte der genutzten ionisierenden Röntgenstrahlung ist daher notwendig, um den Nutzen und die Risiken der Untersuchungen abschätzen und einordnen zu können. Röntgenstrahlung ist insbesondere bei hohen Strahlendosen (>100 mSv) krebserregend. Die gesundheitlichen Langzeiteffekte von niedrigen Dosen sind jedoch noch unbekannt. Um Computertomographieaufnahmen mit potenziellen Nebenwirkungen der Röntgenstrahlung zu korrelieren, sind Studien notwendig, bei denen die resultierende, räumlich aufgelöste Strahlendosis in großen Patientenkohorten über Jahrzehnte hinweg bestimmt werden muss. Die genaueste Möglichkeit, die effektive Dosis von Computertomographieaufnahmen zu untersuchen, um eine räumlich aufgelöste Verteilung der Dosis im Patienten oder in Prüfkörpern (Phantomen) zu erhalten, ohne Patienten oder Personal Röntgenstrahlung auszusetzen, bieten Monte Carlo Methoden. Es gibt bereits mehrere kommerzielle Monte Carlo Programme zur Dosisberechnung in der Computertomographie, allerdings schränken diese häufig den Nutzer durch vorgegebene Scanner- oder Phantomgeometrien, Röntgenspektren oder in der Datenauslese ein.

Ziel dieser Arbeit war daher die Entwicklung einer Monte Carlo Software, die eine flexible Integration von Röntgenspektren, Scannergeometrien, und selbst gestalteten, geometrischen Abdomen- und digitalen Patientenphantomen ermöglicht, und gleichzeitig eine differenzierte Datenauswertung bereithält. Für die Simulation der physikalischen Prozesse in Phantomen bei Computertomographieaufnahmen wurde das Open-Source Toolkit Geant4 genutzt. Nach Anpassung und Weiterentwicklung des Toolkits war es möglich, Informationen (z.B. Position, Interaktionstypen) über die Energiedeposition von Röntgenstrahlung im Phantom zu erhalten und Expositionskarten zu erstellen. Das in dieser Arbeit entwickelte Computertomographiemodell verfügt über die Emission von Röntgenstrahlung mit optionaler Strahlformung, experimentellen und anthropomorphen Phantomen unterschiedlicher Komplexität sowie einem Photonendetektor. Unterschiedliche Aufnahmemöglichkeiten und Röhrenstrommodulation wurden zusätzlich implementiert. Digitalisierte Patientenphantome wurden aus Bilddatensätzen von Computertomographieaufnahmen erstellt, wofür die Datensätze schwellwertbasiert und manuell segmentiert wurden.

Im ersten Schritt wurde die grundlegende Funktionalität des Monte Carlo Modells bezüglich der Strahlformungsmethoden und den spektralen Eigenschaften von 120 kV_p-Photonenverteilungen evaluiert. Dieser Schritt war erforderlich, da Röntgen-

spektren von Computertomographen nur schwierig messbar und häufig proprietär sind, und daher oft simuliert oder aus mathematischen Modellen oder Computerprogrammen generiert werden müssen. Computertomographieaufnahmen werden auch oft bei anderen Röhrenspannungen und unter Zugabe von Kontrastmitteln akquiriert. Da Kontrastmittel Strahlenschäden verstärken können, sind fundierte Studien der Effekte von Kontrastmitteln auf die Energiedeposition von Röntgenstrahlung wichtig, insbesondere bei Materialübergängen von kontrastierten zu nichtkontrastierten Geweben. Daher wurde in einem zweiten Schritt der Einfluss der Röhrenspannung (80, 100, 120 kV_p) und die Zugabe von jodhaltigen Kontrastmitteln auf die Gesamtenergiedeposition (E_{total}) und deren räumlichen Verteilung ($E_{spatial}$) in einem Boxphantom bei verschiedenen Jodkonzentrationen (1-15 mg/ml) untersucht. Die Auswertung des Boxphantoms war Grundlage weiterer Simulationen von Computertomographieaufnahmen eines geometrischen Abdomenphantoms und sechs digitalisierter Patientenphantomen mit unterschiedlicher Morphologie und Body-Mass-Index. Der Einfluss von Röhrenspannung und Kontrastmittel auf E_{total} und $E_{spatial}$ wurde auch für die anthropomorphen Phantome (Abdomen- und Patientenphantome) bestimmt. Kontrastmittelverstärkte Gewebe waren dabei die Aorta, Nieren, Leber, Milz und Pankreas mit einer Jodkonzentration von 5 mg/ml. Die Energiedeposition wurde des Weiteren noch detaillierter an Gewebeübergängen analysiert.

Die Ergebnisse der Arbeit zeigen, dass ein Monte Carlo Modell eines Computertomographen den Effekt des Strahlenformfilters korrekt darstellen muss und dass Röntgenspektren zwischen Geräteherstellern und -modellen austauschbar sind, solange die durchschnittliche Energie und die maximale Röhrenspannung übereinstimmen. Obwohl E_{total} für die verschiedenen Röntgenspannungen im Boxphantom ähnlich war, so variierte $E_{spatial}$ erheblich, was die Notwendigkeit der räumlich aufgelösten Dosimetrie verdeutlicht. Für anthropomorphe Phantome mit einer abdominellen Scanabdeckung nahm die Energiedeposition der exponierten Gewebe (mit Ausnahme der Haut) mit geringerer Röhrenspannung ab. In der Haut nahm die Energiedeposition bei Senkung der Röhrenspannung von 120 auf 80 kV_p um ~4% zu. Der Anstieg der Hautexposition ist im Vergleich zur generellen Abnahme der Gesamtenergiedeposition von ~9% vernachlässigbar, insbesondere wenn die geringe Strahlenempfindlichkeit der Haut mit einbezogen wird. Zugabe von Jod in Geweben erhöhte die Energiedeposition für kontrastverstärkte Gewebe in allen Phantomen (bis zu +50% bei einer Jodkonzentration von 5 mg/ml). Der relative Unterschied in der Energiedeposition zwischen kontrastverstärkten und nicht-kontrastierten Aufnahmen nahm mit zunehmender Jodkonzentration und Röhrenspannung zu. In den umliegenden nicht-kontrastierten Geweben nahm die Energiedeposition leicht ab. Ein Energieaufbaueffekt war bereits für nicht-kontrastierte Materialübergänge aufgrund von Unterschieden der physikalischen Dichten sichtbar. Bei Zugabe von Jod hat sich dieser Aufbaueffekt jedoch noch verstärkt. Im Gegensatz zu den relativen Unterschieden zwischen nicht-kontrastierten und kontrastierten Aufnahmen nahm der Aufbaueffekt mit abnehmender Röhrenspannung zu. Für geringere Röhrenspannungen (z.B. 80 kV_p) werden größere Unterschiede in der Energiedeposition zwischen Organen und dem umliegenden Gewebe gemessen als für höhere Röhren-

spannungen.

Zusammenfassend ergibt sich, dass die entwickelte Software den Weg in Richtung individualisierter virtueller Dosimetrie für Patienten ebnet. Da die Verteilung der Energiedeposition von der Röhrenspannung, Kontrastmittelgabe und von Materialübergängen abhängt, ist die räumlich aufgelöste Dosimetrie für die korrekte Bestimmung der Strahlenbelastung notwendig. Individualisierte Dosimetrie ist erforderlich, um Unterschiede der Strahlenbelastung bei unterschiedlichen Patientenmorphologien zu verstehen, und um Abschätzungen der Strahlenschäden für häufig untersuchte Patienten zu ermöglichen. Ein tieferes Verständnis der Dosisdeposition im Körper wird dazu beitragen, technische Fortschritte in der Niedrig-Dosis-Computertomographie zu erreichen.

7

BIBLIOGRAPHY

7.1 GENERAL REFERENCES

AAPM (2011). **Size specific dose estimates (SSDE) in pediatric and adult body CT examinations. AAPM Report No. 204**. AAPM Task Group 204, College Park, MD, USA.

Agostinelli, S., Allison, J., Amako, K., Apostolakis, J., Araujo, H., Arce, P., Asai, M., Axen, D., Banerjee, S., Barrand, G., Behner, F., Bellagamba, L., Boudreau, J., Broglia, L., Brunengo, A., Burkhardt, H., Chauvie, S., Chuma, J., Chytracek, R., Cooperman, G., Cosmo, G., Degtyarenko, P., Dell'Acqua, A., Depaola, G., Dietrich, D., Enami, R., Feliciello, A., Ferguson, C., Fesefeldt, H., Folger, G., Foppiano, F., Forti, A., Garelli, S., Giani, S., Giannitrapani, R., Gibin, D., Gomez Cadenas, J. J., Gonzalez, I., Gracia Abril, G., Greeniaus, G., Greiner, W., Grichine, V., Grossheim, A., Guatelli, S., Gumplinger, P., Hamatsu, R., Hashimoto, K., Hasui, H., Heikkinen, A., Howard, A., Ivanchenko, V., Johnson, A., Jones, F. W., Kallenbach, J., Kanaya, N., Kawabata, M., Kawabata, Y., Kawaguti, M., Kelner, S., Kent, P., Kimura, A., Kodama, T., Kokoulin, R., Kossov, M., Kurashige, H., Lamanna, E., Lampen, T., Lara, V., Lefebure, V., Lei, F., Liendl, M., Lockman, W., Longo, F., Magni, S., Maire, M., Medernach, E., Minamimoto, K., Mora de Freitas, P., Morita, Y., Murakami, K., Nagamatu, M., Nartallo, R., Nieminen, P., Nishimura, T., Ohtsubo, K., Okamura, M., O'Neale, S., Oohata, Y., Paech, K., Perl, J., Pfeiffer, A., Pia, M. G., Ranjard, F., Rybin, A., Sadilov, S., Salvo, E. di, Santin, G., Sasaki, T., Savvas, N., Sawada, Y., Scherer, S., Sei, S., Sirotenko, V., Smith, D., Starkov, N., Stoecker, H., Sulkimo, J., Takahata, M., Tanaka, S., Tcherniaev, E., Safai Tehrani, E., Tropeano, M., Truscott, P., Uno, H., Urban, L., Urban, P., Verderi, M., Walkden, A., Wander, W., Weber, H., Wellisch, J. P., Wenaus, T., Williams, D. C., Wright, D., Yamada, T., Yoshida, H. and Zschiesche, D. (2003). **GEANT4 - a simulation toolkit**. Nucl Instrum Methods Phys Res A *506*(*3*), 250–303.

Akin-Akintayo, O. O., Alexander, L. F., Neill, R., Krupinksi, E. A., Tang, X., Mittal, P. K., Small, W. C. and Moreno, C. C. (2018). **Prevalence and severity of off-centering during diagnostic CT: observations from 57,621 CT scans of the chest, abdomen, and/or pelvis**. Curr Probl Diagn Radiol. URL: https://doi.org/10.1067/j.cpradiol.2018.02.007, in press.

Allison, J., Amako, K., Apostolakis, J., Araujo, H., Dubois, P. A., Asai, M., Barrand, G., Capra, R., Chauvie, S., Chytracek, R., Cirrone, G. A. P., Cooperman, G., Cosmo, G., Cuttone, G., Daquino, G. G., Donszelmann, M., Dressel, M., Folger, G., Foppiano, F., Generowicz, J., Grichine, V., Guatelli, S., Gumplinger, P., Heikkinen, A., Hrivnacova, I., Howard, A., Incerti, S., Ivanchenko, V., Johnson, T., Jones, F., Koi, T., Kokoulin, R., Kossov, M., Kurashige, H., Lara, V., Larsson, S., Lei, F., Longo,

F., Maire, M., Mantero, A., Mascialino, B., McLaren, I., Lorenzo, P. M., Minamimoto, K., Murakami, K., Nieminen, P., Pandola, L., Parlati, S., Peralta, L., Perl, J., Pfeiffer, A., Pia, M. G., Ribon, A., Rodrigues, P., Russo, G., Sadilov, S., Santin, G., Sasaki, T., Smith, D., Starkov, N., Tanaka, S., Tcherniaev, E., Tomé, B., Trindade, A., Truscott, P., Urban, L., Verderi, M., Walkden, A., Wellisch, J. P., Williams, D. C., Wright, D., Yoshida, H. and Peirgentili, M. (2006). **Geant4 developments and applications**. IEEE Trans Nucl Sci *53*(*1*), 270–278.

Amato, E., Lizio, D., Settineri, N., Di Pasquale, A., Salamone, I. and Pandolfo, I. (2010). **A method to evaluate the dose increase in CT with iodinated contrast medium**. Med Phys *37*(*8*), 4249–4256.

Amato, E., Salamone, I., Naso, S., Bottari, A., Gaeta, M. and Blandino, A. (2013). **Can contrast media increase organ doses in CT examinations? A clinical study**. AJR Am J Roentgenol *200*(*6*), 1288–1293.

Amber Diagnostics (2018). **CT scanner comparison chart, Philips Brilliance 16 vs. Toshiba Aquilion 16.** URL: https://www.amberusa.com/blog /ct-scanner-comparison-chart-philips-brilliance-16-vs-toshiba-aquilion-16. [Accessed: 09/19/2018].

Andreo, P. (1991). **Monte Carlo techniques in medical radiation physics**. Phys Med Biol *36*(*7*), 861–920.

Angel, E., Yaghmai, N., Jude, C. M., DeMarco, J. J., Cagnon, C. H., Goldin, J. G., Primak, A. N., Stevens, D. M., Cody, D. D., McCollough, C. H. and McNitt-Gray, M. F. (2010). **Monte Carlo simulations to assess the effects of tube current modulation on breast dose for multidetector CT**. Phys Med Biol *54*(*3*), 497–512.

Ay, M. R., Sarkar, S., Shahriari, M., Sardari, D. and Zaidi, H. (2005). **Assessment of different computational models for generation of x-ray spectra in diagnostic radiology and mammography**. Med Phys *32*(*6*), 1660–1675.

Bae, K. T. (2010). **Intravenous contrast medium administration and scan timing at CT: considerations and approaches**. Radiology *256*(*1*), 32–61.

Baró, J., Sempau, J., Fernández-Varea, J. M. and Salvat, F. (1995). **PENELOPE: an algorithm for Monte Carlo simulation of the penetration and energy loss of electrons and positrons in matter**. Nucl Instrum Methods Phys Res B *100*, 31–46.

Bazalova, M. and Verhaegen, F. (2007). **Monte Carlo simulation of a computed tomography x-ray tube**. Phys Med Biol *52*(*19*), 5945–5955.

Behzadi, A. H., Farooq, Z., Newhouse, J. H. and Prince, M. R. (2018). **MRI and CT contrast media extravasation**. Medicine (Baltimore) *97*(*9*), E0055.

Belley, M. D., Segars, W. P. and Kapadia, A. J. (2014). **Assessment of individual organ doses in a realistic human phantom from neutron and gamma stimulated spectroscopy of the breast and liver**. Med Phys *41*(*6*), 063902.

BfS (2016a). **Röntgendiagnostik – Nutzen und Risiken**. Bundesamt für Strahlenschutz (BfS), 1–5.

BfS (2016b). **Umweltradioaktivität und Strahlenbelastung. Jahresbericht 2015**. Bundesamt für Strahlenschutz (BfS), 1–381.

Bongartz, G., Golding, S. J., Jurik, A. G., van Persijn van Meerten, E., Rodríguez, R., Schneider, K., Geleijns, J., Jessen, K. A., Panzer, W., Shrimpton, P. C. and Tosi, G. (1999). **European guidelines on quality criteria for computed tomography (EU 16262)**. European Comission, 1–107.

Boone, J. M. (2010). **Method for evaluating bow tie filter angle-dependent attenuation in CT: theory and simulation results**. Med Phys *37*(*1*), 40–48.

Boone, J. M., Cooper, V. N., Nemzek, W. R., McGahan, J. P. and Seibert, J. A. (2000). **Monte Carlo assessment of computed tomography dose to tissue adjacent to the scanned volume**. Med Phys *27*(*10*), 2393–2407.

Boos, J., Lanzman, R. S., Heusch, P., Aissa, J., Schleich, C., Thomas, C., Sawicki, L. M., Antoch, G. and Kröpil, P. (2016). **Does body mass index outperform body weight as a surrogate parameter in the calculation of size-specific dose estimates in adult body CT?** Br J Radiol *89*(*1059*), 20150734.

Brady, Z., Cain, T. M. and Johnston, P. N. (2012). **Comparison of organ dosimetry methods and effective dose calculation methods for paediatric CT**. Australas Phys Eng Sci Med *35*(*2*), 117–134.

Brun, R. and Rademakers, F. (1996). **ROOT - an object oriented data analysis framework**. Nucl Instrum Methods Phys Res A *389*(*1-2*), 81–86.

Buffa, V., Solazzo, A., D'Auria, V., Del Prete, A., Vallone, A., Luzietti, M., Madau, M., Grassi, R. and Miele, V. (2014). **Dual-source dual-energy CT: dose reduction after endovascular abdominal aortic aneurysm repair**. Radiol Med *119*, 934–941.

Bushberg, J. T., Seibert, J. A., Leidholdt, E. M. and Boone, J. M. (2012). **The essential physics of medical imaging**, 3rd edition, Lippincott Williams & Wilkins, Philadelphia, PA, USA.

Caon, M., Bibbo, G., Pattison, J. and Bhat, M. (1998). **The effect on dose to computed tomography phantoms of varying the theoretical x-ray spectrum: a comparison of four diagnostic x-ray spectrum calculating codes**. Med Phys *25*(*6*), 1021–1027.

Carver, D. E., Kost, S. D., Fraser, N. D., Segars, W. P., Pickens, D. R., Price, R. R. and Stabin, M. G. (2017). **Realistic phantoms to characterize dosimetry in pediatric CT**. Pediatr Radiol *47*(*6*), 691–700.

Chan, H.-P. and Doi, K. (1983). **The validity of Monte Carlo simulation in studies of scattered radiation in diagnostic radiology**. Phys Med Biol *28*(*2*), 109–129.

Chang, S.-J., Hung, S.-Y., Liu, Y.-L. and Jiang, S.-H. (2016). **Construction of taiwanese adult reference phantoms for internal dose evaluation**. PLoS One *11*(*9*), e0162359.

Chantler, C. T., Olsen, K., Dragoset, R. A., Chang, J., Kishore, A. R., Kotochigova, S. A. and Zucker, D. S. (2017). **Detailed tabulation of atomic form factors, photoelectric absorption and scattering cross section, and mass attenuation coefficients for Z = 1-92 from E = 1-10 eV to E = 0.4-1.0 MeV**. URL: https://physics.nist.gov/PhysRefData/FFast/html/form.html. [Accessed: 09/19/2019].

Chen, W., Kolditz, D., Beister, M., Bohle, R. and Kalender, W. A. (2012). **Fast on-site Monte Carlo tool for dose calculations in CT applications**. Med Phys *39*(*6*), 2985–2996.

Christner, J. A., Kofler, J. M. and McCollough, C. H. (2010). **Estimating effective dose for CT using dose-length product compared with using organ doses: consequences of adopting International Commission on Radiological Protection Publication 103 or dual-energy scanning**. AJR Am J Roentgenol *194*(*4*), 881–889.

Cros, M., Joemai, R. M. S., Geleijns, J., Molina, D. and Salvadó, M. (2017). **SimDoseCT: dose reporting software based on Monte Carlo simulation for a 320 detector-row cone-beam CT scanner and ICRP computational adult phantoms**. Phys Med Biol *62*(*15*), 6304–6321.

Deak, P. D., Smal, Y. and Kalender, W. A. (2010). **Multisection CT protocols: sex- and age-specific conversion factors used to determine effective dose from dose-length product**. Radiology *257*(*1*), 158–166.

Deak, P., Straten, M. van, Shrimpton, P. C., Zankl, M. and Kalender, W. A. (2008). **Validation of a Monte Carlo tool for patient-specific dose simulations in multi-slice computed tomography**. Eur Radiol *18*(*4*), 759–772.

DeMarco, J. J., Cagnon, C. H., Cody, D. D., Stevens, D. M., McCollough, C. H., O'Daniel, J. and McNitt-Gray, M. F. (2005). **A Monte Carlo based method to estimate radiation dose from multidetector CT (MDCT): cylindrical and anthropomorphic phantoms**. Phys Med Biol *50*(*17*), 3989–4004.

DeMarco, J. J., Solberg, T. D. and Smathers, J. B. (1998). **A CT-based Monte Carlo simulation tool for dosimetry planning and analysis**. Med Phys *25*(*1*), 1–11.

Ding, A., Gao, Y., Liu, H., Caracappa, P. F., Long, D. J., Bolch, W. E., Liu, B. and Xu, X. G. (2015). **VirtualDose: a software for reporting organ doses from CT for adult and pediatric patients**. Phys Med Biol *60*(*14*), 5601–5625.

Dowling, J. A. (2013). **Importing contours from DICOM-RT structure sets with ITK4**. URL:

http://hdl.handle.net/10380/3401.
[Accessed: 10/13/2018].

Duan, X., Wang, J., Yu, L., Leng, S. and McCollough, C. H. (2011). **CT scanner x-ray spectrum estimation from transmission measurements**. Med Phys *38*(*2*), 993–997.

Fewell, T. R., Hawkins, K. R. and Shuping, R. E. (1981). **Handbook of computed tomography x-ray spectra**, U.S. Dept. of Health, Human Services, Public Health Service, Food, and Drug Administration, Bureau of Radiological Health, Rockville, MD, USA.

Fogliata, A., Vanetti, E., Albers, D., Brink, C., Clivio, A., Knöös, T., Nicolini, G. and Cozzi, L. (2007). **On the dosimetric behaviour of photon dose calculation algorithms in the presence of simple geometric heterogeneities: comparison with Monte Carlo calculations.** Phys Med Biol *52*(*5*), 1363–1385.

Foray, N., Arlett, C. F. and Malaise, E. P. (1997). **Radiation-induced DNA double-strand breaks and the radiosensitivity of human cells: a closer look**. Biochimie *79*(*9-10*), 567–575.

Fujii, K., Nomura, K., Muramatsu, Y., Obara, S., Akahane, K. and Kusumoto, M. (2017). **Organ dose evaluations based on Monte Carlo simulation for CT examinations using tube current modulation**. Radiat Prot Dosimetry *174*(*3*), 378–394.

Graser, A., Johnson, T. R. C., Hecht, E. M., Becker, C. R., Leidecker, C., Staehler, M., Stief, C. G., Hildebrandt, H., Godoy, M. C. B., Finn, M. E., Stepansky, F., Reiser, M. F. and Macari, M. (2009). **Dual-energy CT in patients suspected of having renal masses: can virtual nonenhanced images replace true nonenhanced umages?** Radiology *252*(*2*), 433–440.

Hall, E. J. and Brenner, D. J. (2008). **Cancer risks from diagnostic radiology**. Br J Radiol *81*(*965*), 362–378.

Hsieh, J. (2015). **Computed Tomography: principles, design, artifacts, and recent advances**, 3rd edition, SPIE Press, Bellingham, WA, USA.

Hsieh, S. S. and Pelc, N. J. (2013). **The feasibility of a piecewise-linear dynamic bowtie filter**. Med Phys *40*(*3*), 031910.

Hubbell, J. H. and Seltzer, S. M. (2018a). **Tables of x-ray mass attenuation coefficients and mass energy-absorption coefficients from 1 keV to 20 MeV for elements Z = 1 to 92 and 48 additional substances of dosimetric interest - Table 2: material constants and composition for compounds and mixture**. URL: https://physics.nist.gov/PhysRefData/XrayMassCoef/tab2.html.
[Accessed: 09/19/2019].

Hubbell, J. H. and Seltzer, S. M. (2018b). **Tables of x-ray mass attenuation coefficients and mass energy-absorption coefficients from 1 keV to 20 MeV for elements Z = 1 to 92 and 48 additional substances of dosimetric interest -**

Table 4: compounds and mixtures. URL:
https://physics.nist.gov/PhysRefData/XrayMassCoef/tab4.html.
[Accessed: 09/19/2019].

Huda, W. (2007). **Radiation doses and risks in chest computed tomography examinations**. Proc Am Thorac Soc *4*, 316–320.

Huda, W., Magill, D. and He, W. (2011). **CT effective dose per dose length product using ICRP 103 weighting factors.** Med Phys *38*(*3*), 1261–1265.

Huda, W. and Mettler, F. A. (2011). **Volume CT dose index and dose-length product displayed during CT: what good are they?** Radiology *258*(*1*), 236–242.

IBA Dosimetry (2009). **ImpactDose**. URL:
http://test.scanditronix-wellhoefer.com
/Software-ImpactDose.1313+M52087573ab0.0.html?{&}cHash=5baba317bf{&}cHash=5baba317bf.
[Accessed: 09/19/2018].

ICRP (1975). **Report of the task group on reference man. ICRP Publication 23**. ICRP, Pergamon Press, Oxford, UK.

ICRP (1977). **Recommendations of the International Commission on Radiological Protection. ICRP Publication 26**. ICRP, Ann. ICRP 1 (3).

ICRP (1991). **The 1990 recommendations of the International Commission on Radiological Protection. ICRP Publication 60**. ICRP, Ann. ICRP 21 (1-3).

ICRP (2007). **The 2007 recommendations of the International Commission on Radiological Protection. ICRP Publication 103**. ICRP, Ann. ICRP 37 (2-4).

ICRP (2018). **Composition of SKIN (ICRP)**. URL:
https://pml.nist.gov/cgi-bin/Star/compos.pl?matno=250.
[Accessed: 09/19/2019].

ICRU (2012). **ICRU Report No. 87: Radiation dose and image-quality assessment in computed tomography**. ICRU, Journal of ICRU 12 (1), Oxford University Press, UK.

ICRU (2018). **Composition of BONE, COMPACT (ICRU)**. URL:
https://pml.nist.gov/cgi-bin/Star/compos.pl?matno=119.
[Accessed: 09/19/2019].

Iliakis, G. E. and Okayasu, R. (1990). **Radiosensitivity throughout the cell cycle and repair of potentially lethal damage and DNA double-strand breaks in an X-ray-sensitive CHO mutant**. Int J Radiat Biol *57*(*6*), 1195–1211.

Imaging Technology News (2014). **Comparison chart computed tomography (CT) systems**. URL:
https://www.itnonline.com/article
/most-popular-radiology-comparison-charts-itn-2016.
[Accessed: 09/19/2018].

ImPACT (2011). **ImPACT CT dosimetry calculator, version 1.0.4**. URL: http://www.impactscan.org/ctdosimetry.htm. [Accessed: 09/19/2018].

Jarry, G., DeMarco, J. J., Beifuss, U., Cagnon, C. H. and McNitt-Gray, M. F. (2003). **A Monte Carlo-based method to estimate radiation dose from spiral CT: from phantom testing to patient-specific models**. Phys Med Biol *48*(*16*), 2645–2663.

Jiang, H., Seco, J. and Paganetti, H. (2007). **Effects of Hounsfield number conversion on CT based proton Monte Carlo dose calculations**. Med Phys *34*(*4*), 1439–1449.

Kalender, W. A. (2014). **Dose in x-ray computed tomography**. Phys Med Biol *59*(*3*), R129–R150.

Kalender, W. A., Deak, P., Kellermeier, M., Van Straten, M. and Vollmar, S. V. (2009). **Application- and patient size-dependent optimization of x-ray spectra for CT**. Med Phys *36*(*3*), 993–1007.

Kalender, W. A., Schmidt, B., Zankl, M. and Schmidt, M. (1999a). **A PC program for estimating organ dose and effective dose values in computed tomography**. Eur Radiol *9*(*3*), 555–562.

Kalender, W. A., Wolf, H. and Suess, C. (1999b). **Dose reduction in CT by anatomically adapted tube current modulation. II. Phantom measurements**. Med Phys *26*(*11*), 2248–2253.

Kim, S., Song, H., Movsas, B. and Chetty, I. J. (2012). **Characteristics of x-ray beams in two commercial multidetector computed tomography simulators: Monte Carlo simulations**. Med Phys *39*(*1*), 320–329.

Kim, S., Yoshizumi, T. T., Yin, F.-F. and Chetty, I. J. (2013). **Spiral computed tomography phase-space source model in the BEAMnrc/EGSnrc Monte Carlo system: implementation and validation**. Phys Med Biol *58*(*8*), 2609–2624.

Kramer, R., Cassola, V. F., Andrade, M. E. A., Araújo, M. W. C. de, Brenner, D. J. and Khoury, H. J. (2017). **Mathematical modelling of scanner-specific bowtie filters for Monte Carlo CT dosimetry**. Phys Med Biol *62*(*3*), 781–809.

Lamba, R., McGahan, J. P., Corwin, M. T., Li, C.-S., Tran, T., Seibert, J. A. and Boone, J. M. (2014). **CT Hounsfield numbers of soft tissues on unenhanced abdominal CT scans: variability between two different manufacturers' MDCT scanners**. AJR Am J Roentgenol *203*(*5*), 1013–1020.

Lee, S. Y., Rhee, C. M., Leung, A. M., Braverman, L. E., Brent, G. A. and Pearce, E. N. (2015). **A review: radiographic iodinated contrast media-induced thyroid dysfunction**. J Clin Endocrinol Metab *100*(*2*), 376–383.

Lee, Y. and Hwang, K. (2002). **Skin thickness of Korean adults**. Surg Radiol Anat *24*(*3-4*), 183–189.

Li, X., Samei, E., Segars, W. P., Sturgeon, G. M., Colsher, J. G., Toncheva, G., Yoshizumi, T. T. and Frush, D. P. (2011a). **Patient-specific radiation dose and cancer risk es-**

timation in CT: Part I. Development and validation of a Monte Carlo program. Med Phys *38*(*1*), 397–407.

Li, X., Samei, E., Segars, W. P., Sturgeon, G. M., Colsher, J. G., Toncheva, G., Yoshizumi, T. T. and Frush, D. P. (2011b). **Patient-specific radiation dose and cancer risk estimation in CT: Part II. Application to patients**. Med Phys *38*(*1*), 408–419.

Lin, Y., Ramirez-Giraldo, J. C., Gauthier, D. J., Stierstorfer, K. and Samei, E. (2014). **An angle-dependent estimation of CT x-ray spectrum from rotational transmission measurements**. Med Phys *41*(*6*), 062104.

Lira, D., Padole, A., Kalra, M. K. and Singh, S. (2015). **Tube potential and CT radiation dose optimization**. AJR Am J Roentgenol *204*(*1*), W4–W10.

Liu, H., Gao, Y., Ding, A., Caracappa, P. F. and Xu, X. G. (2015). **The profound effects of patient arm positioning on organ doses from CT procedures calculated using Monte Carlo simulations and deformable phantoms**. Radiat Prot Dosimetry *164*(*3*), 368–375.

Ljungberg, M. (1998). **Introduction to the Monte Carlo method**. In: Monte Carlo calculations in nuclear medicine: Applications in diagnostic imaging, Eds. Ljungberg, M., Strand, S. E. and King, M. A., 1st edition, Institute of Physics Publishing, London, United Kingdom, pp. 1–12.

Lopez-Rendon, X., Zhang, G., Bosmans, H., Oyen, R. and Zanca, F. (2014). **Implementing the complete beam hardening effect of the bowtie filter versus scaling beam intensities: effects on dosimetric applications in computed tomography**. J Med Imaging (Bellingham) *1*(*3*), 033507.

Lusic, H. and Grinstaff, M. W. (2013). **X-ray-computed tomography contrast agents**. Chem Rev *113*(*3*), 1641–1666.

Massoumzadeh, P., Don, S., Hildebolt, C. F., Bae, K. T. and Whiting, B. R. (2009). **Validation of CT dose-reduction simulation**. Med Phys *36*(*1*), 174–189.

Matscheko, G. and Ribberfors, R. (1987). **A Compton scattering spectrometer for determining x-ray photon energy spectra**. Phys Med Biol *32*(*5*), 577–594.

Matsumoto, M. and Nishimura, T. (1998). **Mersenne Twister: a 623-dimensionally equidistributed uniform pseudo-random number generator**. ACM Trans Model Comput Simul *8*(*1*), 3–30.

McCollough, C. H., Leng, S., Yu, L., Cody, D. D., Boone, J. M. and McNitt-Gray, M. F. (2011). **CT dose index and patient dose: they are not the same thing**. Radiology *259*(*2*), 311–316.

Mettler, F. A. (2012). **Medical effects and risks of exposure to ionising radiation**. J Radiol Prot *32*(*1*), N9–N13.

MHRA (2004). **MHRA Evaluation report 04045: Toshiba Aquilion 16 - CT scanner technical evaluation**. ImPACT report, Crown Copyright.

Nekolla, E. A., Schegerer, A. A., Griebel, J. and Brix, G. (2017). **Häufigkeit und Dosis diagnostischer und interventioneller Röntgenanwendungen: Trends zwischen 2007 und 2014**. Radiologe *57*(*7*), 555–562.

NHS (2009). **Comparative specifications 16 slice CT scanners CEP08025**. NHS - Purchasing and Supply Agency.

Nowik, P., Bujila, R., Kull, L., Andersson, J. and Poludniowski, G. (2017). **The dosimetric impact of including the patient table in CT dose estimates**. Phys Med Biol *62*(*23*), N538–N547.

Pathe, C., Eble, K., Schmitz-Beuting, D., Keil, B., Kaestner, B., Voelker, M., Kleb, B., Klose, K. J. and Heverhagen, J. T. (2011). **The presence of iodinated contrast agents amplifies DNA radiation damage in computed tomography**. Contrast Media Mol Imaging *6*(*6*), 507–513.

Pérez-López, C. E. and Garnica-Garza, H. M. (2011). **Monte Carlo modeling and optimization of contrast-enhanced radiotherapy of brain tumors**. Phys Med Biol *56*(*13*), 4059–4072.

Perisinakis, K., Tzedakis, A., Spanakis, K., Papadakis, A. E., Hatzidakis, A. and Damilakis, J. (2018). **The effect of iodine uptake on radiation dose absorbed by patient tissues in contrast enhanced CT imaging: implications for CT dosimetry**. Eur Radiol *28*(*1*), 151–158.

Raeside, D. E. (1976). **Monte Carlo principles and applications.** Phys Med Biol *21*(*2*), 181–197.

Randazzo, M. and Tambasco, M. (2015). **A rapid noninvasive characterization of CT x-ray sources**. Med Phys *42*(*7*), 3960–3968.

Sahbaee, P., Abadi, E., Segars, W. P., Marin, D., Nelson, R. C. and Samei, E. (2017a). **The effect of contrast material on radiation dose at CT: part II. A systematic evaluation across 58 patient models**. Radiology *283*(*3*), 749–757.

Sahbaee, P., Segars, W. P., Marin, D., Nelson, R. C. and Samei, E. (2017b). **The effect of contrast material on radiation dose at CT: part I. Incorporation of contrast material dynamics in anthropomorphic phantoms**. Radiology *283*(*3*), 739–748.

Salvadó, M., López, M., Morant, J. J. and Calzado, A. (2005). **Monte Carlo calculation of radiation dose in CT examinations using phantom and patient tomographic models**. Radiat Prot Dosimetry *114*(*1-3*), 364–368.

Sandborg, M., Dance, D. R., Persliden, J. and Carlsson, G. A. (1994). **A Monte Carlo program for the calculation of contrast, noise and absorbed dose in diagnostic radiology**. Comput Methods Programs Biomed *42*(*3*), 167–180.

Schegerer, A. A., Nagel, H.-D., Stamm, G., Adam, G. and Brix, G. (2017). **Current CT practice in Germany: results and implications of a nationwide survey**. Eur J Radiol *90*, 114–128.

Schneider, U., Pedroni, E. and Lomax, A. (1996). **The calibration of CT Hounsfield units for radiotherapy treatment planning**. Phys Med Biol *41*(*1*), 111–124.

Seyal, A. R., Arslanoglu, A., Abboud, S. F., Sahin, A., Horowitz, J. M. and Yaghmai, V. (2015). **CT of the abdomen with reduced tube voltage in adults: a practical approach**. RadioGraphics *35*(*7*), 1922–1939.

Shaqdan, K. W., Kambadakone, A. R., Hahn, P. and Sahani, D. V. (2018). **Experience with iterative reconstruction techniques for abdominopelvic computed tomography in morbidly and super obese patients**. J Comput Assist Tomogr *42*(*1*), 124–132.

Sharma, N. and Aggarwal, L. M. (2010). **Automated medical image segmentation techniques**. J Med Phys *35*(*1*), 3–14.

Siegel, J. A., McCollough, C. H. and Orton, C. G. (2017). **Advocating for use of the ALARA principle in the context of medical imaging fails to recognize that the risk is hypothetical and so serves to reinforce patients' fears of radiation**. Med Phys *44*(*1*), 3–6.

Siemens Healthineers (2018). **Simulation of x-ray spectra: online tool for the simulation of x-ray spectra**. URL: https://www.oem-xray-components.siemens.com/x-ray-spectra-simulation. [Accessed: 09/19/2019].

Smith, K. B. and Smith, M. S. (2016). **Obesity statistics**. Prim Care *43*(*1*), 121–135.

Stepusin, E. J., Long, D. J., Marshall, E. L. and Bolch, W. E. (2017). **Assessment of different patient-to-phantom matching criteria applied in Monte Carlo-based computed tomography dosimetry**. Med Phys *44*(*10*), 5498–5508.

Stiller, W. (2011). **Grundlagen der Mehrzeilendetektor-Computertomographie: Teil 1: Technischer Aufbau und physikalisch-technische Grundlagen**. Radiologe *51*(*7*), 625–639.

Stiller, W. (2018). **Basics of iterative reconstruction methods in computed tomography: a vendor-independent overview**. Eur J Radiol *109*, 147–154.

Streitmatter, S. W., Stewart, R. D., Jenkins, P. A. and Jevremovic, T. (2017). **DNA double strand break (DSB) induction and cell survival in iodine-enhanced computed tomography (CT)**. Phys Med Biol *62*(*15*), 6164–6184.

Taleei, R. and Shahriari, M. (2009). **Monte Carlo simulation of x-ray spectra and evaluation of filter effect using MCNP4C and FLUKA code**. Appl Radiat Isot *67*(*2*), 266–271.

Teeuwisse, W. M., Geleijns, J., Broerse, J. J., Obermann, W. R. and Van Persijn Van Meerten, E. L. (2001). **Patient and staff dose during CT guided biopsy, drainage and coagulation**. Br J Radiol *74*(*884*), 720–726.

The Geant4 Collaboration (2008). **Geant4 Physics Reference Manual 4.9.2.**

Toepker, M., Moritz, T., Krauss, B., Weber, M., Euller, G., Mang, T., Wolf, F., Herold, C. J. and Ringl, H. (2012). **Virtual non-contrast in second-generation, dual-energy computed tomography: reliability of attenuation values**. Eur J Radiol *81*(*3*), e398–e405.

UKHD (2017). **Strukturierter Qualitätsbericht für das Berichtsjahr 2016**. Universtitätsklinikum Heidelberg, Heidelberg, Germany.

Vanderstraeten, B., Chin, P. W., Fix, M., Leal, A., Mora, G., Reynaert, N., Seco, J., Soukup, M., Spezi, E., De Neve, W. and Thierens, H. (2007). **Conversion of CT numbers into tissue parameters for Monte Carlo dose calculations: a multi-centre study**. Phys Med Biol *52*(*3*), 539–562.

Veloza, S. (2012). **Experimental dosimetry and simulation of computed tomography radiation exposure: approaches for dose reduction**. Scientific dissertation. University of Heidelberg, Heidelberg, Germany.

Verhaegen, F., Reniers, B., Deblois, F., Devic, S., Seuntjens, J. and Hristov, D. (2005). **Dosimetric and microdosimetric study of contrast-enhanced radiotherapy with kilovolt x-rays**. Phys Med Biol *50*(*15*), 3555–3569.

Wang, L., Li, Q., Wang, X.-M., Hao, G.-Y., Jie-Bao, Hu, S. and Hu, C.-H. (2017). **Enhanced radiation damage caused by iodinated contrast agents during CT examination**. Eur J Radiol *92*, 72–77.

Wang, R., Schoepf, U. J., Wu, R., Reddy, R. P., Zhang, C., Yu, W., Liu, Y. and Zhang, Z. (2012). **Image quality and radiation dose of low dose coronary CT angiography in obese patients: sinogram affirmed iterative reconstruction versus filtered back projection**. Eur J Radiol *81*(*11*), 3141–3145.

Wei, J. C. J., Edwards, G. A., Martin, D. J., Huang, H., Crichton, M. L. and Kendall, M. A. F. (2017). **Allometric scaling of skin thickness, elasticity, viscoelasticity to mass for micro-medical device translation: from mice, rats, rabbits, pigs to humans**. Sci Rep *7*(*1*), 15885.

Xu, X. G. (2014). **An exponential growth of computational phantom research in radiation protection, imaging, and radiotherapy: a review of the fifty-year history**. Phys Med Biol *59*(*18*), R233–R302.

Zhou, H. and Boone, J. M. (2008). **Monte Carlo evaluation of CTDI (infinity) in infinitely long cylinders of water, polyethylene and PMMA with diameters from 10 mm to 500 mm**. Med Phys *35*(*6*), 2424–2431.

Zubal, I. G. (1998). **Anthropomorphic phantoms**. In: Monte Carlo calculations in nuclear medicine: Applications in diagnostic imaging, Eds. Ljungberg, M., Strand, S.-E. and King, M. A., 1st edition, Institute of Physics Publishing, London, United Kingdom, pp. 25–35.

8

OWN CONTRIBUTIONS

8.1 PUBLISHED RESULTS OF THIS WORK

Steuwe, A., Veloza, S., Skornitzke, S., Pahn, G., Kauczor, H.-U. and Stiller, W. (2018). **Modeling spectral properties of x-ray sources for dosimetric Monte Carlo simulations of computed tomography: influence on total energy deposition and spatial distribution of deposited energy**. Nucl Instruments Methods Phys Res A *904*, 130–139.

This publication is based on the results of section 3.1 and their discussion in section 4.1 of this doctoral thesis. Study design, execution, data analysis, and manuscript preparation were primarily performed by the author of this thesis.

8.2 OTHER OWN PEER-REVIEWED JOURNAL CONTRIBUTIONS

Koulouri, O., Steuwe, A., Gillett, D., Hoole, A., Powlson, A., Donnelly, N., Burnet, N., Antoun, N., Cheow, H., Mannion, R., Pickard, J. and Gurnell, M. (2015). **A role for ^{11}C-methionine PET imaging in ACTH-dependent Cushing's syndrome**. Eur J Endocrinol *173*(*4*), M107–M120.

Steuwe, A., Geisbüsch, P., Schulz, C., Böckler, D., Kauczor, H.-U. and Stiller, W. (2016). **Comparison of radiation exposure associated with intraoperative cone-beam computed tomography and follow-up multidetector computed tomography angiography for evaluating endovascular aneurysm repairs**. J Endovasc Ther *23*(*4*), 583–92.

Stiller, W., Veloza, S., Steuwe, A., Skornitzke, S., Pahn, G. and Kauczor, H.-U. (2019). **Characterization and modeling of the beam-shaping filter of a CT system on the basis of spectral measurements: comparison of measured and Monte Carlo simulated filtered x-ray transmission spectra**. In preparation.

8.3 FIRST AND CO-AUTHORSHIP CONFERENCE CONTRIBUTIONS

Fink, M. A., Steuwe, A., Cattelaens, M., Born, L., Stiller, W., Kauczor, H.-U. and Rengier, F. (2018). **Dual-energy computed tomography imaging of the aorta after endovascular repair: potential for decreasing radiation dose**. Poster ESR EuroSafe Imaging *ESI-0037*.

Koulouri, O., Hoole, A., Steuwe, A., Gillett, D., Powlson, A., Akker, S., Aylwin, S., Brooke, A., Buch, H., Drake, W., Levy, M., Siddiqi, A., Simpson, H., Chatterjee, K., Burnet, N., Antoun, N., Heak, C., Mannion, R., Pickard, J. and Gurnell, M.

(2015). **A role for ^{11}C-methionine PET/CT-MRI in the management of de novo and residual acromegaly**. Endocr Abstr *38*(*P299*).

Powlson, A., Koulouri, O., Steuwe, A., Gillett, D., Heard, S., Hoole, A., Scott, M., Challis, B., Antoun, N., Cheow, H., Mannion, R. and Gurnell, M. (2015). **'Pseudo-resistance' in macroprolactinomas treated with dopamine agonists; recognising delayed radiological response and a role for ^{11}C-methionine PET-CT in guiding management**. Endocr Abstr *37*(*GP20.08*).

Steuwe, A., Geisbüsch, P., Schulz, C., Böckler, D., Kauczor, H.-U. and Stiller, W. (2016a). **Comparison of radiation exposure associated with intraoperative CBCT and follow-up MDCT for evaluating EVAR procedures**. Insights Imaging *7*(*S 01*), S162–S465 (B–1210).

Steuwe, A., Geisbüsch, P., Schulz, C., Böckler, D., Kauczor, H.-U. and Stiller, W. (2016b). **Vergleich der Strahlenexposition von intraoperativer „Cone-beam" CT und Follow-up Mehrzeilendetektor-CT Untersuchungen zur Evaluierung der endovaskulären Aortenreperatur**. Fortschr Röntgenstr (RöFo) *118*(*S 01*), WISS302–7.

Steuwe, A., Kauczor, H.-U. and Stiller, W. (2017a). **Monte Carlo simulation of contrast-agent induced local dose build-up in an anthropomorphic abdomen phantom: effects of different CT x-ray spectra on relative absorption increase**. Med Phys *44*(*6*), 2612–2720 (TU–RPM–GePD–IT–02).

Steuwe, A., Kauczor, H.-U. and Stiller, W. (2017b). **Monte-Carlo simulation of iodine enhancement in an anthropomorphic abdomen phantom: effects of different primary MDCT x-ray spectra on energy deposition**. Insights Imaging *8*(*S 01*), S1–S583 (B–0131).

Steuwe, A., Kauczor, H.-U. and Stiller, W. (2017c). **Properties of primary MDCT x-ray source spectra: influence on total energy deposition and spatial absorption distribution**. Insights Imaging *8*(*S 01*), S1–S583 (B–0656).

Stiller, W., Pahn, G., Steuwe, A., Hansen, J., Skornitzke, S. and Kauczor, H.-U. (2016). **Appropriate image quality of computed tomography examinations: what is "appropriate" & how can it be reproducibly achieved?** Poster ESR EuroSafe Imaging *ESI-0052*.

A

SCANNER SPECIFICATIONS

Two CT scanners were implemented in the MC simulation software, including simplified models of the corresponding detectors. The specification of both scanners are given below. Since spectral measurements, including transmission measurements, have only been performed on the Toshiba Aquilion™16 (Toshiba Medical Systems Corporation, Nasu, Japan) this scanner model was used for the simulation of all CT acquisitions.

A.1 AQUILION™16

Table A.1: Computed tomography scanner information of an Aquilion™16, Toshiba Medical Systems Corporation, Nasu, Japan. Information obtained from Amber Diagnostics (2018), MHRA (2004), and NHS (2009).

Parameter name	**Value**
Scanner type	3rd generation
Gantry opening [mm]	720
Source-to-object distance [mm]	600
Source-to-detector distance [mm]	1072
Fan-beam angle [degree]	49.2
Pitch	0.625-1, 1.125-1.5
Scan field-of-view (FOV) [cm]	18, 24, 32, 40, 50
Reconstruction matrices [pixel x pixel]	512 x 512
Dose modulation technique	SureExposure3D
X-ray tube	CXB-750D
X-ray tube anode	tungsten, molybdenum, graphite
kV_p-range	80, 100, 120, 135
mA-range	10-500
Detector type	solid-state Gd_2O_2S
Number of rows along z-axis	40
Detector width at isocenter [mm]	32
Number of detector elements	14336
Elements per row	896

A.2 SOMATOM® DEFINITION FLASH

Table A.2: Computed tomography scanner information of a Somatom® Definition Flash, Siemens Healthineers, Forchheim, Germany. Information obtained from Amber Diagnostics (2018), Imaging Technology News (2014), and Lin et al. (2014).

Parameter name	**Value**
Scanner type	3rd generation
Gantry opening [mm]	780
Source-to-object distance [mm]	595.0
Source-to-detector distance [mm]	1085.6
Fan-beam angle [degree]	49.95
Pitch	0.35 - 3.2
Scan field-of-view (FOV) [cm]	50
Reconstruction matrices [pixel x pixel]	512 x 512
Dose modulation technique	CARE Dose4D, CARE kV
X-ray tube anode	Straton MX P
kV_p-range	70, 80, 100, 120, 140
mA-range	20-800
Detector type	2 x multislice Stellar detector
Number of rows along z-axis	128 (2 x 64)
Detector width at isocenter [mm]	38.4
Number of detector elements	77824 (47104 system A; 30720 system B)
Elements per row	1216 (736 system A; 480 system B)

B

MATERIAL COMPOSITIONS

Table B.1: Basic material composition and densities of the human body materials employed in the simulations. Material density was not altered for geometrical phantoms. For digitized patient phantoms, density was altered according to the Hounsfield units of the image pixels. The source code of Geant4 included several example simulations which provided the material definitions for the bones (e.g. file path: geant4.9.2.p04/examples/extended/medical/DICOM/DicomDetectorConstruction.cc). Abbreviations: trabec.: trabecular, exp.: expiration, in.: inspiration.

		Percentage Z-fraction by weight [%]											
	ρ	1	6	7	8	11	12	15	16	17	19	20	26
Material	$[\frac{g}{cm^3}]$	H	C	N	O	Na	Mg	P	S	Cl	K	Ca	Fe
[a]Blood	1.060	10.2	11.0	3.3	74.5	0.1		0.1	0.2	0.3	0.2		0.1
[b]Bone-dense	1.575	5.6	23.5	5.0	43.4	0.1	0.1	7.2	0.3	0.1	0.1	14.6	
[b]Bone-trabec.	1.159	8.5	40.4	5.8	36.7	0.1	0.1	3.4	0.2	0.2	0.1	4.4	0.1
[a]Breast	1.020	10.6	33.2	3.0	52.7	0.1		0.1	0.2	0.1			
[a]Fat	0.950	11.4	59.8	0.7	27.8	0.1			0.1	0.1			
[c]Kidney	1.050	10.3	13.2	3.0	72.4	0.2		0.2	0.2	0.2	0.2	0.1	
[d]Liver	1.060	10.2	13.9	3.0	71.6	0.2		0.3	0.3	0.2	0.3		
[a]Lung (exp.)	0.508	10.3	10.5	3.1	74.9	0.2		0.2	0.3	0.3	0.2		
[a]Lung (in.)	0.217	10.3	10.5	3.1	74.9	0.2		0.2	0.3	0.3	0.2		
[a]Muscle	1.050	10.2	14.3	3.4	71.0	0.1		0.2	0.3	0.1	0.4		
[d]Pancreas	1.040	10.6	16.9	2.2	69.4	0.2		0.2	0.1	0.2	0.2		
[e]Skin	1.100	10.1	22.8	4.6	61.9	*							
[a]Soft tissue	1.060	10.2	14.3	3.4	70.8	0.2		0.3	0.3	0.2	0.3		
[d]Spleen	1.060	10.3	11.3	3.2	74.1	0.1		0.3	0.2	0.2	0.3		
[a]Water	1.000	11.2			88.8								

* additional components: Na, Mg, P, S, Cl, K, Ca, Fe, Zn: 0.6% together

a (Hubbell and Seltzer 2018a)
b (Geant4-Dicom-example)
c (Chang et al. 2016)
d (Carver et al. 2017)
e (ICRP 2018)

C

ANALYSIS OF SIMULATION RUN TIME AND DATA STORAGE

One major difference between the software developed in this work and commercially available software is the extensive data output available from the simulations. Commercially available software usually only provides dose maps and organ doses. The output in this work contains additional information e.g. about the interaction type, material information, and incident photon energy. The additional information comes with large volumes of data and a longer run time of the simulations.
To compare the potential for time and data volume saving, a simulation with the same seed was run twice – once with the extensive data output, and once with only the storage of a 3D-energy map. For this purpose, a non-enhanced acquisition of the modified abdomen phantom was simulated at a tube potential of 80 kV_p (including aluminum filtration) for $129 \cdot 10^6$ photons (z-coverage of 40 cm + 3.2 cm [-21.6 cm, 21.6 cm], $3 \cdot 10^6$ photons per cm, source collimation 32 mm, pitch 1.0). Run time, data file volume, and energy maps were compared.

The simulation with full data output took 16.5 hours, whereas the simulation with the reduced output took 16.4 hours for the simulation of $129 \cdot 10^6$ photons. Hence, run times were almost identical. In general, run times depended more on the number of cores that were active during run time (how many simulations run simultaneously) than on the output storage.
However, the file size was reduced considerably for the reduced output. A file size of 144.7 MiB (151.7 MB) was obtained for the reduced output, whereas a file size of 21.5 GiB (23.1 GB) was obtained from the full simulation output.
Since the disk space was not critical during this work, full data output was obtained for all of the performed simulations. Simulations were performed using an Intel® Core™ i7-3930K processor, 3.20 GHz (Intel Corporation, Santa Clara, USA) with 64 GB RAM.

D

SOFTWARE TOOLS USED FOR DATA ANALYSIS

D.1 MASKS FROM RT-STRUCTURE SET BINARY STACKS

The radiotherapy (RT) structure sets obtained from Oncentra® External Beam (version 4.5.2, Nucletron B.V, Veenendaal, the Netherlands) were processed using an open-source program ("Importing Contours from DICOM-RT Structure Sets with ITK4") based on ITK4 to obtain binary masks of the contoured organs and tissues (output: niftii-file stack for each contoured organ, Dowling 2013).

D.2 IMAGEJ 1.51J8

ImageJ, version 1.51j8 (Wayne Rasband, National Institutes of Health, USA) was employed for the post-processing of structure sets and analysis of ROIs.

STRUCTURE SETS The binary image stacks (values inside mask 1, outside mask 0) of the contoured organs were multiplied in ImageJ with fixed value (material ID). All processed organ/tissue mask stacks were added, to obtain a single stack containing all masks (each mask is distinguishable by its value, the material ID). The final stack is then saved into individual image files. These files can then be further processed in the segmentation process (see figure 2.14), to combine them with the material files from 'gdcm_setup'.

ROI ANALYSIS The energy deposition and relative differences between simulated enhanced and non-enhanced acquisitions in the ROIs in the modified abdomen and digitized patient phantom were measured in *ImageJ* 1.51j8 for the analysis of the energy build-up effect.

D.3 TABULAR EVALUATION

Microsoft Excel 2016 (Microsoft Corporation, Redmond, Washington, USA) and LibreOffice Calc (version 5.3.5.2, The Document Foundation, Berlin, Germany) were used for data analysis and statistical calculations.

E

EMPLOYED MEASURED AND GENERATED X-RAY SPECTRA

In the following, the spectra plotted in figure 2.2 and figure 2.5 are plotted in more detail. Siemens spectra are available from Siemens Healthineers (2018). An aluminum filter of 3.3 mm was employed for all spectra, as this filtration shifts the mean spectral energy of the unfiltered generated spectrum (51.5 keV) at 120 kV_p to the mean spectral energy, $E_{mean,ref}$, of the measured reference spectrum (57.7 keV) at 120 kV_p at 0° fan angle.

E.1 MEASURED REFERENCE SPECTRUM

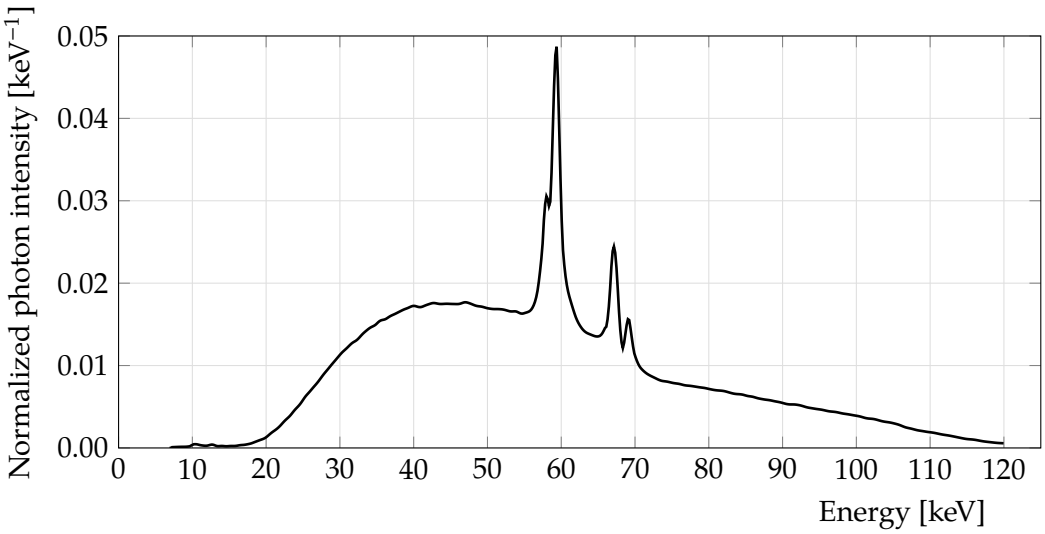

Figure E.1: Measured, normalized central spectrum at 120 kV_p. Mean spectral energy of this spectrum is 57.7 keV. This spectrum was measured prior to this work, see Stiller et al. (2019) and Veloza (2012) for details on the measurement procedure.

E.2 GENERATED SPECTRA

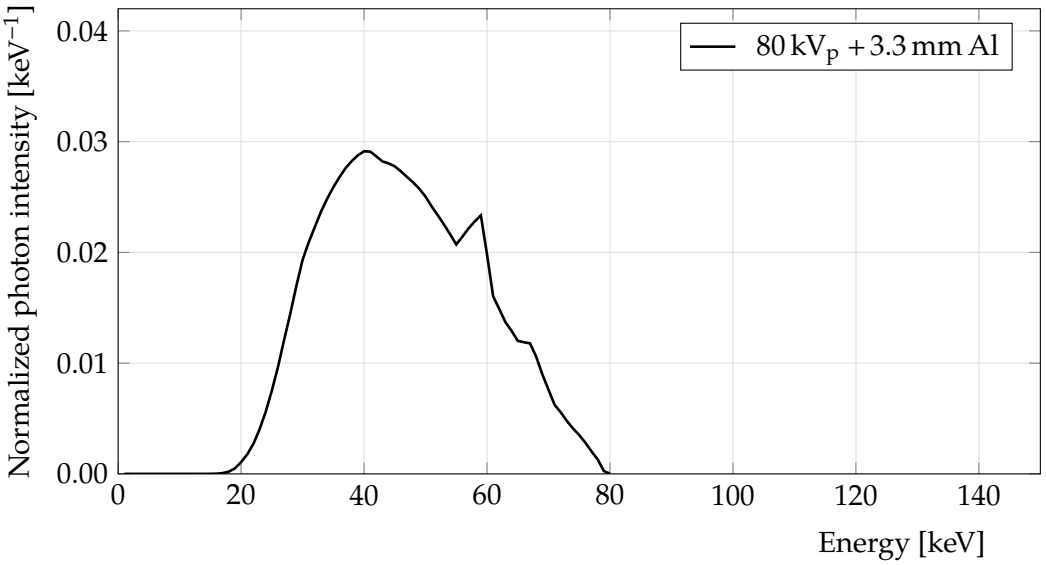

Figure E.2: Generated spectrum at 80 kV_p with 3.3 mm aluminum (Al) filtration. Mean spectral energy of this spectrum is 46.6 keV. Siemens spectra available from Siemens Healthineers (2018).

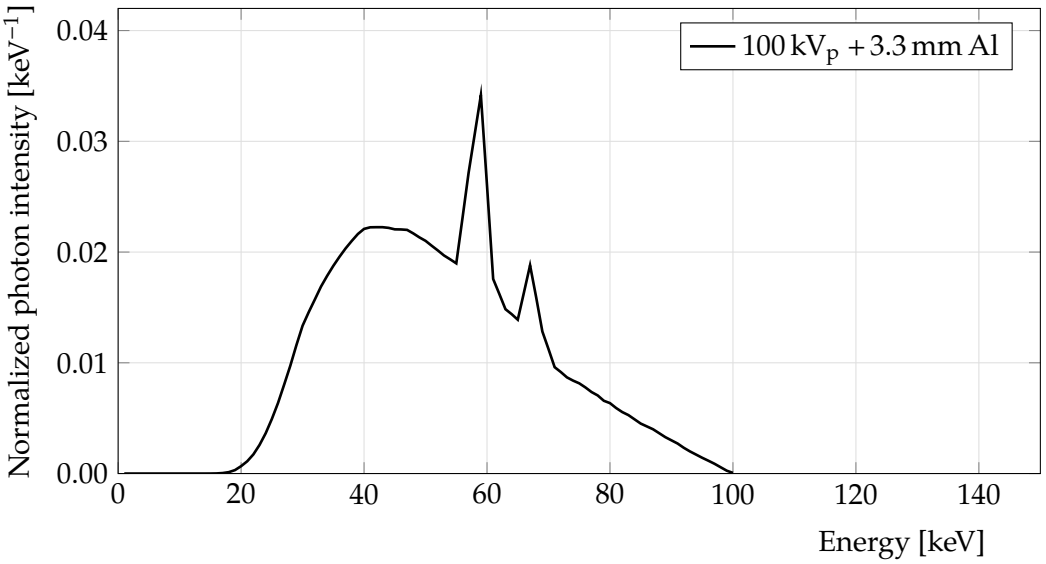

Figure E.3: Generated spectrum at 100 kV_p with 3.3 mm aluminum (Al) filtration. Mean spectral energy of this spectrum is 52.7 keV. Siemens spectra available from Siemens Healthineers (2018).

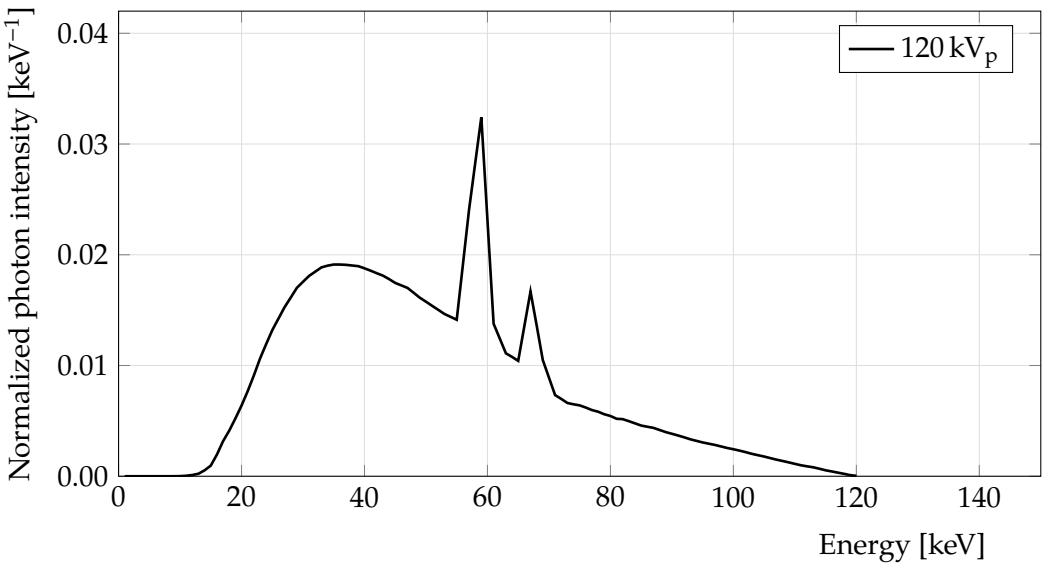

Figure E.4: Generated, unfiltered spectrum at 120 kV_p. Mean spectral energy of this spectrum is 51.5 keV. Siemens spectra available from Siemens Healthineers (2018).

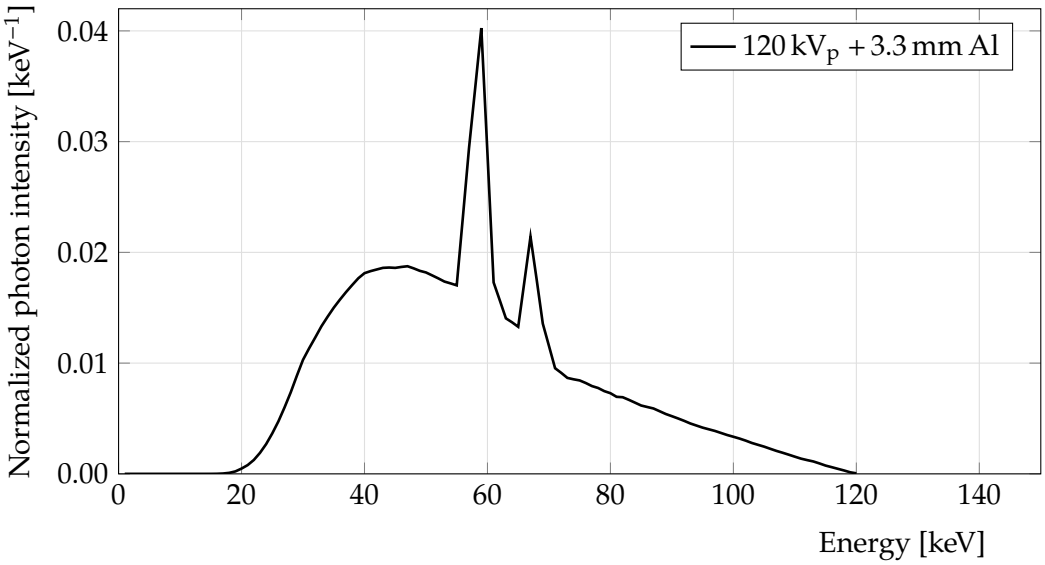

Figure E.5: Generated spectrum at 120 kV_p with 3.3 mm aluminum (Al) filtration. The additional filtration removes photons with energies < 20 keV, thereby increasing the relative peak-height of the characteristic peaks. By adding the aluminum filtration, the mean spectral energy increases from 51.5 keV to 57.7 keV. Siemens spectra available from Siemens Healthineers (2018).

F

BEAM-SHAPING FILTER DIMENSIONS

Prior to the work presented here, a physical beam-shaping filter model for MC simulations has been developed (Stiller et al. 2019; Veloza 2012). This appendix presents the shape and size of the developed and employed beam-shaping filter. The beam-shaping filter was constructed by subtraction of regular trapezoidal Boolean solids from a rectangular box (Steuwe et al. 2018; Veloza 2012).

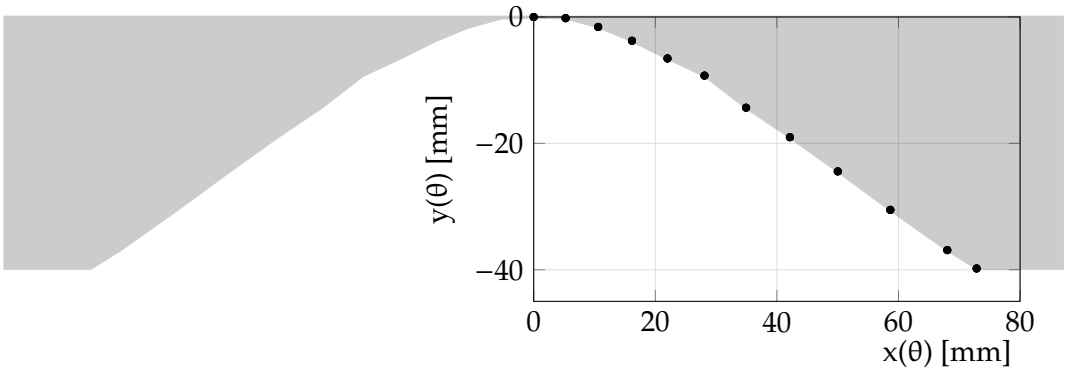

Figure F.1: Employed physical beam-shaping model. Adapted from Stiller et al. (2019). The model was developed prior to this work (Veloza 2012).

Table F.1: X-ray path length through the physical beam-shaping filter and corresponding dimensions (Stiller et al. 2019; Veloza 2012).

	X-ray path	**Beam-shaping filter**	
Fan angle [°]	**length [mm]**	**length x(0) [mm]**	**thickness y(0) [mm]**
0	0.0000	0.0000	- 0.0000
2	0.1954	5.2449	- 0.1953
4	1.5818	10.5994	- 1.5779
6	3.7910	16.1619	- 3.7702
8	6.6335	22.0043	- 6.5689
10	9.4248	28.0856	- 9.2816
12	14.6800	34.9356	-14.3592
14	19.6062	42.1424	-19.0238
16	25.4191	50.0183	-24.4344
18	32.0951	58.6559	-30.5242
20	39.2600	68.0232	-36.8923
21	42.6265	72.8556	-39.7953

G

CT ACQUISITION MODE IMPLEMENTATION

In the following, the different CT acquisition modes, implemented in the MC model, are shortly described.

G.1 STEP-AND-SHOOT/AXIAL ACQUISITION MODE

For the step-and-shoot/axial acquisition mode, the point source moves in a 360°-rotation around the patient during which is patient remains stationary. After one rotation, the patient is moved by the length of the detector coverage or a defined larger or smaller step. Figure G.1 depicts the influence of the step size on energy deposition, for a fixed z-collimation of 32 mm.

G.2 HELICAL/SPIRAL ACQUISITION MODE

For the helical/spiral acquisition mode, the x-ray source rotates around the patient while the patient table is moving through the scanner gantry (continuous movement with fixed table speed). The pitch describes the relationship between table displacement during a full source rotation and z-collimation of the x-ray source (see section 1.2.3). Figure G.2 presents the influence of the pitch on the energy deposition. Z-collimation was fixed to 32 mm, whereas table displacement was increasing from 16 mm (pitch of 0.5) to 64 mm (pitch of 2.0).

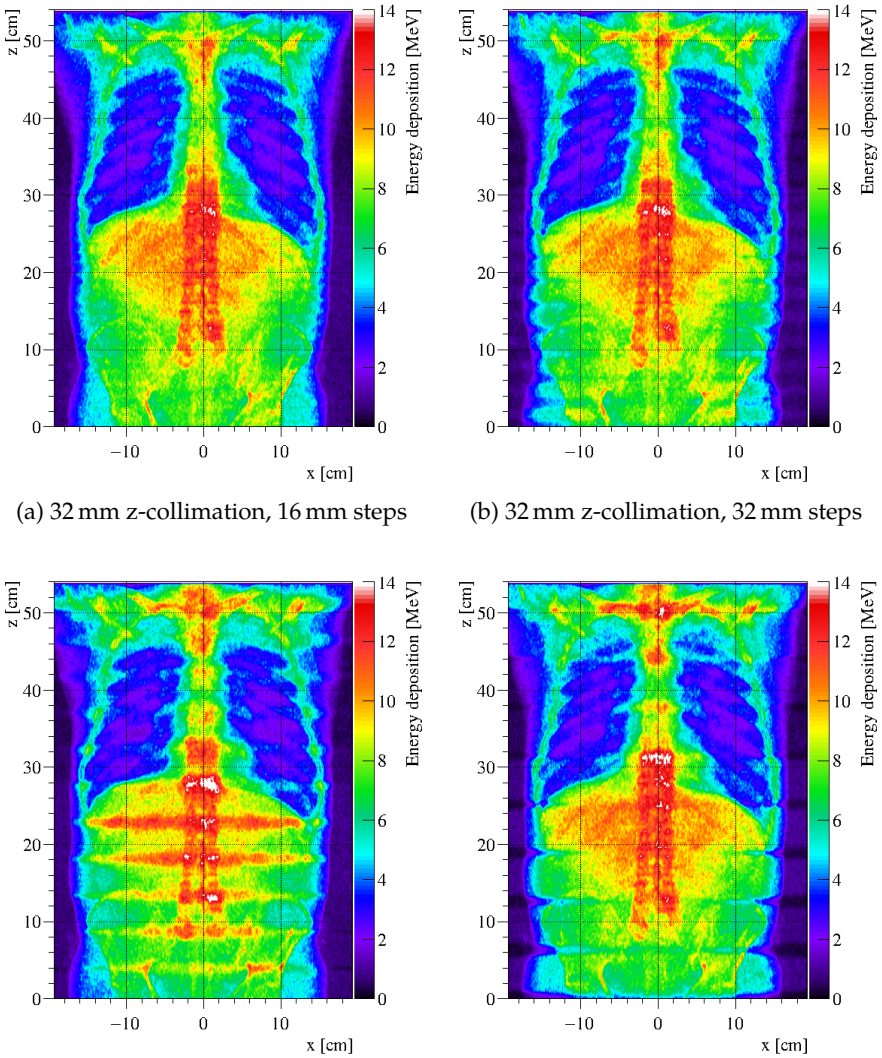

(a) 32 mm z-collimation, 16 mm steps

(b) 32 mm z-collimation, 32 mm steps

(c) 32 mm z-collimation, 48 mm steps

(d) 32 mm z-collimation, 64 mm steps

Figure G.1: Implementation of the step-and-shoot acquisition mode for a z-collimation of 32 mm at the isocenter, and steps of 16, 32, 48, and 64 mm. An increasing step size between two adjacent 360°-rotations results in a streaky pattern in the spatial distribution of energy deposition in the patient. Energy maps presented here show the summed energy deposition along the y-axis of the patient. Although the z-collimation of the x-ray source is set to 32 mm at the isocenter, energy deposition from one "shoot" is spread over an area of ~ 6-7 cm in z-direction, due to energy deposition emerging from scattered photons. The high-energy streaks in (c) are due to overlaps of these "scatter areas" (streak width of ~ 1.5 cm).

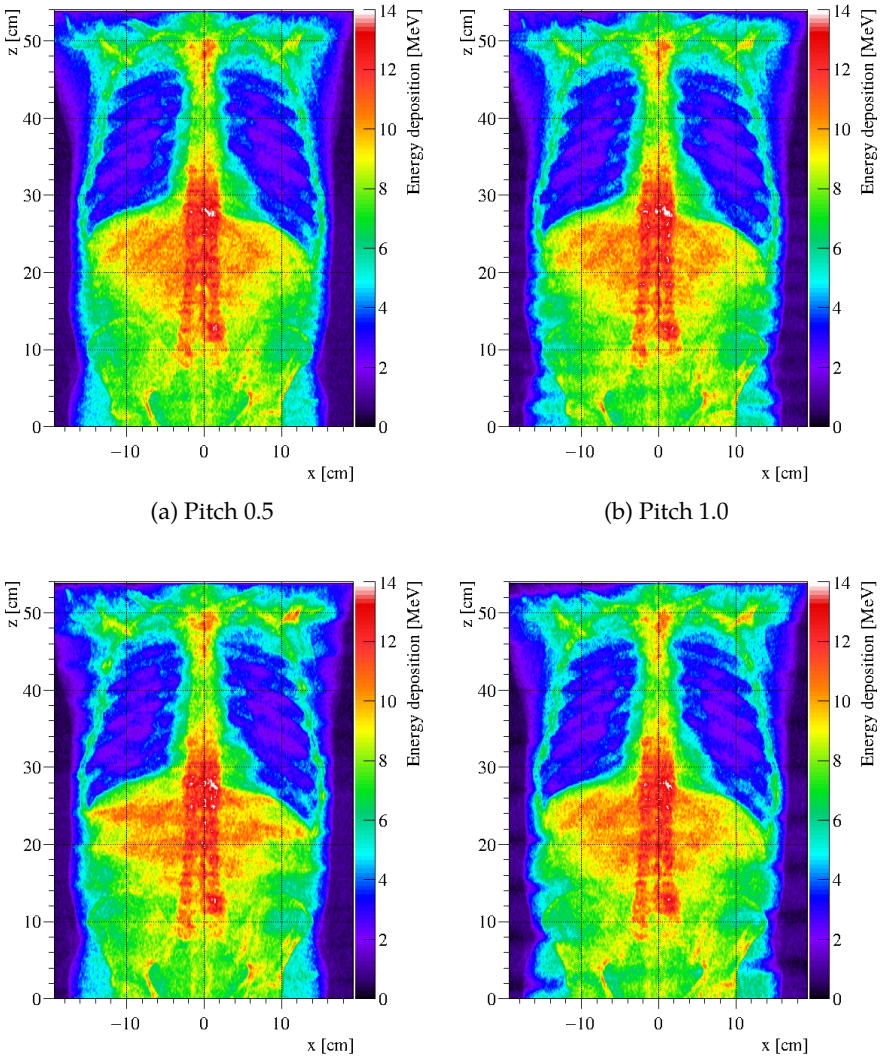

(a) Pitch 0.5

(b) Pitch 1.0

(c) Pitch 1.5

(d) Pitch 2.0

Figure G.2: Implementation of the helical acquisition mode, for pitches of 0.5, 1.0, 1.5, and 2.0. With increasing pitch value, the z-displacement of the x-ray source per 360°-rotation increases, resulting in a streaky pattern of the spatial distribution of energy deposition in the patient. Energy maps presented here show the summed energy deposition along the y-axis of the patient.

G.3 LONGITUDINAL TUBE-CURRENT MODULATION (LTCM)

The exposure along the patient length is determined from the topograms/scout scans, acquired at the start of each CT acquisition. Figure G.3 depicts the normalized exposure values along the patient length with the corresponding lateral topogram. Figure G.4 shows the corresponding energy maps. In figure G.4a, a homogeneous photon distribution was applied, resulting in a high energy deposition at the heart. Employing LTCM reduces the exposure in the lungs and the heart and increases exposure in the abdomen and towards the pelvis. This increases the signal-to-noise ratio in the detector, while increasing the energy deposition in the pelvic region.

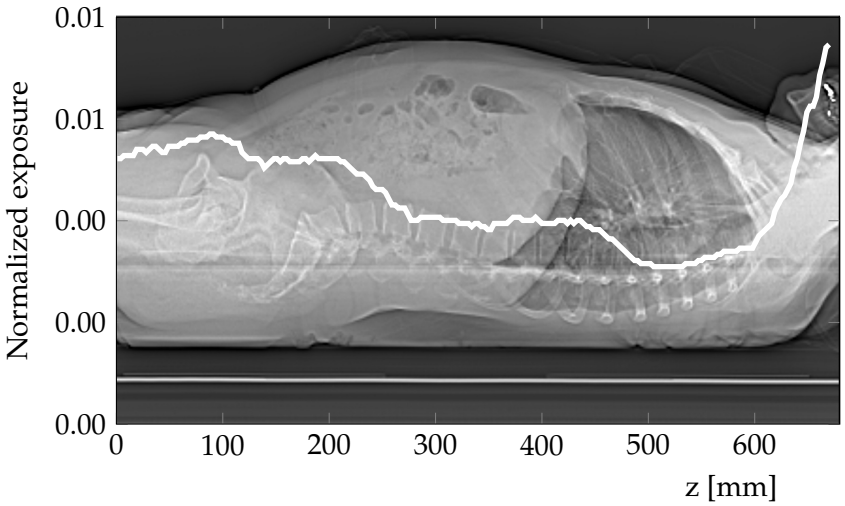

Figure G.3: Modulated tube current along the z-axis of the patient. The longitudinal tube-current modulation (LTCM) decreases the tube current in areas of low attenuation (e.g. the lungs) and increases tube current in highly attenuating areas, such as the shoulders or hips. The resulting spatial distribution of energy deposition is presented in figure G.4.

G.4 ANGULAR TUBE-CURRENT MODULATION (ATCM)

Angular tube-current modulation (ATCM) alters the exposure during a single rotation of the x-ray source. In this implementation, the attenuation of the table is not accounted for, hence, tube current at 0° and at 180° are equal. Figure G.5 depicts the increase in energy deposition at the patients lateral sides and the decrease in energy deposition at the a.p. sides (especially in the paravertebral muscles), due to the increased x-ray exposure from the lateral directions and decreased x-ray exposure from the a.p. directions.

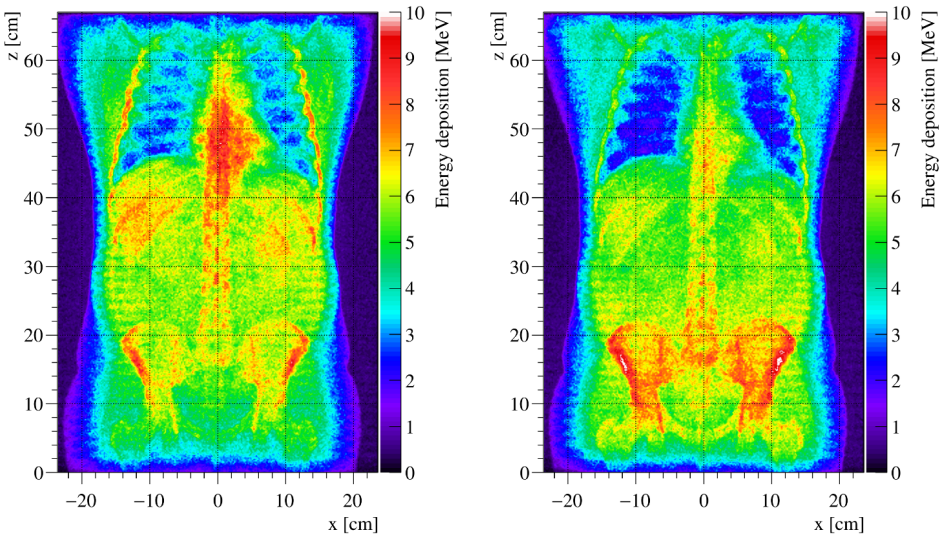

(a) 32 mm collimation, 16 mm steps, without LTCM

(b) 32 mm collimation, 16 mm steps, with LTCM

Figure G.4: Effect of longitudinal tube-current modulation (LTCM) on spatial distribution of energy deposition. LTCM increases the tube-current time product in areas of higher density (bones in the pelvic region) and diameter (shoulders), causing an increased energy deposition, especially in the pelvic region. Energy deposition in the lungs and heart is reduced if the modulated tube current is applied. The correspoding modulated exposure progression is plotted in figure G.3.

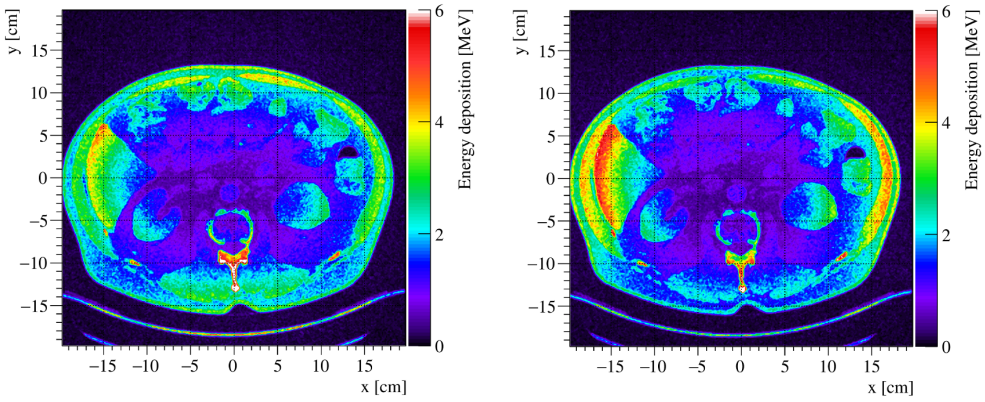

(a) Without ATCM

(b) With ATCM

Figure G.5: Implementation of angular tube-current modulation (ATCM) to increase exposure in lateral direction and to reduce exposure in anterio-posterior direction. Increased energy deposition is visible in the liver, whereas a decreased energy deposition is visible in the paravertebral muslces, if ATCM is applied.

H

DIGITIZED PATIENT PHANTOM

H.1 AUTOMATIC SEGMENTATION USING THRESHOLDING

In the gd4cm_setup program, CT images are automatically segmented using a thresholding method. In this automatic method, the tissues air, lung (in- and exhale), fat, water, soft tissue, and bone (trabecular and dense) are assigned (other individual organs are segmented in a later, manual step). The input file (g4dcm-data.dat) is required to start the automatic segmentation of DICOM images. The input file (listing H.1) includes information about the compression (1), number (5), and names of image files (Patient1A_nat33_101-105), and material selection with maximum density values (e.g. Air 0.03 g/cm^3, DenseBone 1.654 g/cm^3). In this example, only five CT images are automatically segmented.

Listing H.1: gdcm-data.dat input file

```
1                                  %compression
5                                  %number of input files
input_dcm/Patient1A_nat33_101      %input files
input_dcm/Patient1A_nat33_102
input_dcm/Patient1A_nat33_103
input_dcm/Patient1A_nat33_104
input_dcm/Patient1A_nat33_105
8                                  %number of materials
Air 0.03                           %materials with maximum density
LungInhale 0.390
LungExhale 0.910
AdiposeTissue 0.98
Water 1.02
SoftT 1.09
TrabecularBone 1.165
DenseBone 5.0
```

The CT2Density.dat file (listing H.2) is required for the calculation of density values for each pixel. The density (given in g/mm^3) is calculated by interpolation between the CT number/density pairs given in the lookup table (see also figure H.1). The calculated density values, in contrast to the material IDs, are not altered during the segmentation process.

Listing H.2: CT2Density.dat input file

```
9                                  %number of CT number-density pairs
-5000   0.0                        %CT number-density pairs
-1000   0.0
-400    0.602
-130    0.95
```

```
0       1.0
100     1.075
300     1.145
2000    1.856
4927    3.379
```

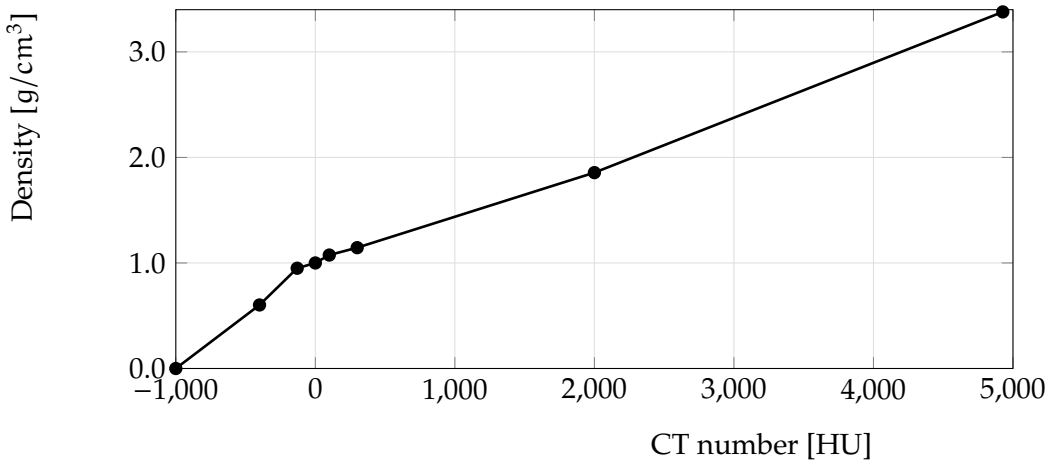

Figure H.1: Plotted computed tomography (CT) number - density pairs, used to calculate the densities of each voxel in the first step of the segmentation process (gdcm_setup) via interpolation between the CT number - density pairs. An additional entry was placed at (-5000,0), but was not plotted in the graph.

H.2 MANUAL SEGMENTATION USING ONCENTRA® EXTERNAL BEAM

Oncentra® External Beam (version 4.5.2, Nucletron B.V, Veenendaal, the Netherlands) was used for manual segmentation of body structures (see figures H.2-H.3). The external outline and the lungs are determined in Oncentra® using a threshold method.
The skin varies in thickness for different body regions (eye lids, vs. mechanically stressed regions (back, feet)), between 521 to 2400 µm for the epidermis and dermis (Lee and Hwang 2002; Wei et al. 2017). In this work, a thickness of 4 mm was used for the skin, by using an inner ROI margin of -4 mm on the external contour of the patient. As the external contour of the patient often includes a thin air or clothing seam, the actual skin thickness is between 3 and 4 mm. A thinner skin thickness was unfortunately not feasible due to computational limitations of the software (ROI margins of -2 mm or -3 mm resulted in "holes" in the skin, especially in the shoulder and hip region).

For the shell structures of the segmented organs, ROIs were defined with a margin of 2.5 mm inside and around the organs. Figure H.4 depicts the liver shell inside the organ and the surrounding tissue shell, each with a seam width of 2.5 mm.

Figure H.2: Screenshot of the contouring tool ("Target Definition") of the Oncentra® External Beam software. Structures are contoured on the axial computed tomography (CT) reconstructions.

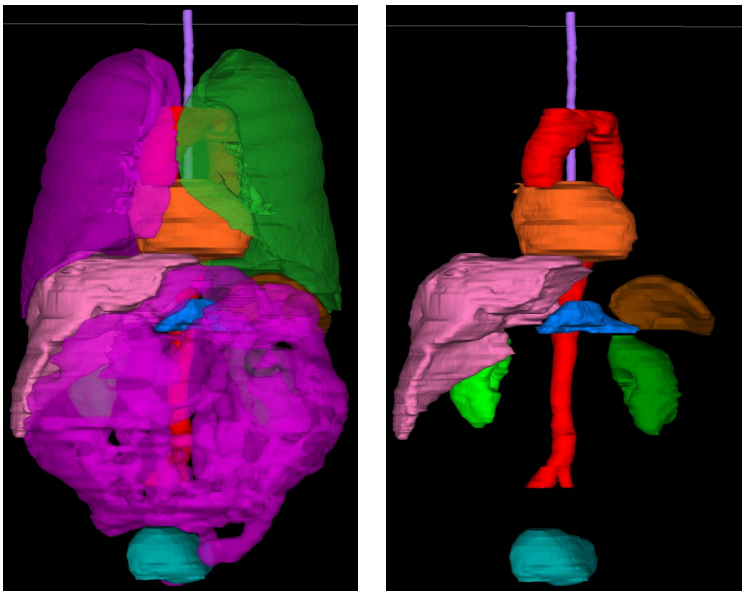

(a) All internal structures

(b) Lungs, stomach, and GI-tract removed for better visibility

Figure H.3: Contoured internal structures: Bone marrow (purple), lungs (right: pink, left: green), heart (orange), aorta (red), spleen (brown), kidneys (light and dark green), pancreas (blue), bladder (turqoise), and gastro-intestinal (GI) tract (pink). The skin is not shown.

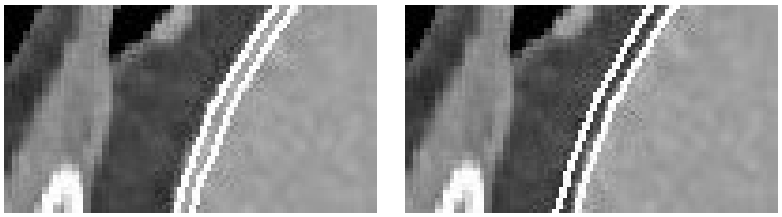

(a) Liver shell inside the organ

(b) Surrounding tissue shell

Figure H.4: Shell structure in the liver. The liver consists of an organ core (inside), an organ shell (a), and an outer tissue shell surrounding the liver (b).

H.3 COMBINATION OF SEGMENTED TISSUES AND STRUCTURES

Automatically and manually segmented materials for the acquisition of digitized patient phantoms are described in table H.1.

H.4 INITIALIZATION OF A SIMULATION

The input dicomdata.dat file (listing H.3) contains the compression value (1), number of files (5), file names and paths, the number of materials (15) and the individual

Table H.1: Automatic segmentation was performed for air, lung tissue, fat, water, soft tissue, and bones. Manual segmentation was performed for the pancreas, kidneys, heart, spleen, aorta, liver, and the skin (rows shaded in light gray). For contrast-enhanced acquisitions, iodine ($\psi_{iodine} = 0.005$) was added to the materials marked with an asterisk. The material compositions and densities are described in appendix B.

Structure/tissue	**Assigned material**	**Material ID**
air	air	[0]
lung inhale	lung inhale	[1]
lung exhale	lung exhale	[2]
fat	fat	[3]
water	water	[4]
pancreas	pancreas*	[5]
kidneys	kidney*	[6]
heart	muscle	[7]
soft tissue	soft tissue	[8]
spleen	spleen*	[9]
aorta	blood*	[10]
liver	liver*	[11]
skin	skin	[12]
trabecular bone	trabecular bone	[13]
dense bone	dense bone	[14]

material names with corresponding maximum density (density in g/cm^3). A compression value of 1 uses the matrix size taken from DICOM header, whereas a compression value of 2 reduces the number of pixels per file by a factor of 4 (e.g. instead of a 512 x 512 matrix, a matrix of 256 x 256 pixels is used). Each individual processed image file (provided in listing H.4) contains the number of materials (15), the material IDs and names, matrix size, x-,y-, and z-coverage, the relative TCTP value, followed by the individual material IDs and density values of each pixel.

Listing H.3: Input file (dicomdata.dat) to start simulations of digitized phantoms. In this example, only five computed tomography images are inserted in the simulation. The file includes information about the compression (1), number (5) and names of image files (Patient1A_nat33_101-105), number of materials (15), and material selection with maximum density values.

```
1                                              %compression
5                                              %number of input files
../filesforsimulation/Patient1A_nat33_101      %input files
../filesforsimulation/Patient1A_nat33_102
../filesforsimulation/Patient1A_nat33_103
../filesforsimulation/Patient1A_nat33_104
../filesforsimulation/Patient1A_nat33_105
```

```
15                              %number of materials
Air 0.03                        %materials with maximum density
LungInhale 0.390
LungExhale 0.910
AdiposeTissue 0.98
Water 1.02
Pancreas 1.05
Kidney 1.06
Muscle 1.06
SoftT 1.09
Spleen 1.06
Blood 1.07
Liver 1.07
Skin 1.11
TrabecularBone 1.165
DenseBone 1.654
```

Listing H.4: For each image, one simulation file (Patient1A_nat33_ImageNumber.g4dcm) is produced. It contains the number of materials (15), the material identifications (ID) and names, image matrix size, x-, y- and z-coverage (in mm) of the image, the exposure value (in mAs), and all material IDs and densities (in g/cm^3) per pixel. In this example, material IDs and densities do not correspond to each other and are solely exemplary chosen.

```
15                              %number of materials
0 Air                           %material ID and name
1 LungInhale
2 LungExhale
3 AdiposeTissue
4 Water
5 Pancreas
6 Kidney
7 Muscle
8 SoftT
9 Spleen
10 Blood
11 Liver
12 Skin
13 TrabecularBone
14 DenseBone
512 512 1                       %matrix size
-229 229                        %x-coverage [mm]
-229 229                        %y-coverage [mm]
-1428 -1425                     %z-coverage [mm]
162                             %exposure [mAs]
12 4 8 8 4 3 3 5                %material IDs
1.51154 0.950769 0.551923 0.958077 0.356538 0.23846 0.756538
   0.956154                     %densities [g/cm3]
```

I

COMPARISON OF PATIENT MORPHOLOGY

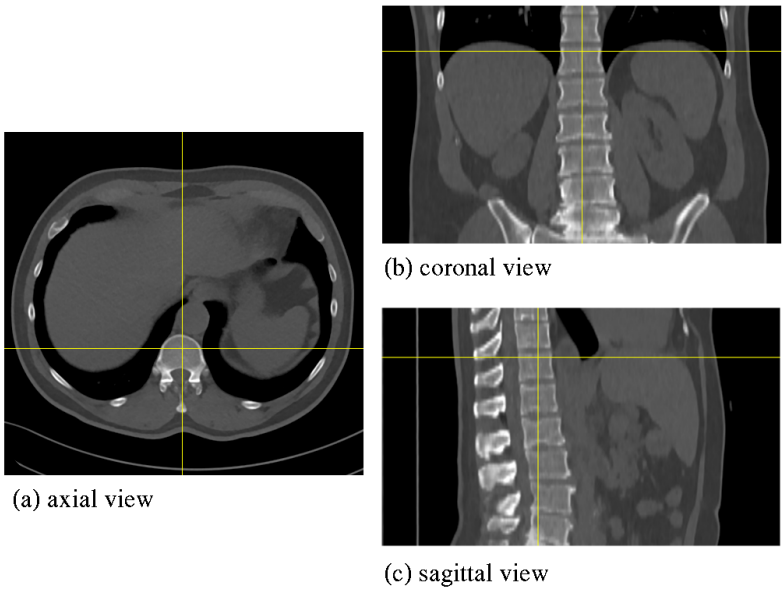

(a) axial view

(b) coronal view

(c) sagittal view

Figure I.1: Corresponding axial, coronal, and sagittal computed tomography (CT) images of patient 3A for the 2D-energy maps presented in the results (figure 3.19).

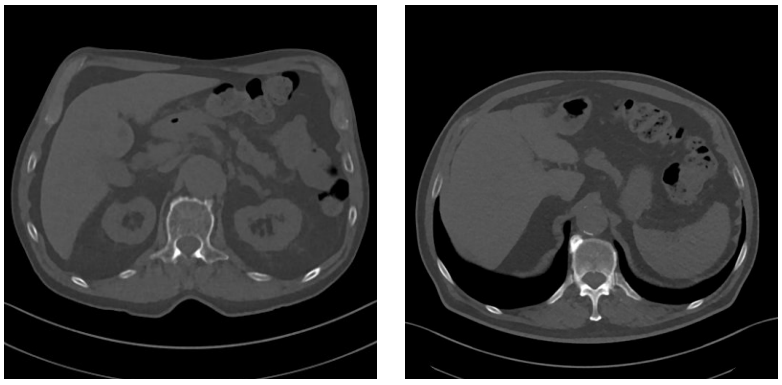

(a) Patient1A (b) Patient 2A

Figure I.2: Corresponding axial computed tomography (CT) images of patients 1A and 2A for the 2D-energy maps presented in the results. (a) Patient 1A from figure 3.20 and (b) patient 2A from figure 3.19.

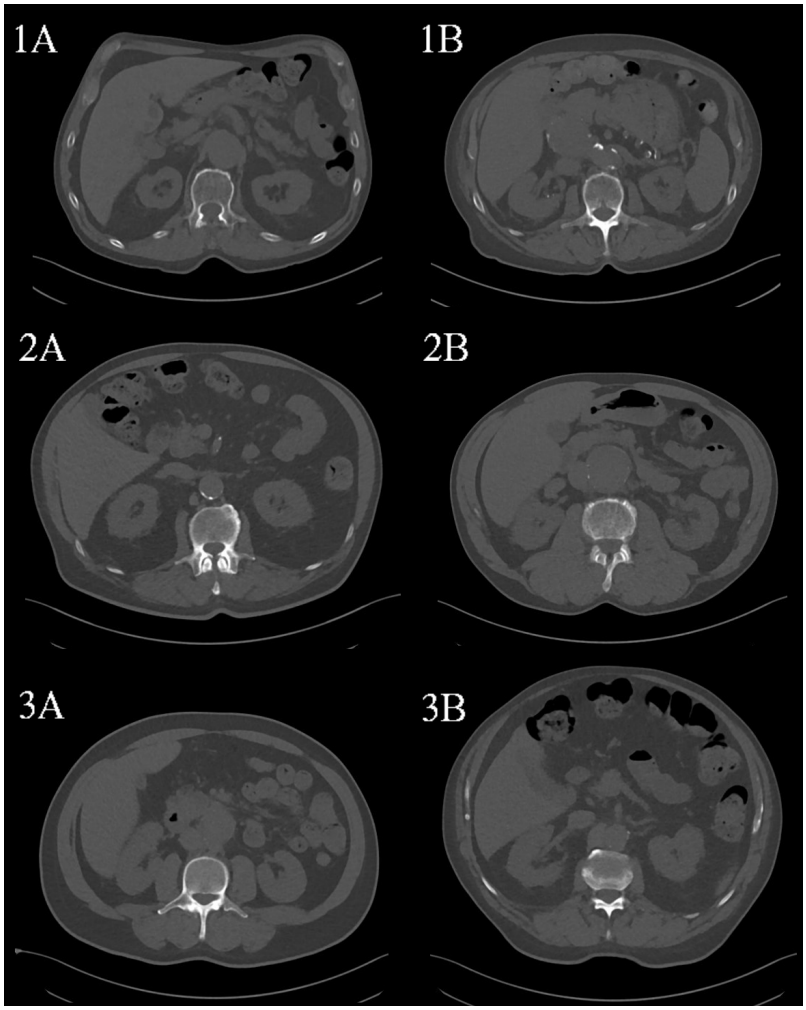

Figure I.3: Axial slices through the liver and kidneys for the six patients of this study. Patients 1A and 1B belong to the group with the lowest body mass index (BMI) (BMIs 21.0 and 22.0, respectively), patients 2A and 2B belong to the group with a medium BMI (BMIs 26.4 and 25.4, respectively) and, patient 3A and 3B belong the group with the highest BMI (BMIs 28.1 and 28.4, respectively). In each group, patients have simular heights and weights (see table. 2.2). Abdominal diameters varied considerably among patients.

J

ERROR CALCULATION IN MC SIMULATIONS OF CT ACQUISITIONS

This section of the appendix provides a small review about the error calculation in MC simulations of CT acquisitions available in the literature and evaluates the simulated number of incident photons on the accuracy of the performed simulations. Regarding MC simulations in CT, there are only a handful of publications which provide information on the used MC method, CT acquisition parameters, and error calculations in detail. Most publications employ commercial software, where only a specific TCTP-value, but not the corresponding number of incident photons (or a conversion factor) are given.

Li et al. (2011a) aimed at a relative error in dose of 1% or below, defined "as one standard deviation divided by the average tally result". In their subsequent study, determining the patient-specific radiation dose in patients, they tracked $80 \cdot 10^6$ photons for each CT acquisition (chest, abdomen-pelvis) of each patient (Li et al. 2011b). Patients in their study were a newborn female and a teenaged male, for which digitized phantom models were voxelized at 0.5 and 1 mm isotropic resolutions, respectively. For the employed $80 \cdot 10^6$ photons, they calculated relative dose errors of <1% in organs in the scan coverage (chest or abdomen-pelvis), and < 3% in organs outside the scan coverage. However, they claim that $7 \cdot 10^6$ photon histories were sufficient to achieve relative dose errors of <1% for all organs in the scan coverage and < 10% for other organs (Li et al. 2011b).

Nowik et al. (2017) use the commercial available software package ImpactMC (AB-CT Advanced Breast-CT GmbH, Erlangen, Germany) and employed $1 \cdot 10^{10}$ photons with 72 projections per rotation, and $5 \cdot 10^9$ photons for a projection scan (similar to a topogram) for a full body scan (no automatic tube-current modulation (TCM) was included). They repeated their simulations until the relative standard deviation of their mean achieved dose was <2% in the noisiest ROI in the phantom (Nowik et al. 2017).

Fujii et al. (2017) employed $1 \cdot 10^{11}$ photon histories for chest and abdominal-pelvic CT acquisitions, independent on the exact scan range, using the ImpactMC software. They obtained an uncertainty of the MC results of <1% within the scan range.

Salvadó et al. (2005) employed $3 \cdot 10^6$ photon histories per 1 cm-image slice for patients and anthropomorphic phantoms. Voxelized phantoms consisted of a 256 x 256 x N_s matrix, with a slice thickness of 1 cm. The minimum voxel size was $1.4 \times 1.4 \times 10\,mm^3$, the maximum voxel size was $1.7 \times 1.7 \times 10\,mm^3$. A relative standard error of the average dose in one slice of <0.5% was reached for slices directly scanned. Outside the scan region, a relative error of 1% is reached (Salvadó et al. 2005). During this work, the employed number of photons for the anthropomorphic phantoms ($3 \cdot 10^6$ tracked photons per 1 cm-image slice) was calculated based on Salvadó et al. (2005). Although uncompressed CT images were used in the simulations

in this work (512 x 512 matrix), energy maps were calculated for a 256 x 256 matrix.

PHOTON INTERACTION TYPES IN REDUCED INCIDENT PHOTON STATISTICS DATA STACKS To evaluate the possibility of reducing the number of initial photons in a MC simulation of a CT acquisition, photon interaction data was subdivided into data sets with reduced number of photon statistics (see section 2.6). Of these reduced statistics data sets, 2D-energy maps were calculated and compared to the original energy map.

Figure J.1 confirms that the reduced statistics data sets contain the same type and frequency of photon interactions. Multiple scattering and Compton effects are most frequent, whereas the photoelectric interactions are less frequent. All reduced data sets also contain equal energy deposition distributions of the individual interactions (results not shown). Since the reduced statistics data sets contain the same type and frequency of photon interactions, and equal energy deposition distributions, a comparison of the resulting energy maps is reasonable and feasible.

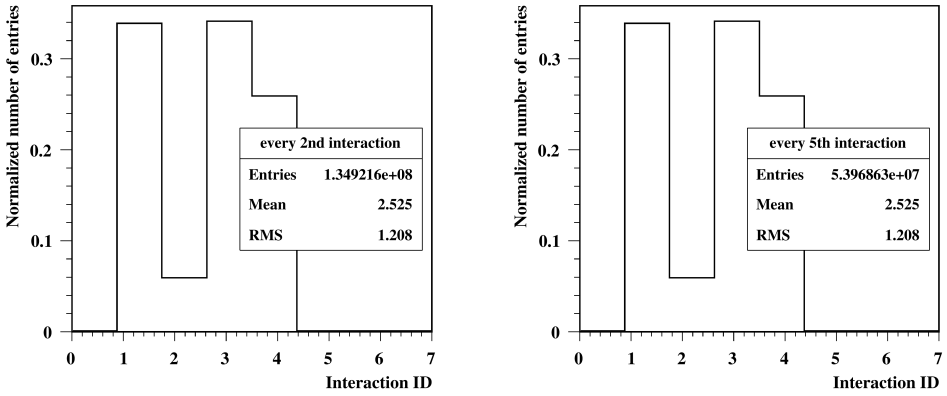

(a)

(b)

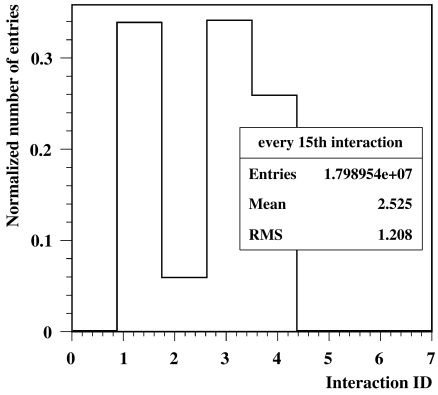

(c)

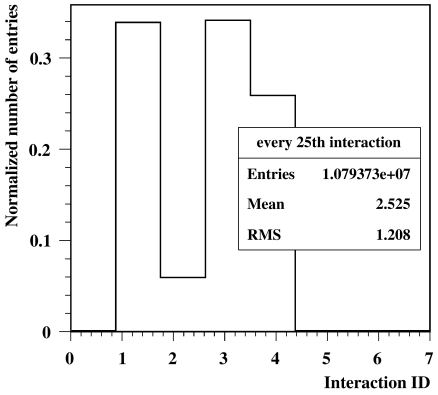

(d)

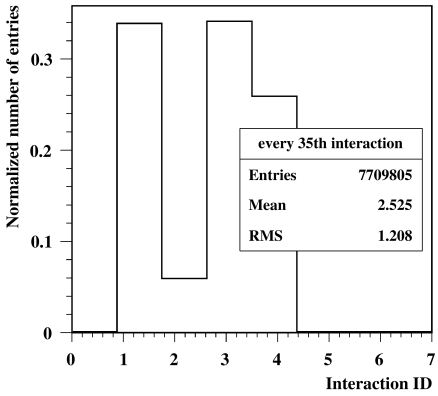

(e)

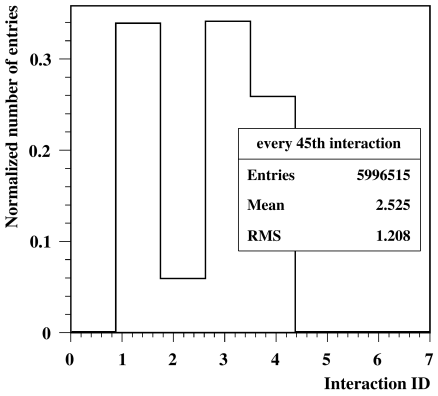

(f)

Figure J.1: Present interactions in reduced statistics data sets. For each of the reduced statistics data sets, photon interactions were histogrammed and normalized to allow for direct comparison. For all reduced statistics data sets, the same type and frequency of photon interactions are occurring. Interaction IDs: Compton effect (1), photoelectric effect (2), ionization (3), multiple scattering (4), bremsstrahlung (5), coupled transportation (6).

ACKNOWLEDGMENTS

Zum Ende dieser Doktorarbeit möchte ich mich noch einmal ganz herzlich bei den Menschen bedanken, die diese Arbeit begleitet haben. Zum einen möchte ich mich bei Dr. Wolfram Stiller für die Betreuung, für stets gute Einfälle, Übersicht und Unterstützung bei der Arbeit bedanken, und zum anderen bei meinem Doktorvater Prof. Dr. Hans-Ulrich Kauczor für die Ermöglichung des Projekts.
Ein besonderer Dank gilt auch Dr. Stephan Skornitzke, Dr. Oyunbileg von Stackelberg, Dr. Simon Triphan, Iven Fellhauer, Dr. Fabian Rengier, Matthias Fink, Gregor Pahn, Dr. Jens Hansen, für die gute Zusammenarbeit, Diskussionen rund um's Forschen und Backen und die ein oder andere Kaffeepause.
Vielen Dank an die Bestrahlungsplanungs-MTRAs in der Strahlentherapie bei denen ich die Patienten konturieren durfte.
Ein großes Dankeschön geht an alle Freunde aus Heidelberg, der Heimat und dem Studium, die für die notwendige Ablenkung und den Abstand von der Doktorarbeit gesorgt haben. Zu guter Letzt geht noch einen riesen Dank an meine Familie, die mir während der Doktorarbeit und darüber hinaus mit Rat und Tat zur Seite stand.

EIDESSTAATLICHE VERSICHERUNG

1. Bei der eingereichten Dissertation zu dem Thema *„Spatially resolved quantification of radiation exposure associated with computed tomography examinations: Towards the development of virtual dosimetry“* handelt es sich um meine eigenständig erbrachte Leistung.

2. Ich habe nur die angegebenen Quellen und Hilfsmittel benutzt und mich keiner unzulässigen Hilfe Dritter bedient. Insbesondere habe ich wörtlich oder sinngemäß aus anderen Werken übernommene Inhalte als solche kenntlich gemacht.

3. Die Arbeit oder Teile davon habe ich bislang nicht an einer Hochschule des In- oder Auslands als Bestandteil einer Prüfungs- oder Qualifikationsleistung vorgelegt.

4. Die Richtigkeit der vorstehenden Erklärungen bestätige ich.

5. Die Bedeutung der eidesstaatlichen Versicherung und die strafrechtlichen Folgen einer unrichtigen oder unvollständigen eidesstaatlichen Versicherung sind mir bekannt. Ich versichere an Eides statt, dass ich nach bestem Wissen die reine Wahrheit erklärt und nichts verschwiegen habe.

Heidelberg, 2019

Andrea Steuwe